COMPUTATIONAL SIMULATION OF PLATELET TRANSPORT, ACTIVATION, AND DEPOSITION

by

Erik Nathaniel Sorensen

BSE, Mechanical Engineering, The University of Michigan, 1996

Submitted to the Graduate Faculty of

the School of Engineering, Bioengineering Department, in partial fulfillment

of the requirements for the degree of

Doctor of Philosophy

University of Pittsburgh

2002

UNIVERSITY OF PITTSBURGH

SCHOOL OF ENGINEERING

This dissertation was presented

by

Erik Nathaniel Sorensen

It was defended on

October 17, 2002

and approved by

Harvey S. Borovetz, Ph.D., Professor, Departments of Bioengineering and Surgery

Greg W. Burgreen, Ph.D., Adjunct Assistant Professor, Department of Bioengineering

William J. Federspiel, Ph.D., Associate Professor, Departments of Chemical Engineering, Bioengineering, and Surgery

William R. Wagner, Ph.D., Associate Professor, Departments of Bioengineering, Surgery, and Chemical Engineering

Dissertation Director: James F. Antaki, Ph.D., Associate Professor, Departments of Bioengineering and Surgery

ABSTRACT

COMPUTATIONAL SIMULATION OF PLATELET TRANSPORT, ACTIVATION, AND DEPOSITION

Erik Nathaniel Sorensen, Ph.D.

University of Pittsburgh, 2002

Platelet-mediated thrombosis is a significant source of morbidity and mortality in cardiovascular device patients. Although Virchow elucidated the mechanisms governing thrombus formation over 100 years ago, the underlying processes have proven difficult to describe mathematically. A reliable, predictive thrombosis model would be a valuable aid to designers of artificial organs.

A comprehensive model of platelet-mediated thrombogenesis should simulate red-cell-enhanced platelet transport, platelet activation, kinetics and mechanics of platelet deposition and aggregation, flow disturbances due to thrombus growth, thrombus disruption by fluid forces, and interactions between platelets and the coagulation cascades. Most models focus on these components individually; a unified approach is lacking.

The contribution of this thesis is a computational model of platelet thrombosis which incorporates many, though not all, of these essential components. This two-dimensional continuum model, based on prior work, is comprised of seven coupled species conservation equations, which model shear-enhanced platelet transport, platelet-platelet and platelet-surface adhesion, agonist-induced platelet activation, platelet-phospholipid-dependent thrombin generation, and heparin-catalyzed thrombin inhibition.

The model is first validated for Poiseuille flow of whole human blood over collagen. Very good agreement between predicted and experimentally measured platelet deposition is obtained for wall shear rates ranging from 100 to 1000 s^{-1}. At 1500 s^{-1}, however, the model fails to predict the shape of the experimental curve. This may be due to the higher shear rate, or to unmodeled effects of the chelating agent used as the anticoagulant in this study.

Next, two-dimensional flow over collagen is considered. For a tubular expansion with no agonists, good agreement with experiments can be obtained in the recirculation zone, but deposition in the fully-developed downstream region is greatly under-predicted. Surprisingly, deviation from experiments is worse at 0% than at 20% hematocrit. Similarly, for an axisymmetric stenosis with agonists present, the model does most poorly at predicting deposition in the downstream regions.

These discrepancies are attributed to the approximation of blood as a single continuum, rather than as a suspension. In a preliminary step toward correcting these deficiencies, an attempt is made to use existing two-phase flow models to predict platelet and red blood cell concentrations in fully-developed tube flow.

PREFACE

Since no one reads this, I'll try to keep it brief. First, I need to acknowledge the folks who paid the bills during my six-year tenure at Pitt. My first year was supported by the Keck Foundation. The five remaining years were supported by a Whitaker Foundation Graduate Research Fellowship, for which I am extremely grateful. It is probably one of the most generous fellowships available, providing not only tuition and stipend support for up to five years, but also funds for educational expenses and meeting travel. Additionally, the State of Pennsylvania provided a generous grant to Dr. Burgreen which funded a much-needed upgrade to our computing facilities, thereby allowing me to churn out irreproducible results at break-neck speed.

Next, I'd like to thank the faculty who helped me along the way. My co-advisor, Greg Burgreen, taught me not only most of what I know about computational methods, but also about how to think and work independently…and he somehow manage to stifle his laughter every time I had to tell him my last three months of case runs were worthless because of an undiscovered bug in the code. My other co-advisor, Jim Antaki, was there to help when I needed it, and, like Greg, left me alone to do my work the rest of the time. He also spent an inordinate amount of time helping me edit and improve this dissertation, despite my desire to just crank it out and get it over with. Bill Wagner was in essence a third co-advisor. His insights into the biological aspects of thrombosis were invaluable in guiding the development of the model, as well as in gearing it toward having as much "real-world" relevance as possible. Finally, any Pitt BioE student whose experience here hasn't been enhanced by knowing Harvey Borovetz shouldn't be allowed to have a diploma. He's basically always there to help with whatever you need, and has helped me in more ways than I can mention, although I'm not sure whether I should count talking me into running a marathon among them or not. He was an excellent mentor for my TA rotations, helping me discover I enjoyed teaching undergrads a lot more than I ever thought I would…I can only hope I retain his sunny disposition if I end up doing it for as many years as he has!

Finally and most importantly, I doubt anybody can make it through the frustrations of Ph.D. research without a social support system. I'm fortunate to have two parents, Marilyn and George, who've not only supported me unconditionally in all my endeavors, but who also instilled in me the work ethic and values to be (more or less) successful at most of them. Not only that, but they never once uttered the parental phrase every grad student dreads: "So when are you gonna graduate and get a job?". I also need to specifically thank the friends who've listened to my bitching and moaning, chiefly Eric Ruka, who has endured more hours of complaints than anyone should have to; my brother Doug comes in a close second. Of course, there's no one better to commiserate with than a fellow grad student, especially one with whom you can tour the great breweries of the world, and for that purpose Ken Gage has always been available (probably too available, if you ask Mrs. Gage). And there are plenty of other friends and colleagues too numerous to mention who've helped make my stay here more pleasant – hopefully if you're in this group, you know who you are and that I appreciate you!

TABLE OF CONTENTS

LIST OF TABLES

LIST OF FIGURES

NOMENCLATURE

Abbreviations

$[a_j]$	Concentration of *j*th PLT-activating species, μM (TxA_2, ADP) or U ml^{-1} (thrombin)
$[a_{j,crit}]$	Threshold concentration of *j*th PLT-activating species for PLT activation, μM (TxA_2, ADP) or U ml^{-1} (thrombin)
$[a_{pr}]$	Concentration of a PLT-released agonist, μM
$[a_{ps}]$	Concentration of a PLT-synthesized agonist, μM
A	Augmentation factor for skewed PLT concentration profile at inlet
A_{ROI}	Area of a region of interest in collagen-coated stenosis, cm^2
ADP	Adenosine diphosphate
$[AP]$	Concentration of activated PLTs, PLT ml^{-1}
$[AT]$	Concentration of antithrombin III (ATIII), μM
ATIII	Antithrombin III
C_S	Constant for Reynolds stress term in effective fluid viscosity, $s^{-1/2}$
C_0	Bulk resting or activated PLT concentration for skewed profile at inlet, PLT ml^{-1}
C_∞	Bulk platelet concentration in Wootton model (Equation 24), PLT ml^{-1}
Ca^{++}	Calcium ion
CFD	Computational fluid dynamics
div	Divergence operator
d_p	Particle diameter, cm
d_{rbc}	Red blood cell diameter, cm
d_T	Tube diameter, cm
Da	Damkohler number (for PLT-surface reactions) = $k \cdot H / D_{PLT}$
$D_{b,i}$	Brownian diffusivity of species *i*, $cm^2\ s^{-1}$

NOMENCLATURE (CONTINUED)

$\mathbf{D_f}$	Fluid-phase rate-of-deformation tensor
D_i	Total diffusivity of species i, $cm^2\ s^{-1}$
D_s	"Shear-enhanced" diffusivity, $cm^2\ s^{-1}$
e	Particle-particle coefficient of restitution
e_w	Particle-wall coefficient of restitution
$\mathbf{F_L}$	"Slip-shear" lift force, $g\ cm^{-2}\ s^{-2}$
g	Gravitational constant, $cm\ s^{-2}$
g_0	Equilibrium radial distribution function
GpIIbIIIa	Glycoprotein IIbIIIa receptor complex
GpIb	Glycoprotein Ib receptor complex
grad	Gradient operator
H	Flow channel half-height, cm
$[H]$	Concentration of heparin, μM
Hct	Hematocrit
HMWK	High-molecular-weight kininogen
$J_a(x,t)$	Flux of adhering activated PLTs at a reactive wall, PLT $cm^{-2}\ s^{-1}$
$J_{pr}(x,t)$	Flux of a PLT-released agonist at a reactive wall, nmol $cm^{-2}\ s^{-1}$
$J_{ps}(x,t)$	Flux of a PLT-synthesized agonist at a reactive wall, nmol $cm^{-2}\ s^{-1}$
$J_{pt}(x,t)$	Flux of prothrombin at a reactive wall, nmol $cm^{-2}\ s^{-1}$
$J_r(x,t)$	Flux of adhering resting PLTs at a reactive wall, PLT $cm^{-2}\ s^{-1}$
$J_t(x,t)$	Flux of thrombin at a reactive wall, U $cm^{-2}\ s^{-1}$
k''	Second-order reaction rate constant for thrombin inhibition by ATIII alone, $\mu M^{-1}\ s^{-1}$
k_{aa}	Heterogeneous reaction rate constant for activated PLT-PLT adhesion, $cm\ s^{-1}$
k_{as}	Heterogeneous reaction rate constant for activated PLT-surface adhesion, $cm\ s^{-1}$
k_{at}	Rate of thrombin generation from prothrombin on activated PLTs, U $PLT^{-1}\ s^{-1}\ (\mu M\ PT)^{-1}$
k_j	First-order reaction rate constant for inhibition of jth PLT agonist, s^{-1}

NOMENCLATURE (CONTINUED)

k_{pa}	First-order reaction rate constant for PLT activation by agonists, s^{-1}
k_{rs}	Heterogeneous reaction rate constant for resting PLT-surface adhesion, cm s^{-1}
k_{rt}	Rate of thrombin generation from prothrombin on resting PLTs, U PLT^{-1} s^{-1} $(\mu M\ PT)^{-1}$
k_T	First-order reaction rate constant for thrombin inhibition model, s^{-1}
K_{AT}	Heparin/ATIII dissociation constant, μM
K_T	Heparin/thrombin dissociation constant, μM
L_b	PLT excess boundary layer thickness, cm
L_G	Measure of average grid element length over entire grid, cm
L_{CV}	Measure of local grid element length, cm
$M(x,t)$	Total surface coverage with PLTs, PLT cm^{-2}
$M_{as}(x,t)$	Surface coverage due to activated PLTs, PLT cm^{-2}
$M_{at}(x,t)$	Total activated PLT deposition, PLT cm^{-2}
$M_r(x,t)$	Surface coverage due to resting PLTs, PLT cm^{-2}
p	Fluid pressure, dynes cm^{-2}
p^i	Pressure of phase i, dynes cm^{-2}
PKn	Prekallikrein
PEG	Poly(ethylene glycol)
PLT	Platelet
$[PT]$	Prothrombin concentration, μM
$q^s{}_r$	Wall flux of particle kinetic energy, dynes cm^{-1} s^{-1}
Q^{i*}	Non-dimensional volumetric flow rate for phase i
RBC	Red blood cell
Re	Reynolds number (in tube flow) = $\rho \cdot U \cdot d_T / \mu$
ROI	Region of interest
$[RP]$	Resting PLT concentration, PLT ml^{-1}
S_i	Volumetric source term for species i
S^i_j	Body force for phase i in j-momentum equation, g cm^{-2} s^{-2}

NOMENCLATURE (CONTINUED)

S_{cyl}	r-direction source term due to cylindrical coordinate system, g cm^{-2} s^{-2}
S_{Dj}	j-direction drag source term, g cm^{-2} s^{-2}
$S_{\Gamma j}$	j-direction diffusion source term, g cm^{-2} s^{-2}
S_R	Reynolds-stress-like fluid viscosity term, s^{-1}
S_T	Solid-phase external kinetic energy source term, dynes cm^{-2} s^{-1}
S_ψ	Solid-phase volume-fraction-gradient-dependent kinetic energy source term, dynes cm^{-2} s^{-1}
$S(x,t)$	Fraction of surface available for PLT-surface adhesion
$s_{p,j}$	Rate of synthesis of jth agonist by PLTs, nmol PLT^{-1} s^{-1}
t	Time, s
t_{act}	Characteristic time for PLT activation, s
T	Granular temperature, cm^2 s^{-2}
$[T]$	Thrombin concentration, U ml^{-1}
TF	Tissue factor
TxA_2	Thromboxane A_2
$\mathbf{u}$	Velocity vector, (u_x, u_y) or (u_z, u_r), cm s^{-1}
u^i_j	Velocity of phase i in j-direction, cm s^{-1}
U	Mean velocity, cm s^{-1}
U_{max}	Maximum velocity of Poiseuille flow profile, cm s^{-1}
V_{max}	Maximum platelet accumulation velocity, cm s^{-1}
w_j	Agonist-specific weight for PLT activation function
W_p	Solid-phase pressure work term, dynes cm^{-2} s^{-1}
x	Distance in axial direction or along reactive surface, cm
y	Distance in longitudinal direction, cm

Greek Symbols

β	Conversion factor to convert thrombin from U ml^{-1} to μM, nmol U^{-1}
Δ	Laplacian operator
ϕ	Generic dependent variable
ϕ'	Specularity factor for particle-wall collisions

NOMENCLATURE (CONTINUED)

Φ^s	Solid-phase viscous dissipation source term, dynes cm^{-2} s^{-1}
γ_B	Solid-phase energy exchange source term, dynes cm^{-2} s^{-1}
γ_C	Solid-phase collisional dissipation source term, dynes cm^{-2} s^{-1}
γ_D	Solid-phase drag dissipation source term, dynes cm^{-2} s^{-1}
$\dot{\gamma}$	Local fluid shear rate, s^{-1}
$\dot{\gamma}_w$	Fluid shear rate at the wall, s^{-1}
Γ	Catalytic reaction model for thrombin inhibition by heparin-ATIII, s^{-1}
Γ_e	Generic effective diffusion coefficient
Γ_b	Generic bulk diffusion coefficient
η	Constant related to e, $\eta = (1 + e)/2$
κ^s_T	Granular temperature diffusion coefficient, g cm^{-1} s^{-1}
κ^s_ψ	Coefficient for volume-fraction-gradient-induced diffusion, g cm s^{-1}
λ_j	Amount of agonist j released per activated PLT, nmol PLT^{-1}
μ, μ^f	Fluid viscosity, g cm^{-1} s^{-1}
μ^i_b	Bulk viscosity of phase i, g cm^{-1} s^{-1}
μ^i_e	Effective viscosity of phase i, g cm^{-1} s^{-1}
μ^f_r	Fluid-phase relative viscosity, g cm^{-1} s^{-1}
θ	Fraction of adhering, resting PLTs which activate upon surface contact
ρ	Fluid density, g cm^{-3}
ρ^i	Density of phase i, g cm^{-3}
σ^i_{rz}	Wall shear stress of phase i, dynes cm^{-2}
Ω	Weighted PLT activation function
ξ	Change in (ATIII, thrombin) affinity of heparin when bound to (thrombin, ATIII)
ψ^i	Volume fraction of phase i
ζ_D	Drag force coefficient, g cm s^{-3}

1.0 BACKGROUND

"The average Ph.D. thesis is nothing but a transference of bones from one graveyard to another."

-J. Frank Dobie

1.1 Introduction

When damage to a blood vessel occurs, the body's hemostatic mechanisms are called into action to create a clot (thrombus) at the site of injury, thereby preventing unnecessary bleeding. However, in certain abnormal situations, these mechanisms fail to work as intended. Simply put if they do too little, the result is a hemorrhage; if they do too much, the result is pathologically overactive clotting, or thrombosis.

Thrombosis is a serious medical complication because excessive clot formation can lead to obstruction of blood vessels, resulting in tissue ischemia or death. In addition to occluding the blood vessel where it was formed, it is also possible for a thrombus to break free (embolize) and lodge somewhere downstream in the microcirculation, the most deleterious possibility being a brain infarction if it finds its way into a cerebral artery.

Thrombosis and thromboembolism are important from an engineering perspective because they are significant sources of morbidity and mortality in cardiovascular device patients (1). For example, thrombotic complications afflict approximately 1-2% of coronary artery stent recipients (2-4), from 4-5% (5) to > 20% (6) of those receiving prosthetic heart valves, and anywhere from approximately 5% (7) to 45% (8) of ventricular assist device patients. Thrombosis is also the primary reason for early failure of small-diameter (≤ 6 mm) synthetic vascular grafts (9, 10), which are essentially unusable due to their low patency rates. An important objective in designing the next generation of these devices is to minimize their thrombotic complication rates. As in any engineering analysis, this requires a mathematical model which can predict the failure mode(s) one wishes to avoid. At present, there is no such model for thrombosis or thromboembolism. The **specific aims** of this thesis are to develop and to validate a computational model of thrombosis relevant to the conditions prevalent in cardiovascular devices. It is hoped that this will one day lead to improved computational design strategies for these devices.

1.2 Virchow's Triad

Although unraveling the many complex and intertwined chemical and biological processes that lead to thrombus formation is a continuing challenge for modern medical research, the primary factors governing thrombosis were identified nearly 150 years ago by the German pathologist Rudolf Virchow (11). He described three participating elements – the well-known "Virchow's triad" of blood, surface, and flow. The contributions of each "leg" of the triad to the thrombotic process are described below.

1.2.1 Blood

To maintain normal hemostasis, it is necessary to have the appropriate balance between pro- and anti-coagulant constituents in the blood. The blood elements primarily responsible for coagulation are the coagulation factors, typically identified by Roman numerals I – XIII, and platelets. Clotting can be achieved via either of two coagulation factor cascades, or via platelet aggregation and deposition. However, all three feed into and depend upon one another, meaning none usually occurs independent of the others. What follows is a brief overview of these complex processes. More detail can be obtained from any basic physiology text, e.g. Guyton & Hall (12), and the references therein.

Figure 1 illustrates the coagulation cascades. In the figure and the ensuing text, the lowercase suffix "a" after the Roman numeral representing a coagulation factor refers to the activated form of that factor. In the intrinsic cascade, all factors necessary for coagulation are present in the blood. Factor XII adsorbs to a foreign surface, which may be the subendothelium of an injured blood vessel or the man-made material in an implanted device. Prekallikrein (PKn) and high-molecular-weight kininogen (HMWK) contact the surface-bound factor XII, activating it and transforming PKn to kallikrein, which dissociates from HMWK. The free HMWK can now bind to factor XI, and this complex adsorbs to the same surface as XIIa, resulting in activation of factor XI. Next, XIa activates factor IX. Ionic calcium (Ca^{++}) facilitates the binding of IXa, X, and VIII to a negatively charged phospholipid bilayer surface, such as the membrane of a procoagulant platelet. Once the factor VIII in this complex is activated by thrombin (factor IIa), activation of factor X ensues.

The extrinsic cascade, on the other hand, requires the exposure of tissue factor (TF), typically on an injury site or on the membranes of inflammatory cells such as monocytes. In the presence of Ca^{++} and a phospholipid bilayer, TF activates factor VII. The TF-VIIa complex then

activates factor X. Both cascades terminate in the common pathway, which begins when Xa combines with membrane-bound factor V. Factor Xa alone can activate prothrombin (factor II), but its action is greatly accelerated once thrombin begins to activate factor V to create the factor Va-Xa complex. Thrombin then cleaves fibrinogen (factor I) into fibrin monomer (Ia_M). In the presence of Ca^{++}, thrombin also activates factor XIII. XIIIa facilitates creation of cross-links between the Ia_M molecules, thereby forming a much stronger fibrin polymer (Ia_P), which comprises the hemostatic "plug".

Figure 2 illustrates platelet-mediated coagulation. This process begins when platelets (PLTs) are activated by stimuli (agonists) such as adenosine diphosphate (ADP), thromboxane A_2 (TxA_2), serotonin, or thrombin. These stimuli cause platelets to: 1) change shape, from discoid to spherical; 2) extrude pseudopodial filaments from their outer surfaces; 3) "flip-flop" their phospholipid bilayer membranes so that procoagulant phosphatidylserine is exposed; 4) express adhesive receptors (glycoproteins IIbIIIa and Ib, GpIIbIIIa and GpIb, respectively) on their outer membranes; and 5) release serotonin and ADP from their storage granules, as well as synthesize TxA_2. The exposed receptors allow activated platelets to adhere to proteins on a foreign surface (e.g., man-made biomaterial) or to the subendothelium exposed by an injury; once adherent, the pseudopodia allow them to spread out and become firmly anchored. The released agonists combine with those already present to activate any resting platelets in the vicinity. Then, using fibrinogen as a bridge between GpIIbIIIa receptors, these activated platelets, with the aid of Ca^{++}, can adhere to those already on the surface, forming an aggregate which stems the flow of blood. More detailed reviews of these mechanisms are available (13-15).

As mentioned above, the three hemostatic mechanisms interact. TF-VIIa from the extrinsic cascade can activate factor IX, starting the intrinsic cascade without the factor XII- and XI-dependent steps shown in Figure 1. Also, thrombin from the coagulation cascades is a potent activator of platelets, and, in a feedback loop, phosphatidylserine on the outer membrane of activated platelets provides the phospholipid bilayer surface needed by the coagulation cascades to generate additional thrombin. This thrombin generation not only results in activation of more resting platelets, but also induces formation of a fibrin mesh on top of the platelet aggregate, forming an even stronger clot. Finally, activated platelets release factors I, V, and XIII, thereby further contributing to the common pathway of coagulation and to further platelet aggregation and fibrin mesh stabilization.

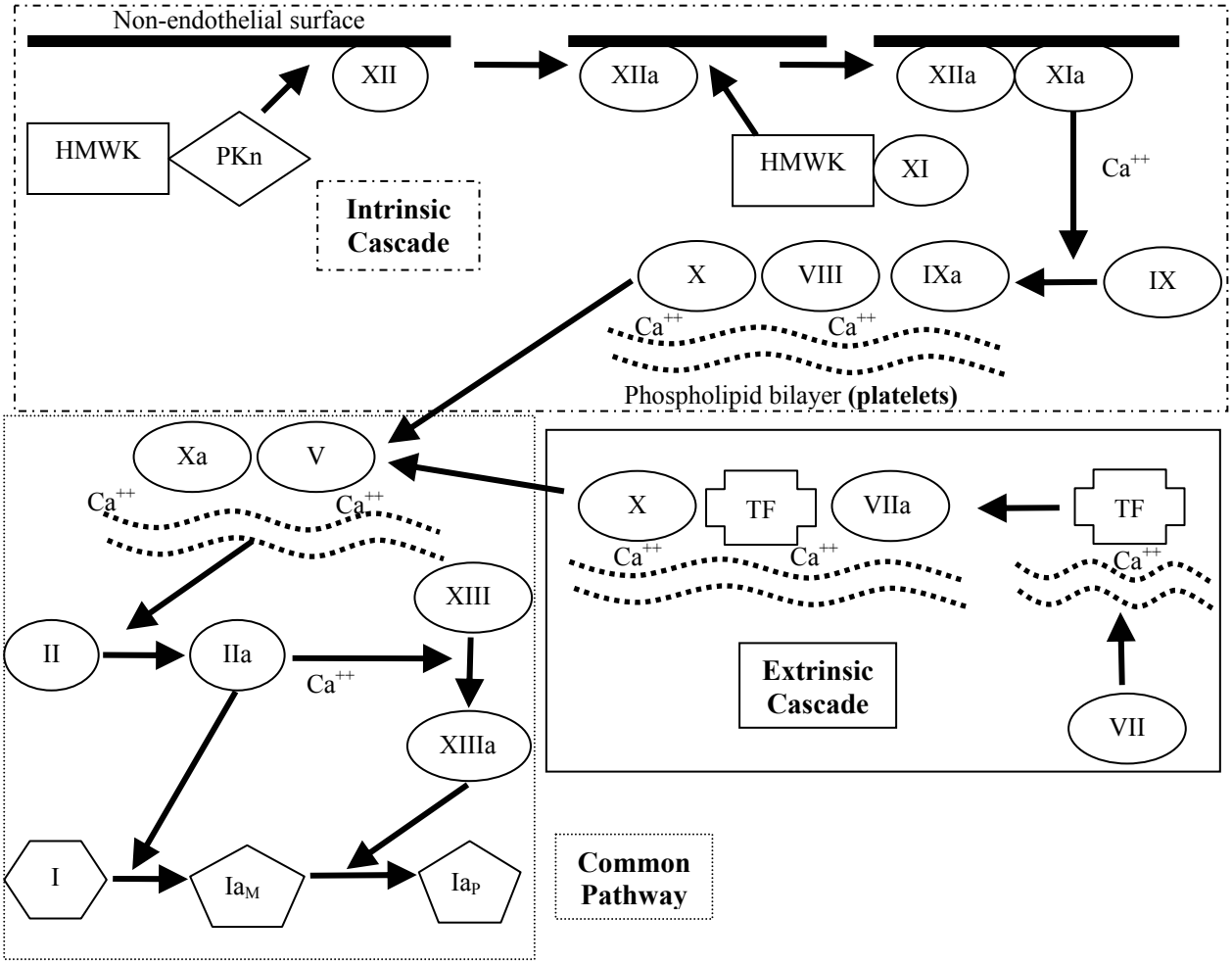

Figure 1. Coagulation cascades

Inhibitory and feedback pathways omitted. See text for abbreviations.

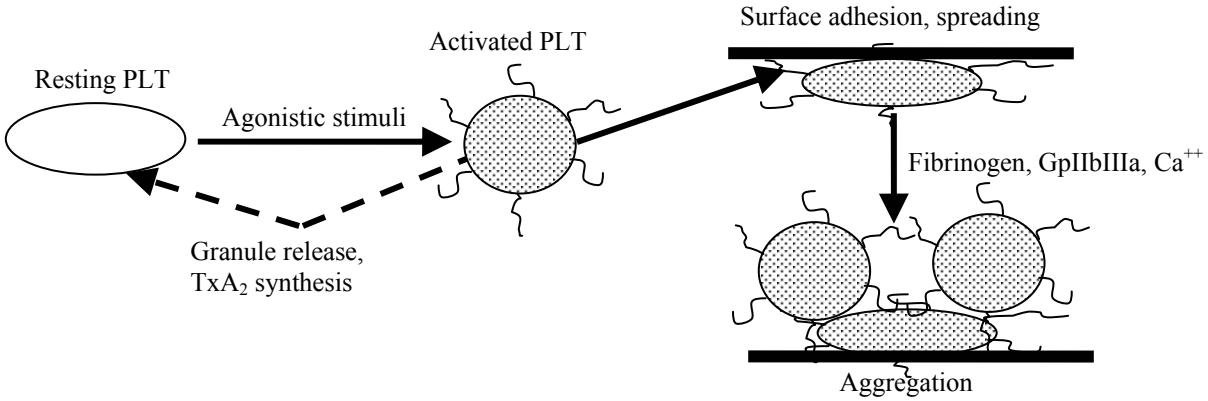

Figure 2. Platelet-mediated hemostasis

See text for abbreviations.

The effect of red blood cells (RBCs) on coagulation is exerted primarily through flow-induced physical effects on platelets, which will be described later. However, red cells should be also be discussed in the context of blood composition because their physical effects are hematocrit-dependent, so that the relative amount of them in blood is clearly important. Also, there is evidence that the membranes of a small percentage (~0.5%) of RBCs express phosphatidylserine and can support significant thrombin generation (16). Additionally, red cells contain ADP, which, if released, can enhance platelet activation (17).

Thus far, the discussion has focused only on the pro-coagulant aspects of blood clotting. Clearly, some mechanism is needed to keep the positive feedback loops of hemostasis in check so that thrombus formation is restricted to the site of an injury. There are many anticoagulants in both clinical and laboratory use, so what follows is a brief and selective overview. Table 1 is a summary of common anticoagulants, the blood elements they exert their inhibitory effects on, and whether they are commonly used clinically (*in vivo*) and/or in the laboratory (*in vitro*).

Table 1. Selected anticoagulants

Inhibitor	Acts on:	*in vivo*?	*in vitro*?
Antithrombin III ± Heparin	IIa, IXa, Xa, XIIa	Y	Y
Coumadin, Coumarin, Warfarin	II, VII, IX, X	Y	N
Hirudin, PPACK	IIa	Y (Hirudin)	Y
Aspirin	TxA_2	Y	N
CP/CPK, PK/PEP, Apyrase	ADP	N	Y
Clopidogrel, Ticlopidine	ADP	Y	N
Dipyridamole	Platelet activation	Y	Y
GpIIbIIIa inhibitors	Platelet adhesion/aggregation	Y	Y
Ca^{++} chelators (EDTA, sodium citrate)	Ca^{++}	N	Y

The first three entries in Table 1 are inhibitors of coagulation factors. Of these substances (and of all the others listed), only antithrombin III (ATIII) and heparin are naturally present in blood. ATIII acts on the common pathway of the coagulation cascades, combining with thrombin to produce thrombin-antithrombin III complex, which has no procoagulant effect (12). The

action of ATIII is catalyzed by heparin, which increases its rate of action by two to three orders of magnitude. The heparin-ATIII combination also inactivates factors IXa, Xa, and XIIa (18). To increase the anticoagulant effect of heparin beyond that due to its naturally occurring concentration in the blood, it is administered intravenously in the clinical setting.

Factors II, VII, IX, and X are synthesized by the liver, in a process requiring vitamin K. Coumadin, coumarin, and warfarin disrupt the vitamin K-dependent steps in the formation of these factors, so that the liver produces much smaller amounts of them (19). Because these anticoagulants disrupt the production, rather than the action, of clotting factors, they are not suitable for *in vitro* use. However, clinically they have the advantage of being administered orally.

Hirudin (20),which in its natural form is derived from the saliva of medicinal leeches, and PPACK (21), a synthetic compound, are direct thrombin inhibitors, binding to thrombin and preventing its further action in the coagulation cascades.

The next three entries in the table describe inhibitors of platelet-released platelet-activating factors. Aspirin disrupts the cyclo-oxygenase pathway that culminates in the synthesis of TxA_2 by activated platelets (22). While a widespread clinically administered oral anticoagulant, it is not commonly used in the laboratory. CP/CPK, PK/PEP and apyrase all prevent ADP from activating platelets by transforming it into another adenine nucleotide, either phosphorylating it to adenosine triphosphate (CP/CPK and PK/PEP) (23) or dephosphorylating it to adenosine monophosphate (apyrase) (24). While none of the three is used clinically, ticlopidine and clopidogrel are ADP inhibitors which are orally administered and which are used *in vivo*. Both work by binding to and inactivating the site on platelets where ADP binds to induce platelet activation (25, 26). However, because both must be metabolized to have an anticoagulant effect, they are of little use *in vitro.*

The following two entries also list anti-platelet agents. Dipyridamole acts by preventing uptake and breakdown of adenosine, a substance which inhibits platelet activation, but which is quickly removed from the blood by tissue and red blood cells (27). GpIIbIIIa inhibitors prevent platelet aggregation and adhesion by binding to the GpIIbIIIa receptor sites on platelets, preventing those receptors from binding to fibrinogen (28). Both these anticoagulants can be used *in vitro* or *in vivo*.

Finally, it is apparent from Figures 1 and 2 that many of the steps necessary for both cascade- and platelet-mediated thrombus formation depend heavily on Ca^{++}. Chelating agents such as EDTA and sodium citrate bind to Ca^{++} and prevent it from acting as it does when it is a free ion. Since many life-sustaining processes besides coagulation depend on Ca^{++}, however, this is not a suitable method of clinical anticoagulation.

1.2.2 Surface

Blood vessels are lined with endothelial cells which, in their normal state, express anticoagulant activity and do not support platelet adhesion (29). Exposure of the subendothelial surface by injury, however, initiates coagulation. This is due both to exposure of tissue factor, which activates the extrinsic cascade (Figure 1), and to the presence of collagen, which not only activates platelets, but also avidly supports their adhesion (30).

When the blood-contacting surface is a foreign material, the interactions are mediated by blood proteins. Within seconds of blood contact, proteins begin to adsorb to the foreign surface (31). Initial adsorption is dominated by proteins which are present at higher concentrations in the blood, such as albumin, with later displacement occurring if a less-concentrated protein with a higher affinity for the surface arrives (32). Once adsorbed, the proteins can change their conformations to interact more strongly (or in some cases, weakly) with cells and platelets than their bulk counterparts do (33). In terms of thrombosis, adsorption of HMWK can lead to initiation of the intrinsic coagulation cascade (Figure 1), while adsorption of fibrinogen or von Willebrand factor (vWf) will support platelet adhesion via the GpIIbIIIa and GpIb receptors, respectively, with aggregation and thrombus formation following thereafter.

Clearly, one way of controlling the thrombogenicity of a device is by controlling the interactions of blood with its surface. By and large, the materials used in blood-contacting devices are based on off-the-shelf industrial polymers and metals which possess the necessary physical properties (strength, elasticity, corrosion resistance, etc.) for the device being manufactured (34). While these substrates are not designed to prevent thromboembolism, one might suspect that perhaps they could be modified to be more blood-friendly. This seemingly intuitive conjecture has motivated the great majority of biomaterials research to date.

A relatively simple approach is to change the surface topography, with the expectation that a smoother surface will accumulate less protein and fewer cells and a rougher one more.

Although the latter approach seems counterintuitive when the objective is reduced thrombogenesis, both have met with some success. For example, some investigators have found reduced thrombus formation with polished metallic stents which are smoother than their standard-issue counterparts (35). On the other hand, the Thoratec Heartmate ventricular-assist device, whose pump sac is made from a textured polyurethane which is (deliberately) much rougher than competitors' designs, has a very low thromboembolic complication rate even with minimal anticoagulation (36). This surface appears to support the formation of a stable pseudo-intimal lining, which, though comprised at least in part of thrombotic material, is held tightly enough not to embolize and does not appear to support enough ongoing procoagulant activity to activate the blood passing over it (37).

Another way of improving biocompatibility is by modifying the material's surface chemistry to alter its interactions with blood proteins. The enormous variety of both modification techniques and materials modified precludes a review here; see Lee *et al.* (38) for a general description of medical polymers and currently used surface modifications. The reason for the great heterogeneity in approaches to this problem is that no one has yet determined conclusively which surface properties correlate with different levels of protein adsorption. Some attributes believed to be important are degree of hydrophobicity, surface charge, surface energy, crystallinity, and homogeneity (33, 39). As with surface texture, approaches using surface modifications at both ends of the spectrum have performed well; these contrasting examples will be discussed briefly. The first, more conventional approach takes the view that the best way to keep thrombogenic phenomena from occurring at the surface is by preventing as much protein deposition as possible. The most successful modification based on this philosophy is immobilization of poly(ethylene glycol) (PEG) hydrogel. PEG's properties exemplify the current conventional wisdom on what makes a "good" biomaterial: it is a hydrophilic (at the blood interface), non-ionic, non-crystalline, inhomogeneous polymer (39). It can, among other methods, be incorporated into a surface as a copolymer (40) or delivered to injured subendothelium or to an artificial surface pre-adsorbed with protein (41). With either method, platelet adhesion and surface aggregation from flowing platelet suspensions can be reduced by > 90% on the modified substrates relative to unmodified controls (40, 42). Nearly the opposite approach would be to bind proteins rapidly, indiscriminately, and very tightly, which is exemplified by the behavior of pyrolytic-carbon-coated surfaces. Akin to the surface-roughening

philosophy discussed above, this material displays relatively good biocompatibility despite its having properties not thought to be conducive to thromboresistance: it is hydrophobic, crystalline, and electrically conductive (33). And, as expected based on these properties, it does adsorb large amounts of protein. However, it absorbs them non-specifically, almost irreversibly, and, in the case of albumin and fibrinogen, with equal affinity (33). This means that albumin, a relatively inert protein which does not participate in either cascade- or platelet-mediated coagulation, will be prevalent on the surface due to its high plasma concentration. And, in contrast to its typical behavior on polymers, it will be resistant to displacement by more thrombogenic proteins. Additionally, it is believed that fibrinogen, typical of pro-adhesive proteins, is so strongly held and heavily denatured that most of it which adsorbs is held in a conformation that prevents it from binding to activated platelets (33).

The next logical step beyond making surfaces passively un-thrombogenic by altering their affinity for proteins would be to make them actively anti-thrombogenic by endowing them with anticoagulant functions. An example of this strategy which is now in widespread clinical use is the immobilization of heparin onto biomaterials, mostly commonly the tubing and oxygenator surfaces of cardiopulmonary bypass circuits. The heparin is typically immobilized by covalent or ionic bonding, with some type of spacer molecule used to attach it to the device surface while allowing its active site enough room to interact with ATIII (43). Ideally, using a heparin-coated surface should deliver anticoagulation only where it is needed, allowing reduced use of systemic heparinization and thereby reducing the risk of bleeding complications. However, despite over a decade of clinical use of heparin-coated circuits, it is still not clear whether this theoretical benefit is actually realized (43).

In addition to heparin, immobilization of anti-thrombin anticoagulants hirudin (44) and thrombomodulin (45), an endothelial-cell-expressed factor which reverses the action of thrombin from pro- to anti-coagulant, has also been reported. An advantage of immobilized hirudin over heparin is that it is a direct thrombin inhibitor, rather than merely a catalyst, as heparin is for the action of ATIII. However, this also works to its disadvantage, since, unlike heparin which can turn over and continually inactivate additional thrombin, it is possible for all the surface-bound hirudin to become saturated with bound thrombin, after which no anticoagulant activity remains.

This behavior was observed at high thrombin loadings in the work of Phaneuf *et al.* (46). Additionally, in the event of bleeding, heparin can be rapidly reversed with protamine sulfate (18), while hirudin is irreversible.

Like heparin, thrombomodulin both requires cofactors, proteins C and S, to have significant anticoagulant activity (a disadvantage), and acts enzymatically, so that its anticoagulant activity will not become saturated by excess thrombin (an advantage) (47).

Obviously, the ultimate blood-contacting surface for an implant would be one identical to that already in the body – endothelial cells. Creating such cellularized biomaterials and even whole replacement organs is the lofty goal of the emerging field of tissue engineering. The initial cardiovascular-related efforts in this area were concentrated on developing a biocompatible small-diameter vascular graft by seeding endothelial cells onto commonly used biomaterials, an approach which has met with spotty success due to the difficulty of retaining the cells once the grafts are implanted in the circulation (48). While these efforts continue, a more forward-looking approach would be to recreate not just the surface of the native organ, but the entire organ itself. One would expect this to eliminate the cell-adhesion problem seen in hybrid biomaterial/cell vascular grafts, because the surface cells would be in their native milieu, rather than being forced to interact with an artificial surface. Some current frontiers in cardiovascular tissue engineering involve efforts to grow blood vessels, heart valves, and heart muscle (9, 48). While this work is far from clinical application, it has the potential to one day revolutionize organ replacement therapy.

In spite of all this work, however, the goal of developing a truly biocompatible implant material has yet to be reached. In part, the lack of success of these endeavors is due to the absence of even a straightforward, consensus definition of their ultimate aim, i.e. blood compatibility (49). As Haycox and Ratner (50) point out, whether or not a material is deemed blood-compatible may depend on what measure is used to make the assessment. Their argument is forcefully made by their test results for four polymers, each of which exhibits a distinct mode of interaction with platelets. In order from least to most platelet-compatible, the materials and their responses are (50): 1) Biomer, which supports continuous platelet adhesion and activation; 2) poly(vinyl alcohol), which supports little adhesion but appears to fragment and activate platelets that contact it; 3) polyethylene, which develops a relatively passive, non-thrombogenic covering of spread platelets after an initial transient of adhesion and activation; and 4) a custom-

made polyurethane with octadecyl pendant groups that supports neither adhesion nor activation. These studies illustrate the importance of considering all salient variables in making a determination of whether or not a surface is blood compatible. In this case, not only endpoint platelet deposition (the most common single measure of blood compatibility used in the literature), but also bulk platelet activation and changes in the properties of the deposited platelet layer over time must be considered (50). Furthermore, these considerations apply only to platelet compatibility; as Ratner (49) discusses, other measures may be needed to determine a biomaterial's effect on the coagulation cascades, inflammatory pathways, etc., and some materials compatible with one of these systems may not be compatible with the others. The take-home message here is that the blood-artificial surface interaction problem is a multifactorial one, and this leg is perhaps the most complex part of Virchow's triad to address when attempting to model thrombogenesis.

1.2.3 Flow

The last leg of the triad is the one that ties everything together. Clearly, in order for platelets and coagulation factors to reach an artificial surface or the site of an injury, they must be transported there. The effects of local flow patterns on the coagulation reactions and on platelet aggregation and deposition play a substantial role in determining not only where a thrombus will form, but also what its composition will be, how large it will grow, and whether or not it will remain at its nidus or embolize.

The composition of blood itself determines how it flows and can thereby aid thrombus formation. The rheological behavior of normal whole blood is dominated by RBCs, which typically account for about 40% of the total blood volume and 99% of the volume of particulate matter (51). Largely due to their deformability (51), an excess of RBCs develops in the central core of a steady tube flow, while an RBC-depleted layer develops near the wall; this is the well-known "Fahraeus effect" (52). Due to the crowding of RBCs in the center of the tube, platelets are expelled to the near-wall region, where an excess which has been observed to be as high as nine times the bulk concentration can develop (53). RBC collisions and rotational motions also enhance mixing and transport of platelets.

The shear-rate-dependent effective platelet dispersion coefficient due to this RBC-enhanced transport has been calculated as approximately two to three orders of magnitude greater than the Brownian value (54, 55). Having platelets transported rapidly to and located near the surface in this way obviously enhances their ability to either initiate thrombus formation or to attach to an already growing aggregate.

A thrombus's composition is largely determined by its location in the vasculature. It is generally accepted that thrombi formed in the arterial circulation are primarily comprised of platelets ("white thrombi"), while those formed in the venous circulation mainly contain fibrin, which then entraps platelets and RBCs to create "red thrombi" (56). This is due to the relatively high shear rates and fluid velocities in the arterial tree versus the relatively slower flow on the venous side (57). As Figure 1 shows, the coagulation cascades which lead to fibrin formation require several consecutive reactions, each of which needs some finite amount of time to complete. Rapid arterial flow will tend to convect the reactants away before they have time to assemble in the appropriate configurations. The platelet cascade, on the other hand, requires only that platelets have an adhesion site available on the surface; the only kinetic step other than adhesion itself is the activation of other platelets by agonists, thus allowing this process to complete in a relatively short time.

However, the aforementioned considerations assume undisturbed tube flow. Geometrical features that create flow disturbances, such as atherosclerotic stenoses, vessel bifurcations, and venous valves may create low-shear recirculation regions where increased fibrin formation will be likely on either the venous or arterial side (57). Furthermore, these disturbed flow patterns will enhance the transport of both platelets and coagulation factors to the vessel wall or device surface, making such regions "hot zones" for thrombus formation (58, 59).

Additionally, as recently reviewed by Kroll *et al.* (60), pathologically high fluid shear stresses (> ~50 dynes/cm^2), as might be found, for example, in an atherosclerotically narrowed artery, in the jets produced at closure of mechanical heart valves, or in the impeller of a rotary blood pump, can directly induce platelet activation and aggregation via a mechanism that requires vWF and both the GpIb and GPIIbIIIa receptors. This shear-induced activation is enhanced by ADP released both from platelets due to activation or lysis (61) and from RBCs due to what is believed to be stress-induced leakage (62). However, it is not only the level of shear stress, but also the length of time a platelet is exposed to it that determines whether or not

activation takes place. In general, it is observed that the higher the shear stress level, the shorter the threshold exposure time for observable prothrombotic events to ensue (63); the exact relationship between exposure time and shear stress has yet to be formally quantified.

The level of fluid shear stress also modulates platelet-surface interaction. At lower shear rates (e.g, < 600 – 900 s^{-1}), GpIIbIIIa binding to fibrinogen typically is sufficient to fully arrest platelets (64). At higher shear rates, though, vWF-GPIb binding is the initial event, its function apparently being to slow the passing platelet sufficiently for GpIIbIIIa binding to occur and bring it to a halt (65). Thus, fluid shear stress is, in effect, an additional platelet agonist, acting not only in the bulk flow but also at the fluid-surface interface and enhancing thrombus formation at arterial (and higher) shear rates.

Finally, a growing wall-bound thrombus will create its own upstream and downstream flow disturbances, further promoting localization of hemostatic factors. It will also be subjected to increased pressure due to the restriction it creates on upstream flow. If the fluid dynamic forces on the thrombus are greater than the tensile strength of the bonds holding the aggregate together, some or all of the clot will break off, creating a possibly deadly embolus. Although such an event is the thrombotic complication one would most like to avoid, it is also the least studied. Apart from some preliminary theoretical work by Basmadjian (66-68) and Wilson *et al.* (69) and *in vitro* experimental investigations by Goodman *et al.* (70), almost no studies characterizing the critical thrombus size and strength for embolization have been done. This is likely due to the complexity of the problem, both from an experimental standpoint (an unpredictable, three-dimensional, time-dependent event must be observed in a dense suspension) and a mathematical one (fluid-structure interaction and fracture mechanics must be modeled).

1.3 Thrombosis Modeling[1]

The majority of internal cardiovascular devices, such as prosthetic heart valves, synthetic vascular grafts, and ventricular-assist devices, are placed in the arterial circulation and generally harbor high hemodynamic shear rates. The thrombotic deposition encountered in these devices is thus composed primarily of platelets, with less fibrin involvement than one would encounter in low-shear venous thrombosis (56). Despite Virchow's prescient elucidation of his triad of blood, surface, and flow over 100 years ago, the underlying chemical, physical, and biological

[1] The majority of the text in this section and its subsection were adapted with permission from Sorensen *et al., Ann. Biomed. Eng.,* 1999;27(4):436-448 (71). Copyright 1999, Biomedical Engineering Society.

processes which culminate in thrombus formation have proven difficult to model in a systematic, quantitative fashion. If a model were available which could reliably predict regions of platelet activation and deposition within a cardiovascular device, engineers could potentially optimize the design of the device flow path after appropriately considering the thrombogenicity of the blood-contacting materials and the status of the patient's hemostatic system.

A truly comprehensive model of platelet-mediated thrombogenesis requires components which describe all the phenomena discussed in the previous section: platelet activation (via shear and agonists); effects of disturbed flow and RBCs on platelet transport; effects of artificial surfaces (if present) on protein adsorption; kinetics and mechanics of platelet-platelet and platelet-surface adhesion; flow alteration by a growing thrombus and thrombus disruption by fluid dynamic forces (embolization); and interplay between platelet- and cascade-mediated hemostatic mechanisms. To date, most models in the literature have focused on these components individually without attempting to integrate them into a single, comprehensive approach. Furthermore, we are not aware of any attempts to model the distinct types of platelet-biomaterial interactions that occur on materials of differing chemical composition, as investigated by Haycox and Ratner (50) (see section 1.2.2).

1.3.1 Prior Work

Numerous studies have analyzed platelet transport and deposition in unidirectional tube or channel flow in the context of the convection-diffusion equation (72-76). While the equations derived by these authors are often quite complex, the following simplifying assumptions are commonly made to them to allow analytical solutions: 1) negligible axial diffusion; 2) diffusion-limited platelet-surface adhesion, i.e. rate of reaction at the surface >> rate of transport to the surface ; 3) linearly varying near-surface velocity fields; 4) steady-state behavior; 5) no decrease in adhesion rate due to surface site occupation, i.e. 100% surface availability at all times; and 6) constant platelet diffusivity. Basmadjian (72) presents several such solutions and discusses their applicability for different surface reaction conditions and vessel sizes. Stubley *et al.* (75) also review the early efforts to model platelet deposition and compare their results to those of the authors' own more complex model. They conclude that, for platelet adhesion onto glass, assumptions 1-3 typically have little effect on predicted platelet adhesion. They argue that the most crucial element to include is a surface saturation term of the type proposed by Grabowski *et al.* (73). When this term is neglected (assumption 5 above), poor agreement with experiments at

long perfusion times is obtained, since observed adhesion tends to a constant asymptote, while the 100% availability model predicts continuous adhesion at a constant rate. The authors also state that neglecting time-dependent behavior (assumption 4) can lead to inaccurate predictions at low shear rates, due to the longer initial transients for those cases. Assumption 6 was not examined.

While limited in scope, the results of such modeling have proven helpful in describing the relative effects of convection, diffusion, and surface reaction on platelet deposition. They have also helped elucidate the effects of RBCs in augmenting platelet transport, as platelet diffusivities used to fit the experimental results simulated in these studies were found to be both dependent on shear rate and two to three orders of magnitude greater than the Brownian value (73, 74, 76). However, these models have not seen wide application for predicting experimental results, since they cannot be extended to real-world situations such as two- and three-dimensional flows. Furthermore, these studies consider the transport of platelets as a single species, neglecting the different adhesive properties of activated and resting platelets. They also assume the only relevant surface phenomenon is platelet adhesion, thereby neglecting platelet-platelet aggregation and its flow-modifying effects. Additionally, they neglect the effects of agonist production and transport in creating "hot spots" for increased platelet activation, as well as ignoring the effects of the coagulation cascades in producing platelet-activating thrombin.

In the studies just discussed, effective RBC-enhanced platelet diffusivities were merely adjusted so that the solutions obtained for the convection-diffusion equation would best fit experimental platelet deposition results. Rather than treating platelet diffusivity as a parameter to be estimated, it may be preferable to have a model to account for the effects of shear-induced RBC motion on platelet transport. However, developing such a model is an onerous task because the exact mechanisms which lead to shear-enhanced particle migration are not fully understood. As explained by Zydney and Colton (77) in their thorough review of such modeling efforts, most models assume that the driving force for lateral platelet transport is fluid motion due to shear-induced red cell rotation. The prototype of such models would be that of Keller (78), who uses an analogy to the Prandtl mixing length analysis used to calculate turbulent diffusivities to obtain an enhancement factor that depends on fluid shear rate and particle diameter. The next level of sophistication is typified by the model of Antonini *et al.* (55), who extended Keller's analysis to obtain an enhancement factor with a different functional form and a dependence on particle

volume fraction (hematocrit) in addition to shear rate and particle diameter. In contrast, Zydney and Colton (77) ignore the effects of shear-induced RBC rotation and focus instead on RBC migration due to deformation and collisions, which they argue will be the dominant effect in a concentrated suspension such as blood. The diffusion enhancement factor they derive also depends on shear rate, particle diameter, and hematocrit. Because they fit their function to experimental results for a wide range of hematocrits and for both rigid and deformable particles, however, agreement with experimental results is better than for previous work, which rested mostly on purely theoretical analysis.

Another alternative approach is the one taken by Eckstein and Belgacem (79), who add a convection-like "drift flux" term to the traditional convection diffusion equation. This term acts as a source which drives the platelet concentration profile to a predetermined fully-developed profile. The obvious drawback of this model is that knowledge of that fully-developed profile is necessary *a priori.* While experimentally measured platelet concentration profiles are available for tube flow (53, 80), no such results exist for more complex flows. Nevertheless, Buchanan and Kleinstreuer (81) applied the Eckstein and Belgacem model to platelet transport in a stenotic tube, adding a shear-rate-dependent term to the drift flux to account for the effect of geometric variations. The computed results they present were not compared to any experimental studies, so the validity of their modeling approach remains to be seen.

Modeling the coagulation cascades is also a daunting prospect due to their complexity and their interactions with each other and the platelet system (see Figures 1 and 2). Rather than tackling the entire problem at once, most researchers have chosen to model parts of the cascades while assuming that sufficient products from upstream reactions are available to start the reactions being modeled. Additionally, so that the equations to be solved can remain ordinary, rather than partial, differential equations, the reactions are often assumed to take place in well-mixed vessels, so that spatial variations in concentrations can be ignored. For the intrinsic cascade, examples of such spatially invariant models are: those which attempt to cover the entire cascade and the common pathway (82, 83); those which ignore the common pathway (84); and those which consider only the initial "contact activation" of XII by HMWK and PKn (85). For the extrinsic cascade, most models focus on everything from VIIa-TF through the common pathway (86-89); however, a partial differential equation model which considers only the intrinsic cascade but which takes into account spatial variations due to fully-developed tube flow

was developed by Gir *et al.* (90). Some models ignore the upstream cascades to focus on thrombin generation via the common pathway, either ignoring the effects of flow (91) or including it via lumped mass-transfer coefficients (84).

To illustrate the complexity involved in modeling these reactions, the state of the art is embodied by the recent work of Kuharsky and Fogelson (88). They model the extrinsic cascade and common pathway, taking into consideration effects of transport via lumped mass-transfer coefficients and accounting for both bulk and surface-adherent platelets and coagulation factors, as well as platelet activation and three inhibitory pathways. This comprehensive model, which still ignores the intrinsic cascade and spatial variations in reactant concentrations, requires the solution of a system of 59 coupled ordinary differential equations.

Additionally, models which focus solely on the final steps of agonist generation and subsequent transport away from the production site have been developed. Basmadjian and Sefton (92) simulated thrombin transport from a constantly-produced wall source and its inactivation by surface-bound and bulk heparin, mapping critical thrombin concentration ranges as a function of dimensionless mass transfer coefficients. Chung and O'Rear (93) simulated thrombin generation from prothrombin in tube flow assuming a fixed concentration of Va-Xa-phospholipid complex. Adams and Feuerstein (94, 95) used a convection-diffusion equation to estimate the release rate of ADP from platelet thrombi at the wall of a tube, while Fogelson (96) modeled the release of ADP from a single spherical platelet, showing the agonist's effect is prolonged if it is released from granules centralized within the platelet, rather than extruded at the surface. Generation and transport of TxA_2, ADP, and thrombin were investigated by Folie and McIntire (97) in a study of two-dimensional flow that extended the results for one-dimensional flow of Hubbell and McIntire (98). They studied the influence of small (5-20 μm) rectangular and semicircular model thrombi on flow and agonist transport in a micro-domain (200 × 200 μm) computational model, using constant surface fluxes to simulate agonist generation. They predicted shear-rate-dependent accumulation of platelet-activating agonist concentrations in the recirculation regions near the thrombi, with thrombin the dominant species.

As mentioned in section 1.2.3, embolization has not been widely studied, one exception being Basmadjian's series of papers using classical fluid dynamical correlations to estimate critical ranges of thrombus height and fluid shear rate which predispose to embolization (66-68). He also predicts that thrombus porosity and fluid inertial effects have relatively less effect on thrombus stability than drag forces. Wilson *et al.* (69) simulated time-dependent protein and platelet deposition and embolization. Rather than directly accounting for fluid dynamic forces, their model used a constant critical height to determine when embolization would occur, and included a fixed detachment time after which proteins desorbed from the surface.

Recent computational studies have attempted more detailed modeling of platelet deposition and activation than could be undertaken in the early efforts. Using a single-species convection-diffusion equation for platelet transport, with deposition simulated by the saturable surface-flux boundary condition of Grabowski *et al.* (73) and treating the platelet-surface reaction rate and diffusivity as adjustable parameters, Strong *et al.* (99) obtained excellent correspondence between average predicted and experimental platelet deposition values for collagen, glass, and polymeric biomaterials. Since the model equations were solved numerically, there were few restrictions on the possible flow fields or boundary conditions that could be simulated. Although the model predicts platelet deposition as a function of position, the authors reported only a single, domain-averaged value as a function of time. This was done to match the form of the experimental results to which the model was being fit. As numerous studies have shown (59, 100-102), platelet deposition can be highly spatially variable, especially when flow disturbances or highly reactive surfaces are present. Predicting such variations may be important if one is to accurately determine where clinically significant thrombi will form.

Similar models which specifically attempt to predict spatially varying platelet deposition in the presence of two-dimensional disturbed flow have recently been published by David *et al.* (103), who consider stagnation-point flow, and Wootton *et al.* (104), who simulated axisymmetric stenoses. Both models use steady-state two-dimensional convection-diffusion equations to model platelet transport, with adhesion simulated by a non-saturating surface-flux boundary condition whose rate constant is the only adjustable parameter in the model. Wootton *et al.* (104) also modify their platelet concentration and diffusivity to mimic the effects of red cell-augmented platelet transport, whereas David *et al.* (103) neglect these effects because they are modeling deposition from RBC-free platelet-rich plasma. The latter group also employ a

shear-stress dependent surface reaction coefficient, in contrast to the former group's assumption of a constant value. Surprisingly, both models show the poorest agreement between predicted and experimental results in the downstream, fully-developed-flow regions of their geometries, rather than in the disturbed flow regions.

Perhaps the most comprehensive models of platelet activation and aggregation have been developed by Fogelson, who simulates platelet activation, agonist generation and transport, and bulk aggregation with a continuum model (105) which includes a fictitious fluid-dynamic body force to mimic flow disturbances due to platelet aggregation. Although surface adhesion and embolization are not simulated, bulk aggregates can be broken up by hydrodynamic forces. The same author has also proposed a discrete-platelet model of platelet-surface adhesion and bulk aggregation (106). The former model, although never experimentally validated, provided much guidance in the development of our equations, explained in the next chapter. The latter version, while perhaps more physically realistic in its depiction of thrombosis as an event resulting from interactions of discrete cells with each other and with surfaces, may be computationally untenable, since transport, deposition, and aggregation would have to be simulated on a single-platelet basis for each of the approximately 2×10^5 platelets μl^{-1} in human blood, putting milliliter-size simulations out of reach.

Finally, numerous computational and experimental studies have been performed which attempt to qualitatively relate flow features such as recirculation and separation regions (59, 101, 107), low-velocity flow (108), wall-directed streamlines (59), vortex shedding (109, 110), turbulence (111), and shear stress (101, 112) to platelet deposition and aggregation. One would expect *a priori* that such features would correlate with a high predilection to thrombosis, and these studies tend to bear out that expectation. However, by focusing solely on fluid dynamics, they neglect many important aspects of the thrombogenic process and therefore tend to lack predictive ability across surface types or blood conditions. That is, these models can only predict that a higher-than-average level of platelet deposition will occur in a region with a given flow pattern, while some of the more urgent questions from a thrombosis standpoint would be whether the platelet mass is composed primarily of resting or activated platelets, whether the rate of deposition will increase, decrease, or go to zero, and whether the thrombus is likely to embolize. Answering such questions requires attention to the other two legs of Virchow's triad.

2.0 MODEL DEVELOPMENT[2]

"Well, it should be obvious to even the most dim-witted individual who holds an advanced degree in hyperbolic topology…"

-Prof. Frink, "The Simpsons" #3F04

2.1 Introduction

The first specific aim of this thesis is to develop a comprehensive model of platelet-mediated thrombogenesis. Chapter 1 described the key attributes of such a model, as well as previous modeling efforts. In an effort to improve upon that work, we have combined parts of several previously published models with additional elements we deemed necessary to make our equations more widely applicable. The result of these efforts is a two-dimensional model which attempts to simulate the following phenomena: 1) platelet-platelet and platelet-surface adhesion; 2) platelet activation by relevant agonists; 3) platelet-phospholipid-dependent thrombin generation; and 4) thrombin inhibition by antithrombin III (ATIII) with heparin catalysis. This chapter describes the development of the model and its sensitivity to several key variables.

2.2 Model Equations

As discussed in Chapter 1, thrombosis in blood-wetted prosthetic organs is largely a platelet-mediated phenomenon. For this reason, our model focuses on platelet thrombus formation as the process of primary interest. Since platelets are discrete elements suspended in blood, it would be most physically realistic to simulate thrombus formation and growth on a platelet-by-platelet basis. However, as was pointed out in Section 1.3.1, the high number concentration of platelets in blood makes this an infeasible approach at present due to limitations in computing power. For this reason, we have chosen to follow the majority of previous work and adopt a continuum approach, treating platelets, agonists, and coagulation factors as dilute species dissolved in plasma. Thus our model is described by a coupled set of convection-diffusion equations, each of which has the form:

$$\frac{\partial [C_i]}{\partial t} + \mathbf{div}\left(\mathbf{u} \cdot [C_i]\right) = \mathbf{div}\left(D_i \cdot \mathbf{grad}\,[C_i]\right) + S_i . \qquad [1]$$

[2] This chapter was adapted with permission from Sorensen *et al., Ann. Biomed. Eng.,* 1999;27(4):436-448 (71). Copyright 1999, Biomedical Engineering Society.

Here, **div** is the divergence operator and **grad** is the gradient operator. D_i refers to the diffusivity of species *i* in blood (in $cm^2\ s^{-1}$); **u** is the two-dimensional fluid velocity vector (in $cm\ s^{-1}$); $[C_i]$ is the concentration of species *i*; and S_i is a source term representing generation or consumption of species *i*. The model is comprised of equations to describe the transport of: 1) normal, resting platelets (PLTs); 2) activated platelets; 3) platelet-granule-released and platelet-synthesized platelet agonists, which can be inhibited via first-order reactions; 4) prothrombin; 5) thrombin, generated from prothrombin on platelet phospholipid membranes; and 6) ATIII, which inhibits thrombin and whose action is catalyzed by heparin via the kinetic model of Griffith (113, 114). Table 2 lists the appropriate form for the source terms S_i, along with the abbreviation and units used for C_i, for each species included in the model. The subscript *j* in the table and as used hereafter refers to the *j*th platelet agonist, i.e. thrombin or any of the platelet-released or platelet-synthesized agonists.

Table 2. Model species and source terms

Reprinted with permission from Sorensen *et al., Ann. Biomed. Eng.,* 1999;27(4):436-448 (71). Copyright 1999, Biomedical Engineering Society.

Species	C_i abbrev.	C_i units	S_i function
Resting PLT	$[RP]$	PLT ml^{-1}	$-k_{pa}\cdot[RP]$
Activated PLT	$[AP]$	PLT ml^{-1}	$+k_{pa}\cdot[RP]$
PLT-released agonists	$[a_{pr}]$	nmol ml^{-1} (μM)	$+\lambda_j\cdot k_{pa}\cdot[RP]-k_j\cdot[a_{pr}]$
PLT-synthesized agonists	$[a_{ps}]$	μM	$+s_{p,j}\cdot[AP]-k_j\cdot[a_{ps}]$
Prothrombin	$[PT]$	μM	$-\beta\ [PT](k_{at}\cdot[AP]+k_{rt}\cdot[RP])$
Thrombin	$[T]$	NIH Units (U) ml^{-1}	$[PT](k_{at}\cdot[AP]+k_{rt}\cdot[RP])$, and: $-\Gamma\cdot[T]$, $[H]>0$, or $-k''\cdot[AT]\cdot[T]$, $[H]=0$
ATIII	$[AT]$	μM	$-\Gamma\cdot\beta\ [T]$, $[H]>0$, or $-k''\cdot[AT]\cdot\beta\cdot[T]$, $[H]=0$

The equations for [*RP*], [*AP*], and [a_{pr}] (see Equation 1 and Table 2) are based on Fogelson's continuum model (105) of platelet transport, activation by a single, lumped agonist, and bulk aggregation. We have extended Fogelson's work by adding the capability for multiple platelet agonists, rather than a single, lumped one, as well as the possibility of agonist inhibition via first-order reactions. In these equations, k_{pa} represents a first-order reaction rate constant (in s^{-1}), for platelet activation. This phenomenon is modeled as the "consumption" of resting platelets and the "generation" of activated platelets by the first-order reaction $k_{pa}\cdot[RP]$. The coefficient k_{pa} is a function of local agonist concentrations [a_j], as indicated below. In the agonist generation equations, λ_j is the amount of agonist *j* released per platelet (in nmol PLT^{-1}), so that $\lambda_j \cdot k_{pa} \cdot [RP]$ represents the rate at which agonist *j* is generated from newly activated platelets. It is assumed that agonist release from platelet granules takes place instantly upon platelet activation. Fogelson (105) did not specify a functional form for k_{pa} in his model, but rather assumed a static distribution of initially activated platelets in his simulations. Although platelet agonists are known to act synergistically (115, 116), very little quantitative information is available about the kinetics of these interactions (or of platelet activation itself, for that matter). For this reason, we have assumed a linear rate equation with an activation threshold:

$$k_{pa} = \begin{cases} 0, & \Omega < 1.0 \\ \dfrac{\Omega}{t_{act}}, & \Omega \geq 1.0 \end{cases} \qquad [2]$$

where Ω is the activation function:

$$\Omega = \sum_{j=1}^{n_a} w_j \frac{\lfloor a_j \rfloor}{\lceil a_{j,crit} \rceil}. \qquad [3]$$

In Equations 2 and 3, n_a is the total number of agonists in the model; [a_j] is the concentration of the *j*th agonist; [$a_{j,crit}$] is the concentration of that agonist causing platelet activation when platelets are exposed to that agonist alone; w_j is an agonist-specific weighting coefficient to mimic the relative strength of each agonist in the activation reaction; and t_{act} is a "characteristic" time constant for platelet activation (in s). For all simulations reported in this dissertation, the weights w_j have all been set to one, meaning the contribution of each agonist to the cumulative activation function is neither amplified nor attenuated. We have also assumed t_{act} = 1 s, based on the observation by Frojmovic *et al*. (117, 118) that expression of platelet GpIIbIIIa receptors,

which signals platelet activation and incipient aggregation, occurs within approximately 1-3 s after maximal platelet stimulation by ADP. One will note from the form of Equation 2 that no activation takes place until the weighted sum of the normalized agonist concentrations reaches unity, which represents an "on-switch" threshold for platelet activation. However, beyond this threshold, we allow the rate of platelet activation to increase linearly with agonist concentration, with no limit to the maximal rate. It should also be noted that only chemical activation is being considered; platelet activation by fluid shear stresses is ignored. One reason for this is because a quantitative, experimentally validated function relating shear-induced activation to the magnitude and duration of the applied shear stress is not yet available. Even if it were, tracking exposure times in the continuum Eulerian framework of our model equations would extract a very high computational cost.

The behavior of the $[RP]$ source term $-k_{pa}\cdot[RP]$ can be better understood by considering a static (i.e., convection- and diffusion-free), but well-mixed, suspension of resting platelets being activated by a first-order reaction. In this case, the rate of consumption of resting platelets is given by $d[RP]/dt = -k_{pa}\cdot[RP]$, so that $[RP] = [RP]_0\cdot\exp(-k_{pa}\cdot t)$, where t is time and $[RP]_0$ is the initial concentration of resting platelets. If all $w_j = 1$ and the normalized sum of the agonist concentrations is equal to one, then $k_{pa} = 1$, and 36.7% of the initial concentration of resting platelets will remain after one second, meaning 63.3% will have become activated. This rate can be adjusted to yield exponentially faster or slower activation by scaling t_{act} by a constant.

The source-term equation for $[a_{ps}]$ represents the generation and inhibition of an agonist which is synthesized by the activated platelet, rather than released from its granules. In this equation and that for $[a_{pr}]$, k_j is a first-order reaction rate constant (in s^{-1}) for the inhibition of agonist j. We have assumed that activated platelets synthesize these agonists at a constant, non-diminishing rate, represented by the term $s_{p,j}$ (nmol PLT^{-1} s^{-1}). This would represent a worst-case scenario in terms of thrombogenesis.

The equations for $[PT]$, $[T]$, and $[AT]$ represent the coagulation-cascade-related portion of our model. We assume the generation of thrombin from prothrombin takes place both on surface-bound and bulk platelets. The equations for surface-based thrombin generation are incorporated into the boundary conditions, described below. As demonstrated by Rosing *et al.* (119), activated platelets support phospholipid-mediated thrombin generation at a much higher rate than do resting platelets. This is likely due to the procoagulant effect of the phosphatidylserine residues

exposed on the outer surface of the activated platelet. To simulate this phenomenon, we employ the rate constants k_{rt} and k_{at} in the source terms for [PT] and [T] to represent the different conversion rates of prothrombin to thrombin at the surface of resting and activated platelets, respectively, in units of U PLT^{-1} s^{-1}. In the source terms for [T] and [AT], Γ (in s^{-1}) is Griffith's template model for the kinetics of the heparin-catalyzed inactivation of thrombin by ATIII (113, 114):

$$\Gamma = \frac{k_T \cdot [H] \cdot [AT]}{\xi \cdot K_{AT} \cdot K_T + \xi \cdot K_{AT} \cdot \beta \cdot [T] + [AT] \cdot \beta \cdot [T]}. \quad [4]$$

In Equation 4, k_T is a first-order rate constant (in s^{-1}); K_T and K_{AT} are the dissociation constants (in μM) for heparin/thrombin and heparin/ATIII, respectively; ξ represents a factor to simulate a change in affinity of heparin for ATIII when it is bound to thrombin or for thrombin when it is bound to ATIII; and β is a conversion factor to convert thrombin concentration from U ml^{-1} to μM. The bulk heparin concentration, [H] (in μM), is assumed constant in both space and time. Note that this kinetic model yields zero thrombin inhibition by ATIII at zero heparin concentration regardless of ATIII concentration, which is incorrect. Therefore, in the absence of heparin, this model is replaced by a second-order reaction for the inhibition of thrombin by ATIII alone (120), as given in Table 2, where *k"* is a second-order rate constant.

Platelet adhesion to the biomaterial surface and to other deposited, activated platelets is modeled via surface-flux boundary conditions. Platelet activation due to surface adhesion, as occurs on collagen and many biomaterials, is also included, as are surface-based agonist generation and agonist-induced activation of wall-bound resting platelets. The equations for these boundary conditions are as follows, where a positive term indicates an efflux or consumption from the domain, and a negative term indicates an influx or generation (x here is distance along a reactive wall, in cm):

<u>Reactive wall flux boundary condition (BC) for resting platelets:</u> Adhesion to surface only, not to other platelets (PLT cm^{-2} s^{-1}):

$$J_r(x,t) = S(x,t) \cdot k_{rs} \cdot [RP] \quad [5]$$

Reactive wall flux BC for activated platelets: Adhesion to surface and to deposited, activated platelets, but not to deposited, resting platelets (PLT cm^{-2} s^{-1}):

$$J_a(x,t) = \left(S(x,t) \cdot k_{as} + \left(\frac{M_{as}(x,t)}{M_\infty} \right) \cdot k_{aa} \right) \cdot [AP] \quad [6]$$

Reactive wall flux BCs for platelet-released agonists: Generation due to platelet activation (nmol cm^{-2} s^{-1}):

$$J_{pr}(x,t) = -\lambda_j \left(\theta \cdot S(x,t) \cdot k_{rs} \cdot [RP] + k_{pa} \cdot M_r(x,t) \right) \quad [7]$$

Reactive wall flux BCs for platelet-synthesized agonists: Generation due to platelet activation (nmol cm^{-2} s^{-1}):

$$J_{ps}(x,t) = -M_{at}(x,t) \cdot s_{p,j} \quad [8]$$

Reactive wall flux BC for prothrombin: Consumption due to thrombin generation (nmol cm^{-2} s^{-1}):

$$J_{pt}(x,t) = \beta \cdot \left(M_{at}(x,t) \cdot k_{at} + M_r(x,t) \cdot k_{rt} \right) \cdot [PT] \quad [9]$$

Reactive wall flux BC for thrombin: Generation from prothrombin on surface-adherent platelets (U cm^{-2} s^{-1}):

$$J_t(x,t) = -\left(M_{at}(x,t) \cdot k_{at} + M_r(x,t) \cdot k_{rt} \right) \cdot [PT] \quad [10]$$

Here, species concentrations are the values at a reactive wall. Equations 5-6 are based in part on the single-component platelet-transport model of Strong *et al.* (99). In these equations, k_{rs}, k_{as}, and k_{aa} are heterogeneous reaction rate constants (in cm s^{-1}) that govern the rates of adhesion between, respectively: resting platelets and the surface; activated platelets and the surface; and depositing and surface-bound activated platelets. It is assumed that all three parameters are dependent on blood composition; k_{rs} and k_{as} are also surface-dependent. These surface-deposition equations include a saturation effect that prevents additional platelet-surface adhesion once the capacity of the surface for platelets, M_∞, is reached. In contrast to the work of Strong *et al.* (99) in which M_∞ is material-dependent, we assume it to be independent of surface composition and equal to monolayer coverage. This amounts to the assumption that all surfaces will asymptotically approach monolayer coverage at sufficiently long times, with the surface reactivity parameters determining the rate.

This saturation effect is embodied in the $S(x,t)$ term in Equations 5-7, where:

$$S(x,t) = 1\text{-}M(x,t)/M_\infty \quad [11]$$

$$M(x,t) = \int_0^t \left(J_r(x,t) + k_{as} \cdot S(x,t) \cdot [AP]\right) dt. \quad [12]$$

$M(x,t)$ is the sum of activated and resting platelet-surface adhesion (in PLT cm^{-2}). Our model augments that of Strong *et al.* by adding a platelet-platelet adhesion term (the second term in parentheses in Equation 6). We believe this more accurately represents the growth patterns of a thrombus, as platelets should continue to adhere to those already deposited on the surface after monolayer surface coverage is reached. In this expression, $M_{as}(x,t)$ (PLT cm^{-2}) represents the portion of the total surface coverage $M(x,t)$ comprised of activated platelets:

$$M_{as}(x,t) = \int_0^t \left(\theta \cdot J_r(x,t) + k_{as} \cdot S(x,t) \cdot [AP] + k_{pa} \cdot M_r(x,t)\right) dt. \quad [13]$$

Here, θ is the surface-dependent fraction of adhering, resting platelets which activate upon surface contact; k_{pa} is the activation rate constant of Equation 2 evaluated at the wall; and $M_r(x,t)$ (PLT cm^{-2}) is the portion of the total surface coverage due to resting platelets:

$$M_r(x,t) = \int_0^t \left((1-\theta) J_r(x,t) - k_{pa} \cdot M_r(x,t)\right) dt = M(x,t) - M_{as}(x,t), \quad [14]$$

so that $k_{pa} \cdot M_r(x,t)$ is the rate of activation of deposited, resting platelets by agonists. The reaction coefficient k_{aa} in Equation 6 is scaled by the fraction of the surface covered with activated platelets, M_{as}/M_∞. This scaling reflects the notion that as the number of surface-bound, activated platelets increases, more surface area is available for platelet-platelet adhesion, and the surface flux of activated platelets should increase accordingly.

The agonist-related surface fluxes are described by Equations 7-10. Equation 7, based loosely on prior theoretical work by Adams and Feuerstein (94, 95), is the surface-flux counterpart of the agonist generation term for $[a_{pr}]$. As in the bulk source function, those platelets which activate are assumed to degranulate instantaneously. Likewise, Equation 8 is the surface-flux counterpart of the agonist source term for $[a_{ps}]$, with activated platelets assumed to synthesize the relevant agonists at a constant rate for their entire lifespan.

Equations 9-10 are the thrombin-related surface fluxes and are identical to the bulk thrombin generation source terms with bulk concentrations replaced by surface concentrations. In these equations, $M_{at}(x,t)$ is the total surface coverage (in PLT cm^{-2}) with deposited, activated platelets (equal to activated platelet-surface plus platelet-platelet adhesion):

$$M_{at}(x,t) = \int_0^t \left(\theta \cdot J_r(x,t) + J_a(x,t) + k_{pa} \cdot M_r(x,t)\right) dt. \quad [15]$$

Obviously, thrombin generation is considerably more complicated than the simple conversion of prothrombin at a platelet phospholipid surface, as we have modeled it. However, simulating the upstream coagulation reactions was deemed too computationally expensive. For example, simulating only the extrinsic and common pathways using the model of Kuharsky and Fogelson (88) would require 59 equations, rather than three, so that the computational expense of merely computing thrombin concentration would greatly exceed the cost of solving the rest of the model (four equations). Consequently, we assume that the common pathway has been reached and that local concentrations of factors Xa and Va are not rate-limiting. Also, we allow the rate of thrombin generation to increase linearly with the amount of platelet surface area present, with no lower or upper limit. Evidence supporting this assumption can be found in Rosing *et al.* (119), where it was shown that the rate of platelet-phospholipid-mediated thrombin generation (albeit in buffer medium, rather than whole blood) is approximately linear in platelet phospholipid concentration over the range 0 to 4 μM phospholipid. They also showed thrombin generation by platelets stimulated by thrombin, collagen, or both to increase without saturating over the range 0 to 3×10^7 PLT ml^{-1}. However, the upper limit studied represents activation of roughly 10% of the normal platelet concentration, so further investigation of this assumption may be warranted if higher levels of activation are expected.

Finally, the fluid velocity field for the convection-diffusion-reaction equations is obtained by solving the incompressible, laminar Navier-Stokes equations. As a first approximation, we neglect the effect of the geometry of the growing thrombi on the flow field. That is, we obtain a single flow solution and assume it holds for all time. The impact of this assumption is discussed further in Chapters 3 and 4, where the model predictions are compared to experimental results. Several additional simplifying assumptions are made when solving these equations. First, blood is assumed to be a continuous medium, rather than a suspension of cells and proteins. This means that the physical effect of RBCs on the platelet concentration profile cannot be simulated

directly. Second, blood is assumed to be an incompressible, Newtonian fluid. The assumption of Newtonian behavior is considered valid at high shear rates (> ~200 s^{-1}) (121), which are typical of the arterial flows that are our primary interest. However, this assumption may not be valid in regions of retarded flow, such as stagnation zones following an obstruction. Finally, we have assumed the flow is in local chemical equilibrium, so that the Navier-Stokes equations can be solved decoupled from the convection-diffusion-reaction equations. With these assumptions, the appropriate form of the steady-state Navier-Stokes equations is (122):

$$\rho(\mathbf{u} \bullet \mathbf{grad}(\mathbf{u})) = -\mathbf{grad}(p) + \mu\Delta\mathbf{u} \quad [16]$$

$$\mathbf{div}(\mathbf{u}) = 0 \quad [17]$$

Here, Δ is the Laplacian operator; ρ is fluid density (in g cm^{-3}); p is pressure (in dynes cm^{-2}); and μ is the asymptotic (high-shear) viscosity of blood (in g cm^{-1} s^{-1}).

2.3 Methods

Values for the species-specific parameters required in Equations 1 and for the boundary and initial conditions were taken from various sources in the literature and are summarized in Table 3. In addition to thrombin, we have incorporated the agonists ADP and TxA_2. ADP is a platelet-released agonist, stored in the dense granules, while TxA_2 is synthesized enzymatically by the activated platelet. Once released, TxA_2 is rapidly hydrolyzed to thromboxane B_2, which is relatively inactive. This process is incorporated into the model via a first-order inhibition reaction whose rate constant is given in Table 3. In selecting a value of $[a_{j,crit}]$ for TxA_2, we have adopted the reasoning of Folie and McIntire (97) and Hubbell and McIntire (98) and have assumed that the platelet-activating behavior of this agonist is similar to that of its stable synthetic analogue, U46619. The values for resting platelet concentration in Table 3 represent roughly a normal range for whole blood. The value of $[RP]$ for a particular simulation would typically be given as part of the experimental conditions. For the preliminary studies in this chapter and Chapter 3, we also assume a level of background platelet activation equal to 5% of the initial concentration of resting platelets, i.e. $[AP]$ is set to $0.05 \cdot [RP]$ at the inlet. This value is consistent with that reported by Matzdorff *et al.* (123) for platelet P-selectin expression in normal subjects; values in the literature range from 1% (124) to nearly 20% (125). Table 4 gives values for the additional parameters required in the model.

As discussed in Section 1.2.3, RBCs have been shown to have a shear-dependent, diffusion-augmenting effect on the transport of platelets and large proteins. One way to simulate this is by adjusting the diffusivities D_i of the "larger" species (thrombin, prothrombin, and ATIII) from the Brownian values reported in Table 3. The most common methods are ones such as those proposed by Keller (78) and Zydney and Colton (126), in which the augmentation factor is linearly proportional to local shear rate and to particle size. We have selected Keller's version (78) for our initial studies, where $D_i = D_{b,i} + D_s$, and $D_{b,i}$ and D_s are the Brownian and "shear-enhanced" diffusivities, respectively. Keller's formula for D_s is:

$$D_s = 0.18 \cdot d_{rbc}^{\,2} \cdot \dot{\gamma} \,/4, \qquad [18]$$

where d_{rbc} is the diameter of a red blood cell (assumed to be 5.5 μm) and $\dot{\gamma}$ is the local fluid shear rate in s^{-1}. Following Folie and McIntire (97), we use the shear rate at the wall, $\dot{\gamma}_w$, in Equation 18 to compute a constant enhancement factor which is applied at all locations throughout the domain.

We believe applying a constant enhancement, rather a shear-proportional one, is justifiable because increasing diffusivity with local shear rate (for Poiseuille-type flows) results in the level of enhancement being the opposite of what one would expect intuitively – zero at the centerline, where most of the red cells reside, and highest at the wall, where they are excluded.

For platelets, we use a combination of a wall-skewed inlet boundary condition and an enhanced diffusivity to mimic the near-wall platelet excess which red cells induce (53, 79). The skewed platelet inlet boundary conditions are set using the quadratic profile applied previously by Wagner (127), and derived from unpublished work by Hubbell. This equation is:

$$[RP]_{inlet} = \begin{cases} C_0, & |H-y| \le H - L_b \\ C_0\left(1 + A\dfrac{\left(|H-y| - H + L_b\right)^2}{L_b^{\,2}}\right), & |H-y| \ge H - L_b, \end{cases} \qquad [19]$$

where y is the vertical coordinate (in cm) measured from the bottom of the channel; H is the channel half-height; L_b is the excess-platelet boundary layer thickness, assumed to be 35% of the channel half-height; A is an augmentation factor that determines the degree of excess at the wall, taken as 5.6; and C_0 is the uniform concentration outside the boundary-layer region. For L_b and A as assumed here and for parallel-plate Poiseuille flow, C_0 would be 60% of the desired bulk average (cup-mixed) platelet concentration.

Table 3. Species-specific parameter values

Reprinted with permission from Sorensen *et al., Ann. Biomed. Eng.,* 1999;27(4):436-448 (71). Copyright 1999, Biomedical Engineering Society.

Species	$D_{b,i}$ ($cm^2\ s^{-1}$)[a]	k_j (s^{-1})[b]	λ_j (nmol PLT^{-1})[c]	$s_{p,j}$ (nmol $PLT^{-1}\ s^{-1}$)[d]	Initial conc. in simulations	$[a_{j,crit}]$[e]
RP	1.58×10^{-9}	N/A	N/A	N/A	1.5×10^8 - 3×10^8 PLT ml^{-1}	N/A
AP	1.58×10^{-9}	N/A	N/A	N/A	0.05·[*RP*]	N/A
ADP	2.57×10^{-6}	N/A	2.4×10^{-8}	N/A	0.00 μM	2.00 μM
TxA_2	2.14×10^{-6}	0.0161	N/A	9.5×10^{-12}	0.00 μM	0.60 μM
PT	3.32×10^{-7}	N/A	N/A	N/A	1.100 μM	N/A
T	4.16×10^{-7}	N/A	N/A	N/A	0.00 U	0.10 U ml^{-1}
ATIII	3.49×10^{-7}	N/A	N/A	N/A	2.844 μM	N/A

N/A = not applicable for this species

[a]see (97, 98) for agonists, (128) for platelets

[b]see (98), for hydrolysis to inactive compound TxB_2

[c]see (95)

[d]see (97)

[e]see (129) for thrombin, (130) for TxA_2 (based on activity of U46619); see (131), fig. 9 for ADP, assuming approximately 60% activation

Table 4. Additional parameter values

Reprinted with permission from Sorensen *et al., Ann. Biomed. Eng.,* 1999;27(4):436-448 (71). Copyright 1999, Biomedical Engineering Society.

Parameter	Value	Units	Ref.
k_T	13.33	s^{-1}	(113, 114)
k''	7.083×10^{-3}	$\mu M^{-1}\ s^{-1}$	(120)
K_{AT}	0.10	μM	(113, 114)
K_T	3.50×10^{-2}	μM	(113, 114)
ξ	1.00	--	(113, 114)
β	9.11×10^{-3}	nmol U^{-1}	--[a]
M_∞	7.00×10^{6}	PLT cm^{-2}	(132)[b]
k_{at}	3.69×10^{-9}	U $PLT^{-1}\ s^{-1}\ (\mu M\ PT)^{-1}$	(119)[c]
k_{rt}	6.50×10^{-10}	U $PLT^{-1}\ s^{-1}\ (\mu M\ PT)^{-1}$	(133)
μ	0.035	g $cm^{-1}\ s^{-1}$	(128)
ρ	1.1064	g cm^{-3}	(97)

[a]assuming thrombin specific activity 3000 U mg^{-1} and molecular weight 36.6 kDa

[b]see fig. 8 of (132): value for asymptotic level of deposition of washed PLTs in buffer medium onto collagen at shear rate of 300 s^{-1} in cone-and-plate device (approximate monolayer coverage assumed)

[c]see table 1 of (119): value for PLTs stimulated by thrombin

In numerical experiments with non-reactive walls, we discovered that combining the skewed inlet profile given by Equation 19 with the Keller diffusion-enhancement factor proved self-defeating because the very high diffusivity rapidly obliterated the non-uniform profile. On the other hand, using only the Brownian diffusivity neglects the red-cell-enhancement factor. For these reasons, we have decided to adopt the approach of Strong *et al.* (99) and estimate a constant platelet diffusivity that gives the best fit to experimental results.

The system of species transport equations is solved using a finite-volume method for unstructured triangular meshes (134). In our algorithm, the convection terms are treated using first-order low-numerical-diffusion fluctuation-splitting schemes (135). The coupled system of equations is solved with a segregated iterative procedure involving equation-level and system-level convergence criteria. A time-accurate solution is obtained by sub-iterating the solution to a steady-state using either pseudo-time stepping or successive under-relaxation, and then advancing that solution forward in physical time (136). This dual time-stepping approach allows the use of arbitrarily long physical time steps without affecting the stability of the scheme, although, as one would expect, temporal accuracy decreases as longer physical time steps are used. Unstructured meshes are generated using the public-domain program *Triangle* (JR Shewchuk, Carnegie Mellon University).

2.4 Model Behavior and Parameter Sensitivity

In fitting the model to experimental results, the independent parameters are: 1) platelet concentration; 2) heparin concentration; 3) percent of resting platelets activated by surface contact; 4) platelet diffusivity; and 5) the three platelet reaction rate constants k_{rs}, k_{as}, and k_{aa}. The first three should be deducible from the experimental data, while the last four must be estimated for each experiment, although one would expect platelet diffusivity to be a function of shear rate and hematocrit and the platelet-platelet reaction rate to be constant given constant blood composition (i.e. it would only have to be changed if the simulation involved an adhesive-protein-deficient suspension rather than normal whole blood).

Preliminary simulations were performed on a simple flow geometry to establish the baseline performance of the model. A hypothetical experiment was simulated wherein whole blood was perfused within a parallel-plate flow channel. This enabled the analysis of the relative importance of the aforementioned variable model parameters.

For these studies, a micro-domain (200 μm high × 11 mm long) rectangular flow channel was simulated. This configuration was selected because it is similar to the design of the parallel-plate flow chambers employed in the experimental platelet deposition studies discussed in Chapter 3. Vertical symmetry about the channel centerline was assumed, so that the computational domain was 100, rather than 200 μm tall, and the lower surface was modeled as a platelet-adhesive biomaterial. Assuming fully-developed flow at the inlet to the computational domain, the incompressible Navier-Stokes equations for these cases are exactly satisfied by the Poiseuille solution (122), which is independent of blood density and viscosity:

$$u_x = U_{\max}\left(1 - \frac{(H-y)^2}{H^2}\right), \qquad [20]$$
$$u_y = 0,$$

where y is again measured from the bottom of the channel, and U_{max} is the maximum velocity (at the centerline) in cm s^{-1}. Note that for a Newtonian fluid,

$$\dot{\gamma}_w = \left(\partial u_x / \partial y\right)_{wall} = \left(2 \cdot U_{\max} \cdot (H-y)/H^2\right)_{y=0} = 2 \cdot U_{\max}/H, \qquad [21]$$

and hence u_x can be written as a function of $\dot{\gamma}_w$. To simulate the high-shear arterial flow typical of a cardiovascular device, a $\dot{\gamma}_w$ = 1000 s^{-1} was prescribed and was used for computing both the flow field and the Keller diffusivity correction factors discussed above.

The sensitivity of the model to mesh density was investigated through refinement studies. The model solution for a given set of test conditions was found to vary negligibly (less than ~5% change in peak concentration and platelet deposition magnitudes) as the mesh was progressively refined from approximately 10,000 to approximately 24,000 mesh nodes. Therefore, all results reported have been obtained on a 10,000 node domain. Figure 3A shows the dimensions of the computational domain and the inlet velocity profile, while Figure 3B shows a portion of the 10,000 node mesh. A 25 μm-high region near the reactive surface was refined to better capture the near-wall phenomena being simulated. The elements in this region have areas roughly 40% the size of those in the rest of the domain. The height of this region was somewhat arbitrarily chosen, as there was no *a priori* way of calculating the mass transfer boundary layer thickness. Finally, we have chosen to simulate 300 s of perfusion, for which 100 three-second time steps were used in our algorithm.

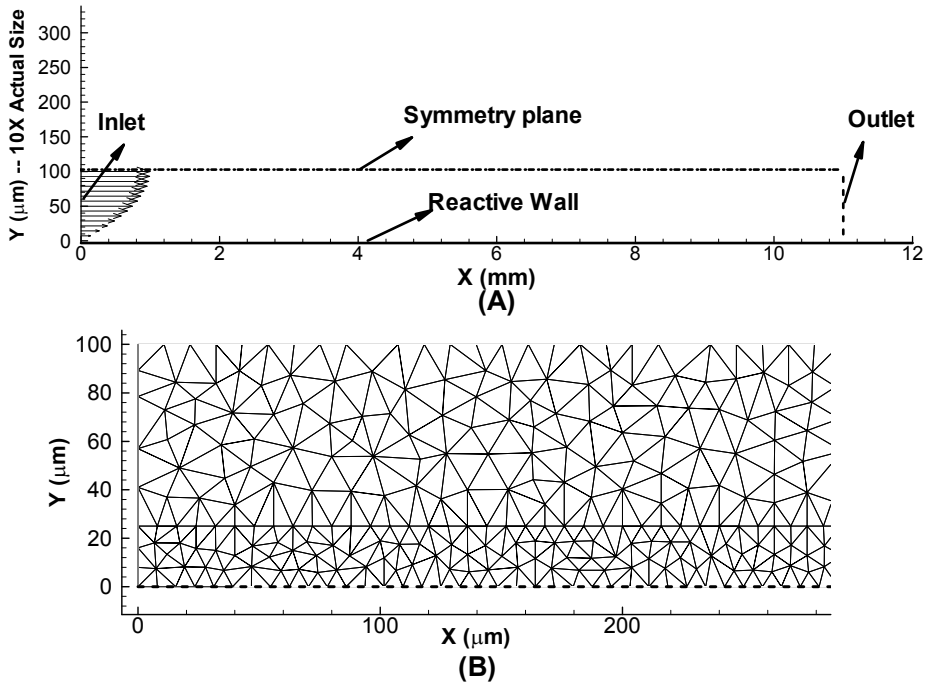

Figure 3. Details of computational domain

(A) Dimensions (note discrepancy in scale between *x* and *y* axes), boundary zones and inlet velocity profile. (B) Zoomed detail of unstructured triangle mesh. Reprinted with permission from Sorensen *et al., Ann. Biomed. Eng.,* 1999;27(4):436-448 (71). Copyright 1999, Biomedical Engineering Society.

The initial condition $C_i = 0$ was imposed on all species everywhere in the computational domain except the inlet, where uniform, constant-concentration Dirichlet boundary conditions were employed. In simulating experimental data, we generally used the resting and activated platelet concentration profiles given by Equation 19. However, to more clearly demonstrate the effects of diffusion and surface reaction effects without the added complexity of the artificial concentration gradient created by that profile, we have assumed a nominal uniform inlet [*RP*] value of 2×10^8 PLT ml^{-1} for these parameter studies. Additionally, we have set the inlet concentration of activated platelets to zero, rather than our typical 5% "background activation" value. This was done to avoid "seeding" the field with initially activated platelets so that the effects of the surface and generated agonists on platelet activation would be more readily apparent.

At the lower, reactive wall, the surface-flux boundary conditions given in Equations 5-10 were imposed. Since ATIII is not involved in surface-based reactions, a zero-normal-flux boundary condition, $\left(\partial[AT]/\partial y\right)_{wall} = 0$, was applied for that species. At the outlet, a fully developed concentration profile was assumed, which allowed a zero-normal-flux boundary condition to be imposed for all species, i.e. $\left(\partial[C_i]/\partial x\right)_{outlet} = 0$. Since the 100 μm upper plane of our computational domain was treated as a symmetry plane, the boundary condition $\left(\partial[C_i]/\partial y\right)_{y=100\,\mu m} = 0$ was imposed on all species.

Figures 4-7 show total platelet deposition (platelet-surface plus platelet-platelet adhesion) versus distance along the reactive wall after 300 seconds of simulated flow. The numerically predicted deposition values have been averaged over 200 μm intervals to facilitate viewing.

Figure 4 shows the effects of the ratio of surface reactivity to platelet diffusivity, as measured by the Damkohler number based on a heterogeneous reaction, $Da = k \cdot H / D_{PLT}$. For these cases, it was assumed that $k_{rs} = k_{as} = k_{aa}$, i.e. all reaction rates (and the three corresponding Damkohler numbers) are equal. Additionally, a relatively low heparin concentration ([*H*]) of 2 $U \cdot ml^{-1}$ was used, and it was assumed that all resting platelets became activated on surface contact ($\theta = 1$ in Equations 7 and 13-15) so that large amounts of agonist generation and bulk platelet activation would be induced.

As the figure shows, increasing the reaction rates results in a transition from a reaction-limited regime, represented by the relatively flat deposition curve at *Da* =1, to a clearly diffusion-limited regime at *Da* =100, where most of the platelets are consumed upstream, resulting in a rapid drop-off in deposition in the downstream tail of the curve. The highly nonlinear variation in deposition magnitude as the Damkohler number is increased shows the effects of the positive feedback created by the platelet activation process: platelet deposition leads to increased platelet activation on the surface, which leads to increased surface-based agonist generation, which in turn induces bulk platelet activation and agonist generation, and which then completes the loop by increasing platelet-platelet adhesion.

The relatively jagged curve for *Da* = 100 (and in subsequent figures where surface reaction rates are high) is due to the discretization process necessary to numerically solve the governing partial differential equations. Since the discrete equations are solved point-wise, numerically predicted platelet deposition is a very local event determined by the concentration of

platelets at a given wall node. At a very high reaction rate, the concentration of platelets in the boundary layer will be greatly decreased through deposition within a few upstream nodes, thereby locally depleting the boundary layer and resulting in a much lower level of deposition at the next few downstream nodes, since diffusive mechanisms cannot replenish the boundary layer rapidly enough.

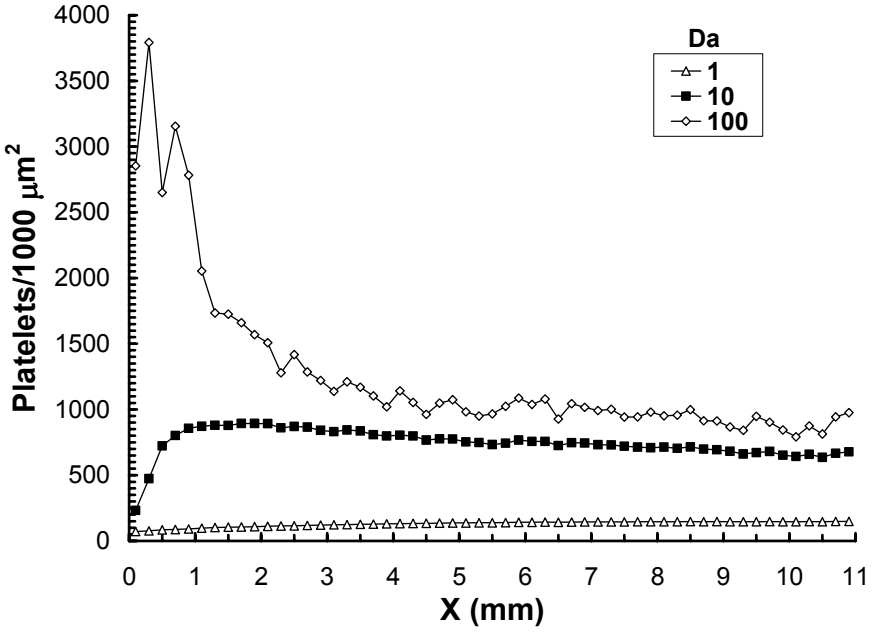

Figure 4. Dependence of axial platelet deposition on platelet Damkohler number

Reprinted with permission from Sorensen *et al., Ann. Biomed. Eng.,* 1999;27(4):436-448 (71). Copyright 1999, Biomedical Engineering Society.

Figure 5 shows effects of the ratio of activated-to-resting platelet reaction rate k_{as}/k_{rs}, again for $[H]$ = 2 U·ml^{-1} and $\theta = 1$. Here, it was assumed that $k_{as} = k_{aa}$, i.e. activated platelets adhere to the surface and to each other with equal affinity. The figure shows deposition versus distance as a function of the ratio k_{as}/ k_{rs}, for a fixed platelet Damkohler number (based on k_{rs}) of 10. Again, the amount of upstream deposition and the accompanying rapid drop in downstream values both increase with increased activated platelet reactivity, with diffusion-limited behavior shown for all ratios greater than one. The effects of the large reaction rates on depletion of the platelet boundary layer are apparent when one compares the curves for k_{as}/ k_{rs} = 5 and k_{as}/ k_{rs} = 10. The two curves have very similar shapes; however, upstream deposition for k_{as}/ k_{rs} = 10 is

approximately 50% higher than for $k_{as}/\ k_{rs} = 5$, while for x greater than about 3 mm, the two curves are essentially identical. The difference in upstream deposition is likely a result of increased agonist generation and bulk activation due to the higher number of platelets depositing near the inlet at the higher ratio, while for both cases, most of the available activated platelets are consumed from the boundary layer by $x = 3$ mm.

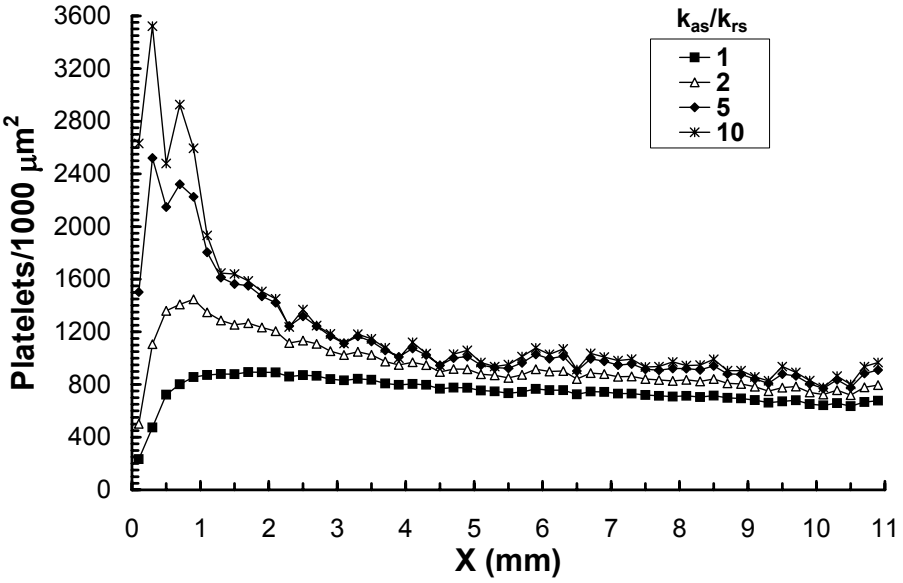

Figure 5. Dependence of axial platelet deposition on ratio of activated to resting platelet-surface reactivity
Reprinted with permission from Sorensen *et al., Ann. Biomed. Eng.,* 1999;27(4):436-448 (71). Copyright 1999, Biomedical Engineering Society.

Figure 6 shows the effects of surface-induced activation (modeled by the parameter θ, the fraction of adherent resting platelets activated by surface contact), for the same conditions as in Figure 4, but with platelet Damkohler number fixed at 10. In Figure 6A, agonist-induced activation occurs both in the bulk flow and on the surface, while in Figure 6B only bulk activation is permitted. When $\theta = 0$, no surface-induced platelet activation occurs. Since there are no activated platelets and no agonists in the domain at the start of the simulation, and since the rate of thrombin generation by resting platelets is too low to result in a supra-threshold thrombin concentration for these simulation conditions, no agonist-induced platelet activation occurs.

Hence, there is no platelet-platelet adhesion; the only event occurring is resting platelet-surface adhesion, which ceases at the saturation limit $M_{\infty,}$ resulting in a monolayer of resting platelets regardless of whether agonist-induced activation is permitted at the surface. For $\theta = 1$, 100% of adherent platelets are activated by surface contact. Hence, identical deposition values are obtained for both sets of simulations, since agonist activation of surface-bound platelets is irrelevant. For $\theta = 0.25$ or 0.5, however, the relative effects of agonist- and surface-induced activation are apparent. When agonist-induced activation is allowed to occur at the surface, it appears to overwhelm any surface-induced activation effects for the parameter values chosen, resulting in the deposition values for $\theta = 0.25$ and 0.5 being identical to those for $\theta = 1$. Without agonist-induced activation at the surface (Figure 4B), however, platelet deposition increases fairly steadily with increasing θ as expected, since a higher surface concentration of activated platelets leads to a larger platelet-platelet adhesion flux (cf. Equation 6).

Figure 7 shows the effect of heparin concentration, and therefore thrombin generation, on platelet deposition for the same conditions as in Figure 6, but with θ fixed at one. It is clear from these results that thrombin is the dominant agonist as modeled in our system, since decreasing thrombin generation by increasing heparin concentration greatly decreases overall platelet deposition, with platelet-platelet adhesion nearly abolished for the $[H] = 20$ U ml^{-1}case. Note that this occurs despite thrombin having been given the same weight (when normalized by its platelet activation threshold) as the weaker agonists ADP and TxA_2 in the platelet activation function (Equation 3). However, these results also indicate that heparin is typically not 100% effective in removing thrombin. That is, thrombin concentrations sufficient to activate platelets (i.e., ≥ 0.1 U ml^{-1}) were observed at 300 s in all cases except $[H] = 20$ U ml^{-1}, and even for that case the maximum predicted thrombin concentration had reached 80% of threshold.

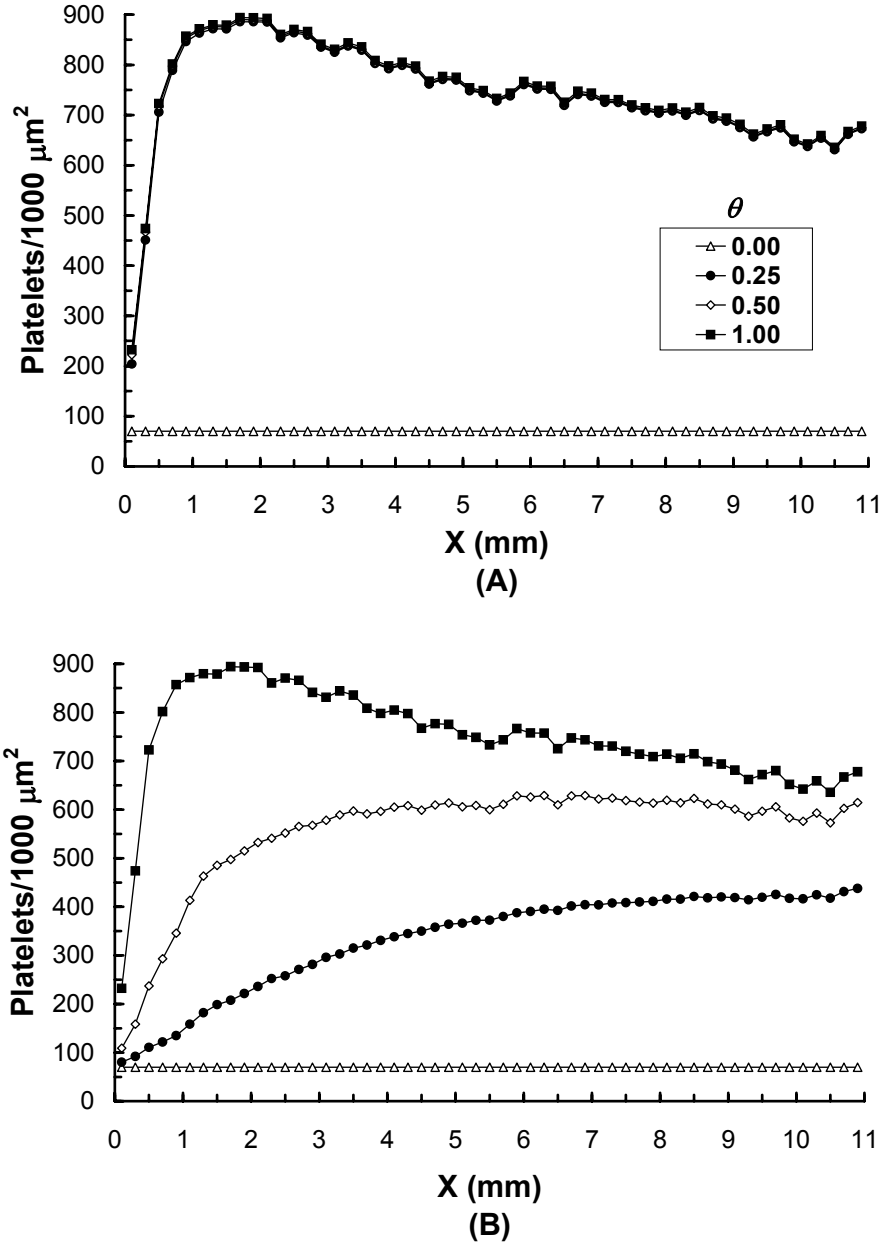

Figure 6. Dependence of axial platelet deposition on degree of surface-induced activation

(A) Agonist-induced activation of surface-adherent platelets allowed. (B) Agonist-induced activation of surface-adherent platelets not allowed. Reprinted with permission from Sorensen *et al., Ann. Biomed. Eng.,* 1999;27(4):436-448 (71). Copyright 1999, Biomedical Engineering Society.

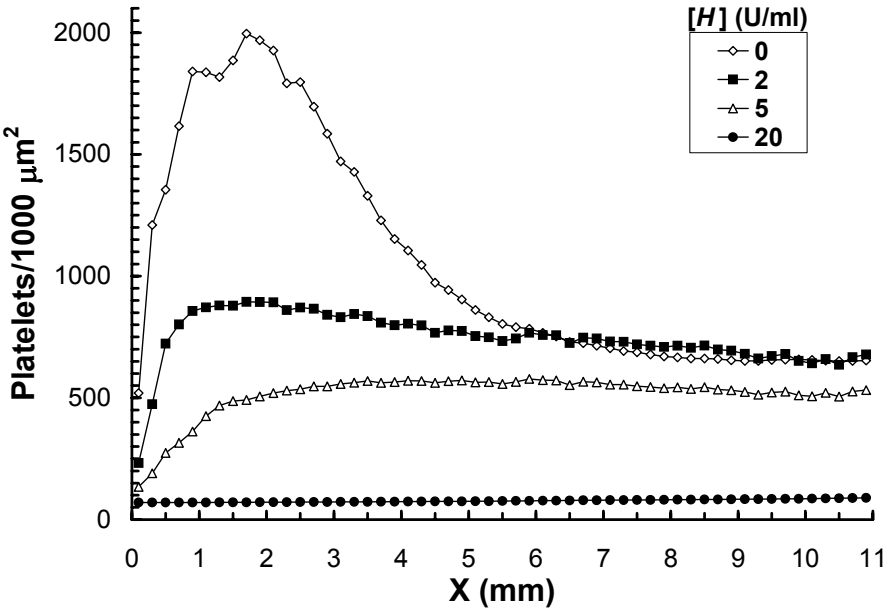

Figure 7. Dependence of axial platelet deposition on bulk heparin concentration

Reprinted with permission from Sorensen *et al., Ann. Biomed. Eng.,* 1999;27(4):436-448 (71). Copyright 1999, Biomedical Engineering Society.

2.5 Conclusions

This chapter has presented the equations for and basic properties of a computational model of platelet-mediated thrombogenesis which has been designed to capture the crucial aspects of all three components of Virchow's triad. The model attempts to simulate platelet transport, adhesion to reactive biomaterial surfaces, agonist generation and platelet activation. We believe it is easily applicable to a wide range of platelet-biomaterial interactions. As demonstrated by Haycox and Ratner (50), there are four distinct modes of interaction between platelets and polymeric biomaterial surfaces: (a) little or no platelet adhesion or activation; (b) adhesion followed by formation of a passivating platelet monolayer; (c) activation without adhesion; and (d) adhesion with activation. Since our model differentiates between the amount of deposited resting versus activated platelets, allows separate reaction rates for resting platelet-surface, activated platelet-surface, and activated platelet-platelet adhesion, and incorporates the ability to relate the fraction of adhering platelets which activate (θ) to surface properties, it is well-suited to modeling these four types of interactions.

In the next chapters, we examine the model's ability to reproduce experimental results for platelet deposition onto a specific material substrate, type I collagen, both in unidirectional Poiseuille flow and two-dimensional disturbed flow.

3.0 MODEL VALIDATION: POISEUILLE FLOW[3]

"I am a scientist
I seek to understand me
all of my impurities
and evils yet unknown"

-Guided by Voices, "I Am a Scientist"

3.1 Introduction

In Chapter 2, a continuum model of platelet-mediated thrombosis was developed and its sensitivity to key parameters investigated. In this chapter, we focus on the second specific aim, model validation. As such, we attempt to predict experimentally measured platelet deposition, using simple test cases from the literature involving parallel-plate Poiseuille flow of whole blood over a type I collagen substrate. One set of training cases is used to calibrate the independent parameters of the model and to demonstrate its ability to realistically simulate the effect of thrombin inhibition. Then, the model is applied to additional validation cases to investigate its robustness and predictive performance under varying fluid shear rates and additional anticoagulation conditions.

3.2 Methods

3.2.1 Training Cases

The independent model parameters (resting platelet-surface adhesion rate k_{rs} [cm·s^{-1}], activated platelet-surface adhesion rate k_{as} [cm·s^{-1}], activated platelet-platelet adhesion rate k_{aa} [cm·s^{-1}], and shear-dependent platelet diffusivity D_{PLT} [cm·s^{-2}]) were estimated by fitting the model to the experimental results of Wagner and Hubbell (102), who studied the axial dependence of platelet deposition from flowing, heparinized whole blood onto a type I collagen surface, using a parallel-plate flow chamber. Since these studies measured platelet deposition as a function of time and examined the effects of removing thrombin (via the active-site inhibitor PPACK), the results are ideal for calibrating our model.

[3] This chapter was adapted with permission from Sorensen *et al., Ann. Biomed. Eng.,* 1999;27(4):449-458 (137). Copyright 1999, Biomedical Engineering Society.

Model parameters specific to these cases and the equations to which they are relevant are listed in Table 5; all other parameters are as given in Tables 3-4. The resting platelet concentration was estimated by comparing Figure 6 of Wagner and Hubbell (102), which shows maximal platelet deposition for heparinized blood as a function of platelet count, to the maximum value in Figure 1 of that report, which contains the results we are attempting to predict. The parameter D_s is the Keller correction factor (78) to the Brownian diffusivity of the "large" species (prothrombin, thrombin, and ATIII). As mentioned in Chapter 2, this parameter is taken as a constant, with its value computed using Equation 18 and the wall, rather than the local, shear rate. Wagner and Hubbell (102) estimated the wall shear rate for their experiments to be 1000 s^{-1}. Also, the value for the rate of thrombin generation by activated platelets, k_{at}, has been increased at the collagen surface relative to its bulk value. The increase in this parameter relative to its value in Chapter 2 is based on the experimental data of Rosing *et al.,* wherein activated platelets stimulated by both collagen and thrombin supported thrombin generation at a rate 8.7 times greater than did platelets activated by thrombin alone (119). The heparin concentration listed corresponds to the 2 U ml^{-1} used in the experiments. Finally, the value of 1.0 assumed for θ implies that all resting platelets deposited on the thrombogenic type I collagen surface become activated on contact.

The experiments of Wagner and Hubbell (102) employed a 200 μm high × 20 cm long channel, with the inlet portion (3 cm in length) coated with relatively non-adhesive albumin and the remaining 17 cm coated with type I collagen. The width of this channel was 20 times larger than the height, so that two-dimensional flow could be assumed along its axial midline. Using the reported wall shear rate of 1000 s^{-1} and assuming fully-developed flow, a Poiseuille solution for the flow field (Equations 20-21) can be computed, and the resulting velocity terms inserted into the transport equations. Then, the transport model, consisting of the seven coupled species-conservation equations (Equations 1), can be solved once suitable boundary and initial conditions are imposed and values for the platelet-surface and platelet-platelet reactivities and platelet diffusivity are assumed. In the case where PPACK was used to inhibit thrombin, the thrombin-related species (prothrombin, thrombin, and ATIII) were eliminated from the model. This is equivalent to assuming that PPACK completely inhibits platelet-mediated thrombin generation. In the remaining four equations, all parameters were identical to those used for the heparin-only case.

Table 5. Specific parameter values for training cases

Reprinted with permission from Sorensen *et al., Ann. Biomed. Eng.,* 1999;27(4):449-458 (137). Copyright 1999, Biomedical Engineering Society.

Parameter	Value	Equations	Ref.
$[RP]$	2×10^8 PLT·ml^{-1}	1,5,7	(102)[a]
C_0 (for $[RP]$)	1.2×10^8 PLT·ml^{-1}	19	--[a]
D_s	1.36×10^{-5} cm^2 s^{-1}	18	(78)[b]
$[H]$	0.417 μM	4	(102)[c]
k_{at} --surface	3.22×10^{-8} U PLT^{-1} s^{-1} (μM PT)$^{-1}$	9,10	(119)[d]
θ	1.00	7,13-15	--

[a]values for [*AP*] are 5% of these values (to simulate 5% background PLT activation)

[b]used to correct diffusivities of thrombin, prothrombin, and ATIII for effect of red blood cells in shear flow

[c]for 2 U ml^{-1} heparin as used in ref. 13, assuming specific activity 300 U mg^{-1} and molecular weight 16 kDa

[d]see table 1 of (119): value for PLTs stimulated by thrombin + collagen

Our transport model was solved on a 100 μm high × 11 mm long rectangular domain, designed to simulate a portion of the lower half of Wagner and Hubbell's flow chamber. The first 1 mm of the computational domain was designed to replicate a portion of the 3 cm albumin entrance length, where Wagner and Hubbell (102) observed negligible platelet deposition. Accordingly, platelet-surface reactivities there were arbitrarily set to 10^{-8} of the values for the 10 mm collagen region, and the parameter θ was set to zero. This had the effect of preventing the adherent resting platelets in this region from activating and releasing agonists. The results of Wagner and Hubbell (102) indicate that the experimental platelet deposition curves reached an essentially constant, asymptotic value at approximately 10 mm into the collagen portion of the chamber, and those authors report data for only the first 15 mm of collagen. Therefore, we chose 10 mm for the length of the collagen portion of our computational domain, rather than the full 17 cm used in the experiments.

Initial and boundary conditions were imposed as discussed in Chapter 2, with constant inlet concentrations used for all species, a wall-skewed quadratic concentration profile employed for resting and activated platelets, and 5% background platelet activation assumed. Since the upper wall was collagen-coated in Wagner and Hubbell's experiments, the 100 μm upper plane of our computational domain was treated as a symmetry plane, and the boundary condition $\left(\partial[C_i]/\partial y\right)_{y=100\,\mu m} = 0$ was imposed on all species.

The mesh used for these cases was the same 10,000 node unstructured triangle mesh used for the parameter sensitivity studies in Chapter 2; mesh refinement studies were conducted as described therein. Since time accuracy was an important consideration for these cases, time-step refinement studies were also conducted. Negligible variation in root-mean-square species concentrations between simulations was found for physical time steps less than 2.5 s for a 75-second simulation. For the results presented herein, a time step of 0.5 s was used.

The variable model parameters k_{rs}, k_{as}, k_{aa}, and D_{PLT} were adjusted by trial and error until one set of parameters gave the best possible fit (as judged by visual inspection) to the experimental results for both the heparin and heparin + PPACK case. This was done by first varying each parameter independently until a relatively good fit to the heparin-only case was obtained. This took several iterations (roughly on the order of 25), as the sensitivity of platelet deposition to each parameter was observed by varying each parameter over a wide range, after which finer trial-and-error adjustments could be made to obtain an acceptable fit to the experimental data. Once such a fit was obtained for the heparin-only case, the heparin + PPACK case was simulated using the parameters from the most recent best-fit heparin-only case, and those parameters were further tuned to obtain an acceptable fit to the heparin + PPACK data. The tuned parameters from the most recent heparin + PPACK case were then used to simulate the heparin-only case, further tuning was done if necessary, and iteration between the two cases continued until the best visual fit to both cases was obtained.

In tuning the parameters, guidance was obtained from physical arguments. First, since the highly thrombogenic collagen substrate should activate nearly all resting platelets that contact it, the magnitudes of k_{rs} and k_{as} should be similar. Likewise, activated platelets should likely bind to each other with about the same avidity as they attach to this very adhesive surface, so that k_{as} and k_{aa} should be roughly equal. Finally, the Keller model correction factor computed using the wall shear rate (D_s in Table 5) served as a starting point for our estimate of D_{PLT}.

3.2.2 Validation Cases

Two sets of experimental results from the literature, those of Hubbell and McIntire (138) and of Alevriadou *et al.* (139), were selected to validate the model after the platelet reaction rate constants for collagen and the platelet diffusivity were estimated using the training cases. In both studies, parallel-plate flow chambers with 200 μm slit widths were used, human blood was perfused, and type I collagen was the substrate. Thus, the same inlet, outlet, symmetry-plane, and surface boundary conditions as applied for the training cases were used, with inlet concentration magnitudes altered appropriately, and the Poiseuille flow field was re-computed using the prevailing wall shear rate for the corresponding experimental study.

Hubbell and McIntire (138) measured deposition over 25 mm of collagen after 120 s of flow of heparinized (10 U ml^{-1}) whole human blood at wall shear rates of 100, 500, and 1500 s^{-1}; the two lower shear rates were simulated here. The 100 s^{-1} wall shear rate is very near the lower limit for Newtonian blood behavior (121); however, as a first approximation, we have continued to employ a Poiseuille flow field for this case. For both cases, a grid with the same mesh density and 1 mm entrance length as that used in the previous cases, but with the total length extended to 26 mm, was constructed. This larger grid contained 24,000 mesh points, and a time step of 1.2 s was used for the model solution. Alevriadou *et al.* (139) measured platelet deposition along 10 mm of collagen after 60 s of flow of citrated whole human blood at a wall shear rate of 1500 s^{-1}. By the same reasoning as for the heparin + PPACK training case, the thrombin-related equations were not solved for this case, since it was assumed that citrate completely inhibited thrombin generation. Additionally, since the geometry of the flow chamber is basically identical to that of the chamber used in the training cases, the same unstructured 10,000 node mesh was employed, with the first 1 mm again assumed to be a non-adhesive entrance length. A time step of 0.6 s was used in the simulations.

Table 6 lists the parameters that were altered from the training cases to match the experimental conditions for the validation cases. Neither study gave any indication of average platelet counts in the perfusates for which platelet deposition results were reported. For this reason, the concentrations were adjusted to provide the best fits to the experimental results (values in Table 6 are the best fits). Note, however, that this was the only parameter fitting done for these cases. Rather than estimating the shear-dependent platelet diffusivity, which we take as an adjustable constant, we assumed it to vary linearly with wall shear rate and assumed no

augmentation at zero shear, so that the values calculated for the validation cases were extrapolated from the best-fit value for the 1000 s^{-1} wall shear rate of the training cases, given below.

Table 6. Parameter values altered for validation cases

Reprinted with permission from Sorensen *et al., Ann. Biomed. Eng.,* 1999;27(4):449-458 (137). Copyright 1999, Biomedical Engineering Society.

Parameter	Alevriadou *et al.*	Hubbell & McIntire
$[RP]^a$	2.5×10^8 PLT·ml^{-1}	2.0×10^8 PLT·ml^{-1}
C_0 (for $[RP]$)^a	1.5×10^8 PLT·ml^{-1}	1.2×10^8 PLT·ml^{-1}
D_s	N/A[b]	1.36×10^{-6} cm^2 s^{-1} ($\gamma_w = 100$ s^{-1}); 6.80×10^{-6} cm^2 s^{-1} ($\gamma_w = 500$ s^{-1})
$[H]$	0.00 μM	2.09 μM[c]

N/A = not applicable for this case

[a]values for [*AP*] are 5% of these values (to simulate 5% background PLT activation)

[b]"large" species (thrombin, prothrombin, ATIII) eliminated from model for this case due to assumption of 100% thrombin inhibition by citrate

[c]for 10 U ml^{-1} heparin as used in (138), assuming specific activity 300 U mg^{-1} and molecular weight 16 kDa

3.3 Results

3.3.1 Training Cases

The experimental results presented by Wagner and Hubbell (102) and our model solutions correspond to 75 s of flow. The platelet-surface and platelet-platelet reaction rate constants and platelet diffusivity were adjusted by trial and error as explained in Section 3.2.1 to yield the best fit to the data. Figure 8 compares our computational results with the experimental data; $x = 0$ corresponds to the start of the collagen-coated region. This figure shows the axial distribution of total platelet deposition, i.e. platelet-surface plus platelet-platelet adhesion, for heparin only or heparin + PPACK as the anticoagulant. In Figure 8, the numerically predicted deposition values have been averaged over 200 μm intervals. This was done to give approximately the same number of data points as in Wagner and Hubbell's results and to mimic the averaging effect of the 4×10^4 μm^2 field of view of the fluorescent microscope used to track

platelet deposition in that report (102). Best-fit values of $k_{aa} = k_{as} = 4.6 \times 10^{-3}$ cm s^{-1}, $k_{rs} = 3.7 \times 10^{-3}$ cm s^{-1}, and $D_{PLT} = 1050 \cdot D_{b,PLT} = 1.66 \times 10^{-6}$ cm^2 s^{-1} for resting and activated platelets gave the best agreement with both experimental curves. The computational results reproduce the experimental trends in total deposition very well, with the no-thrombin (heparin + PPACK) results an especially close match. However, the heparin-only model under-predicts deposition far downstream of the inlet, while slightly overestimating values near the inlet. Since no uncertainty estimates were given for the platelet deposition values in Wagner and Hubbell's report (102), it is unclear whether our results fall within the range of experimental error.

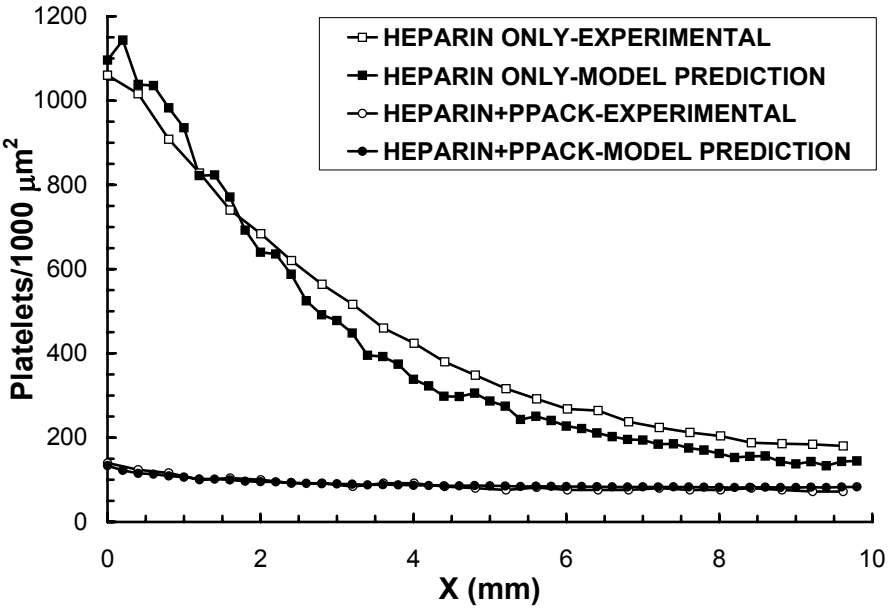

Figure 8. Comparison of predicted axial platelet deposition to experimental results of Wagner & Hubbell
Reprinted with permission from Sorensen *et al., Ann. Biomed. Eng.,* 1999;27(4):449-458 (137). Copyright 1999, Biomedical Engineering Society.

Figure 9 shows the time-varying concentration of each agonist, normalized by its platelet activation threshold concentration, at the representative point $x = 2.5$ mm, $y = 0$ μm (see Table 3 for assumed activation threshold concentrations for each agonist). Thrombin concentration continues to increase somewhat rapidly with time due to continued platelet deposition. For the case with thrombin, ADP concentration rises rapidly for approximately 5 s and then transitions to

a much slower, almost undetectable rate of increase for the rest of the simulation, likely due to its continuing release by platelets being activated in the bulk. While TxA_2 concentration also continues to increase due to platelet activation, its level is well below its activation threshold throughout the simulation. For the case where PPACK was used to completely inhibit thrombin, ADP concentration increases initially, due to surface-induced agonist release, then begins to decrease rapidly as surface saturation is approached and the bulk-released agonists begin to wash away, reaching a relatively negligible value after approximately 30 s of flow. Normalized TxA_2 concentration remains very low throughout. The maximum concentration of TxA_2 observed in all simulations performed in this chapter was approximately 320 nM, slightly more than half its assumed threshold for platelet activation (see Figure 10A, inset).

The effect of flow on the spatial distributions of agonists is shown in Figure 10. This figure shows normalized concentrations as a function of axial position at two lateral stations, the wall ($y = 0$) and $y = 25$ μm, taken as representative of the bulk flow, after 75 s of flow. Results for the no-thrombin case have been omitted because normalized ADP and TxA_2 concentrations are negligible at this point in time (see Figure 9B). At the wall, it is clear that thrombin is the dominant agonist, with concentrations ranging from approximately 40- to 600-fold greater than threshold. ADP concentrations range from about 5- to 8-fold greater than threshold, while levels of TxA_2, when expressed in terms of its platelet activation potential, are about half the threshold level. At a distance of 25 μm from the wall, the ADP trend is the opposite of that at the wall: increasing axially, as compared to the steady decrease at the wall. This is likely due to the increased convection at this location relative to the wall, as ADP released from platelets activated in the bulk at this location will be more rapidly washed downstream. Levels of TxA_2 are negligible. Relative to their respective values at the wall, the level of thrombin at $y = 25$ μm drops approximately two orders of magnitude, whereas the level of ADP decreases by only about a factor of four. Some of the decrease in thrombin concentration is because the rate of thrombin generation on bulk activated platelets is an order of magnitude lower than that selected for platelets activated by both agonists and collagen at the wall. However, given the disparate levels of the two agonists at the wall, it is apparent that heparin has a very noticeable effect on bulk thrombin concentration. This inhibitory effect was confirmed by numerical experiments conducted without heparin (data not shown). In these simulations, ADP and TxA_2 concentrations were similar to the values shown in Figure 12. However, without heparin, the maximum

normalized thrombin concentration at the wall was roughly double the maximum value in the simulation with heparin, while at y = 25 μm, the maximum normalized value was nearly two orders of magnitude greater than the value for blood with 2 U ml^{-1} heparin. We note that these results agree qualitatively with the simulations of Folie and McIntire (97), who considered four agonists (thrombin, ADP, TxA_2, and von Willebrand factor) and heparin inhibition.

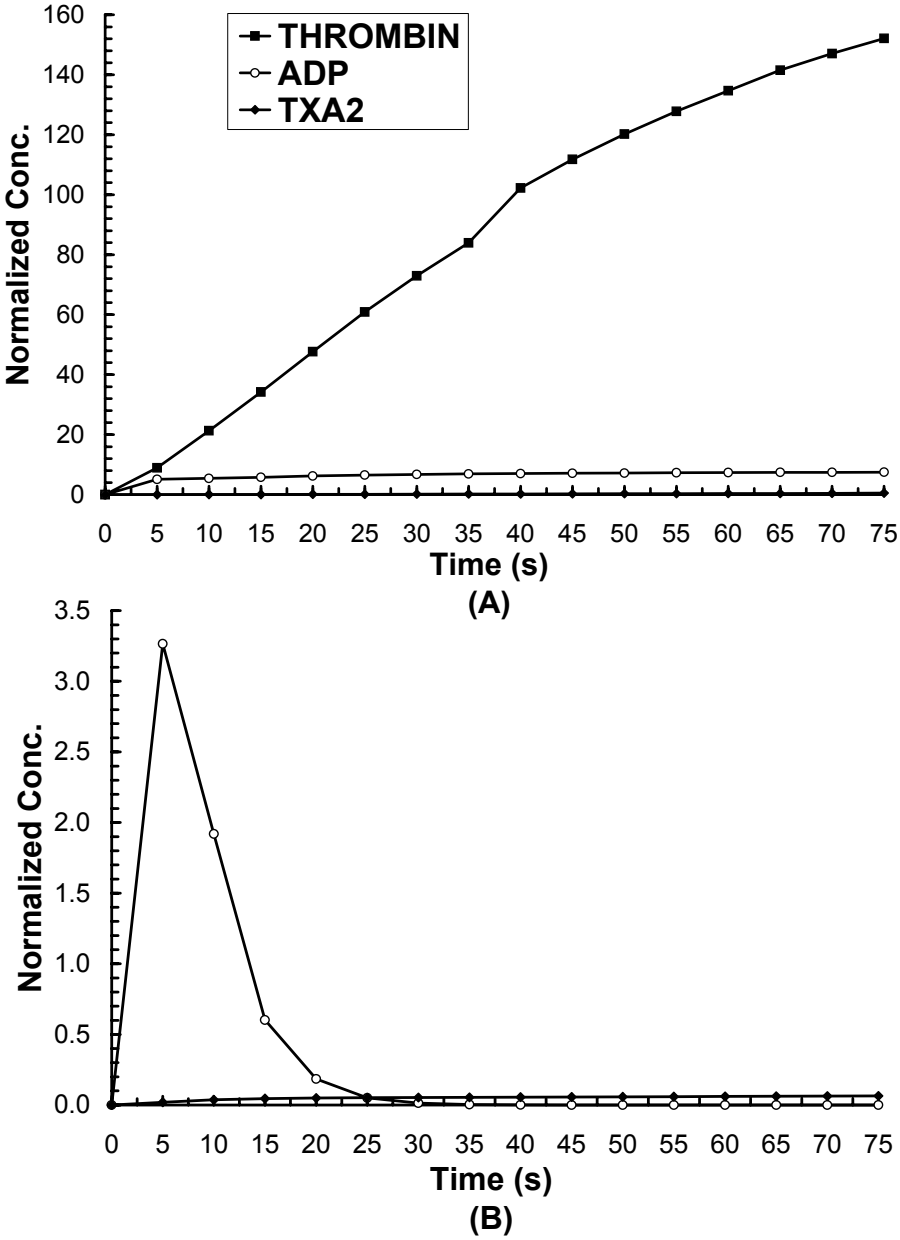

Figure 9. Predicted normalized agonist concentrations vs. time at point 2.5 mm downstream of inlet, training cases

(A) Model with thrombin. (B) Model without thrombin. Reprinted with permission from Sorensen *et al., Ann. Biomed. Eng.,* 1999;27(4):449-458 (137). Copyright 1999, Biomedical Engineering Society.

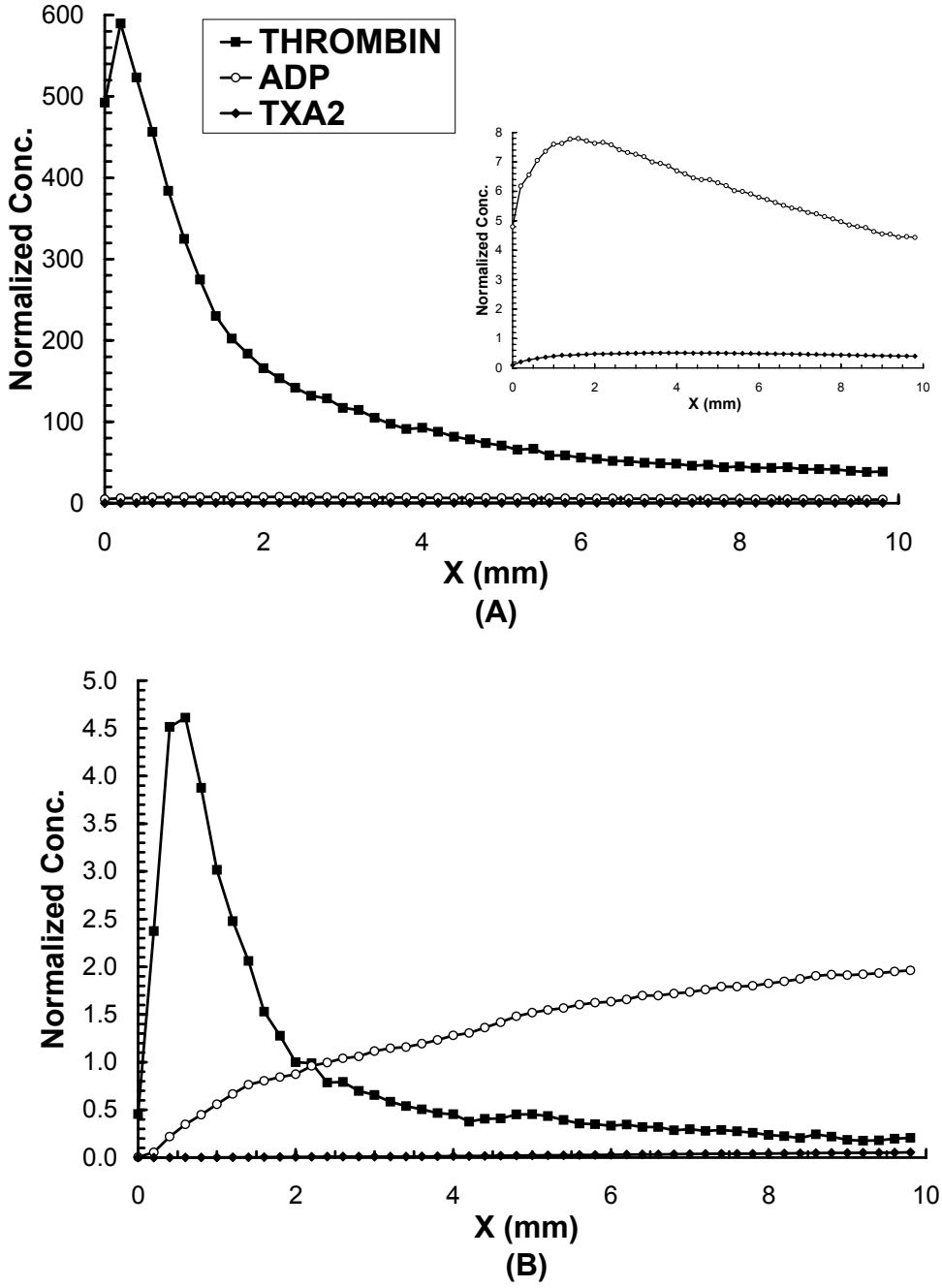

Figure 10. Predicted normalized agonist concentrations vs. distance, training case with thrombin

(A) Concentrations at wall. Inset: Magnified detail of ADP and TxA_2 trends. (B) Concentrations 25 μm from wall. Reprinted with permission from Sorensen *et al., Ann. Biomed. Eng.,* 1999;27(4):449-458 (137). Copyright 1999, Biomedical Engineering Society.

Figure 11 shows the sensitivity of the overall model, as measured by predicted platelet deposition values, to agonist generation for the model-training simulations. Further confirming the dominance of thrombin generation in determining platelet activation, the greatest difference, corresponding to approximately a fivefold decrease in peak deposition, is noted between the full model ("HEPARIN ONLY") and the model with thrombin generation turned off to simulate PPACK inhibition ("HEPARIN+PPACK"). By contrast, removing TxA_2 from the model, either with or without thrombin present, makes essentially no difference in the final platelet deposition values. The removal of ADP makes a noticeable but relatively small difference in platelet deposition for both the thrombin and no-thrombin cases.

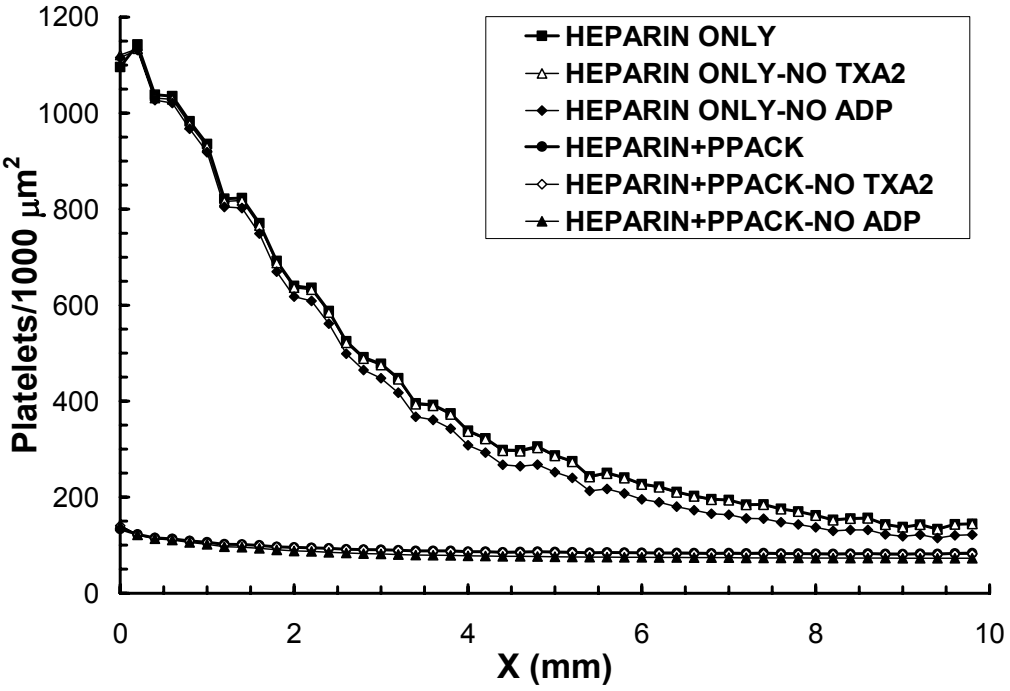

Figure 11. Sensitivity of predicted platelet deposition to agonist generation

The axial distributions of activated platelets for the model with and without thrombin at the same two locations as above (wall, $y = 0$, and $y = 25$ μm) are shown in Figure 12. At the wall, trends in activated platelet concentration for the simulation with thrombin mirror trends in agonist concentration, with more activated platelets located where agonist concentrations are higher. In the bulk flow ($y = 25$ μm), activated platelet concentration increases with downstream

distance due to the concomitant rise in bulk agonists. Despite the much higher concentrations of agonists at the wall, the maximum activated platelet concentration there is only approximately three times the maximum concentration at y = 25 μm. This is due to rapid consumption of activated platelets at the wall by platelet-surface and platelet-platelet adhesion, as modeled by the k_{aa} and k_{as} terms. For the no-thrombin case, the concentration at the wall falls off rapidly due to deposition, while at y = 25 μm the concentration varies only slightly with axial distance since little or no bulk activation occurs in this case. The slight decrease in concentration with downstream distance at y = 25 μm is likely due to diffusion of platelets toward the wall to replace those consumed by the surface.

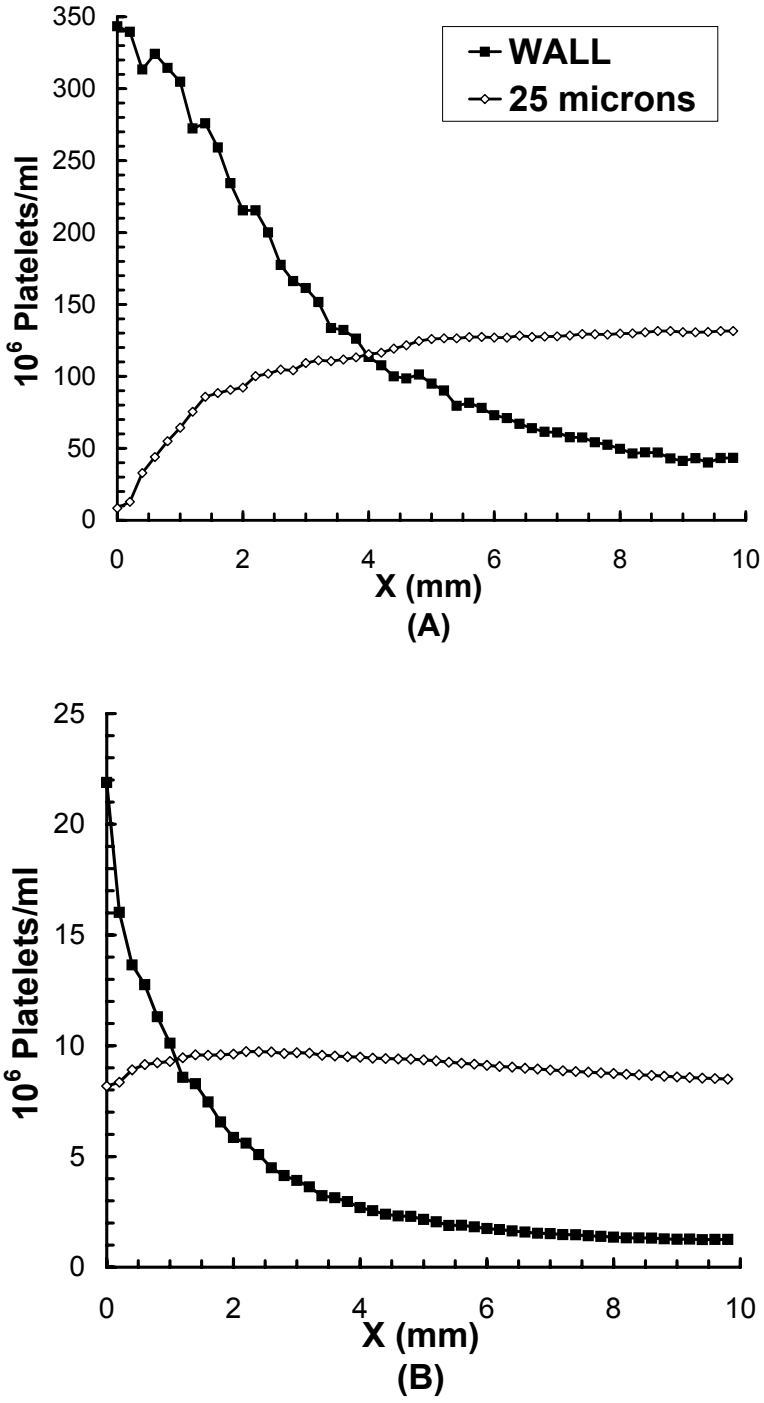

Figure 12. Predicted activated platelet concentrations vs. distance, training cases

(A) Model with thrombin. (B) Model without thrombin. Reprinted with permission from Sorensen *et al., Ann. Biomed. Eng.,* 1999;27(4):449-458 (137). Copyright 1999, Biomedical Engineering Society.

3.3.2 Validation Cases

Figure 13 shows model predictions of total platelet deposition versus the experimental data of Hubbell and McIntire (138) for 120 s of flow of heparinized whole human blood at wall shear rates of 100 and 500 s^{-1}. Extrapolating linearly from the best-fit value $D_{PLT} = 1.66 \times 10^{-6}$ cm^2 s^{-1} at 1000 s^{-1} for the training cases and assuming zero enhancement at zero shear, the D_{PLT} values used for these cases were 1.66×10^{-7} and 8.33×10^{-7} cm^2 s^{-1}, respectively. Aside from the inlet platelet concentration, as listed in Table 6, and the flow rate for the velocity solution, no other parameters were adjusted from the values obtained for the training cases. Again, the model-predicted data were averaged to give approximately the same number of points as for the experimental data. For $\dot{\gamma}_w = 100$ s^{-1}, the model predicts the shape of the deposition curve and its magnitudes fairly well, although, similar to the heparin-only training case, values near the inlet are slightly overestimated, while downstream values are underestimated. For $\dot{\gamma}_w = 500$ s^{-1}, on the other hand, the shape of the curve is well predicted, but the amount of deposition is generally over-predicted, with the error greater than 100% of the experimental values near the inlet and decreasing with downstream distance.

Figure 14 compares the model's predicted total platelet deposition values to the experimental results of Alevriadou *et al.* (139) for 60 s of flow of whole human blood with 0.38% wt/vol sodium citrate at a wall shear rate of 1500 s^{-1}. The experimental results represent the average of two sets of platelet deposition values given in that report for identical perfusion conditions; the model data were spatially averaged to give an equal number of data points. The value for shear-dependent platelet diffusivity used for the simulation, interpolated linearly from the best-fit training-case value, was 2.49×10^{-6} cm^2 s^{-1}. While the predicted values agree roughly with the experimental platelet deposition magnitudes near the inlet and outlet, in general the model greatly underestimates the measured values, by more than 50% at some locations, and the shapes of the two curves do not match at all. Since this case is substantially similar to the no-thrombin training case, which the model fit extremely well, this result is somewhat puzzling. Either the use of citrate, rather than heparin and PPACK, as the anticoagulant, or the higher shear rate, has altered the thrombogenic process for this case in a way that the model does not capture adequately by assuming the only effect of this anticoagulant is 100% thrombin inhibition.

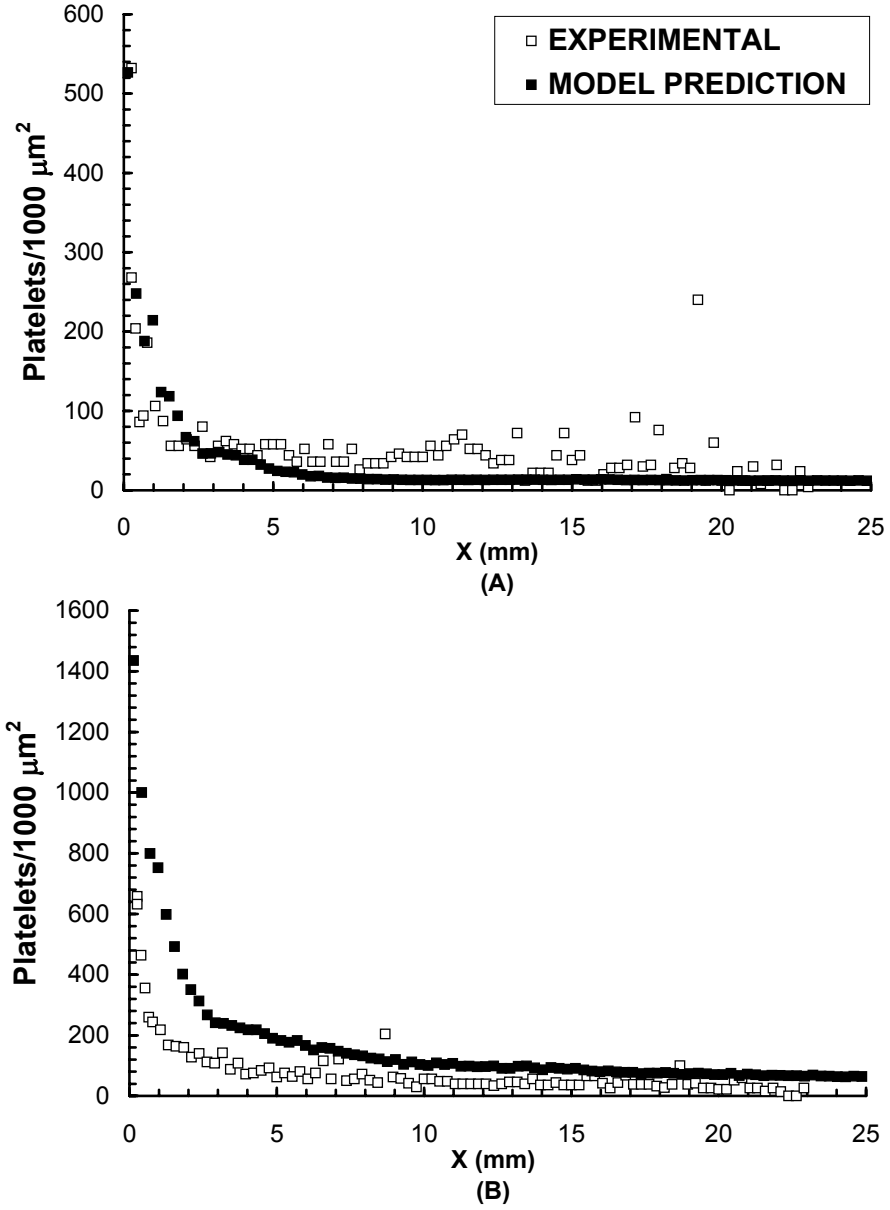

Figure 13. Comparison of predicted axial platelet deposition to experimental results of Hubbell & McIntire (A) Wall shear rate = 100 s^{-1}. (B) Wall shear rate = 500 s^{-1}. Reprinted with permission from Sorensen *et al., Ann. Biomed. Eng.,* 1999;27(4):449-458 (137). Copyright 1999, Biomedical Engineering Society.

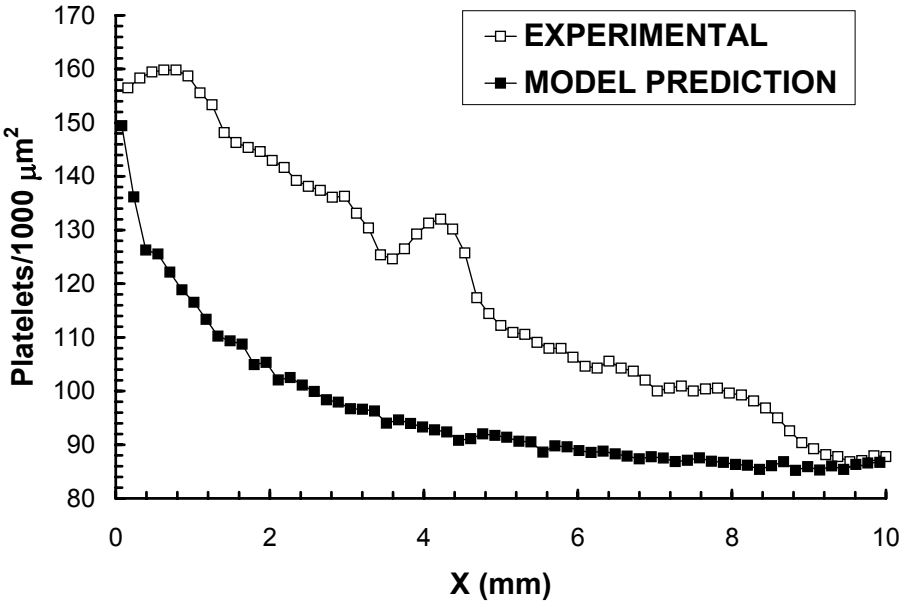

Figure 14. Comparison of predicted axial platelet deposition to experimental results of Alevriadou *et al.*
Reprinted with permission from Sorensen *et al., Ann. Biomed. Eng.,* 1999;27(4):449-458 (137). Copyright 1999, Biomedical Engineering Society.

3.4 Discussion

In our computations, mechanical interactions between platelets and the flow field are neglected. Currently, it is assumed that the scale of the thrombus is not sufficient to cause flow disturbances, and the flow field is not re-computed during the solution process to account for platelet deposition. This assumption could account for some of the observed discrepancies between the model's predictions and the experimental data. If depositing platelets form finite-size aggregates that protrude into the flow, they could lead to local flow disturbances that may produce high local agonist concentrations similar to those obtained by Folie and McIntire (97), and may also trap platelets in downstream eddies. Aggregates that project into the near-wall excess-platelet boundary layer may also alter the pattern of platelet depletion. The latter mechanism was proposed by Sakariassen and Baumgartner (140) to explain results similar to those of Wagner and Hubbell for platelet deposition on type I collagen. These considerations might be germane to a case such as the 100 s^{-1} validation case from Hubbell and McIntire's work (138). One would expect that the high levels of platelet deposition observed near the inlet would

create macroscopic thrombi, which, combined with the low fluid shear rate, would generate slow-moving vortices which could be local "hot spots" for agonist generation and platelet activation, thereby increasing downstream deposition. Since the model does not capture this behavior, it under-predicts downstream deposition. The effects of recirculation zones on agonist generation, platelet activation, and downstream deposition are investigated in Chapter 4.

An additional mechanical aspect of fluid-thrombus interaction which is neglected in our model is platelet embolization due to fluid dynamic forces. Our model allows the simulated thrombus to continue to grow as long as there are activated platelets available for platelet-platelet adhesion and some activated platelets are deposited on the surface to initiate a platelet-platelet flux. Furthermore, the process of platelet deposition is not limited by local fluid dynamics. That is, there is no part of the model that explicitly accounts for the time scale of platelet interactions with each other and the surface. Hence, we have assumed that the reaction rates governing agonist generation and platelet activation are not shear-dependent. These would be important factors in limiting thrombus growth, since a sufficiently high local shear rate could: 1) prevent a passing platelet from having sufficient time to "recognize" a biomaterial surface and adhere to it; 2) prevent a passing platelet from having enough time to form a sufficiently tight bond with an already deposited platelet; or 3) inhibit local agonist generation, thereby decreasing platelet activation and activated platelet-platelet adhesion.

The neglect of these shear-dependent phenomena would provide a reasonable rationale for the model's very poor fit for the 1500 s^{-1} case, as that high shear rate would be expected to inhibit upstream deposition, as well as to create a higher predilection for embolization of weakly adherent platelets or platelet aggregates, resulting in a deposition pattern with an irregular, "bumpy" shape similar to that of the experimental curve. For the simulation performed at 500 s^{-1} with heparin as the anticoagulant, the model's inability to simulate embolization of platelets from thrombi near the entrance might explain the over-fitting of upstream deposition values. However, it would not explain the continued over-fitting of downstream values. Additionally, if embolization were important at this shear rate, one would expect its effects to be even more pronounced for the 1000 s^{-1} model training case, for which a much better fit was observed. One explanation for this discrepancy would be that the shorter perfusion time used in the 1000 s^{-1} case (75 s, vs. 120 s for the 500 s^{-1} case) was not sufficient for thrombolysis or embolization to begin.

The issues of shear-dependent platelet adhesion and activation reaction rates could be addressed by investigating functional kinetic relationships which are more complex than the simple first-order ones included in the present model and which take into account the shear-dependence of the reactions. Addressing the problems of fluid-thrombus interaction is a more challenging task. First, simulating thrombus growth would require coupling the mass transport equations to the fluid flow equations, necessitating a computationally expensive flow-field solution at every iteration of the mass transport equations. Second, a reasonably accurate way of introducing the mechanical interactions between the thrombus and the flow field would have to be incorporated into both sets of equations. Fogelson (105) has proposed doing this by incorporating a fictitious body force into the Navier-Stokes equations which would account for deformation of the flow field by thrombus growth. However, simulating embolization would be more challenging, since it would require depicting the shape of the thrombus somehow so that the fluid dynamic forces on it could be accurately computed, as well as knowing something about the fracture mechanics of the thrombus structure.

Despite the computational complexity of simulating these phenomena, the possibility of their inclusion in the model needs to be considered, as they have a direct bearing on the usefulness of the simulations as design aids. For example, in attempting to design a relatively "thrombosis-proof" device for long-term use, one would need to know when or if thrombus growth will stabilize. The present model would only be able to simulate such a phenomenon in a particular way: for a given geometry and a sufficiently high shear rate, generated agonists might be convected quickly away and would not be able to accumulate in concentrations sufficient to cause platelet activation. Combined with a sufficiently low rate of platelet-surface adhesion, this would lead to a cessation of deposition, i.e. to the formation of a passive, stable thrombus, but not until the surface concentration reached a monolayer level, which would clearly not be representative of all biomaterials. The time at which this passivated monolayer was reached could be controlled by varying the platelet-surface and platelet-platelet reaction rates, but surface deposition would never reach a sub-monolayer steady state.

Since the concentration of platelets at a reactive surface directly determines the amount of platelet deposition in our simulations, solution accuracy depends heavily on the model for lateral transport of platelets to the wall. One of the most important deficiencies in the present model is its relatively crude method of inducing a near-wall excess. With a true near-wall platelet

excess, the RBC-enhanced diffusivity of platelets should be low near the wall, where red cells are excluded, and much higher near the core region, where most of the red cells reside. Our model uses a single value for diffusivity at all transverse locations, which could help explain its predictive error, since the higher diffusivity near the wall gradually destroys the skewed concentration profile. Furthermore, red-cell-induced platelet motion should be directed away from the channel center regardless of the platelet concentration gradient, whereas an enhanced diffusivity requires a gradient to produce platelet motion. Also, platelet diffusivity is currently an unknown parameter. It cannot be obtained by direct measurement, and must therefore be estimated for each case to be fit. In this chapter, a linear variation of platelet diffusivity with wall shear rate was assumed, so that a great deal of the error in our simulations could be attributed to a linear fit being the wrong functional form for this parameter. To more accurately reproduce this phenomenon, it would be preferable to have a more accurate mathematical description of near-wall excess. One model of this phenomenon which has shown the ability to reproduce experimental platelet concentration profiles for flow in small-diameter tubes is Eckstein's concept of red-cell-induced drift (79, 80).

Thrombin is clearly the most important platelet agonist in the reported simulations, with its concentration at the surface and in the bulk much higher than its threshold for platelet activation. This occurs despite the inhibitory effects of heparin concentrations up to 10 U ml^{-1} and despite the fact that our platelet-activation rate constant (Equation 3) weights threshold-normalized concentrations of all agonists equally. It is possible that thrombin's dominance is due to the agonist generation model we employed, which allows the rate of thrombin production to increase linearly with platelet deposition and imposes no upper bound on this rate. Although a linear increase in thrombin generation with platelet concentration was shown by Rosing *et al.* (119), the studies were conducted using platelets suspended in buffer medium, rather than whole blood, thereby removing the inhibitory effects of various plasma proteins (e.g. C and S). The key contributing factor in thrombin's dominance, however, is likely our choice of an increased rate of thrombin generation at the reactive surface relative to the bulk flow; such an increase is consistent with the behavior of platelets activated by both collagen and thrombin vs. thrombin alone (119).

The agonist ADP was also shown to be an important mediator of platelet activation in these simulations. Its concentration was also generally supra-threshold throughout the domain, with normalized levels 25 μm from the wall comparable to those of thrombin. TxA_2 concentrations were generally well below the platelet activation threshold we proposed. Consequently, this species did not play a significant role in platelet activation in our simulations. This is consistent with the experimental results of Turner *et al.* (141), who observed that aspirin, which inhibits platelets' ability to synthesize TxA_2, failed to decrease platelet deposition on type I collagen and had very little effect on platelet aggregation under flowing conditions. It is notable that our results were obtained despite the fact that the model gave platelets an inexhaustible capacity to generate this agonist. However, it is possible that our simplistic model of agonist interaction may not correctly capture the contribution of TxA_2, or that this agonist might participate in other important thrombogenic processes aside from platelet activation. Wagner and Hubbell (142) postulated a role for TxA_2 in thrombus stabilization, observing that administration of aspirin reduced platelet-platelet adhesion on type I collagen. However, statistically significant reductions in deposition for aspirinized versus control blood were only obtained at longer flow times than those simulated here.

3.5 Conclusions

In this chapter, the model of platelet-mediated thrombogenesis proposed in Chapter 2 has been calibrated against several sets of experimental results for platelet deposition on type I collagen under simple parallel-plate (Poiseuille) flow. In general, the predicted results demonstrate good agreement with the experimental trends in spite of many unmodeled effects, such as fluid-thrombus interactions. Based on a calibration case with a wall shear rate of 1000 s^{-1} and only heparin as the anticoagulant, the model was able to fit cases with: 1) PPACK added as the anticoagulant; and 2) a five-fold increase of heparin concentration, a wall shear rate lowered by a factor of two or ten, a domain 2.5 times as long, and an almost two-fold longer perfusion time. We believe this indicates, at least in a preliminary fashion, the robustness of the model for this range of conditions. However, for the case with a higher wall shear rate (1500 s^{-1}) and sodium citrate as the anticoagulant, the model was not as accurate in predicting deposition along the length of the perfusion channel. This could be due to a shear-dependent decrease in platelet adhesion or agonist generation kinetics which only becomes apparent at shear rates greater than

1000 s^{-1}, or to a fluid-dynamic mechanical effect such as embolization, all of which are neglected in the present model. Alternatively, it could be that citrate's effects on thrombogenesis are more extensive than thrombin inhibition alone. Either way, it is apparent that the citrate case has revealed that the model was not capturing all of the physics of the system being simulated.

As for the model's behavior with regard to agonists, the distinctly different platelet deposition patterns observed when thrombin is present versus when it is inhibited can be explained by considering the ways agonist generation and platelet activation are simulated. Without thrombin, the rate of agonist generation at the surface will depend on: 1) the rate at which resting platelets adhere, activate, and degranulate, releasing ADP; and 2) the rate at which activated, surface-bound platelets synthesize TxA_2. This surface-generated agonist production will induce platelet activation and agonist generation in the bulk fluid. However, our model only allows resting platelets to adhere to the exposed surface, not to other deposited platelets. Also, the surface deposition rate goes to zero at the surface saturation limit (see Equations 11-12). Thus, after surface saturation, only activated platelet-platelet adhesion can occur, and the only sources of agonist generation will be TxA_2 synthesis by activated platelets (at the surface and in the bulk) and ADP release by activating platelets (in the bulk only). At a high shear rate such as that used in the model-training simulations, the bulk agonists will be quickly convected away by the flow. Despite the worst-case assumption that activated platelets have an inexhaustible capacity for TxA_2 synthesis, Figure 9 shows that levels of this agonist remain approximately a factor of two below the level required for platelet activation throughout our simulations. Thus, in the absence of thrombin, the model predicts minimal platelet activation, and therefore minimal activated platelet-platelet adhesion occurs once the surface-saturation limit is reached.

The rate of thrombin generation, on the other hand, is proportional to local platelet concentration, either on the surface or in the bulk. Therefore, when thrombin is not completely inhibited, platelets will adhere to the collagen surface and become activated, generating ADP and TxA_2 and providing a phospholipid surface for additional thrombin production. This will lead to a higher bulk concentration of agonists, causing increased platelet activation and deposition. After the surface saturation limit is reached, activated platelet-platelet adhesion continues, which provides even more phospholipid surface for thrombin generation, thereby leading to increased thrombin production and further bulk activation. Thus, thrombin-mediated platelet activation and deposition behaves as a positive-feedback system. Theoretically, TxA_2 synthesis should have a

similar effect, since its rate is also proportional to the total concentration of activated platelets, both at the surface and in the bulk flow. However, the sub-threshold levels of TxA_2 found in our simulations prevent it from making a significant contribution to the rate of platelet activation. Conversely, in the no-thrombin case surface saturation leads to a negative-feedback cascade, in which increased platelet deposition results in more rapid saturation, which induces decreased ADP generation, which, combined with the washing effect of the high-shear flow and the low rate of TxA_2 synthesis, eventually leads to a cessation of new platelet deposition.

As discussed in Chapter 2, the model is applicable to a much wider range of conditions than the simple flows and single biomaterial studied in this chapter. In Chapter 4, the robustness of the model is further tested by using it to attempt to predict platelet deposition onto collagen from disturbed, fully two-dimensional flows.

4.0 MODEL VALIDATION: TWO-DIMENSIONAL DISTURBED FLOW

"Something is happening here and you don't know what it is
Do you, Mr. Jones?"

-Bob Dylan, "Ballad of a Thin Man"

4.1 Introduction

In this chapter, the validation efforts begun in Chapter 3 continue. Here, we apply the model to flow in two different axisymmetric geometries, a tubular expansion and a stenosis, for which experimental measurements of platelet deposition onto type I collagen are available from the literature. For the tubular expansion cases, the *in vitro* experiments were conducted to minimize platelet aggregation and release. Additionally, results are available at several Reynolds numbers ($Re = \rho \cdot U \cdot d_T / \mu$, where U is mean velocity and d_T is tube diameter) and at both 0% and 20% hematocrit (Hct). These cases are therefore ideal for testing the platelet-transport-related portions of the model, especially our methods of modeling RBC-enhanced platelet motion. For the stenotic geometry, non-anticoagulated blood was used in a baboon *ex vivo* shunt. Thus these two sets of cases allow us to test the effects of disturbed flow both in the presence and absence of agonists on predicted platelet activation and deposition. Furthermore, the model predictions for the stenosis cases can be compared to those of Wootton *et al.* (104), who simulated deposition in this geometry using a one-parameter steady-state model.

4.2 Methods

For both sets of cases considered in this chapter, closed-form solutions to the Navier-Stokes equations (Equations 16 and 17) are unavailable. Thus, it was necessary to solve these equations numerically. A finite volume solver built on top of the existing convection-diffusion code was developed for this purpose. Following the method of Prakash and Patankar (143), a two-dimensional, pressure-based, node-centered computational fluid dynamics (CFD) code for unstructured meshes was written. This code is capable of solving the steady or unsteady Navier-Stokes equations, i.e., incompressible, laminar flow of a Newtonian fluid is assumed. To accelerate convergence of the pressure equation, an algebraic multigrid solver (144) was also developed. The combined CFD and convection-diffusion code was then extended from Cartesian to polar axisymmetric coordinates following the technique of Masson *et al.* (145). As before,

meshes are generated using the freeware program *Triangle.* Additionally, we continue to assume the Navier-Stokes equations can be decoupled from the species conservation equations of the thrombosis model, allowing us to solve for a steady-state flow field. The CFD solver was validated using benchmark cases from the literature; these results are presented in the Appendix.

4.2.1 Axisymmetric Tubular Expansion

Simulations for the case of a sudden expansion of flow in a tube were performed, corresponding to the experimental results of Karino and Goldsmith (59). In their studies, suspensions of platelets and RBCs (at 0% and 20% Hct) were perfused (at Re = 29 – 113, based on upstream tube diameter) through an axisymmetric expansion made from a 0.917 mm i.d. stainless steel tube fit into a 3 mm i.d. collagen-coated glass tube. Experiments were performed for both one and three minutes at 0% Hct and for one minute at 20% Hct. To test the effect of hematocrit on the model's ability to predict platelet transport, we first simulated results for both 0% and 20% Hct for one minute of perfusion at Re = 38. The best-fit model parameters from these simulations were then used to predict deposition for the additional Reynolds numbers and perfusion time.

Since the suspensions used in these experiments contained no clotting factors or adhesive proteins, and since apyrase was added to inhibit platelet-released ADP, it was assumed no agonist activity would take place. Therefore, all platelet agonists and clotting factors were eliminated from the model, leaving resting and activated platelets as the only species simulated. The reaction coefficient governing platelet-platelet aggregation (k_{aa}, see Equation 6) was also set to zero, since aggregation should be essentially negligible in the absence of fibrinogen and vWF. Furthermore, Karino and Goldsmith (59) specifically attempted to minimize aggregation through their choice of perfusion times; very little platelet-platelet contact was observed in their experiments.

Model parameters specific to these cases are listed in Table 7; all other parameters are as given in Tables 3-4. As previously, the surface activation parameter θ has been set to one for all cases, reflecting the assumption that all platelets contacting the collagen surface are activated by it. Viscosity μ was assumed constant at each hematocrit. Its values at 0% and 20% Hct were calculated from the Reynolds number equation, $Re = \rho \cdot U \cdot d_T / \mu$, using the mean velocities given by Karino and Goldsmith at Re = 38, assuming a density of 1.05 g cm^{-3}.

The computational domain consisted of an axisymmetric cross-section of the cylindrical geometry 25 mm in length and with a 1.5 mm inner radius, corresponding to the larger tube. This length was sufficient to ensure fully developed flow at the outlet for all Reynolds numbers in the CFD simulations. The inlet was taken as the leading edge of the sudden expansion (the axial position where the 0.917 mm i.d. tube enters the 3 mm i.d. tube).

For the flow field solution, a fully developed parabolic velocity profile was assumed at the inlet, with U equal to the average velocity reported by Karino and Goldsmith for each Reynolds number and hematocrit. No slip ($u_z = u_r = 0$) was assumed at solid walls, and the symmetry condition was enforced at the centerline $r = 0$ by the imposition of the conditions $\partial u_z / \partial r = u_r = 0$. At the outlet (z = 25 mm), fully-developed flow ($\partial u_z / \partial z = \partial u_r / \partial z = 0$) was assumed. For pressure BCs, a zero normal gradient was imposed at all boundaries, and pressure was fixed at zero in the lower right corner of the domain ($r = 0$, z = 25 mm).

For the platelet transport simulations, most boundary conditions were identical to previous cases, with the adhesion fluxes given by Equations 5 and 6 governing platelet reactions at the collagen-coated wall. Symmetry about $r = 0$ was enforced with BC $\partial [C_i] / \partial r = 0$. Fully developed concentration profiles ($\partial [C_i] / \partial z = 0$) were assumed at the outlet (z = 25 mm). In the interior domain, the initial condition for all species was $[C_i] = 0$.

Table 7. Specific parameter values for tubular expansion cases

Parameter	0% Hct	20% Hct	Equations
$[RP]$	4.5×10^8 PLT·ml^{-1}	4.5×10^8 PLT·ml^{-1}	1,5,7[a]
C_0 (for $[RP]$)	N/A	2.7×10^8 PLT·ml^{-1}	19[a]
M_∞	7.00×10^5 - 7.00×10^6 PLT·cm^{-2}	7.00×10^5 - 7.00×10^6 PLT·cm^{-2}	6,11[b]
D_{PLT}	1.58×10^{-9} cm^2 s^{-1}	Equations 22-23	--
θ	1.00	1.00	7,13-15
μ	1.10×10^{-2} g cm^{-1} s^{-1}	2.30×10^{-2} g cm^{-1} s^{-1}	16
ρ	1.05 g cm^{-3}	1.05 g cm^{-3}	16

N/A = not applicable for this case

[a]values for [*AP*] are 1/9 of this value (for background activation = 10% of total PLT concentration)

[b]two values of this parameter were used; see text for explanation

Because there was no RBC enhancement effect for the 0% Hct cases, the platelet diffusivity was set to its Brownian value, and the inlet condition was a uniform concentration profile.

To simulate RBC-enhanced platelet transport for the 20% Hct cases, the quadratic wall-skewed profile (Equation 19) was used as the inlet boundary condition for resting and activated platelets, as in Chapter 3. However, for both platelets and large species, the constant shear-enhancement factors used for the parallel-plate simulations were replaced with the enhanced diffusivity proposed by Zydney and Colton (77). The relationship they obtained is:

$$D_s = 0.15 \cdot \left(d_{rbc}/2\right)^2 \cdot \dot{\gamma} \cdot Hct \cdot \left(1 - Hct\right)^{0.8} \quad [22]$$

$$D_i = D_{b,i} + D_s, \quad [23]$$

where *Hct* represents the bulk average hematocrit (taken as constant) expressed as a decimal, rather than a percent. Zydney and Colton suggest setting d_{rbc} to the RBC major diameter, rather than the equivalent spherical diameter. Since Karino and Goldsmith used human blood, the appropriate value is approximately d_{rbc} = 8 μm. The Zydney and Colton formula was chosen over others such as the Keller correlation of Equation 18 (78) because it was based on a wide range of experimental results, rather than a purely theoretical treatment, and because it accounts for the effects of both hematocrit and shear rate. Additionally, using an empirical relationship instead of treating D_{PLT} an independent model parameter, as we did for the platelet diffusivity in Chapters 2 and 3, reduces the number of undetermined parameters by one, improving the predictive capacity of the model and reducing the ambiguity of its parameters.

Thus far, we have either estimated a constant diffusion-enhancement factor as a model parameter or calculated it by using the *wall* shear rate -- which is constant for the parallel-plate Poiseuille flow fields considered in Chapters 2 and 3 -- in Equation 18, rather than the *local* shear rate, which varies linearly as a function of *y*. For the current geometry, the wall shear rate will vary spatially, making it impossible to calculate a single enhancement factor for the flow field based on that variable. Thus, in the current simulations, we retain the *local* shear rate in Equation 22, meaning that platelet diffusivity can vary with both *z* and *r*.

The level of background platelet activation was increased from the 5% assumed previously to a value of 10%. Based on Karino and Goldsmith's total platelet concentrations (59), this corresponds to 5×10^7 PLT·ml^{-1}. This value was increased based on the extensive separation and washing procedures used to prepare platelets for these studies, which would inevitably cause increased platelet activation.

Additionally, the surface saturation parameter M_∞ was altered from the value assumed in Chapters 2 and 3. Two values of M_∞ were tried: the previously assumed monolayer concentration (7.00×10^6 PLT·cm^{-2}) and 10% of this value. This parameter was varied in an attempt to mimic experimental conditions reported by Karino and Goldsmith, who observed microscopically that "as little as 5%" of the surface of the glass tubes they used were coated with collagen fibrils. Since there were no adhesive proteins in their suspensions and since they pre-adsorbed the glass surface with non-adhesive albumin, very little platelet deposition was observed on the glass interstices between fibrils (59). However, they measured deposition values greater than 5% of our assumed monolayer value. This motivated our somewhat arbitrary choice of an "effective saturation" of 10% of a monolayer. However, in our pilot studies, we used the standard monolayer value. This was done to keep M_∞ a fixed parameter across all our simulations; the underlying physical assumption was that at longer times than those studied, platelets would spread or be translocated by fluid shear stresses, eventually resulting in a monolayer covering the glass regions of the slide. It was assumed that altering the values of k_{rs} and k_{as} appropriately would control this transient behavior. In the results presented below, the M_∞ value used for a particular case is given.

In summary, the undetermined model parameters for these cases are the reaction coefficients k_{rs} and k_{as}, governing platelet-surface adhesion for resting and activated platelets, respectively. Since these coefficients are assumed to be functions of both surface and blood protein composition, it was necessary to re-fit them for the protein-free suspensions considered here, rather than using the best-fit values for type I collagen in contact with whole blood determined in Chapter 3. Separate trial-and-error fits were conducted for the 0% and 20% Hct cases at $Re = 38$, perfusion time = 1 minute. The best fits at each hematocrit were then applied to the other hematocrit case to see if either set of parameters could fit both data sets. Then, the best-fit parameters for each hematocrit level were used to simulate additional Reynolds number and/or perfusion time cases at that hematocrit.

Due to our assumption that the flow and concentration fields can be decoupled, the steady-state Navier-Stokes equations were solved to obtain the flow field. The unsteady convection-diffusion equations were then solved using a time step of 0.6 s for both one- and three-minute perfusion times. Since mesh-dependence effects play a large role in the results for these cases, that issue is discussed separately.

4.2.2 Axisymmetric Stenosis

The flow within an axisymmetric stenosis was simulated to correspond to the experimental results used by Wootton *et al.* (104) to validate their computational model of acute platelet deposition and vessel occlusion in the presence of disturbed flow. Collagen-coated ePTFE grafts, 4 mm in diameter, with sinusoidal stenoses of 50%, 75%, and 90% area reduction were inserted into baboons in an *ex vivo* shunt preparation. Platelet deposition at several time points was assessed with a gamma camera, which gave average deposition over five regions of interest (ROIs) covering the 2.4 cm long collagen-coated portion of the shunt. The Reynolds number based on upstream velocity and diameter was estimated to be 160. Wootton *et al.* simulated these experiments using a one-parameter model whose only undetermined variable was a lumped mass-transfer coefficient governing platelet activation, aggregation, and adhesion at the reactive wall. This model also used the enhanced diffusivity of Zydney and Colton (77) and incorporated near-wall excess by setting the uniform inlet concentration to twice the normal bulk value. Their normalized measure of predicted platelet deposition was the steady-state maximum platelet "accumulation velocity", V_{max} (units: cm s^{-1}). Re-written in terms of the corresponding variables in our model, this is given by:

$$V_{\max} = \frac{1}{C_{\infty} \cdot A_{ROI} \cdot \Delta t} \iint (J_r + J_a) dt dA, \qquad [24]$$

where C_{∞} is free-stream platelet concentration used in the Wootton model, A_{ROI} is the area of the region of interest, Δt is the total time of the simulation, and J_r and J_a are the resting and activated platelet-surface fluxes, given by Equations 5 and 6. The predicted values for each ROI were compared to the average rate of accumulation derived from gamma camera measurements taken between 10 and 25 minutes after the start of perfusion, during which time the rate of platelet accumulation was approximately constant (104).

Due to the very long computing times for these cases, we chose to simulate the results for only the 50% and 75% stenoses. Baboon blood was assumed to be sufficiently similar to human blood that the kinetic parameters used for the Poiseuille flow collagen training cases could be employed. So, with the exception of those parameters listed in Table 8, the values listed in Tables 3-5 were applied unaltered. The basis for this assumption is the experimental studies of Grabowski *et al.* (146), which found no significant difference in platelet deposition onto the biomaterial Cuprophan (cellulose hydrate) between baboon and human blood. The values selected for [*RP*] and [*AP*] correspond to the average total platelet count measured by Schneider *et al.* for baboons in similar shunt experiments (147); following Wootton *et al.*, appropriate baboon values of d_{rbc} = 8.8 μm and *Hct* = 0.35 were used in Equation 22 to compute D_s. Wootton *et al.* chose twice the bulk-average platelet concentration as their uniform inlet boundary condition rather than attempting to impose a non-uniform near-wall excess profile. For this reason, the value of C_∞ we used in Equation 24 corresponded to $2\cdot([AP] + [RP]) = 7.0 \times 10^8$ PLT·ml^{-1} so that the V_{max} value computed from our platelet deposition results would be scaled by the same factor used by those authors. Since non-anticoagulated whole blood flowed through the shunts, the heparin concentration was set to zero, and the full seven-equation model was solved. The values of μ and ρ used in the CFD solution correspond to the values used by Wootton *et al.* (104) in their simulations.

Additionally, we assumed that the best-fit platelet-surface and platelet-platelet reaction coefficients from the Poiseuille flow collagen training cases could be used. These were $k_{rs} = 3.7 \times 10^{-3}$ cm s^{-1}, $k_{as} = k_{aa} = 4.6 \times 10^{-3}$ cm s^{-1}. These values are very close to the best-fit value of 5.0×10^{-3} cm s^{-1} that Wootton *et al.* obtained for the single surface reaction parameter used in their model (104). There was therefore no parameter re-fitting done for these cases, representing a very stringent test of the applicability of the model

Boundary conditions for the collagen-coated region of the shunt were identical to those described in the previous section for the 20% Hct tubular expansion cases, and a zero initial condition was applied for all seven species in the interior of the domain. A 6 mm long non-adhesive entrance region was added to the inlet of the domain to account for the silicon rubber tubing used in the experiments. The steady-state flow field was computed using the CFD code and then input into the unsteady convection-diffusion problem. To ensure fully developed flow at the outlet, straight 4 mm diameter tubes of 45 mm (50% stenosis) and 56 mm (75% stenosis)

length were added beyond the collagen-coated region. In the platelet deposition simulations, these zones represented the non-adhesive silicone rubber tubing; hence a zero-flux boundary condition was applied at the walls. To minimize the computational cost of the unsteady platelet deposition simulations, solutions corresponding to a time of 10 minutes were run. This time represents the very start of the experimental window during which a constant platelet accumulation rate was observed by Wootton *et al.* (104). The maximum time step used in these simulations was 6 s. Due to the extremely long computing times needed for these cases (several weeks, depending on processor used and load), mesh independence studies were not conducted. The meshes used contained 79144 nodes for the 50% stenosis and 82168 nodes for the 75% stenosis. In the 24 mm long collagen-coated region, a 50 μm wide zone extending out from the wall was filled with elements of approximately the same area as those placed in the near-wall zone of the 77612 node grid used for the tubular expansion cases (discussed below).

Table 8. Specific parameter values for axisymmetric stenosis cases

Parameter	Value	Equations
$[RP]$	3.15×10^8 PLT·ml^{-1}	1,5,7[a]
C_0 (for $[RP]$)	1.02×10^8 PLT·ml^{-1}	19[a]
$[H]$	0.00 μM	4
D_s	Equation 22	--[b]
μ	3.50×10^{-2} g cm^{-1} s^{-1}	16
ρ	1.06 g cm^{-3}	16

N/A = not applicable for this case

[a]values for [*AP*] are 1/9 of this value (for background activation = 10% of total PLT concentration)

[b]used to correct diffusivities of "large" species (thrombin, prothrombin, ATIII) and PLTs for effect of red blood cells in shear flow; D_{PLT} is given by Equation 23

4.3 Results

4.3.1 Axisymmetric Tubular Expansion

a) Baseline case 1: 0% Hct, Re = 38

Figure 15 shows fluid shear rate along the tube wall (r = 1.5 mm) as a function of unstructured mesh density for the 0% Hct, Re = 38 case. In the legend, "non-uniform" and "uniform near-wall" refer to the way the mesh was refined to resolve the boundary layer. The former method involved an option in the grid generation software by which the area of all elements touching a surface could be increased or decreased. While this method did result in a high concentration of elements near the wall, it also interspersed them very non-uniformly with large elements, as illustrated in Figure 16A. The latter approach involved creating a 50 μm domain near the upper wall which was uniformly filled with much smaller elements than were used in the rest of the domain. The results of this approach are illustrated for the 23630 node mesh in Figure 16B.

Neither refinement method nor grid density affected the CFD results, which are mesh-independent at all grid resolutions tested. Figure 17 shows velocity profiles and streamlines in a cross-section extending from r = 0 to r = 1.5 mm, i.e. the upper half of the tube. The plot is truncated at z = 11 mm, after fully-developed flow has been re-established. Figure 17A illustrates the velocity profiles at the inlet (z = 0), inside the vortex (z = 2.5 mm) and in the fully-developed region (z = 10 mm). Figure 17B, which plots streamlines, illustrates the size and extent of the separated-flow region caused by the sudden expansion. The recirculation zone begins at the inlet and extends approximately 4.4 mm (~ 1.5 diameters) downstream, with fully-developed flow reestablished approximately 2.5 – 3 mm (~ 1 diameter) beyond the flow reattachment point. In their studies, Karino and Goldsmith's microscopic observations yielded 4.4 mm as the distance from the expansion to the reattachment point for this case (59); the close agreement between this measurement and the CFD result serves as further validation of the solver.

To predict the experimental platelet deposition values, the surface reaction rate constants k_{rs} and k_{as} were adjusted by trial and error to give the best fit to the data. The first attempts at doing this were made using the 25984 node grid with a non-uniform near-wall mesh (Figure 16A). The saturation parameter M_∞ was set to 7.0×10^6 PLT cm^{-2} for these trials. Best-fit parameter values were $k_{rs} = 3.94 \times 10^{-6}$ cm s^{-1} and $k_{as} = 4.89 \times 10^{-6}$ cm s^{-1}, an almost thousand-fold reduction relative to the whole blood-collagen cases simulated in Chapter 3.

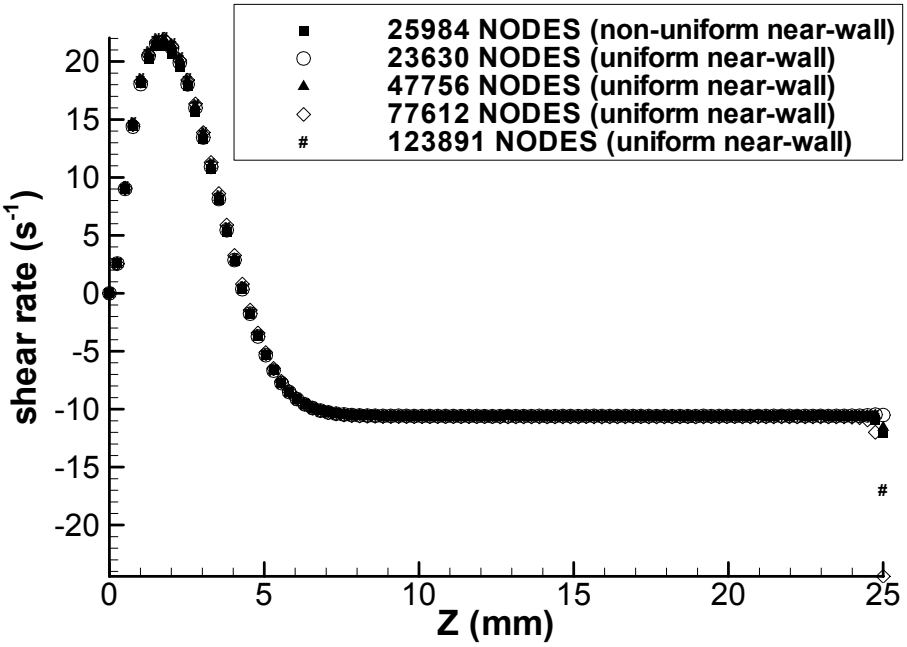

Figure 15. Wall shear rate vs. axial distance, effect of grid density: 0% Hct, *Re* = 38 tubular expansion case

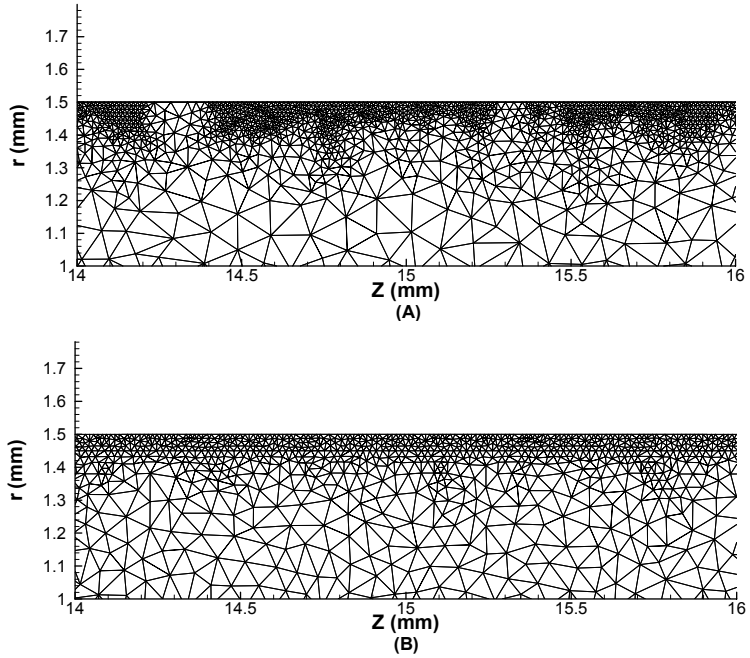

Figure 16. Comparison of near-wall meshes used for tubular expansion cases

(A) 25984 node mesh with non-uniform near-wall refinement. (B) 23630 node mesh with uniform near-wall refinement.

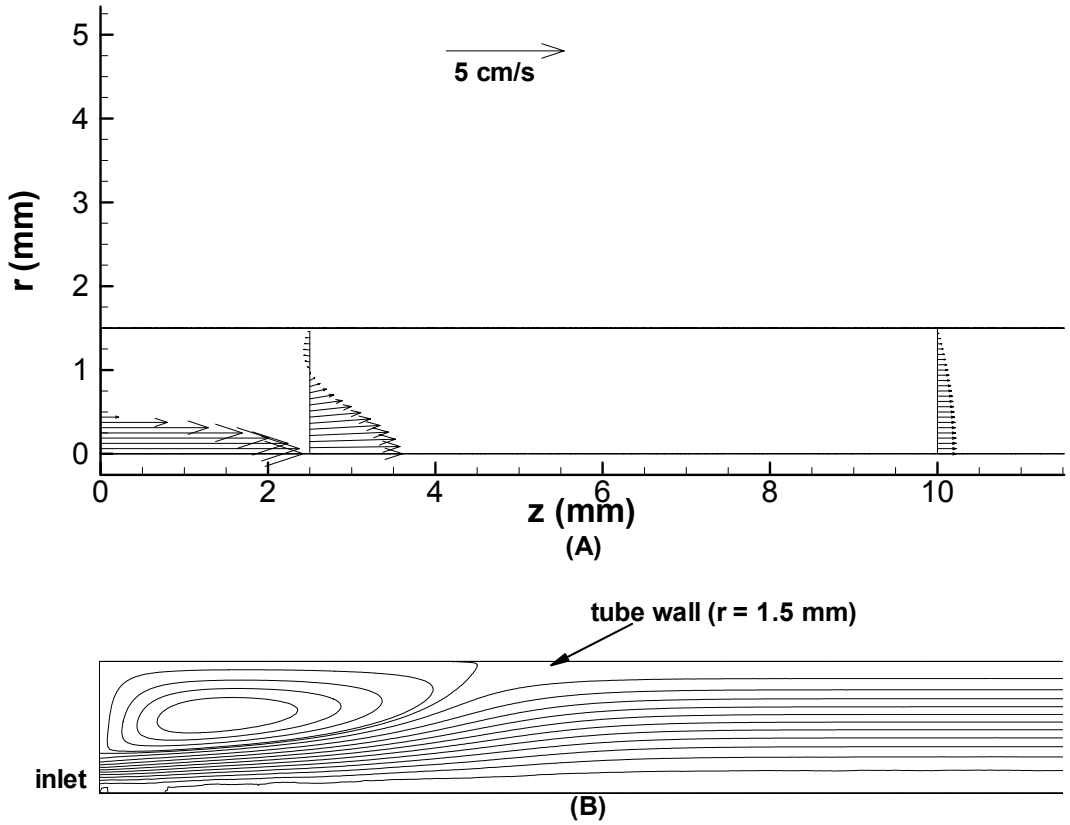

Figure 17. Velocity profiles and streamlines: 0% Hct, *Re* = 38 tubular expansion case
(A) Velocity profiles at z = 0, 2.5, and 10 mm. (B) Streamlines.

To verify grid independence of this result, the case was re-run on the 77612 node, uniformly-refined mesh, which revealed the surprising behavior shown in Figure 18. In the figure, the model results have been averaged to correspond to the experimental grid. Fairly good agreement between the experiment and both sets of predictions is observed in the recirculation zone and near the reattachment point. However, it was necessary to increase the platelet-surface reaction coefficients by more than 50% for the fine-grid case (to $k_{rs} = 6.2 \times 10^{-6}$ and $k_{as} = 8.0 \times 10^{-6}$ cm s^{-1}) to obtain roughly the same agreement between predicted and measured deposition values in this region. The second item of interest is the steep drop-off in platelet deposition downstream of the reattachment point, within the fully-developed region of the flow. While the coarse-grid results decay noticeably relative to the experimental values, the fine-grid values drop much more rapidly, with deposition falling almost to zero beyond z = 14 mm.

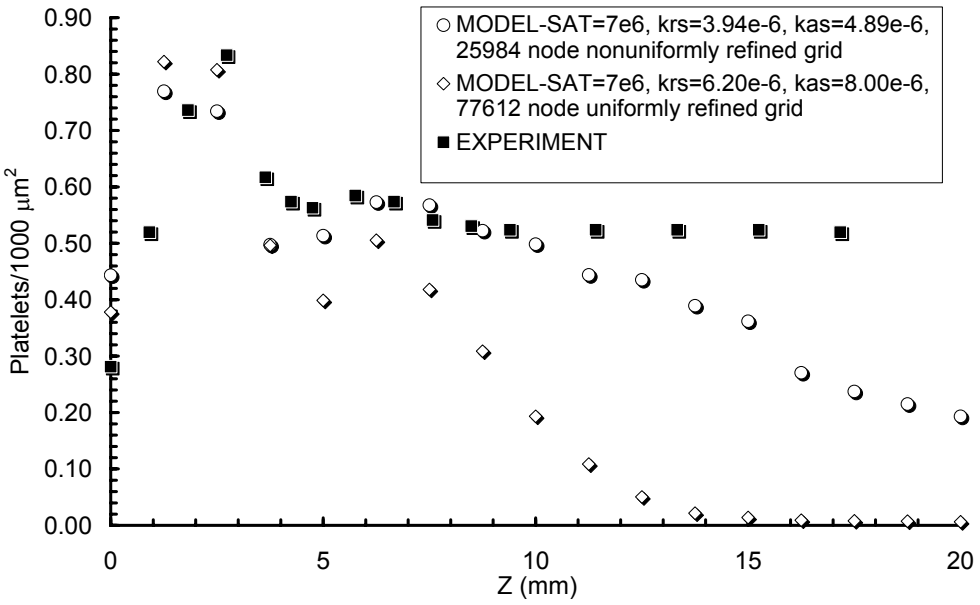

Figure 18. Initial model predictions of platelet deposition: 0% Hct, *Re* = 38 tubular expansion case

"SAT" refers to the surface saturation parameter M_∞.

Additional insight into the differences between the coarse- and fine-grid model results can be obtained by considering platelet concentrations at the wall, which are shown in Figure 19. This figure also shows the results of a simulation run on the fine grid in which $k_{rs} = k_{as} = 0$, i.e. no platelet-surface reaction was allowed, so that unsteady platelet transport was the only mechanism simulated. After 60 s simulation time, the concentrations at the wall on the coarse mesh have reached a virtually constant value everywhere. In contrast, on the fine grid, very few platelets have reached the wall in the downstream, fully-developed-flow region. The nearly identical results obtained for the cases with and without surface reaction indicate that the perfusion time of the simulation is insufficient for platelets to be transported to the wall.

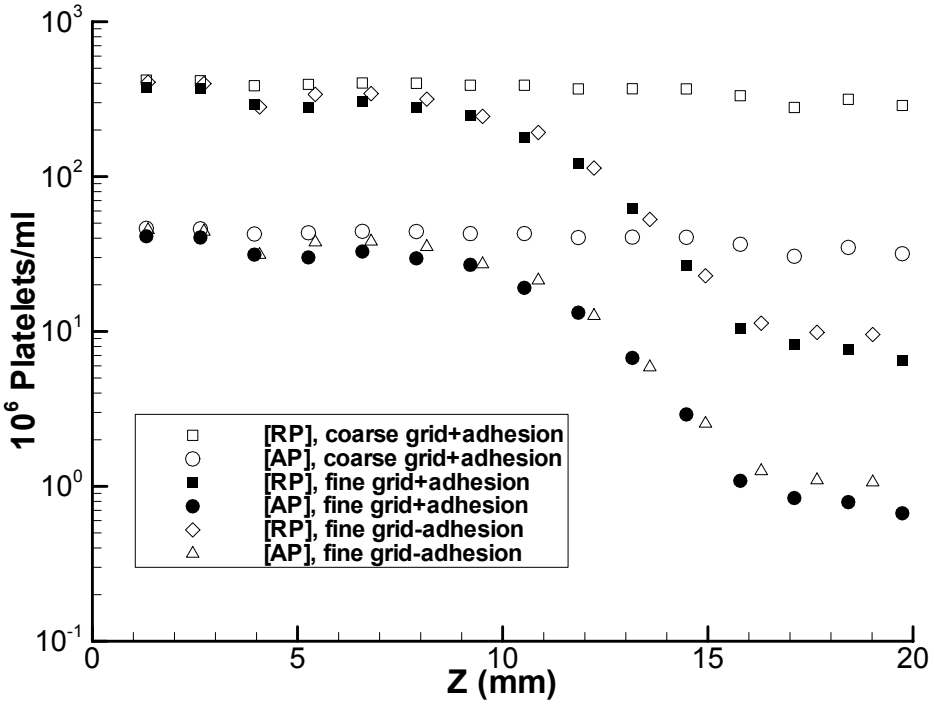

Figure 19. Predicted platelet concentrations at wall: 0% Hct, *Re* = 38 tubular expansion case

"+adhesion": PLT-surface adhesion allowed; "-adhesion": no PLT-surface adhesion allowed.

To examine the effect of platelet diffusion on the near-wall downstream depletion observed on the 77612 node mesh, additional numerical studies were carried out with this case, again at $M_\infty = 7.0 \times 10^6$ PLT cm^{-2} and $k_{rs} = 6.2 \times 10^{-6}$, $k_{as} = 8.0 \times 10^{-6}$ cm s^{-1}. For these simulations, the Brownian diffusivity of platelets in the 0% Hct suspension was augmented by an RBC-enhancement-like, additive shear-dependent factor $D_s = a_0 \cdot \dot{\gamma}$, where a_0 is a constant. The values chosen for a_0 ranged from 10^{-10} to 10^{-8} cm^2, which represent factors ranging from ~10× less to ~10× greater than the RBC enhancement value of 4.02×10^{-9} cm^2 computed using Equation 22 for the 20% Hct case. The results of these studies are shown in Figure 20, where the curve for no enhancement corresponds to the original model. Very little change in platelet deposition values is observed until a_0 reaches 10^{-8} cm^2. The effect of the enhancement is to increase deposition values everywhere along the tube surface. This results in no improvement in agreement between model and simulation as the augmentation is increased, since deposition in the recirculation zone rises too high, while the values computed for the downstream region are still too low relative to the experimental results.

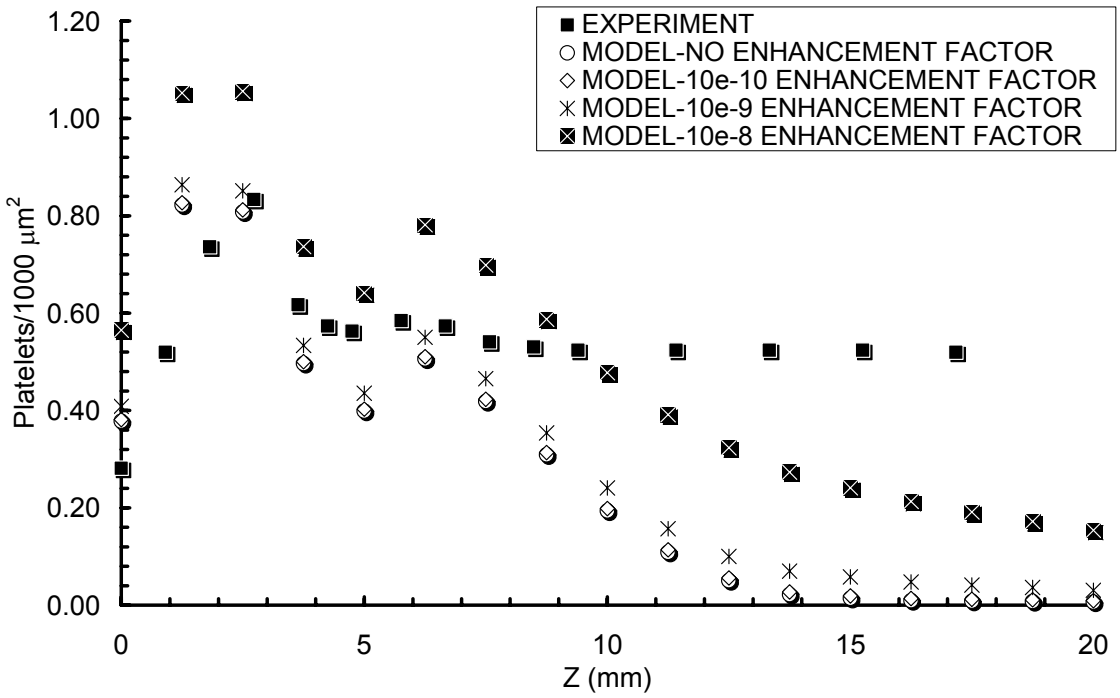

Figure 20. Effect of platelet diffusivity on predicted deposition: 0% Hct, *Re* = 38 tubular expansion case

Next, additional grid-sensitivity studies were conducted by re-running this case on three additional grids, holding k_{rs} and k_{as} fixed at the best-fit values from the 77612 node mesh. An M_∞ value of 7.0×10^6 PLT cm^{-2} was used. Figure 21 shows the results of these numerical experiments; Karino & Goldsmith's experimental results are omitted for clarity. It should be noted here that the differences in mesh density among the uniformly refined grids are entirely due to refinement of the 50 μm near-wall region. The downstream depletion effect is observed for all four such grids, despite an approximately four-fold variation in near-wall cell size. More importantly, although it appears the results grow closer to those of the previous grid at each level of refinement, true mesh independence is not achieved, despite the heavily refined grids used for the 77612 and 123691 node cases.

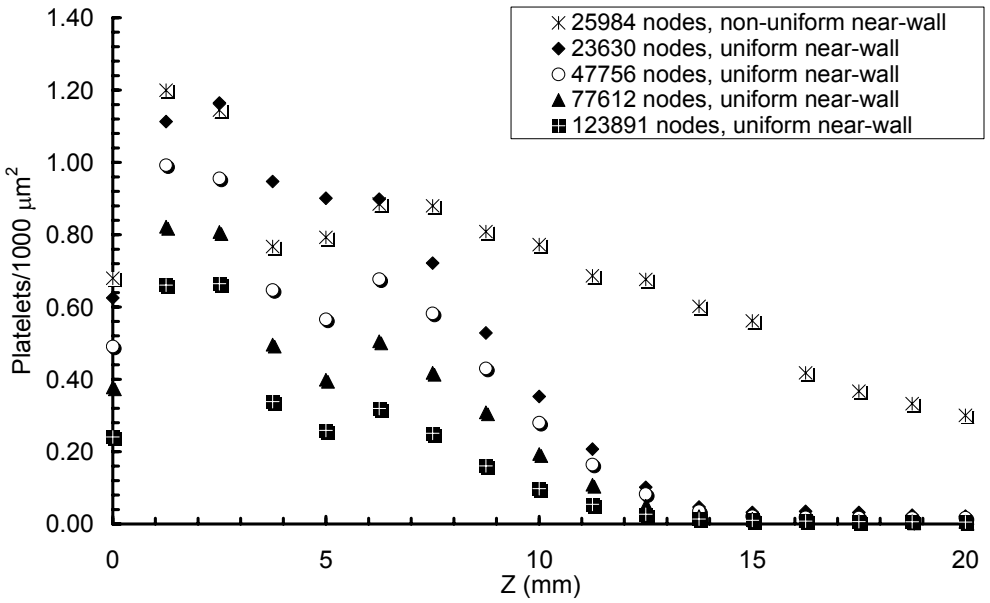

Figure 21. Effect of mesh density on predicted platelet deposition: 0% Hct, *Re*=38 tubular expansion case

Ideally, these grid dependence studies would have been performed prior to conducting the final simulations for the cases discussed subsequently. Unfortunately, however, because of the grid-independent results observed for the CFD solution, it had been assumed that the 77612 node mesh was "refined enough", and all of the remaining platelet deposition simulations had been conducted using that grid. However, given the following considerations, we believe the value of these simulations is not completely lost. First, there is the issue of time. A 60 s case at 0% Hct could typically be completed on the 77612 node mesh in two to four days on a 1 GHz Athlon machine, depending on processor load. The 123691 node case shown in Figure 21 required more than a week on the same CPU. Second, given the slow convergence to grid independence seen in Figure 21, it is likely that even the 123691 node mesh is under-refined, perhaps very much so, so that a much finer mesh, requiring even more CPU time, would likely be necessary to fully resolve this problem. Third, the results for all of the uniformly refined meshes are very similar in shape and in the relative heights of the primary and secondary deposition peaks. This, combined with the somewhat similar deposition magnitudes seen in Figure 18 between the non-uniformly-refined 25984 node grid and the 77612 uniformly refined grid when the reaction coefficients are adjusted, likely implies that similar deposition levels could be achieved on all grids by increasing k_{rs} and k_{as} as the level of grid refinement increases.

What this means is that the k_{rs} and k_{as} values reported in what follows for the 77612 node mesh must be taken as very approximate values which likely underestimate the "true" mesh-independent magnitudes of these parameters. Finally, judging by the results of Figure 21, it appears highly unlikely that increasing mesh density will improve agreement between model predictions and experiments or reveal any new behavior of the model that is not apparent on the 77612 node mesh.

To see if a discrepancy between modeled and experimental conditions could be contributing to the discrepancies between predicted and measured deposition, some of the key underlying assumptions being used for these simulations were examined. As noted above, up to this point, the saturation parameter M_∞ had been set to an assumed monolayer value, 7.0×10^6 PLT cm^{-2}. Based on the justification given in Section 4.2.1, this parameter was reduced by a factor of 10 to account for the sparse distribution of collagen fibrils on Karino and Goldsmith's tubes. It was believed this change might improve the model's predictive ability because a lower M_∞ would decrease the platelet flux more rapidly in the upstream regions where the peaks are seen (see Equations 5-6). A decreased upstream flux would presumably allow more platelets to be transported downstream, possibly correcting the near-wall depletion effect observed there. In conjunction with this parameter change, the possibility that only activated platelets would adhere to the collagen surface in the absence of plasma proteins was investigated. For these cases, k_{rs} was held at zero and M_∞ at 7.0×10^5 PLT cm^{-2} while k_{as} was varied to give the best fit to the data.

A comparison of best-fit values on the 77612 node mesh is given in Figure 22. The first case (filled triangles), for which $M_\infty = 7.0 \times 10^6$ PLT cm^{-2}, $k_{rs} = 6.2 \times 10^{-6}$ cm s^{-1}, $k_{as} = 8.0 \times 10^{-6}$ cm s^{-1}, reproduces the best-fit results from Figure 17. The open circles are predicted deposition values for the case wherein $M_\infty = 7.0 \times 10^5$ PLT cm^{-2}, for which the best-fit values are $k_{rs} = 4.0 \times 10^{-6}$ cm s^{-1} and $k_{as} = 4.0 \times 10^{-5}$ cm s^{-1}. The deposition magnitudes are nearly identical to those for the initial case. Finally, the large X's represent the case with reduced M_∞ and no resting platelet-surface adhesion, obtained using a best-fit k_{as} of 1.35×10^{-4} cm s^{-1}. The same trend in deposition is observed as for the other two cases, but deposition on either side of the reattachment point is slightly reduced.

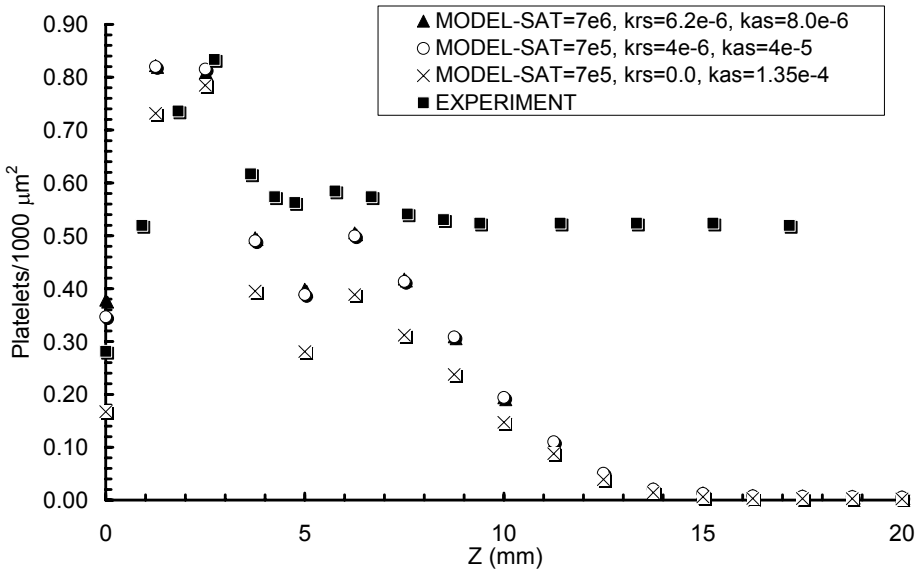

Figure 22. Comparison of best-fit final model predictions to experimentally measured platelet deposition: 0% Hct, *Re* = 38 tubular expansion case

"SAT" refers to the surface saturation parameter M_∞.

Finally, since the "best-fit" values we report are obtained by trial and error, it is helpful to give an idea of the sensitivity of the model to changes in the fit parameters k_{rs} and k_{as}. This is shown in Figure 23 for the 77612 node mesh and $M_\infty = 7.0 \times 10^5$ PLT cm^{-2}. Reducing k_{rs} by 80% with k_{as} fixed reduces peak deposition by approximately 60%. Subsequently halving both k_{rs} and k_{as} reduces peak values by about another 35%. Finally, a one-unit change in both parameters, corresponding to a 20% reduction in k_{rs} and a 25% reduction in k_{as}, further reduces deposition by approximately 20%. Thus, the sensitivities of the two parameters appear to be within the same order of magnitude.

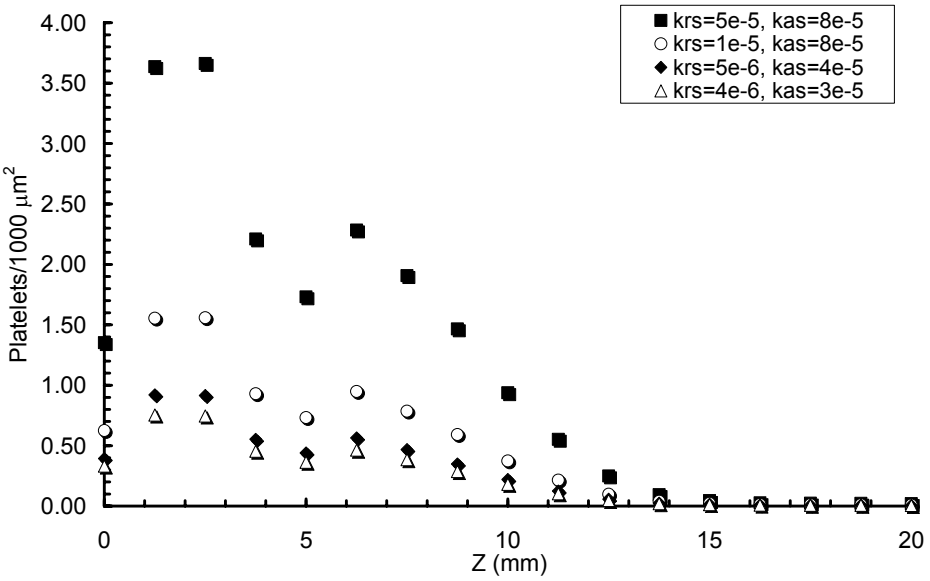

Figure 23. Sensitivity of predicted deposition to k_{rs} and k_{as}: 0% Hct, *Re* = 38 tubular expansion case

b) Baseline case 2: 20% Hct, *Re* = 38

CFD results for the case of 20% Hct, *Re* = 38 are shown in Figures 24 and 25 for the 77612 node mesh, which has been used for all cases discussed in the remainder of this section. Although the shear rate everywhere along the wall is well below the ~200 s^{-1} limit for Newtonian blood flow (121), non-Newtonian effects should not be as large a concern here as they would be in whole blood because the experimental perfusate was free of fibrinogen, so that there should be no RBC rouleaux formed. Due to dynamic similarity with the 0% Hct case, the streamline plot of Figure 25B is basically identical to Figure 17B. Again, the CFD-predicted recirculation zone extends approximately 4.4 mm downstream from the expansion, with fully developed flow re-established approximately 7.5 – 8.0 mm downstream of the inlet. For this experiment, Karino and Goldsmith measured the length of the separated flow region as 5.0 mm. No explanation of how this measurement was made or the degree of uncertainty in it is given in their paper, so it is difficult to determine how large a departure from the computed results this represents. Comparing Figures 25A and 17A, the velocity profiles are similar, although, as expected the magnitudes are higher at 20% Hct due to the higher average velocity needed to obtain the same Reynolds number for the higher viscosity of the suspension at this hematocrit.

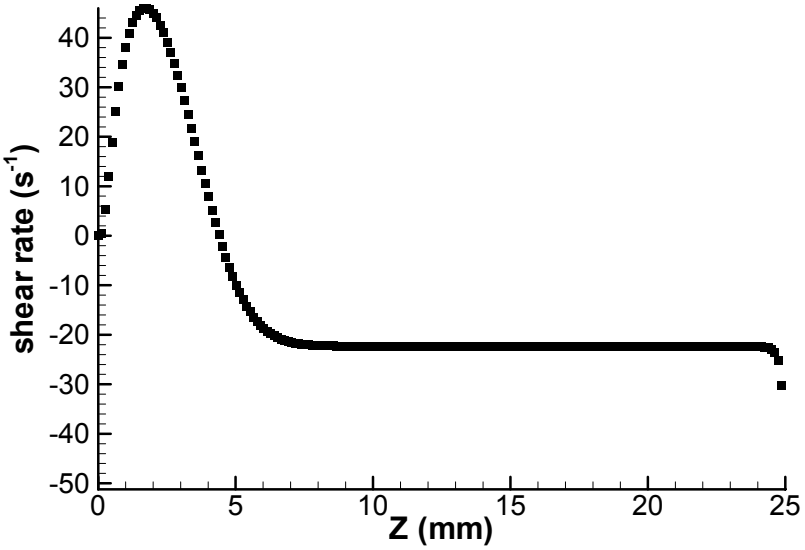

Figure 24. Wall shear rate vs. axial distance: 20% Hct, *Re* = 38 tubular expansion case

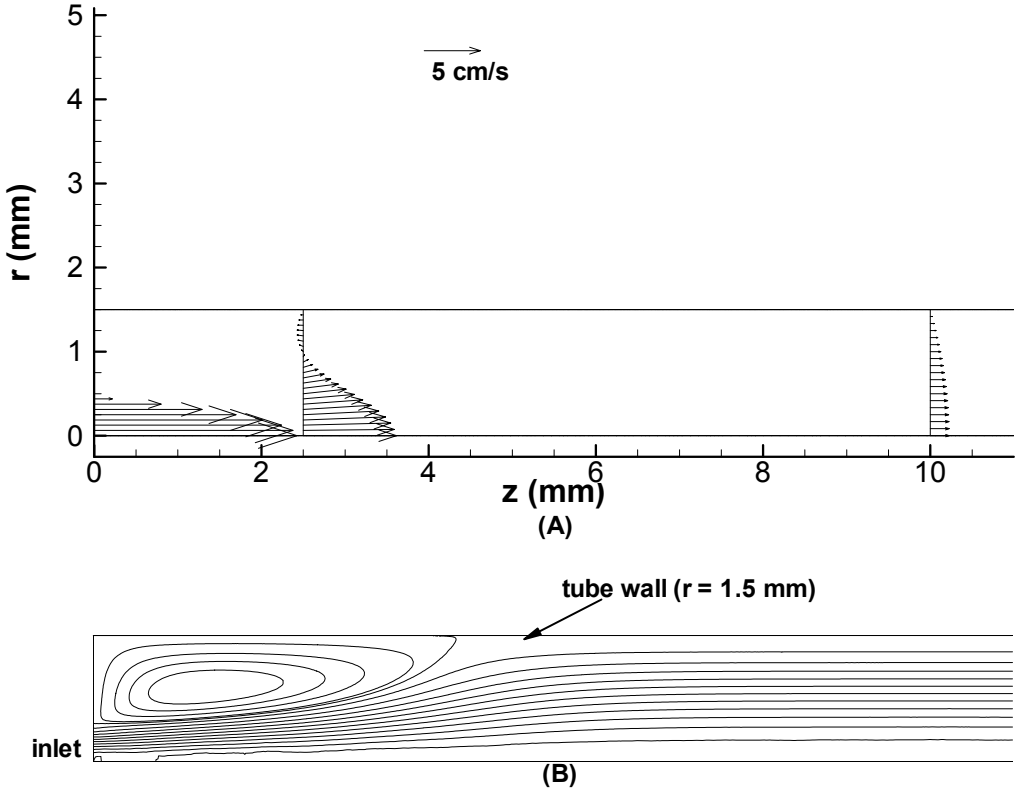

Figure 25. Velocity profiles and streamlines: 20% Hct, *Re* = 38 tubular expansion case

(A) Velocity profiles at z = 0, 2.5, and 10 mm. (B) Streamlines.

For all the platelet deposition cases that follow, an M_∞ value of 7.0×10^5 PLT cm^{-2} was assumed. Figure 26 compares the best-fit predicted deposition values to the experimental values for this case. Two models were fit: one with both resting- and activated platelet-surface adhesion, and one with only activated platelet adhesion. Best-fit parameters were $k_{rs} = 1.0 \times 10^{-5}$ and $k_{as} = 1.0 \times 10^{-4}$ cm s^{-1} for the former and $k_{as} = 3.5 \times 10^{-4}$ cm s^{-1} for the latter.

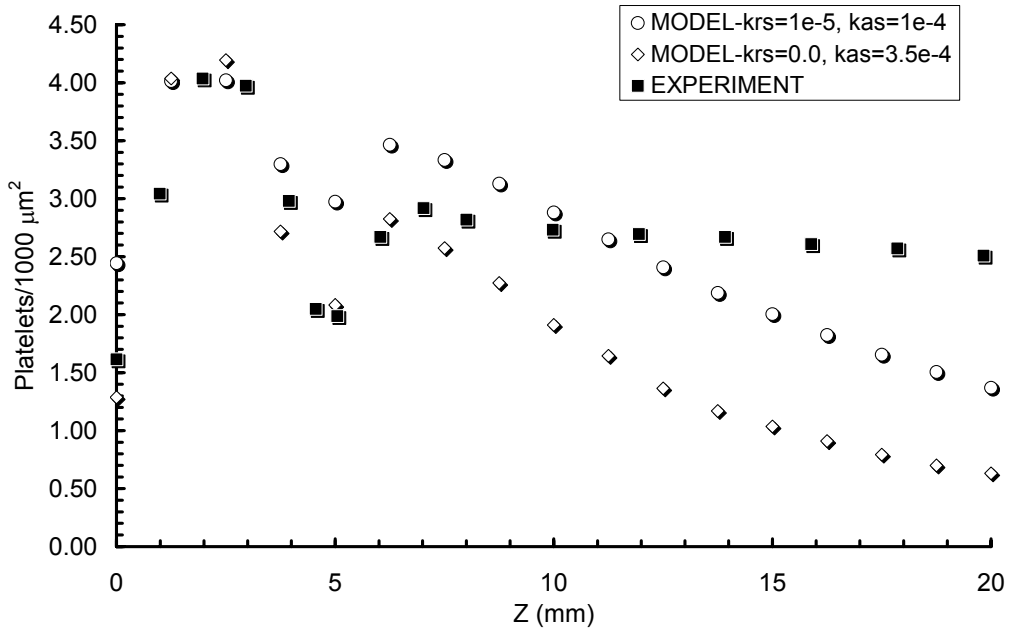

Figure 26. Comparison of best-fit final model predictions to experimentally measured platelet deposition: 20% Hct, *Re* = 38 tubular expansion case

Both models display similar good agreement with the experimental data in the separated-flow region; further downstream, the one with $k_{rs} = 0$ shows better agreement at and just past the reattachment point, while the model with both adhesion terms on appears to fit better overall due to its higher level of predicted deposition in the fully-developed-flow region. In comparison to Figure 22, there is a much less severe downstream diminution of predicted platelet deposition. Based on the hypothesis that this error is due to slow transport to the wall for these cases, the likely explanation for this result is the higher average flow velocity (U = 9.0 cm s^{-1} at the inlet), as compared to the 0% Hct case (4.3 cm s^{-1}).

Sensitivity of the model to variations in k_{rs} and k_{as} for 20% Hct, Re = 38 is shown in Figure 27. The k_{rs} and k_{as} values used here are identical to those tested for the 0% Hct simulations (see Figure 23). In general, the effects of k_{rs} and k_{as} on predicted deposition are approximately identical to the 0% Hct case: an ~35% drop in peak deposition is seen for a 50% decrease in both k_{rs} and k_{as} from the second to the third lowest curves, while an ~20% decrease is seen for a 20% reduction in k_{rs} and a 25% reduction in k_{as} between the third and fourth lowest curves. The only difference is that at 20% Hct only a ~40% decrease in deposition occurs for an 80% reduction in k_{rs} between the two highest curves, versus ~60% for the 0% Hct case. This is likely because deposition values for the highest curve at 20% Hct approach 100% saturation, whereas for the 0% Hct case, the peak value reaches only about 50% saturation.

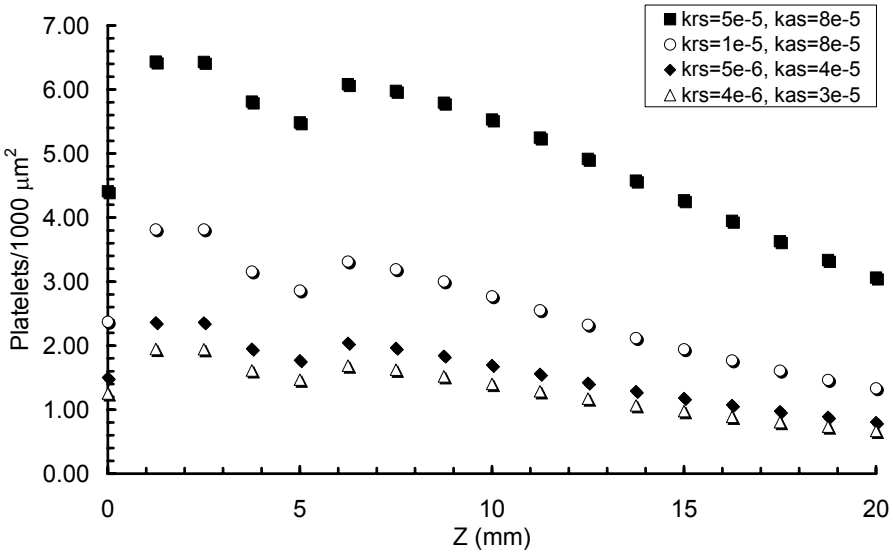

Figure 27. Sensitivity of predicted deposition to k_{rs} and k_{as}: 20% Hct, Re = 38 tubular expansion case

c) Cross-validation cases

Since the only difference between the two Re = 38 test cases is hematocrit, and since the platelet-surface reaction coefficients are assumed to depend only on surface composition and blood protein content, k_{as} and k_{rs} should be the same for both cases. To see if one set of parameters could fit both data sets, the best-fit values of k_{as} and k_{rs} for the 0% Hct, Re = 38 case were used to simulate deposition at 20% Hct, Re = 38, and vice-versa for the 20% Hct best-fit coefficients. For these studies, the "best fit" values were taken as those for which both resting

and activated platelet-surface adhesion were allowed (k_{rs} = 4.0 × 10^{-6}, k_{as} = 4.0 × 10^{-5} cm s^{-1} at 0% Hct; k_{rs} = 1.0 × 10^{-5}, k_{as} = 1.0 × 10^{-4} cm s^{-1} at 20% Hct). These values were chosen because their simulations tended to predict the experimental data better than the simulations with no resting platelet-surface adhesion. Also, since collagen should activate most of the resting platelets that contact it, making them just as likely to adhere as bulk-activated platelets, it was difficult to justify excluding the resting platelet adhesion term. An additional simulation using the mean values of these 0% and 20% Hct best-fit parameters was also conducted.

Figure 28 shows the results of these "cross-validation" studies. Not surprisingly, using the 20% Hct best-fit k_{as} and k_{rs}, which are 2.5× greater than the best-fit 0% Hct values, to simulate the 0% Hct case results in over-prediction of deposition. The peak values are over-estimated by as much as 100%. In the downstream fully-developed flow region, near-wall depletion due to transport limitations again results in nearly zero deposition at locations where z > ~14 mm. Likewise, the 20% Hct simulation using the best-fit 0% Hct parameters under-predicts the experimental results by as much as 50% at the primary peak and in the farthest distal downstream regions, although the discrepancy there is not as great as for the 0% Hct case. When the means of the best-fit values (k_{rs} = 7.0 × 10^{-6}, k_{as} = 7.0 × 10^{-5} cm s^{-1}) are used, the predicted deposition values, unsurprisingly, fall approximately halfway between the predictions using the 0% and 20% Hct best fit values for both simulations, still over-predicting the 0% Hct experimental data and under-predicting the measured 20% Hct values.

In a further attempt to fit both sets of data with one set of parameters, additional cases were run at 20% Hct, Re = 38 using the best-fit 0% Hct coefficients while increasing the 0.15 factor in D_s (see Equation 22) by one to three orders of magnitude. Figure 29 shows the results of these simulations, where "1X ENHANCEMENT" represents the baseline value of D_s given by Equation 22. In general, increasing the level of diffusion enhancement raises deposition levels everywhere, while simultaneously flattening the entire curve, consistent with a transition from diffusion- to reaction-limited behavior. At the highest level of enhancement (1000X) deposition decreases, likely due to homogenization (smearing out) of the wall-skewed inlet boundary condition, which would lead to fewer platelets reaching the wall. Although downstream deposition levels and longitudinal profiles are more consistent with the experiments at the higher enhancement levels, the flattening of the upstream peak prevents further improvement in these predictions over those of the baseline simulations.

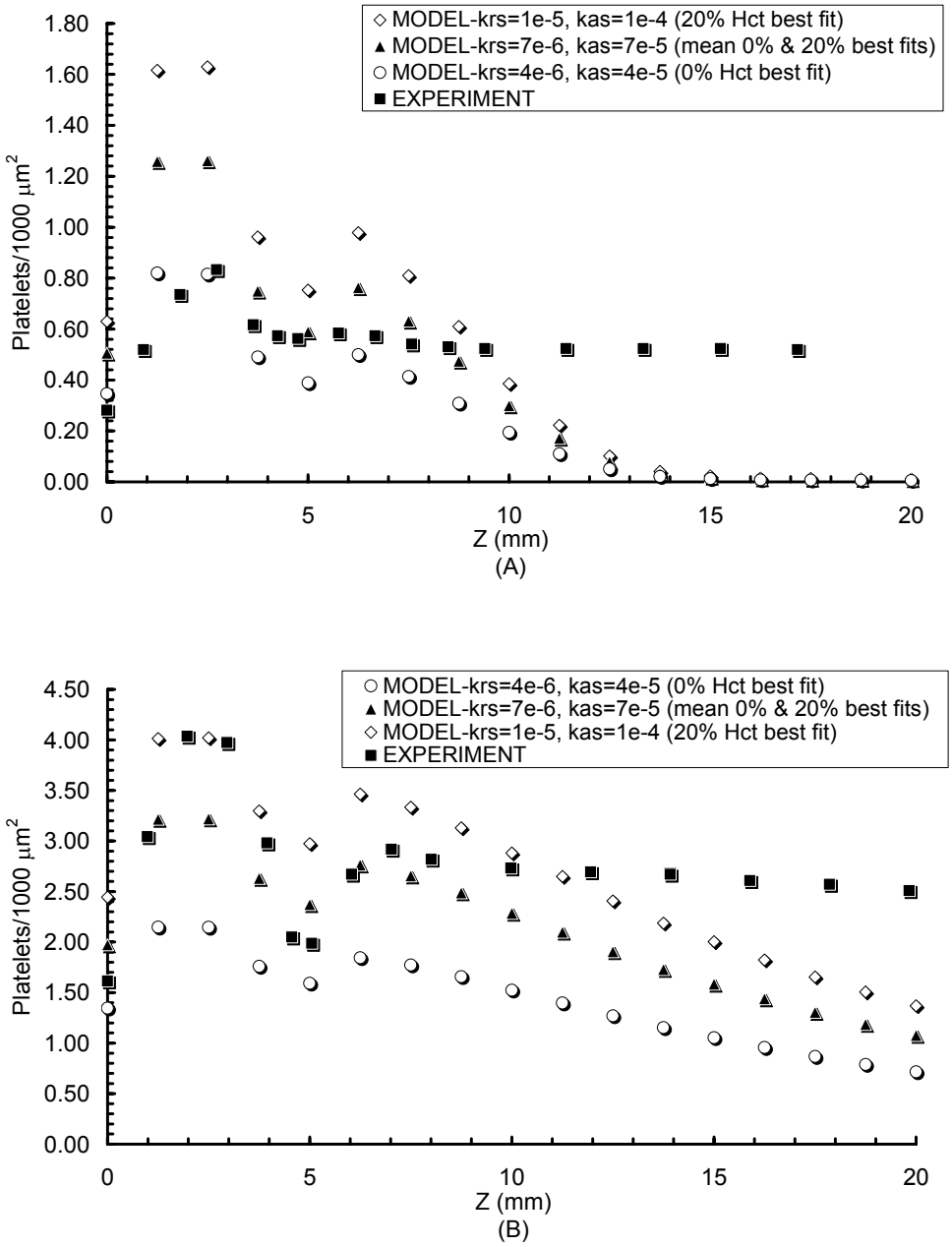

Figure 28. Cross-validation studies: 0% and 20% Hct, *Re* = 38 tubular expansion cases

Predicted vs. experimental deposition values for : (A) 0% Hct. (B) 20% Hct.

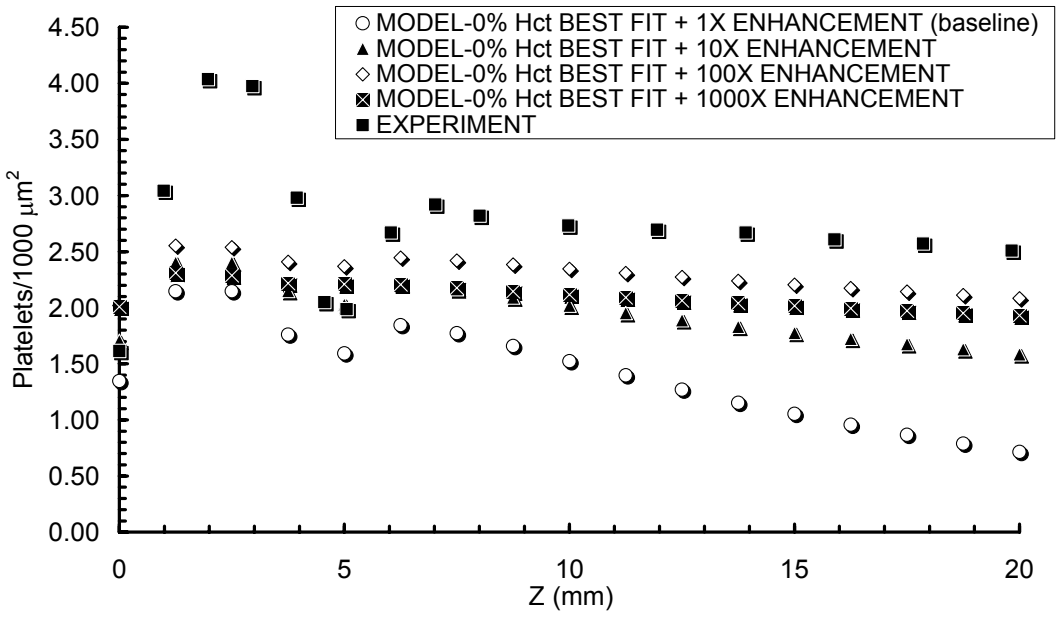

Figure 29. Effect of enhanced diffusivity on predicted deposition using 0% Hct, *Re* = 38 best-fit k_{rs} & k_{as}: 20% Hct, *Re* = 38 tubular expansion case

d) Effect of Reynolds number and perfusion time

To further test the extensibility of the model, the best-fit parameters for 0% Hct, *Re* = 38 were used to simulate the additional 0% Hct steady-flow cases evaluated experimentally by Karino and Goldsmith (59). These consisted of runs at *Re* = 64 for perfusion times of one and three minutes. At 20% Hct, additional cases corresponding to Reynolds numbers of 29, 51, and 113 were simulated. All three were for a perfusion time of one minute – no three-minute experiments were carried out at 20% Hct.

Figures 30 and 31 show the CFD results for the 0% Hct, *Re* = 64 simulation. Due to increased fluid inertia relative to the *Re* = 38 cases, the computed recirculation region extends approximately 7.1 mm downstream from the inlet, with fully-developed flow established approximately 5.5 – 6.0 mm distal to the reattachment point. The reattachment length observed experimentally by Karino and Goldsmith was 7.9 mm.

Figure 32 compares predicted and experimental platelet deposition for 0% Hct, *Re* = 64 at perfusion times of one and three minutes. For the one-minute perfusion case, the magnitudes of the predicted and experimental deposition agree reasonably, within about 20% except in the far-downstream tail, where once again the predicted values drop off. Due to increased convective transport, the downstream wall-depletion effect is not as pronounced as for the *Re* = 38 case at this hematocrit.

However, agreement in the shape of the deposition curves in the recirculation region is poorer than at the lower Reynolds number, with the predicted primary peak flattened and shifted proximally toward the inlet relative to the sharper experimental peak. After three minutes, the shape discrepancy remains. Additionally, the deposition magnitude is over-predicted by a factor of 2.5 – 3, indicating that some time-dependent inhibitory mechanism present in the experiments is not being simulated by the model.

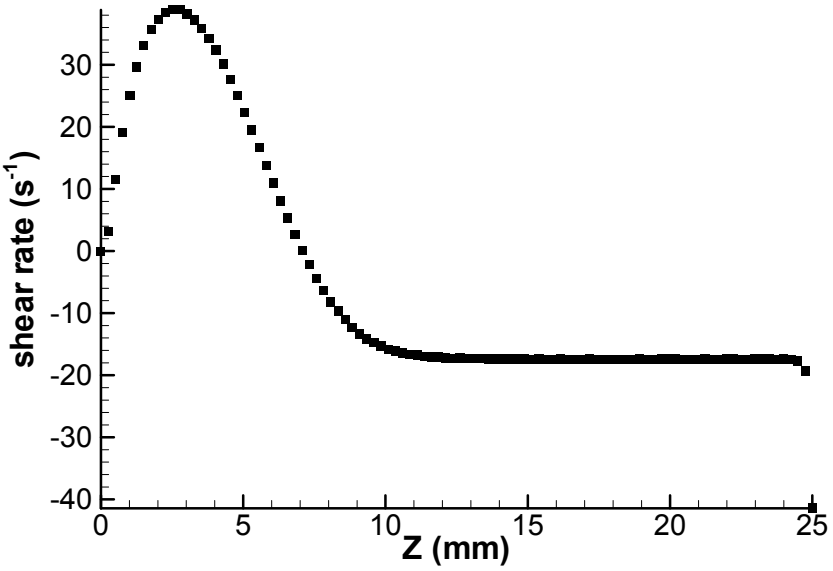

Figure 30. Wall shear rate vs. axial distance: 0% Hct, *Re* = 64 tubular expansion case

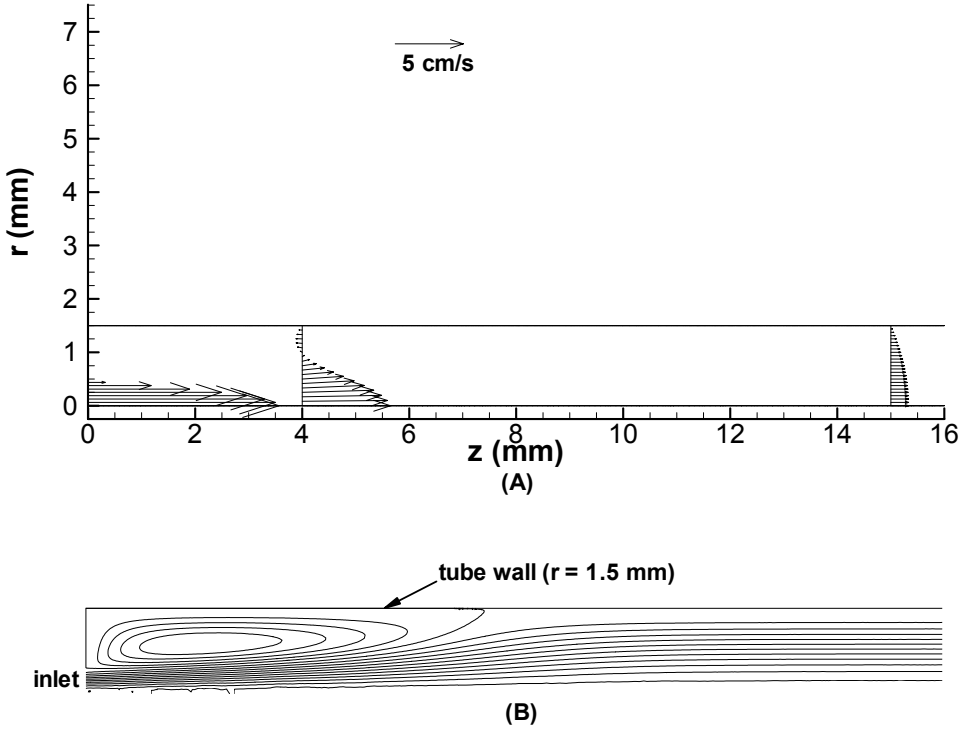

Figure 31. Velocity profiles and streamlines: 0% Hct, *Re* = 64 tubular expansion case
(A) Velocity profiles at z = 0, 4, and 15 mm. (B) Streamlines.

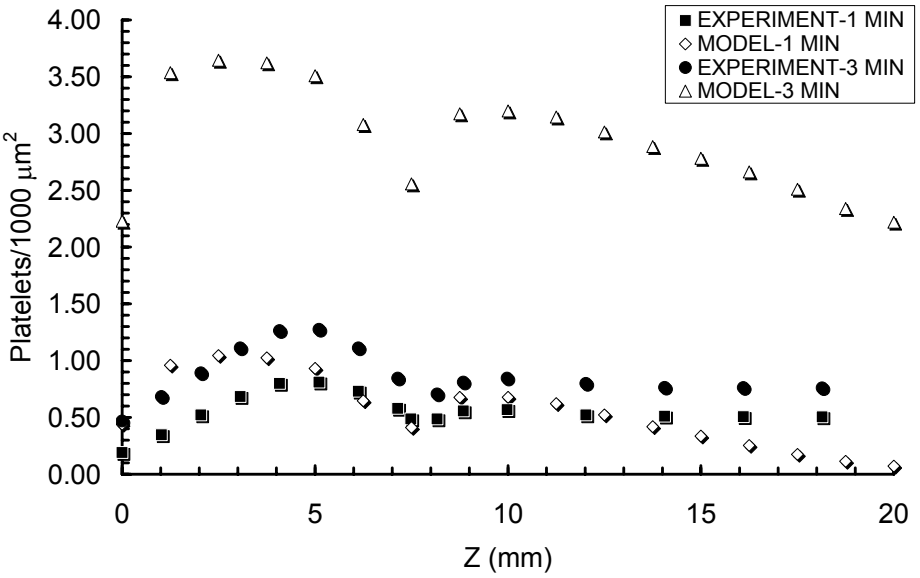

Figure 32. Experimental and predicted platelet deposition after 1 & 3 min flow: 0% Hct, *Re* = 64 tubular expansion case

Figures 33 and 34 depict the CFD solution for 20% Hct, *Re* = 29. As expected, the peak wall shear rate and recirculation zone size are decreased relative to the *Re* = 38 case. The extent of the recirculation zone in the simulation is approximately 3.5 mm, as compared to Karino and Goldsmith's measured value of 3.9 mm. Fully developed flow is established approximately 3 mm beyond the reattachment point.

Figure 35 compares experimental and predicted platelet deposition for this case (at t = 1 minute). Agreement is similar to that observed at *Re* = 38 for this hematocrit (Figure 26, open diamonds), except that the primary peak of deposition in the separated flow region is under-predicted by about 20%, while better prediction of the secondary peak just past the reattachment point is obtained. Again, the predicted deposition levels tail off in the distal fully-developed flow region, while experimentally measured deposition attains an approximately constant level.

Figures 36 and 37 are the results of the fluid dynamic simulation for 20% Hct, *Re* = 51. Peak wall shear rate and recirculation zone size are increased relative to the *Re* = 38 case. The extent of the recirculation zone predicted by the CFD code is approximately 5.5 mm, which is approximately 15% lower than Karino and Goldsmith's measured value of 6.5 mm. Fully developed flow is established approximately 5 – 6 mm past the end of the recirculation zone.

Figure 38 is a plot of experimental vs. predicted platelet deposition for this Reynolds number. Similar to the case at 0% Hct, *Re* = 64, the primary deposition peak is flattened and shifted toward the inlet. Unlike that case, the nadir in deposition at the reattachment point is also shifted proximally. This may be due to the discrepancy in recirculation zone length between the experiment and the CFD model. In contrast to previous cases at both 0% and 20% Hct, deposition in the downstream region is generally over-predicted, although the downward-sloping shape of the curve is consistent with the diffusion-limited behavior observed in this zone in all cases simulated thus far.

Figures 39 and 40 display the CFD simulation results for 20% Hct, *Re* = 113. Continuing the trend observed at 0% Hct, *Re* = 64 and 20% Hct, *Re* = 51, the reattachment length predicted by the code, 10.8 mm, is 21% less the experimentally observed value of 13.7 mm. Fully developed flow is established roughly 20 mm downstream of the inlet.

Figure 41 shows the results of the platelet deposition simulation. The effect of the under-predicted reattachment length is apparent, with the deposition plateau in the recirculation region shifted noticeably upstream as observed at *Re* = 51. Also similar to that case, the predicted upstream deposition peak is flatter and deposition magnitudes are over-predicted in both the recirculation and fully-developed-flow regions, with a slight downward slope to the deposition curve in the distal portion of the tube.

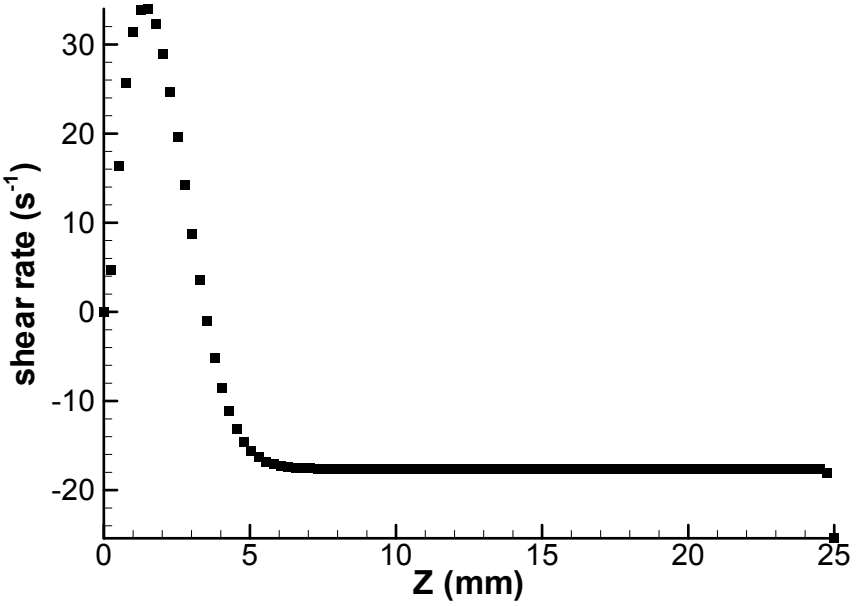

Figure 33. Wall shear rate vs. axial distance: 20% Hct, *Re* = 29 tubular expansion case

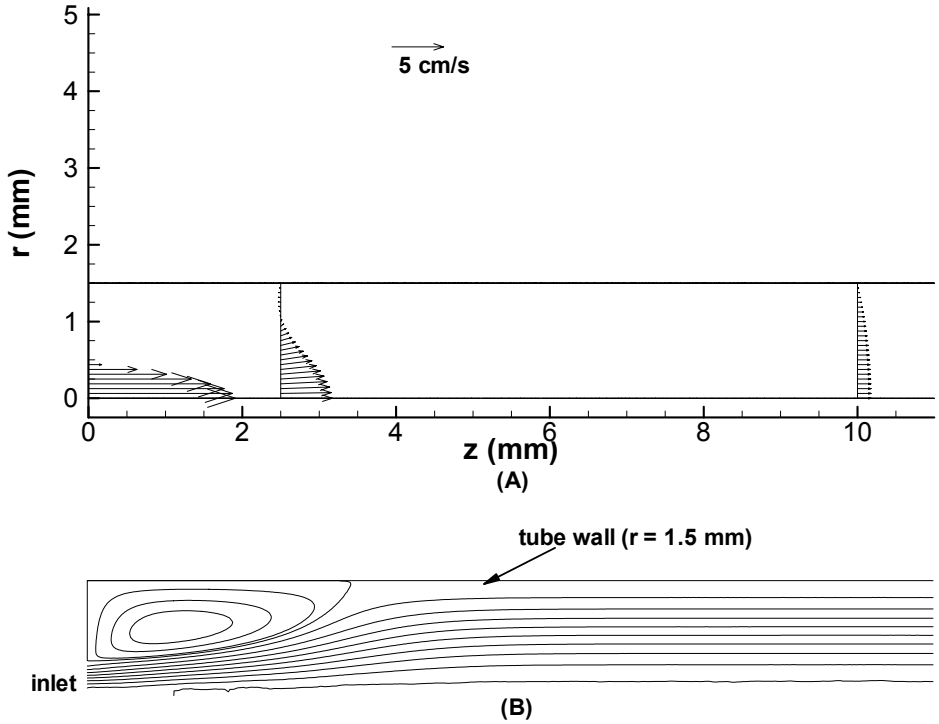

Figure 34. Velocity profiles and streamlines: 20% Hct, *Re* = 29 tubular expansion case

(A) Velocity profiles at z = 0, 2.5, and 10 mm. (B) Streamlines.

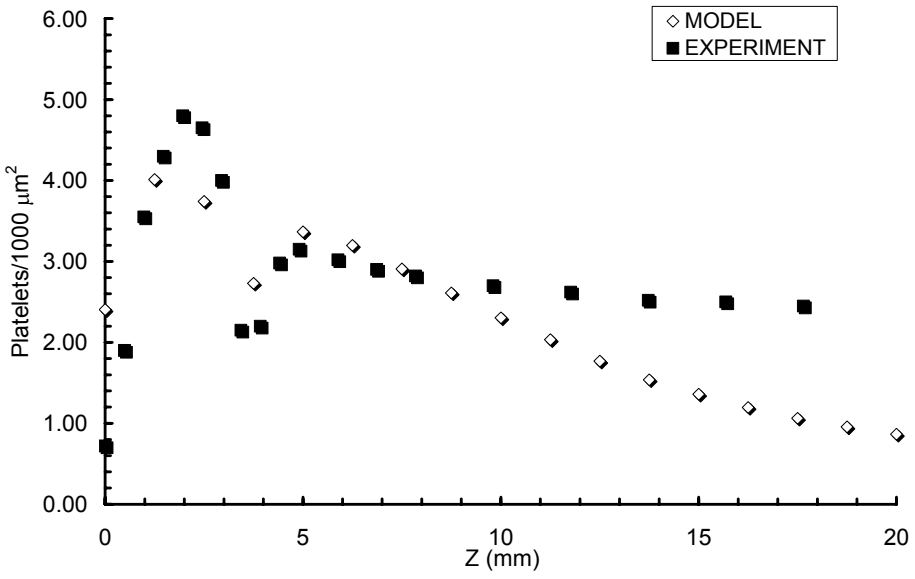

Figure 35. Comparison of best-fit model prediction to experimentally measured platelet deposition: 20% Hct, *Re* = 29 tubular expansion case

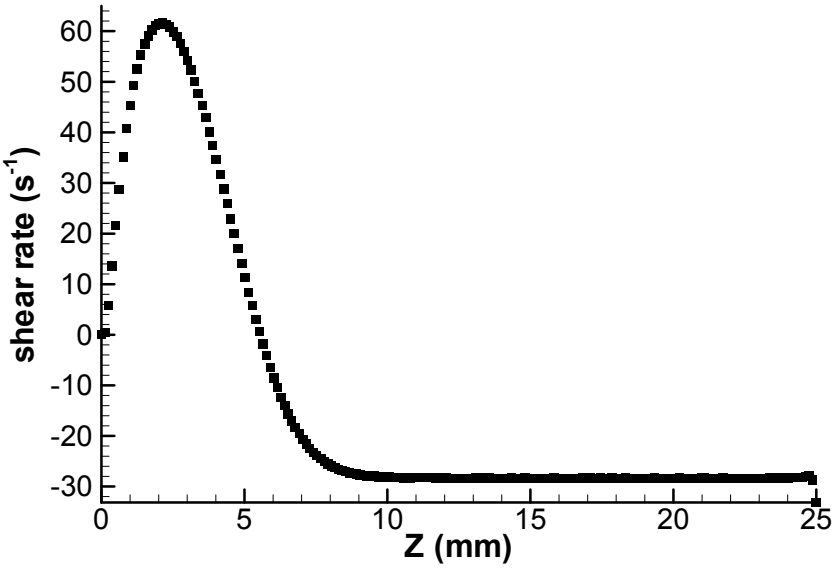

Figure 36. Wall shear rate vs. axial distance: 20% Hct, *Re* = 51 tubular expansion case

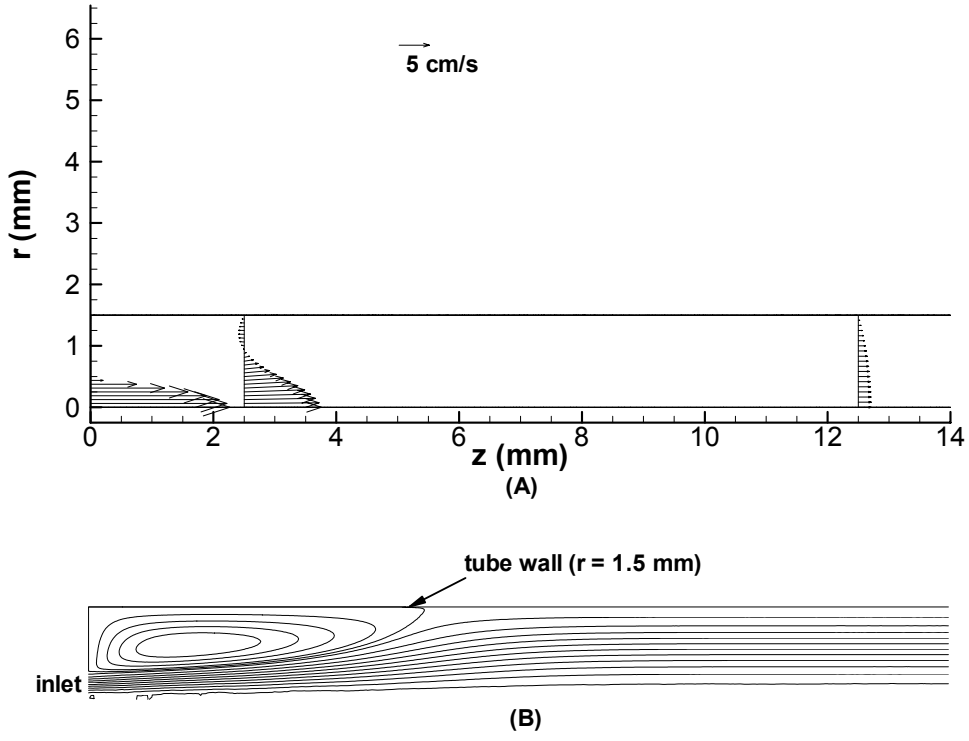

Figure 37. Velocity profiles and streamlines: 20% Hct, *Re* = 51 tubular expansion case

(A) Velocity profiles at z = 0, 2.5, and 12.5 mm. (B) Streamlines.

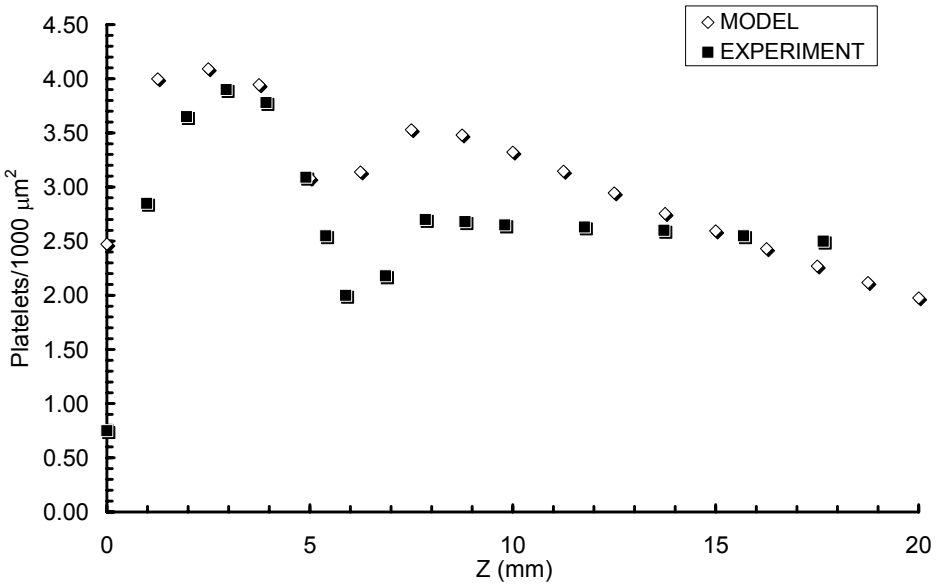

Figure 38. Comparison of best-fit model prediction to experimentally measured platelet deposition: 20% Hct, *Re* = 51 tubular expansion case

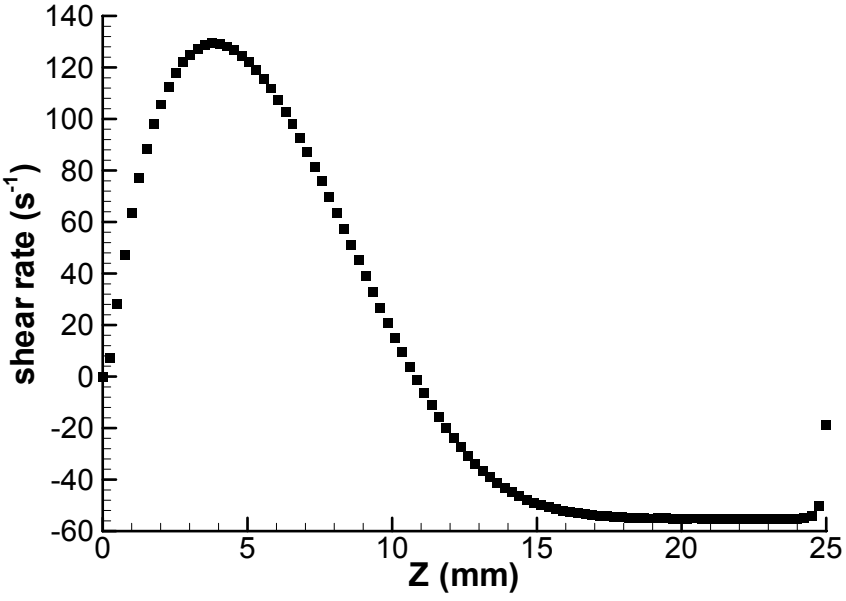

Figure 39. Wall shear rate vs. axial distance: 20% Hct, *Re* = 113 tubular expansion case

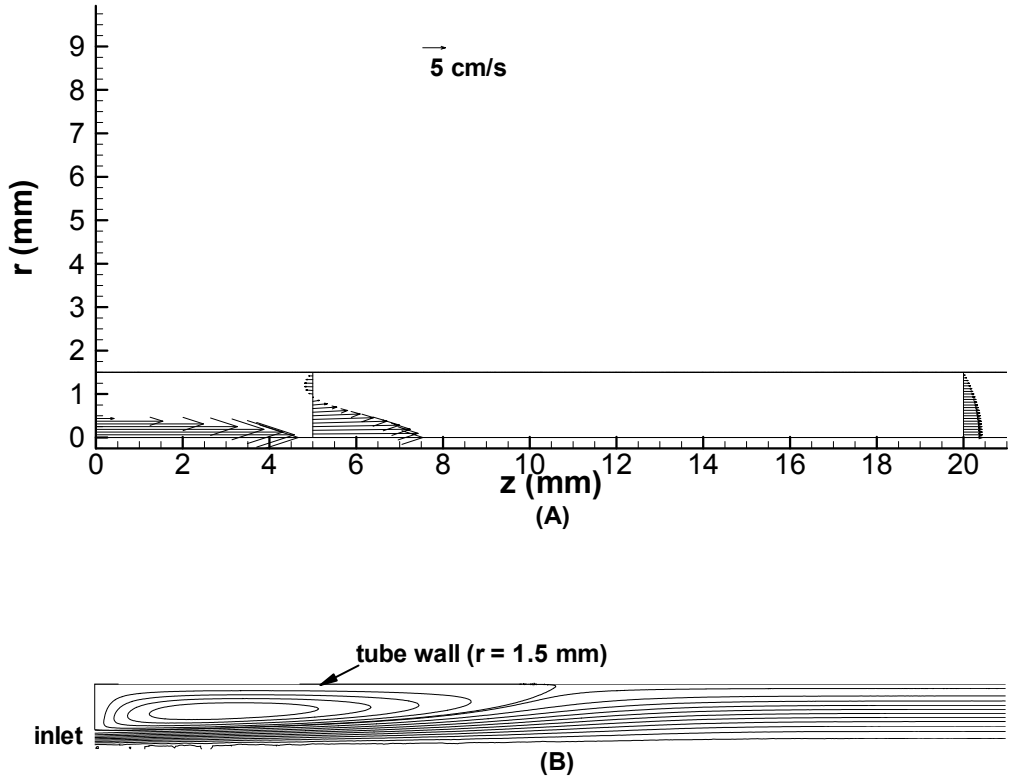

Figure 40. Velocity profiles and streamlines: 20% Hct, *Re* = 113 tubular expansion case
(A) Velocity profiles at z = 0, 5, and 20 mm. (B) Streamlines.

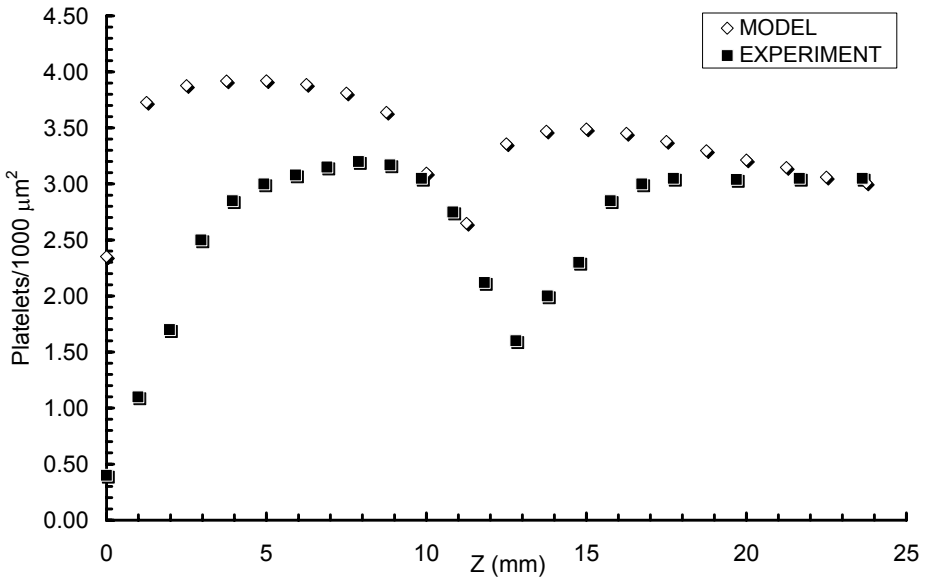

Figure 41. Comparison of best-fit model prediction to experimentally measured platelet deposition: 20% Hct, *Re* = 113 tubular expansion case

4.3.2 Axisymmetric Stenosis

a) 50% area-reduction stenosis

Figure 42 displays wall shear rate and Figure 43 the CFD-predicted streamlines for the 50% area-reduction stenosis. In these figures and all that follow for the stenoses, z = 0 mm represents the beginning of the collagen-coated region. In Figure 43A, the domain has been truncated once the flow becomes fully developed to facilitate viewing. For this case, the flow remains attached downstream of the stenosis throat, so no recirculation region is present. The peak shear rate, with a magnitude of approximately 1380 s^{-1}, occurs proximal to the location of the stenosis throat (z = 12 mm). The flow in the post-stenotic collagen-coated region is not fully developed, as Poiseuille flow is not reestablished until roughly 45 mm beyond the throat.

Table 9 lists the locations of the five ROIs in which Wootton *et al.* (104) measured platelet deposition. Note that ROI 1 begins 3.6 mm before the start of the collagen-coated region, and ROI 5 ends 3.6 mm past the end of the collagen coating. ROI 3 contains the stenosis throat, while ROIs 2 and 4 each contain 2.9 mm of the sinusoidal contraction that forms the stenosis.

Figure 44 is a bar graph comparing the platelet accumulation velocity V_{max} predicted by our model to the experimental data of Wootton *et al.* and to their corresponding simulation results (104). In general, both models show similar agreement with experiments, with a generally good fit to the data obtained upstream and at the throat and a poor one observed downstream of the throat, where both sets of predicted accumulation velocities are much lower than the measured ones. However, our model does not predict the upstream accumulation velocity as accurately as does Wootton's. That model's predictions are basically identical to the mean experimental values in ROIs 1 and 2, while our model under-predicts the experimental data in ROI 1 and over-predicts it in ROI 2. At both locations, our predictions lie outside the experimental error bars, which represent the standard error of the mean.

Figures 45 and 46 display predicted agonist concentrations, normalized by their platelet activation thresholds (see Table 3 for these values), in the collagen-coated stenosis region. Figure 45 shows contours of bulk concentration, while Figure 46 plots concentrations at the wall. For all three agonists, bulk concentrations are greatest downstream of the stenosis throat. Additionally, supra-threshold concentrations (normalized level $\geq$ 1.0) are only observed in a thin region very near the wall. For ADP and TxA_2, this thin region extends noticeably into the bulk flow downstream of the throat, while supra-threshold thrombin concentrations are only barely visible

near the throat and very close to the wall. However, as Figure 46A illustrates, the normalized thrombin concentrations at the wall upstream of and at the throat reach levels one to two orders of magnitude greater than the other two agonists. Figure 46B shows that magnitudes of TxA_2 and ADP are relatively equal over the entire collagen-coated region; downstream of the throat, all three agonists are present at roughly the same levels. Finally, the normalized concentrations of the three agonists are > 1.0 along the entire length of the collagen-coated graft, indicating all are contributing to ongoing platelet activation in this region.

Figure 47 depicts model-predicted concentrations of resting and activated platelets in the bulk and at the wall of the collagen-coated portion of the shunt. Figure 47A shows bulk concentrations of resting platelets, which are very low near the wall along the entire length, but especially so downstream of the stenosis throat. In contrast, the activated platelet concentrations displayed in Figure 47B tended to be higher near the wall and in the downstream region. Both trends track with the agonist concentrations observed in Figures 45 and 46, with resting platelet concentrations lowest where agonist concentrations are highest and vice-versa for activated platelet concentrations. Figure 47C shows the extent of this agonist-induced activation: despite an inlet BC that sets the incoming concentration of resting platelets at the upstream inlet to a value nine times greater than that of activated platelets, the activated platelet concentration at the wall is approximately two orders of magnitude greater than that of resting platelets along the entire collagen-coated graft. In addition, the concentration of resting platelets drops precipitously in the region near z = 17 mm, approximately 1 mm before the end of the sinusoidal expansion portion of the stenosis.

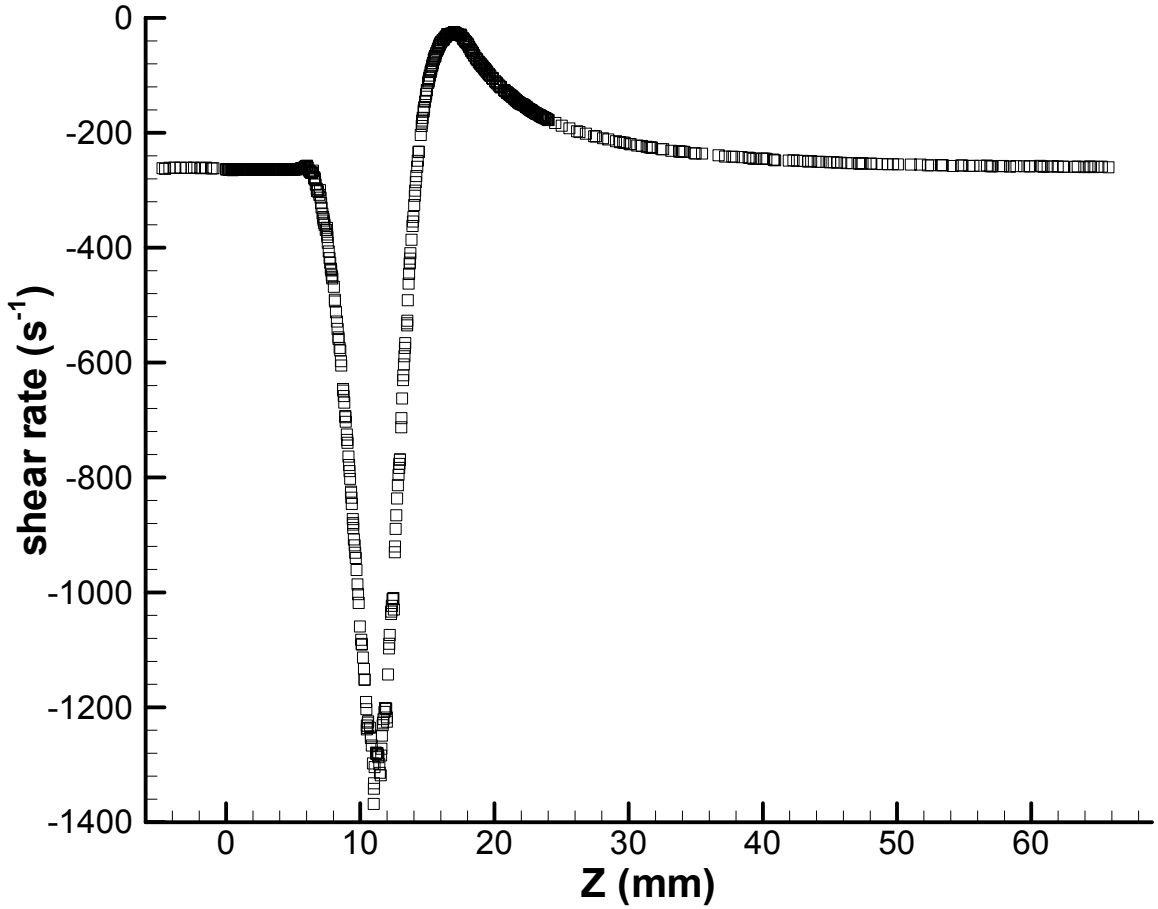

Figure 42. Wall shear rate vs. axial distance: 50% stenosis case

Only every 8th grid point is plotted for viewing clarity. $z = 0$ corresponds to start of collagen-coated region.

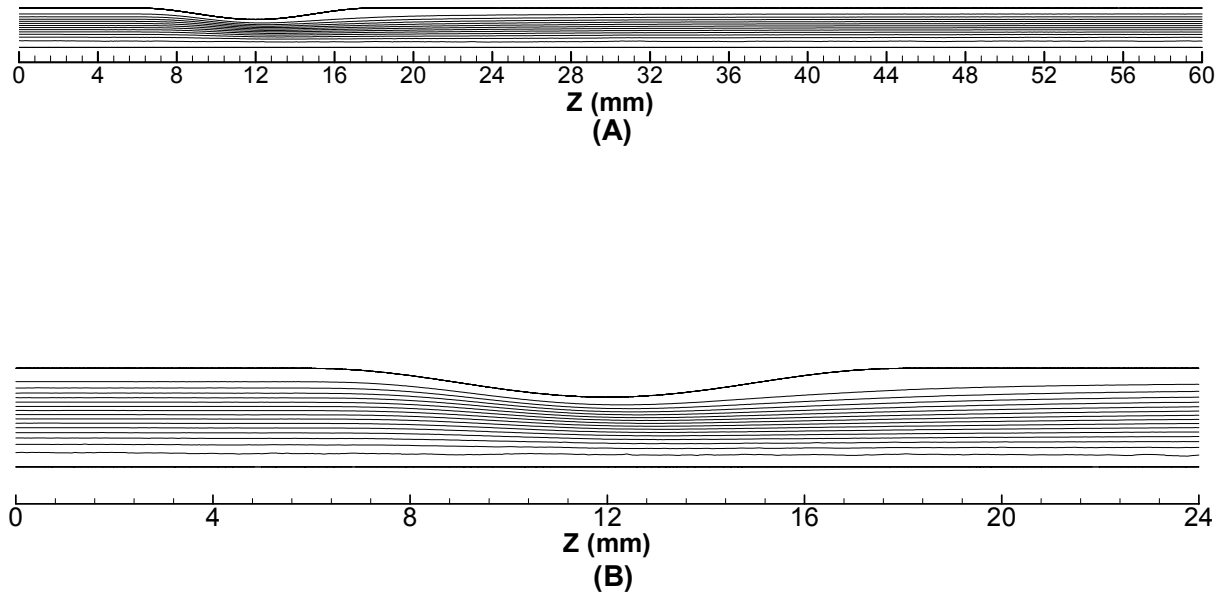

Figure 43. Streamline plots: 50% stenosis case

(A) Plot extending from start of collagen-coated region (z = 0) to establishment of fully-developed flow. (B) Collagen-coated region only.

Table 9. Locations of regions of interest (ROIs): stenosis cases

ROI	Extent in z-direction (mm)
1	-3.6 to +2.6
2	2.6 to 8.9
3	8.9 to 15.1
4	15.1 to 21.4
5	21.4 to 27.6

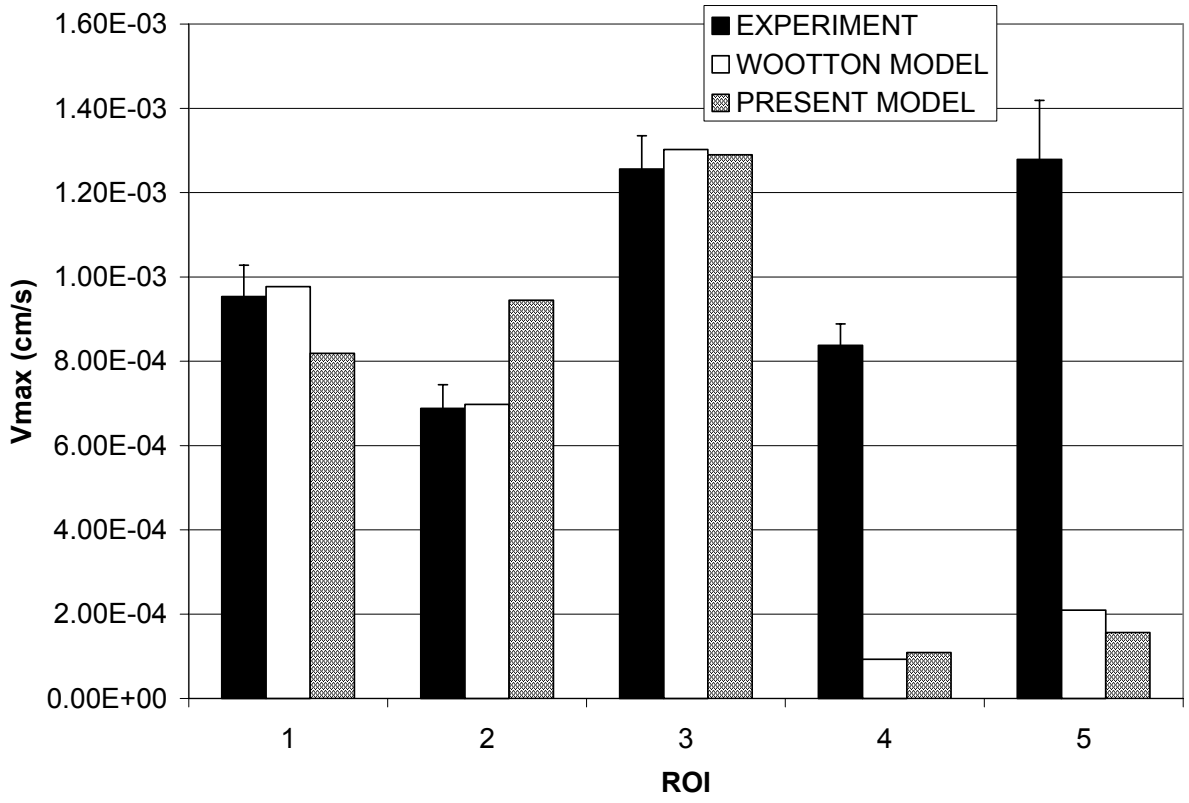

Figure 44. Comparison of model predictions to experimentally measured platelet accumulation velocity, V_{max}: 50% stenosis case

Error bars on experimental results are + standard error of the mean.

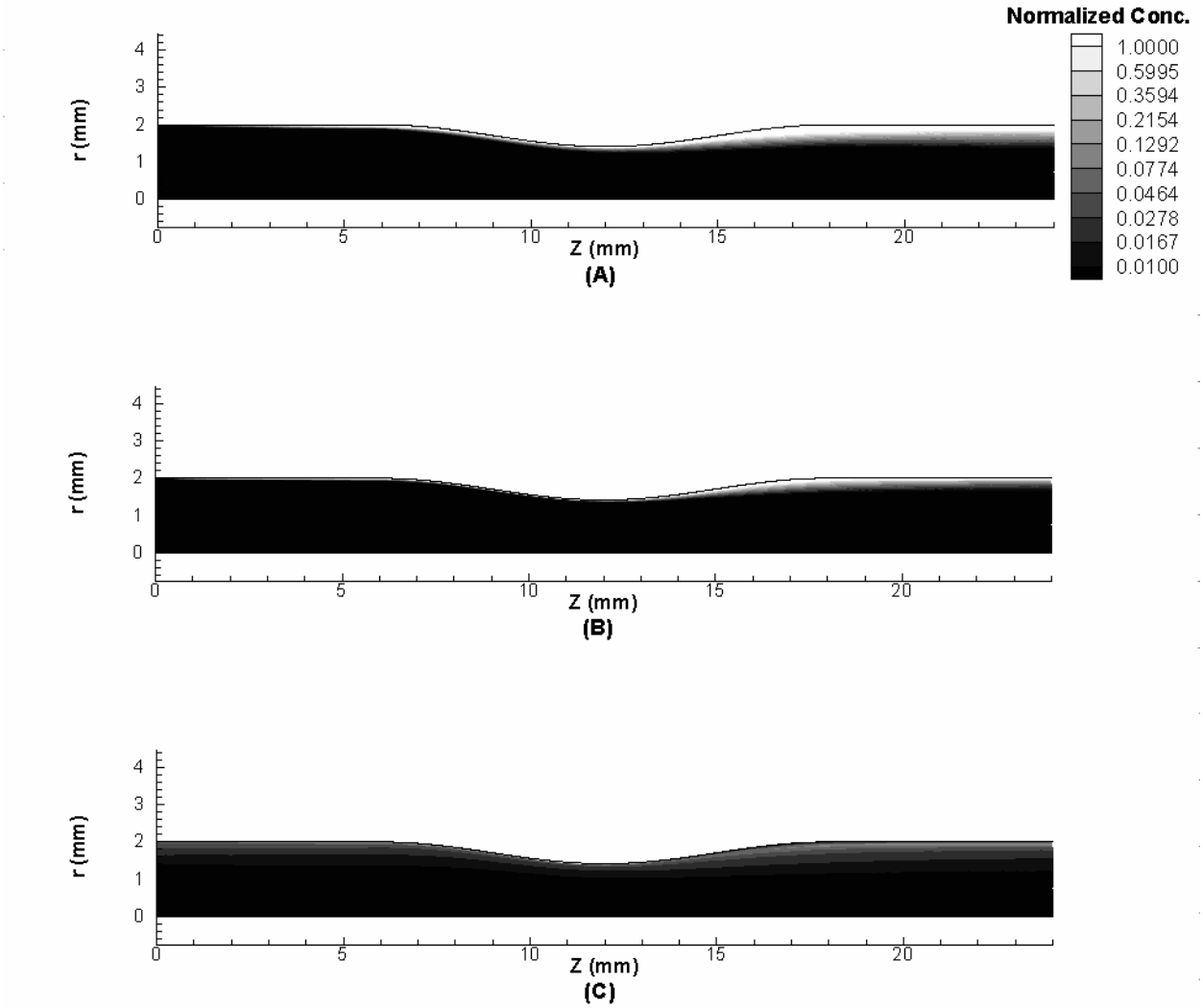

Figure 45. Contours of predicted, activation-threshold-normalized bulk agonist concentrations: 50% stenosis case

(A) ADP. (B) TxA_2. (C) Thrombin. See Table 3 for activation thresholds used in normalization. Note that only collagen-coated region is shown.

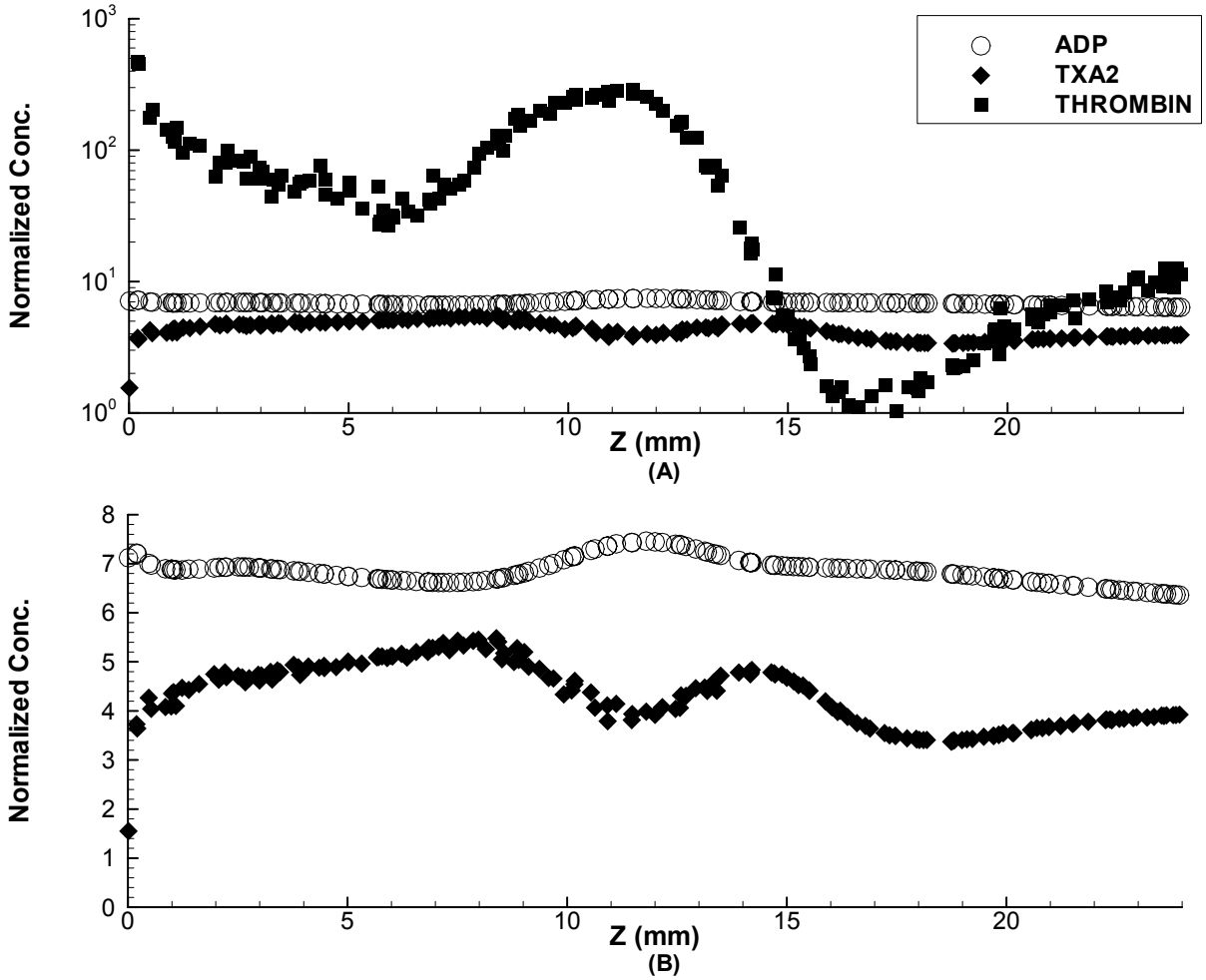

Figure 46. Predicted, activation-threshold-normalized agonist concentrations at wall: 50% stenosis case

(A) All agonists (note log scale). (B) Detail of ADP and TxA_2 concentrations, linear scale. See Table 3 for activation thresholds used in normalization. Note that only the collagen-coated region is shown, and only every 25th grid point is plotted for viewing clarity.

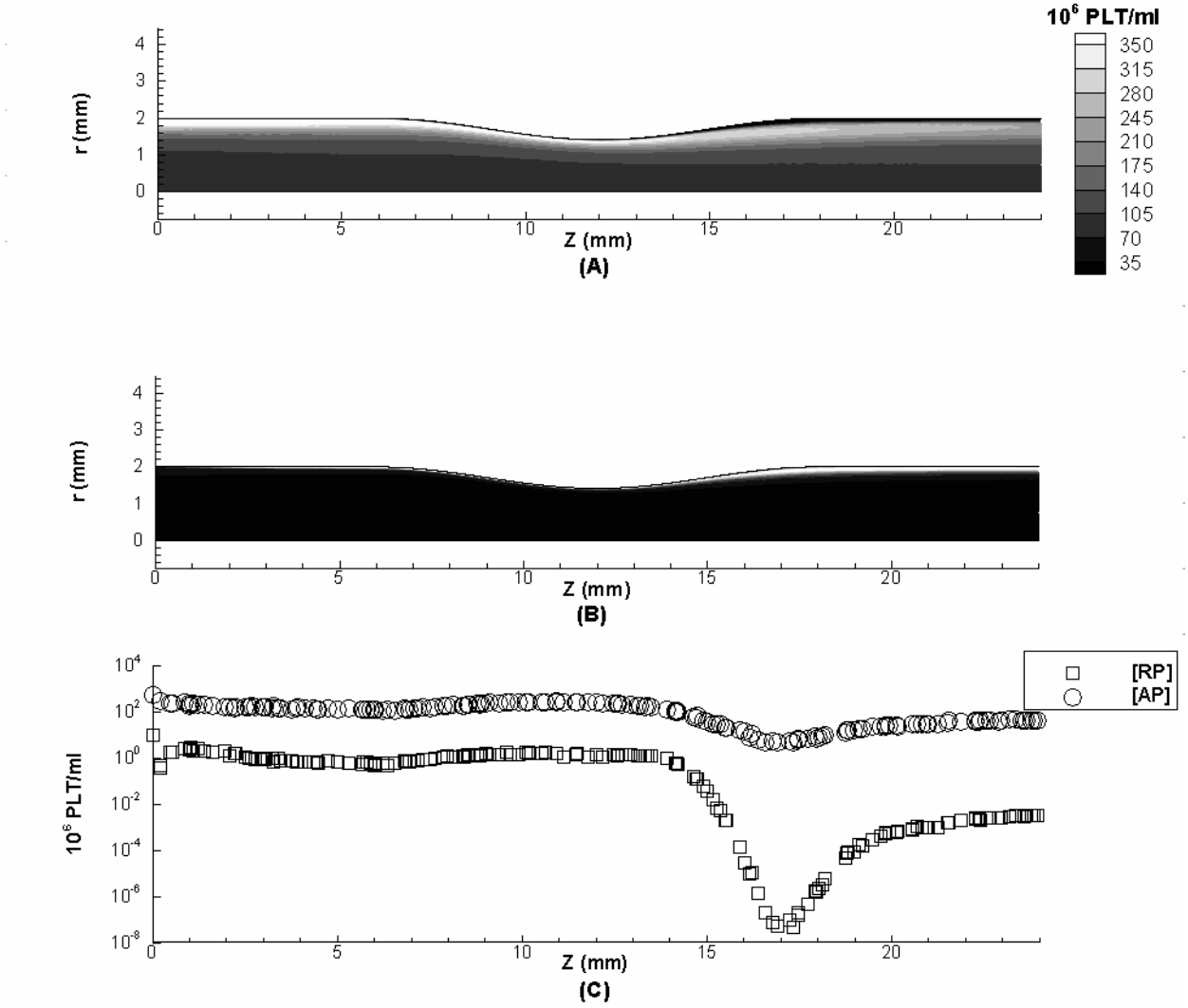

Figure 47. Predicted bulk and wall platelet concentrations: 50% stenosis case

(A) Contours of resting platelet concentration. (B) Contours of activated platelet concentration. (C) Concentrations of resting and activated platelets at the wall (every 25th grid point plotted). Only the collagen-coated region is shown.

b) 75% area-reduction stenosis

Figures 48 and 49 show the CFD results for the 75% area-reduction stenosis. In contrast to the 50% stenosis, a large recirculation zone forms distal to the stenosis throat, as shown by the streamline plot in Figure 49A. The reattachment point is at approximately z = 29 mm, which is 17 mm downstream from the stenosis throat and 5 mm downstream of the end of the collagen-coated region. Thus, as illustrated by the zoomed streamline plot in Figure 49B, the entire collagen-coated area downstream of the throat is covered by the recirculation cell. As seen in the 50% stenosis, the peak shear rate (magnitude 4975 s^{-1}) occurs just before the stenosis throat. Due to the strength of the stenotic jet, fully developed flow is not established until 63 mm downstream of the throat (at approximately z = 75 mm).

Figure 50 compares our predictions of platelet accumulation velocity V_{max} to both the simulations and experiments of Wootton *et al.* (104). Once again, both models tend to fit the data obtained upstream and at the throat fairly well but badly under-predict the downstream accumulation rate. Distinct from the 50% stenosis results, our simulations for this case predict upstream accumulation velocity in ROIs 1-2 as well as or slightly better than do Wootton's; however, our model under-predicts deposition at the throat (ROI 3), while their predictions lie very near the experimental mean.

Figures 51 and 52 show predicted, activation-threshold-normalized agonist concentrations in the collagen-coated stenosis region. Figure 51 shows contours of bulk concentration, and Figure 52 is concentration at the wall. In contrast to the 50% stenosis case, where supra-threshold concentrations were only observed very near the wall, Figure 51 shows that the recirculation zone creates a "hot spot" for agonist accumulation. Bulk concentrations of TxA_2 and thrombin peak just distal to the throat, reaching their highest levels at the stagnation point where the flow separates. Downstream of the throat, ADP concentrations reach supra-threshold levels in a very wide region that spans the recirculation zone. While generally at sub-threshold levels, TxA_2 and thrombin concentrations in the vortex are also elevated. As Figure 52A illustrates, agonist trends at the wall are similar to those observed in the 50% stenosis, with normalized thrombin concentrations near the throat reaching levels one to two orders of magnitude greater those of ADP and TxA_2. Again, magnitudes of TxA_2 and ADP are relatively close over the entire collagen-coated region (Figure 52B). Downstream of the throat, a sharp drop in all three agonist levels is observed beginning at the separation point. Distal to it,

thrombin concentrations begin to rise again, gradually reaching levels roughly 10 times higher than the other two agonists, which remain at the low concentrations seen at the stagnation point. Once again, normalized concentrations of all three agonists are > 1.0 along the entire length of the collagen-coated graft, indicating all are contributing to ongoing platelet activation in this region.

Figure 53 shows simulated concentrations of resting and activated platelets in the bulk and at the wall along the collagen-coated portion of the shunt. In Figures 53A and 53B, contours of bulk resting and activated platelets, respectively, are plotted. These show the post-stenosis vortex to be a region of very active platelet activation, with resting platelet levels highly depleted there and activated platelet concentrations greatly increased. As noted for the 50% stenosis case, these trends agree with the agonist concentrations observed in Figures 51 and 52, with resting platelet concentrations lowest where agonist concentrations are highest and vice-versa for activated platelet concentrations. Also similar is the trend in platelet concentrations at the wall, shown in Figure 53C: the activated platelet concentration at the wall is again roughly two orders of magnitude greater than that of resting platelets along the entire collagen-coated region. However, the sudden drop in resting platelet concentration that was seen downstream of the 50% stenosis does not occur to as great an extent for this geometry.

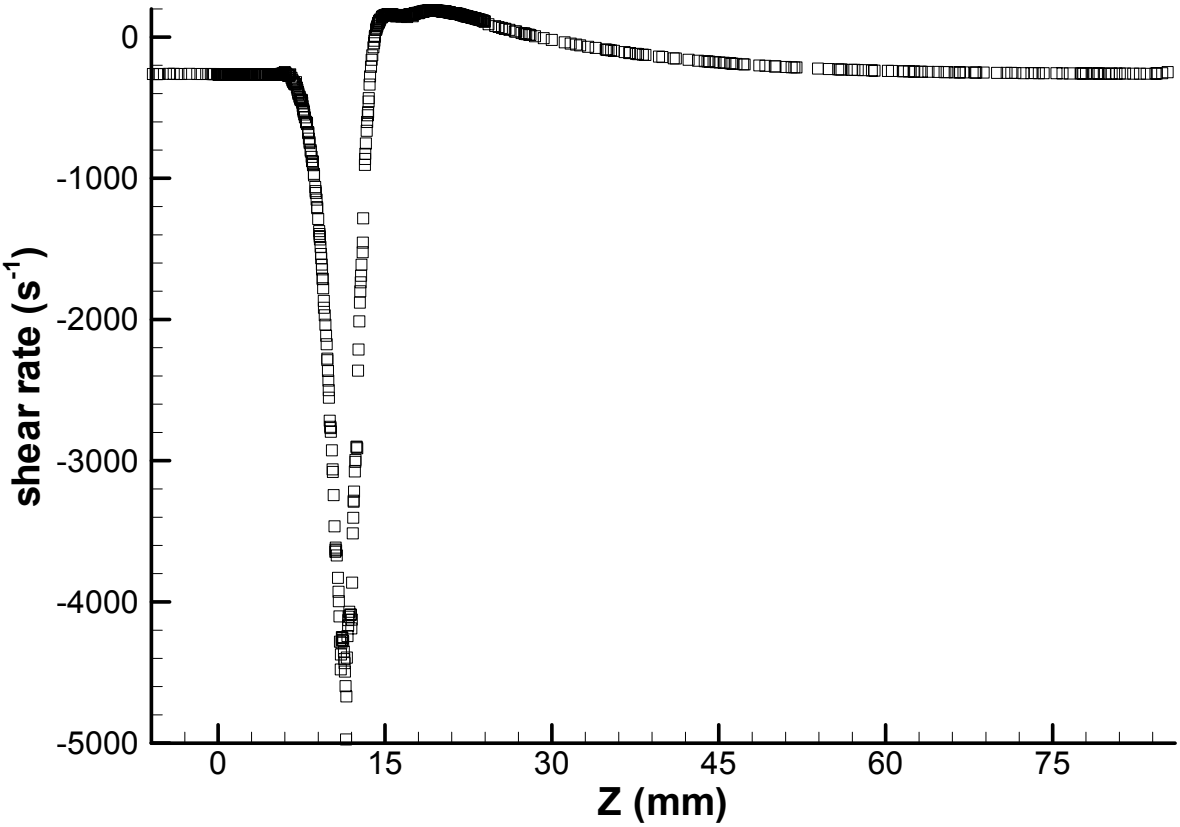

Figure 48. Wall shear rate vs. axial distance: 75% stenosis case

Only every 8th grid point is plotted for viewing clarity. $z = 0$ corresponds to start of collagen-coated region.

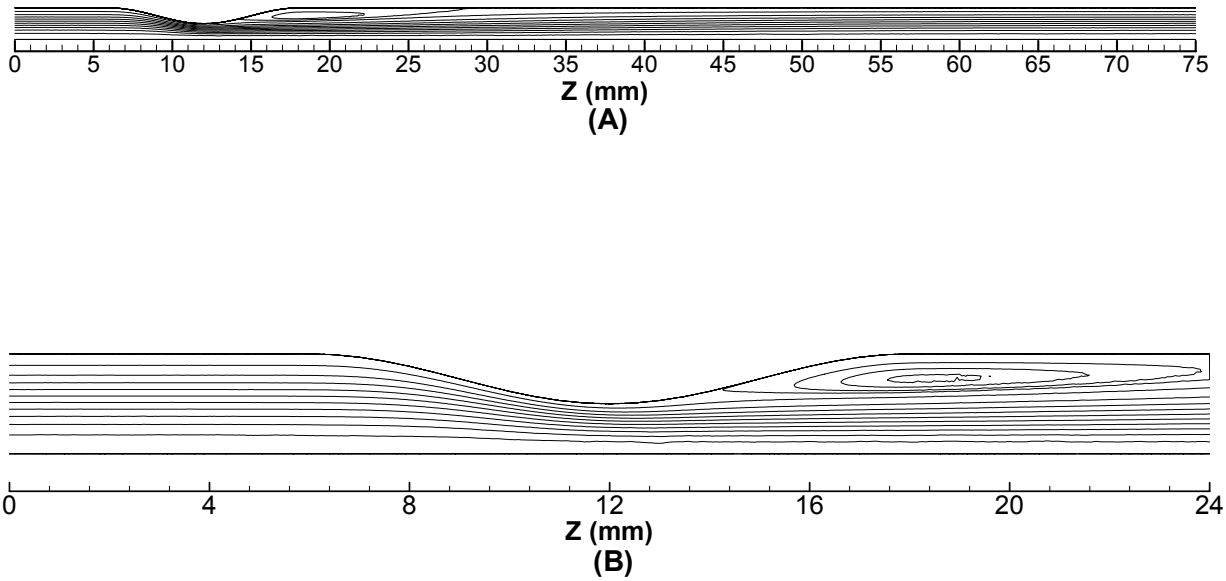

Figure 49. Streamline plots: 75% stenosis case

(A) Plot extending from start of collagen-coated region (z = 0) to establishment of fully-developed flow. (B) Collagen-coated region only.

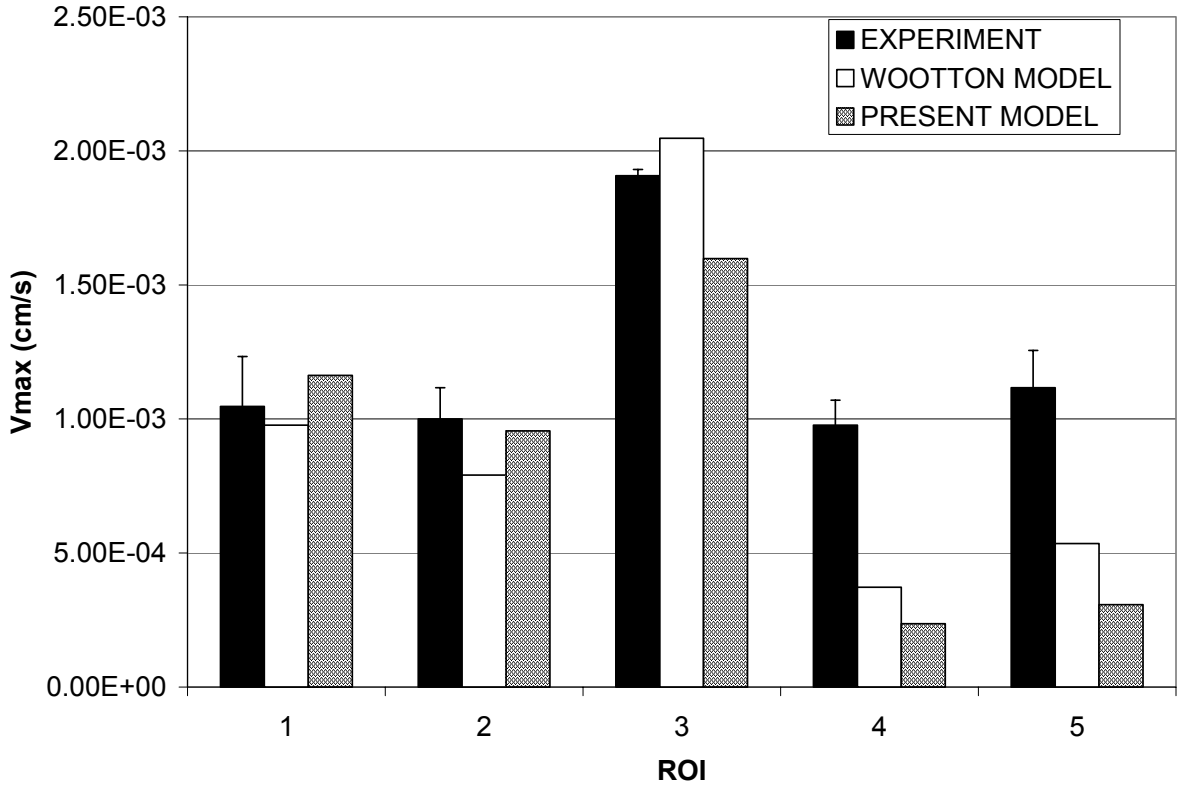

Figure 50. Comparison of model predictions to experimentally measured platelet accumulation velocity, V_{max}: 75% stenosis case

Error bars on experimental results are + standard error of the mean.

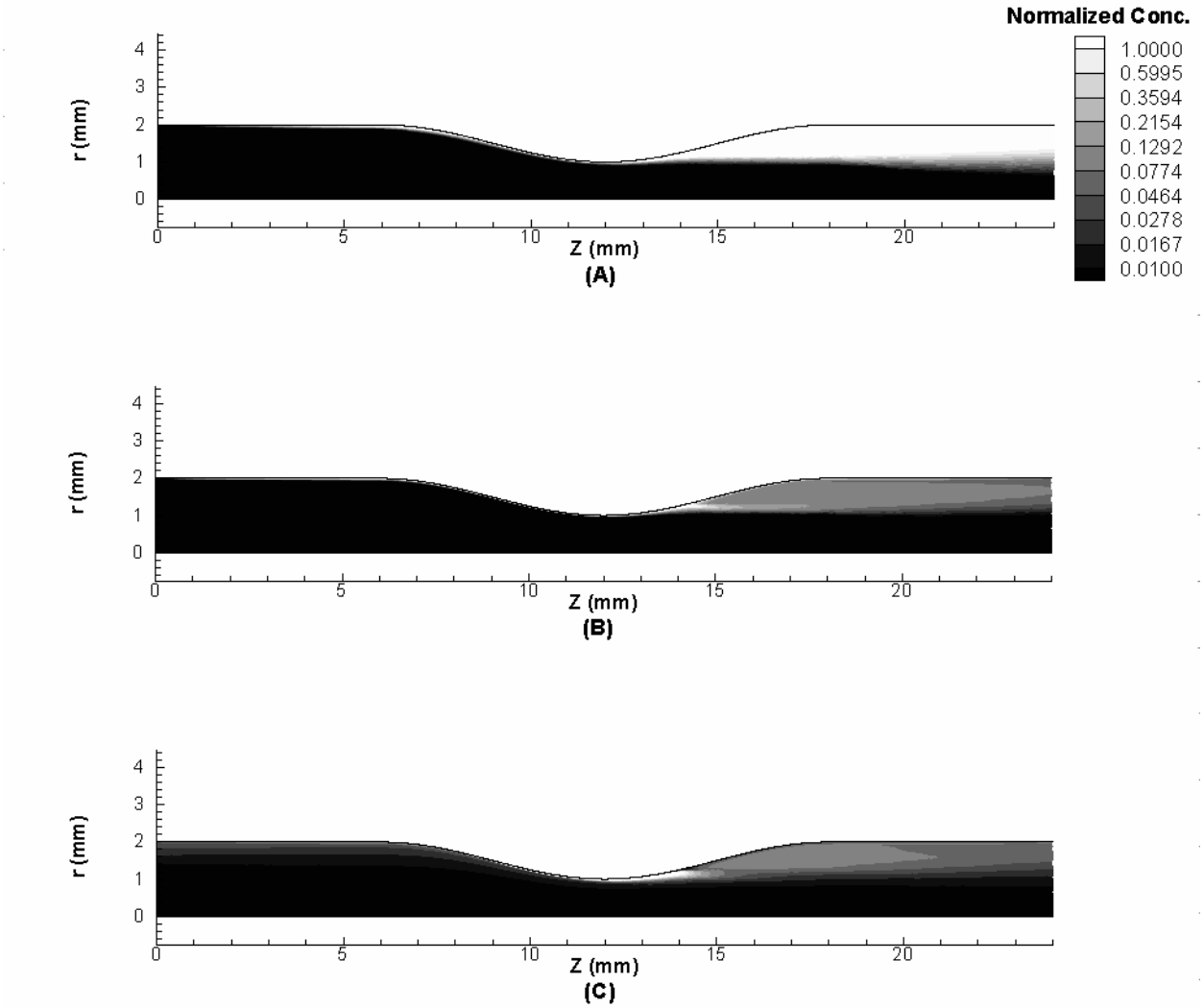

Figure 51. Contours of predicted, activation-threshold-normalized bulk agonist concentrations: 75% stenosis case

(A) ADP. (B) TxA_2. (C) Thrombin. See Table 3 for activation thresholds used in normalization. Note that only the collagen-coated region is shown.

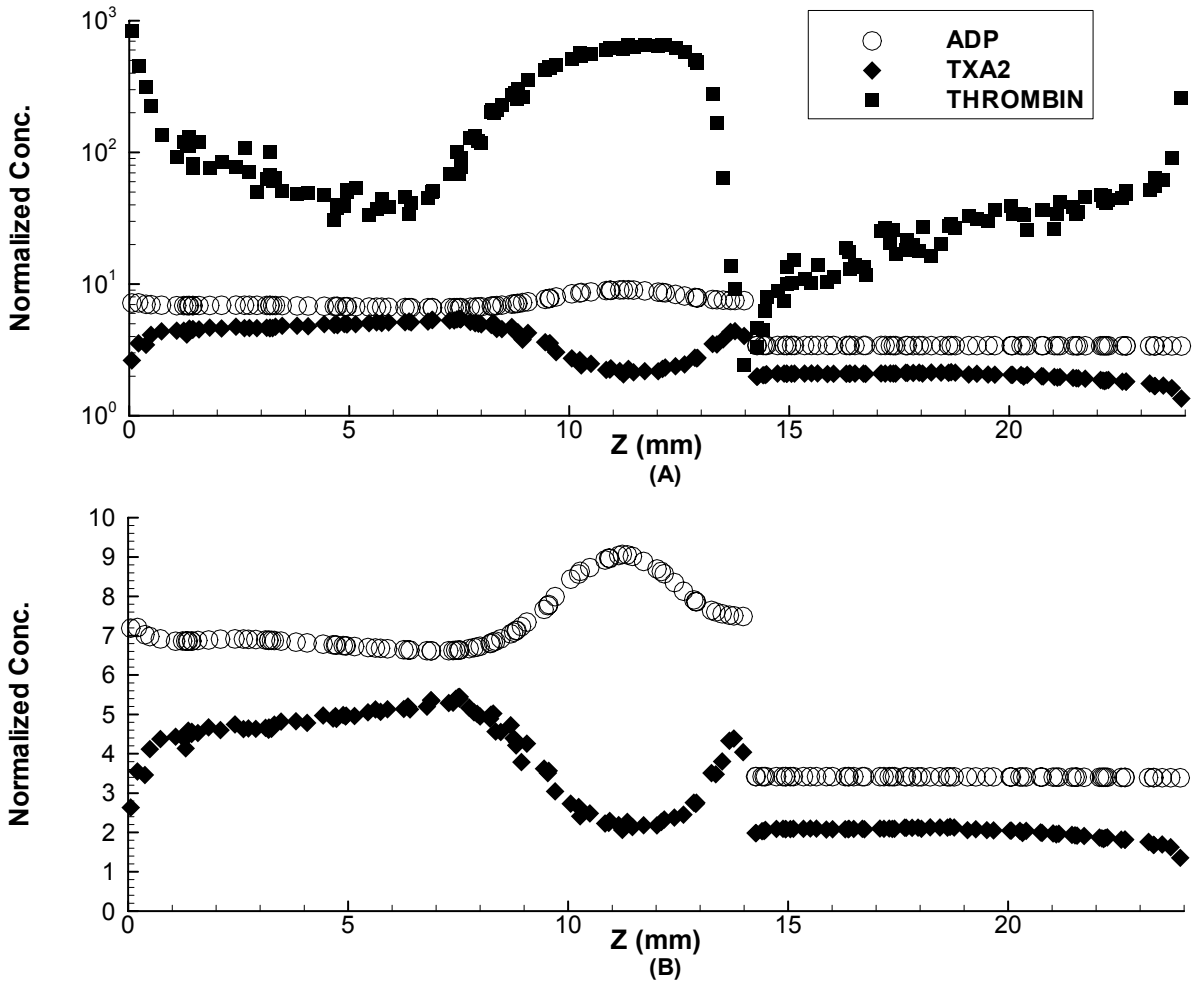

Figure 52. Predicted, activation-threshold-normalized agonist concentrations at wall: 75% stenosis case

(A) All agonists (log scale). (B) Zoomed detail of ADP and TxA_2 (linear scale). See Table 3 for activation thresholds used in normalization. Note that only the collagen-coated region is shown, and only every 25th grid point is plotted for viewing clarity.

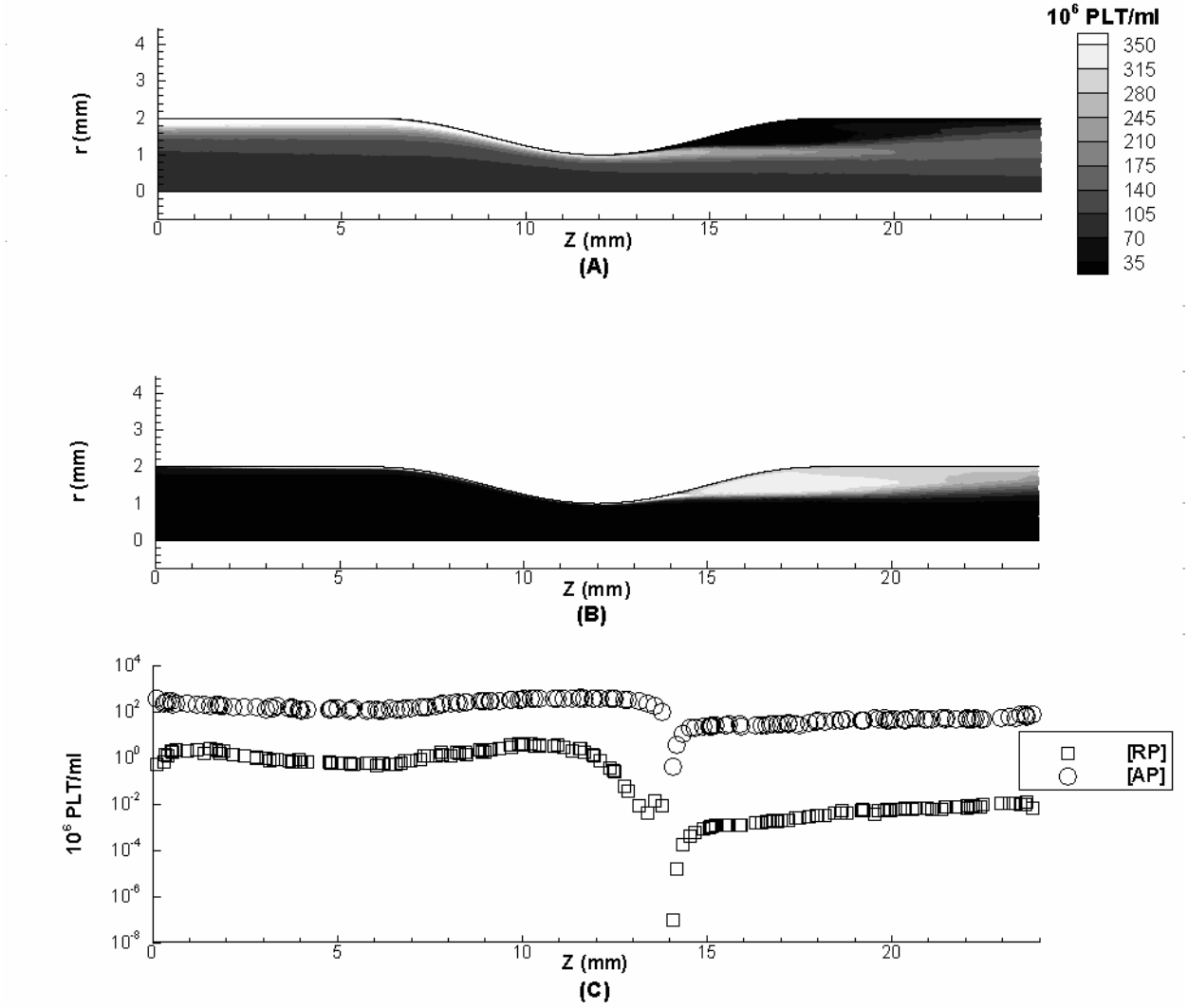

Figure 53. Predicted bulk and wall platelet concentrations: 75% stenosis case

(A) Contours of resting platelet concentration. (B) Contours of activated platelet concentration. (C) Concentrations of resting and activated platelets at the wall (every 25th grid point plotted). Note that only collagen-coated region is shown in all three plots.

4.4 Discussion

4.4.1 Axisymmetric Tubular Expansion

In these simulations, the model applied was greatly simplified compared to the one used to model deposition from whole blood in Chapter 2. Because the experimental perfusates consisted only of washed platelets and RBCs in a protein-free suspension and because perfusion times were chosen to avoid platelet aggregation, the effects of agonist generation by platelets, platelet activation by agonists, and platelet-platelet aggregation could be neglected. Additionally, unmodeled phenomena which were suspected of causing errors in the previous simulations, such as aggregation-induced flow disturbances, aggregate embolization and shear-dependent inhibition of adhesion, could be justifiably neglected. The first was neglected for the aforementioned reasons, the last two because of the relatively low-shear flows studied. Thus, these simulations allowed us to focus on platelet transport in the presence and absence of RBCs and on the kinetics of platelet-surface adhesion. Doing so revealed that our model of platelet transport is grossly deficient.

For the 0% Hct cases, even though diffusion-enhancing red cells are absent, it appears transport of platelets in the near-wall region is not adequately described by the Brownian diffusivity alone. At Re = 38, it was discovered that the model predicts very few platelets reaching the wall in the downstream, fully-developed flow region, even in the absence of platelet-surface adhesion. Similar, though not as severe, behavior was observed at Re = 64. Surprisingly, a grid with non-uniform cells near the wall produced better agreement with experimental data than did one with uniformly fine cells. We attribute this to enhanced numerical diffusion caused by the coarse regions of the non-uniform mesh (see Figure 16A), which artifactually augments platelet transport compared to the fine grid analysis. However, the beneficial effect of the numerical diffusion on downstream deposition could not be replicated on the uniformly refined grid by adding a shear-dependent enhancement factor to the diffusion coefficient, at least for the three orders of magnitude variation in this parameter that were tested.

For the 20% Hct cases, using the best-fit coefficients from the 0% Hct simulations failed to provide agreement between model and experiment. Increasing the diffusivity by up to 1000× still did not reconcile the simulation with the experimental results. Agreement could only be obtained by increasing the platelet-surface reaction coefficients relative to the 0% Hct case.

Thus, in the presence of RBCs, an enhanced diffusivity, even when combined with a wall-skewed inlet concentration profile designed to mimic experimentally observed platelet concentration profiles (53), still gives poor agreement with experimental values.

By re-fitting k_{rs} and k_{as}, we have in essence re-defined these coefficients to be lumped parameters governing not only surface reactivity, as assumed in the development of the model, but also red-cell enhanced near-wall platelet transport. This is very unsatisfactory, since it would imply that these model parameters depend not only on surface composition, but also on hematocrit and shear rate. If k_{rs} and k_{as} were only surface-dependent, they could presumably be determined for a given material by simulating simple parallel-plate flow experiments like those discussed in Chapter 3, after which their best-fit values could be used to predict deposition onto that substrate for different flow rates, geometries, blood conditions, etc. However, if they also depend on shear rate and hematocrit, experimental data for each new case would be needed for parameter fitting, destroying the utility of the model for predicting deposition in complex geometries where such measurements may not be feasible. Of course, it might eventually be possible to determine a functional form for the dependence of k_{rs} and k_{as} on hematocrit and shear rate. This would allow the parameters to be calculated *a priori*, rather than fit, for each new flow situation, but one would expect that quite a large set of "training data" would be needed to determine this relationship. Additionally, these parameters lose their physical meaning, and consequently the model would no longer be mechanistic, but would become semi-empirical.

In all the cases simulated – independent of Reynolds number, hematocrit, and perfusion time – the experimentally observed platelet deposition trend appears to follow reaction-limited kinetics in the fully-developed flow region of the tube, as evidenced by the flat deposition values measured there by Karino and Goldsmith (59). This is especially evident at 20% Hct, where nearly identical downstream deposition values were measured over a Reynolds number range from 29 to 113. In contrast, the model results appear diffusion-limited, with platelet deposition decreasing with increasing axial distance. However, model and simulation results generally agree in the upstream, separated-flow region. One exception is at the higher Reynolds numbers, i.e. Re = 64 at 0% Hct and Re = 51 and 113 at 20% Hct. For these cases, the primary deposition peak is flattened somewhat and occurs closer to the inlet than observed experimentally. For simulations at both hematocrits, this can be partly attributed to numerical diffusion in the convection schemes. For the flow simulations, this resulted in under-prediction of the reattachment length,

while for the platelet deposition simulations, it resulted in smearing of concentration peaks. The more severe discrepancies at 20% Hct are also likely due in part to the suspension having a non-uniform viscosity due to the presence of RBCs. Such effects are not modeled in our Newtonian CFD simulations.

Another departure of the simulation from the experiments occurred in the cases at 20% Hct, Re = 38 wherein the best-fit k_{rs} and k_{as} from 0% Hct, Re = 38 were used and the diffusion enhancement factor was increased. In these cases, reaction-limited deposition profiles were obtained in the downstream region, but at the expense of flattening the upstream deposition peaks and thereby removing the good agreement with experiments previously observed there.

The underlying source of these problems is likely the approximation of blood as a single continuum. This was expected to be an issue for non-zero hematocrits due to the well-known effects of RBCs on platelet concentration profiles (53, 79). However, even in the absence of RBCs, platelets have been shown to exhibit a non-uniform, wall-skewed concentration profile (53) consistent with the "tubular pinch" effect observed for dilute particulate suspensions (148). One explanation for the better agreement of the predicted and experimental results in the recirculation zone could be that such discrete-particle effects are not important there because the vortex creates a relatively uniform, well-mixed solution in which particle segregation does not take place. In contrast, the fully-developed flow in the downstream region will lead to shear-induced particle migration (148, 149), moving platelets toward the wall and RBCs toward the tube centerline (53). Using an enhanced diffusivity in the continuum model fails to replicate this behavior because it enhances transport in both the upstream and downstream regions, thereby destroying the good agreement between prediction and experiment in the recirculation zone, as seen in Figures 20 and 29.

In recent work, David et al. (103) attempted to model platelet adhesion from RBC-free platelet-rich plasma in a stagnation-point flow chamber using a one-equation steady-state model in which the surface reaction coefficient was a linearly increasing function of wall shear stress. This approach is attractive since the platelet deposition experimentally measured by Karino and Goldsmith appears to correlate with the magnitude of wall shear stress. However, it is unlikely that such a strategy would improve our predictions. First, the greatest variations in the shear-dependent reaction coefficients would be obtained in the recirculation zone, where the current model already predicts experimental deposition fairly accurately. Second, since the wall shear

stress is constant in fully-developed tube flow, a shear-dependent reaction coefficient would take on a constant value in the fully-developed downstream region. Thus, it would become equivalent to the current model in this region, where the poorest agreement with the experimental results is observed.

Besides the model's ability to predict platelet transport in disturbed flow over a range of hematocrits and Reynolds numbers, its time-dependent behavior was investigated by simulating one- and three-minute deposition results at 0% Hct, Re = 64. Using the best-fit k_{rs} and k_{as} from the one minute perfusion at 0% Hct, Re = 38, reasonable agreement for the one-minute simulation was obtained. However, the three-minute data were greatly over-predicted. Based on the low shear rate and the fact that little or no aggregation was observed in the experiments (59), it is unlikely that embolization was taking place. It is possible that transient attachment to and detachment from the collagen surface were occurring in the experiments, perhaps because the platelets could not form sufficiently strong bonds with the collagen in the absence of vWF and fibrinogen. However, Savage *et al.* (65) observed that inhibiting either GpIb or GpIIbIIIa had no effect on the levels of initial platelet adhesion onto collagen at a wall shear rate of 100 s^{-1}, which is comparable to the maximum wall shear rate for this case. Furthermore, since such translocation should not be a time-dependent event, it would tend to affect both the one- and three-minute deposition results if it were occurring.

Since the magnitude of the saturation parameter M_∞ determines how rapidly the platelet-surface flux will decrease as deposition increases, it is possible that the value of 10% of a monolayer we chose to mimic the sparse collagen coatings observed on the tubes was too high, resulting in an overestimation of deposition at longer times. The M_∞ value selected was an estimation based on the microscopic observations of the collagen coating by Karino & Goldsmith (59) and on the levels of observed deposition; sensitivity studies on this parameter were not carried out due to time constraints. The lower M_∞ is set, the more rapidly the platelet-surface flux will decrease for a given k_{rs} and k_{as}. Therefore, selecting a low enough value of M_∞ might induce a more reaction-limited character in the predicted deposition curves. However, peak deposition values corresponding to roughly 7% of our assumed monolayer value were observed in the experiments. If M_∞ is set to a value less than the peak of the experimental data, the predicted deposition peaks for those simulations will be clipped due to the saturation effect. This leaves a relatively limited range of M_∞ values available for further investigation, i.e. > 7%

to < 10% of monolayer coverage. Using the results of Figure 22 as a guide, it appears unlikely that the model is sufficiently sensitive to variations in M_∞ that varying it over this narrow range would make a significant difference in its predictive ability.

Finally, in addition to simulations predicting experimental platelet deposition, sensitivity studies were carried out to determine the influence of transport- and deposition-related parameters on the simplified model used for these cases. Predicted deposition levels were relatively insensitive to increases in the diffusion enhancement factor, both at 0% and 20% Hct. Similar sensitivities to k_{rs} and k_{as} were observed at 0% and 20% Hct except when deposition levels neared saturation. The ratio of percent decrease in deposition to percent decrease in reaction coefficients was slightly less than 1:1.

4.4.2 Axisymmetric Stenosis

These cases allowed us to test the robustness of the model including all agonists in disturbed flow, as well as to compare our predictions to those of the simpler, one-parameter, one-equation steady-state model of Wootton *et al.* (104). For a 50% area-reduction stenosis, it was found that both models gave similar predictions, with the Wootton model more accurate upstream of the stenosis throat. For a 75% area reduction stenosis, our model was more accurate upstream of the throat, but predicted platelet accumulation less accurately at the throat. Both models greatly underestimated the rate of platelet accumulation downstream of the stenosis throat for both levels of stenotic narrowing, however.

Completing the simulations for these cases was a very time-consuming process. While the steady-state CFD runs could typically be finished in 2-3 days, completing both unsteady platelet cases for a simulated time of 10 minutes required roughly two and a half months of "wall clock" time. One reason for the excessive time requirement was time-sharing of a single-processor machine for multiple (two to three) simultaneous simulations. However, it was also necessary to frequently adjust the under-relaxation factors and the time step to achieve convergence due to the stiff, coupled nature of the system of equations. This required frequent operator intervention and restarts. And even when only one of these cases was running on an otherwise unloaded machine, a single time step could still take up to four hours of CPU time if convergence difficulties were encountered.

These extremely long simulation durations prohibited us from carrying out parameter sensitivity or mesh refinement studies for these cases. Based on the lack of mesh independence observed even at very fine grid resolutions for the tubular expansion cases, it is very likely that the platelet deposition simulations for the stenosis cases are not grid-independent.

Both our model and that of Wootton under-predicted deposition downstream of the stenosis. However, it is surprising that our model, which predicts persistent agonist production and platelet activation in that region, predicts *less* deposition than Wootton's model, which does not simulate agonist production. The large under-predictions of platelet flux in the post-stenotic expansion region for both stenosis geometries are probably due to the same deficiencies in the platelet transport model that plagued the tubular expansion simulations; it appears that agonist-activation effects are insufficient to overcome the extremely diffusion-limited behavior of the model in these regions. Wootton's simulations, which, like ours, used a very fine near-wall mesh, theirs consisting of elements 1-2 μm thick (104), seem to suffer from the same malady.

Due to the increased complexity of these cases, however, there are other factors that could also have contributed to the discrepancies. One of these is that interactions between the flow field and the thrombus, including streamline alterations by thrombus growth and thrombus embolization by fluid shear stresses, are neglected by both models. This point was discussed in depth with respect to the Poiseuille flow cases of Chapter 3, but it would be even more pertinent at the higher shear rates and longer perfusion times studied here.

Specifically, fluid mechanical forces acting to limit thrombus size could explain both models' under-prediction of platelet deposition downstream of the throat if one admits the possibility of a "moving front" of platelet deposition, characterized by a decrease in upstream platelet-surface flux once a certain level of deposition is reached. If upstream deposition slowed or ceased at some time point because the thrombus had grown to a size where the fluid shear rate at its surface was too high to permit further platelet-platelet adhesion, the near-wall excess boundary layer reaching the downstream surface would be far less depleted than it would be if the upstream surface were still fully reactive. Thus, the downstream platelet flux would be higher, resulting in a more even distribution of platelet deposition, as observed experimentally.

Wootton's model (104) assumes a constant, steady-state platelet-surface flux and is therefore incapable of capturing this phenomenon. While our model forces the resting and activated platelet-surface fluxes to zero once a monolayer level of deposition is reached, we

assume that no such saturation of activated platelet-platelet adhesion occurs. This mechanism therefore continues to deplete the near-wall platelet boundary layer throughout the duration of the simulation. Our model could be altered to simulate this phenomenon by applying a shear-rate- and thrombus-size-dependent saturation term to the platelet-platelet flux equation. However, this term would likely have to be estimated for each new shear rate and geometry.

Whether such an effect is indeed the primary cause of the discrepancy between model predictions and experimental results for these cases could be investigated computationally by simulating a stenosis whose surface is non-reactive from the inlet to the throat, then fully reactive thereafter. If upstream depletion is indeed responsible for the models' under-prediction, much higher levels of downstream deposition should be predicted for this "non-reactive upstream" case than for a case with a fully reactive upstream surface. If other factors (e.g., deficiencies in the platelet transport model) are the primary cause, downstream deposition should be similar between the two cases. Due to time constraints, such studies were not performed.

Experimentally, the existence of such a "moving front" could be verified by using a stenosis coated with collagen along its entire length and perfusing platelets labeled with different (e.g.) fluorescent markers. This would allow one to alter the "color" of the deposited platelets with time, and to observe where each "color" is concentrated along the surface. That is, "red"-labeled platelets could be perfused for the first few minutes, then "green", then "blue". If deposition indeed occurs in a "moving front" fashion, the highest concentration of deposited "red" platelets should be furthest upstream, and the highest levels of "blue" deposition should be furthest downstream.

Another fluid-mechanical modeling issue is our choice to neglect shear stress as a platelet agonist. For the 50% stenosis, this may not be of great importance because the highest wall shear stress value predicted by CFD is 48.3 dynes cm^{-2}. Although this is very near the 50 dynes cm^{-2} threshold for platelet activation determined by Brown *et al.* (150), this value occurs very near the stenosis throat, where exposure times should be low due to the rapid flow. In contrast, Brown *et al.* observed platelet activation at 50 dynes cm^{-2} after five minutes of continuous exposure. For the 75% stenosis, however, the peak wall shear rate of 4975 s^{-1} corresponds to a shear stress of 174 dynes cm^{-2}. Additionally, there is a rather large region on both sides of the stenosis throat where the wall shear rate magnitude is greater than 1430 s^{-1}, which corresponds to a stress of 50 dynes cm^{-2} (see Figure 48). Thus, for this case it is possible that high shear stresses upstream of

and at the throat activate platelets, which subsequently become entrapped in the post-stenotic vortex, enhancing the observed deposition via a mechanism not present in the model. However, merely having more activated platelets present in the recirculation cell due to upstream shear-induced activation would not necessarily enhance the model's predicted deposition if its deficiency is in the kinetic model of platelet-surface adhesion or in the mechanism of simulating platelet transport to the wall.

Similar to the cases of Chapter 3, thrombin is the dominant agonist in these simulations, with model-predicted concentrations at some locations along the tube wall reaching greater than 1000× the activation threshold for both simulations. Of course, this raises the question of whether such high concentrations are realistic. Since no experimental method for measuring local species concentrations in flowing blood is available, this question cannot be answered at this time. In the simulations, these very high levels are localized to a region very close to the tube wall due to our assumption of a much higher rate of thrombin generation from adherent platelets activated by the collagen surface (see Section 3.2.1 for a justification). As demonstrated in Chapter 3, predicted platelet deposition is very sensitive to thrombin generation, so further work on validating the generation function for this agonist is likely warranted.

On the other hand, results different from those of Chapter 3 were observed for TxA_2. In the present simulations, this agonist reached supra-threshold levels comparable to those of ADP (whose levels here are similar those predicted in Chapter 3), whereas in the simulations of Chapter 3, the predicted concentrations of TxA_2 were always well below the critical level for platelet activation. This can be explained by considering the difference in perfusion times simulated, 75 s in Chapter 3 vs. 600 s here. Since we assume TxA_2 is generated in perpetuity both in the bulk and at the surface once a platelet becomes activated, longer simulation times favor increased levels of this agonist. ADP generation, in contrast, is assumed to be a one-time event occurring upon platelet activation. Also, once surface saturation is reached, resting platelet adhesion ceases, and along with it ADP generation due to platelet activation by collagen. Thus, at the long perfusion times studied here, ADP is only being generated by newly activated bulk platelets, which does not allow its levels to outstrip those of TxA_2 to the extent observed at the short times studied previously.

Another interesting observation is that, although the thrombin levels at the wall in the 50% stenosis simulation are greater than those of the other agonists in the upstream region before and at the stenosis throat, the downstream levels of all three agonists are similar, with ADP and TxA_2 levels even higher than thrombin concentrations just downstream of the throat. Again, this can be traced to the much higher value assumed for surface-based thrombin generation as compared to bulk generation. In the post-stenotic region, predicted platelet deposition drops off dramatically, thereby reducing this source of thrombin. Since ADP and TxA_2 are generated at the same rates at the surface as in the bulk, their levels do not drop in this region; rather, they tend to accumulate, possibly due to the nearly stagnant flow near the wall in this area.

By contrast, in the 75% stenosis, ADP and TxA_2 levels at the wall are diminished downstream of the separation point, whereas thrombin levels gradually rise to become an order of magnitude higher than those of the other two agonists. The high downstream thrombin concentrations are explained by increased platelet transport to the wall at the distal reattachment point, which is beyond the collagen-coated region. Since these platelets do not react with the silicone rubber wall there, they are carried back upstream and attach immediately on contacting the collagen-coated region, where they produce thrombin at a higher rate than do bulk-activated platelets. As explained above, ADP release due to surface adhesion will be zero once saturation is reached, so that little generation of this agonist occurs due to downstream adhesion. The drop in TxA_2 concentration is more puzzling, since it is generated perpetually by activated platelets, similar to thrombin. However, its levels do not drop to the same extent as do ADP's, indicating that its behavior is similar to that of thrombin, but its downstream concentration does not increase like thrombin's does because its generation rate is not augmented at the wall as is thrombin's.

Comparing Figures 45 and 51, as well as 46 and 52, one can see the deleterious effects of recirculation regions on platelet activation. In Figure 45, which shows the 50% stenosis with no downstream vortex, agonist concentrations only reach levels noticeably different from zero in a very narrow boundary layer near the tube wall. In contrast, the 75% stenosis results shown in Figure 51 display supra- and near-threshold agonist concentrations throughout the recirculation zone, leading to the greatly increased bulk platelet activation seen in Figure 52B.

Although the model does not predict it, one would anticipate that the high levels of bulk platelet activation here, combined with increased mixing due to the vortex, would create bulk platelet aggregates that could either: 1) attach to the wall and obstruct flow, further narrowing the stenosis; or 2) create macroemboli that could be transported to distal tissue beds. Simulating such phenomena is clearly an interesting area for future study, as one might be able to predict "safe" and "unsafe" levels of narrowing with respect to their thromboembolic proclivities.

A final issue that should be addressed is raised by the results of the time-accurate simulations conducted for the 0% Hct, Re = 64 case, in which it was shown that the model did not accurately predicted the time-dependent change in platelet-surface flux which occurred between one and three minutes. That observation raises the question of whether the accuracy of our predictions for these cases could be dependent on the simulation time chosen. We selected 10 minutes to minimize computing time, but Wootton *et al.* calculated V_{max} from their experimental data based on an average taken between 10 and 25 minutes. Perfusion time is used as a normalizing factor in our calculation of model-predicted V_{max} (see Equation 24). However, it is still possible that different V_{max} levels may have been obtained if the more representative average time of 17.5 minutes had been simulated. This possibility was not investigated due to the prohibitive computing times it would have required.

4.4.3 Comparison to Other Models

Based on the poor predictions of platelet deposition in disturbed flow obtained in the simulations discussed in this chapter, it is difficult to recommend our model over the simpler versions presented recently by David *et al.* (103) and Wootton *et al.* (104). One theoretical advantage of our model is that each parameter is intended to have a physical meaning, and can therefore be estimated *a priori* based on the conditions being simulated: for example, platelet-surface reaction coefficients should be a function only of the surface composition of the material onto which platelets adhere (assuming normal whole blood as the perfusate). In contrast, the single heterogeneous reaction coefficient employed by the simpler models is a lumped parameter governing several phenomena: near-wall platelet transport, activation, adhesion, and aggregation. However, as discussed above, if our surface reaction coefficients k_{rs} and k_{as} need to be altered for different hematocrits (and possibly shear rates), they also become lumped parameters, and our model retains no edge over the others in this respect.

Another advantage of the present model over these recent works is that it can predict local agonist concentrations. But, since agonist generation in our simulations is directly related to local levels of platelet deposition and activation, this information is of little use if it is based on an unreliable model of platelet transport and deposition.

Additionally, the computational cost of our approach weighs heavily against it. When solving the full seven-equation model, convergence is extremely slow due to the stiff nature of the source terms and to the coupling between equations. This issue could be resolved by investigating other solvers or by implementing a coupled, rather than sequential, solution method. A more pressing issue, however, is the excessive amount of time needed to solve the equations in time-dependent form. In essence, this process is equivalent to solving a steady-state problem at each time step, albeit using a reduced convergence criterion relative to a steady problem. Since we typically use 100 time steps for a simulation, this factor alone makes our seven-equation model ~700 times more expensive to solve than the one-equation, steady state versions of David *et al.* (103) and Wootton *et al.* (104). This expense can be justified if the time-accurate predictions of our simulations yield more accurate information than a steady-state simulation. Time-dependent effects are likely to be important at short perfusion times, such as the one and three minute simulations shown in Figure 32. However, for these cases, our model was unable to predict the experimentally observed decrease in platelet-surface flux with increasing time, so to have an actual advantage in this respect, its time-dependent behavior would have to be improved. But this may be a fruitless endeavor, since blood-contact times for medical devices range from hours to years. Unless it can be shown experimentally that the relevant phenomena governing long-term device performance are predicted by early thrombocyte-biomaterial interactions, detailed acute deposition information may be of little utility as a design aid. Furthermore, our predictions of the experimental values obtained by Wootton *et al.* (104) at longer times (10 – 25 min), where the flux appears to be approximately constant in time, were generally slightly worse than those of Wootton's steady-state model. The inability of our model to better fit the data could be attributed to our decision to use kinetic parameters for our agonist generation functions that were derived from experiments and simulations conducted with human blood. This may have led to an incorrect estimation of agonist production in baboon blood, contributing to erroneous predictions of platelet deposition.

Raising this issue, however, reveals another shortcoming of our model relative to the simpler ones: there is a large number of species- and problem-specific parameters to be obtained, either from literature or by a cut-and-try approach. Informal, heuristic sensitivity analyses of some of the key parameters, such as the platelet-surface and platelet-platelet adhesion coefficients, platelet diffusivity, and agonist generation functions were conducted in Chapters 2 and 4. These revealed that the model is very sensitive to the level of thrombin generation, that the ratio of percent change in platelet adhesion to percent change in adhesion coefficients is roughly 1:1, and that very large changes in platelet diffusivity are required to alter the platelet deposition patterns. However, such an analysis gives an incomplete picture, and the sensitivity of the model to most, if not all, of the parameters incorporated into all seven equations should likely be investigated in a systematic fashion to find which ones may have contributed to the shortcomings in the model predictions observed in this chapter. Performing such sensitivity analyses is time-consuming not only because of the number of parameters to be investigated, but also because of the long computing times required, as discussed above. Additionally, it was observed (see Figure 22) that basically identical deposition predictions could be obtained for two different sets of values of k_{rs}, k_{as}, and M_∞. In that case, the issue of which prediction was "correct" was resolved by selecting the M_∞ value that was more consistent with the experimental situation. However, such a clear-cut justification may not always be available, as might be the case with adjusting k_{rs} and k_{as} to obtain best fits. Physically, one would always expect $k_{as} > k_{rs}$ due to the increased expression of GpIIbIIIa receptors on activated platelets, but how much greater should it be? In the simulations of Figure 22, for $M_\infty = 7.0 \times 10^5$ PLT cm^{-2}, the best-fit k_{as} is an order of magnitude larger than k_{rs}, while at $M_\infty = 7.0 \times 10^6$ PLT cm^{-2}, it is only greater by about 30%. Such ambiguity must be regarded as another drawback of the multiple parameters used in our model.

Additional sources of ambiguity are the relative importance of each of the many model parameters, as well as the uncertainties associated with our trial-and-error method of estimating the independent ones. Clearly, a more mathematically rigorous approach to fitting the model to the experimental results than the heuristic algorithm outlined in Section 3.2.1 would be preferable. One way of accomplishing this would be to mathematically optimize the variable model parameters to minimize the difference between the predicted and experimentally measured deposition curves. It may also be possible to combine such an algorithm with non-

linear regression techniques to obtain mathematical estimates of both parameter sensitivities and uncertainties, i.e. confidence intervals for the parameters (151). Such analyses were not conducted because of the additional level of computational complexity that would be created by having to add an outer iteration involving the rather difficult to implement optimization and nonlinear regression algorithms to our already complex code and because it seemed the cut-and-try approach provided acceptable results for the training and validation cases presented in Chapter 3. Furthermore, it would seem unlikely that the large discrepancies between our model predictions and the experimental results for the present simulations could be resolved by a more mathematically rigorous approach to parameter fitting. Also, the model was formulated mechanistically, i.e., each parameter was supposed to have a direct correspondence to some physical event being simulated. However, the possibility that the model is over-determined needs to be considered and explored. The sensitivity information provided by such an analysis would aid in determining which parameters have the greatest effect on the model predictions and which ones, if any, could either be dropped from the model or treated as constants, thereby allowing us to reduce the complexity of our equations. An optimization-based approach, once fully automated, would also speed the fitting process were the model to be applied to additional biomaterials or flow conditions.

Another method of analyzing our simulations that might aid in determining the relative importance of the model parameters would be to explore the possibility that our results could be correlated using dimensionless groups of relevant variables. If such relationships were found, they might reveal, for example, that only the ratios of certain parameters are important, rather than their individual absolute magnitudes. Additionally, it might be possible to develop correlations between dimensionless groups analogous to those used in determining conventional mass transfer coefficients. One example of where such relationships would be invaluable would be for determining k_{as} and k_{rs} as a function of surface composition, hematocrit, and shear rate, since the tubular expansion cases seem to suggest such a dependence for them. Rather than heuristically re-fitting these parameters for each case, they could be determined from the dimensionless variable correlations. This approach was not attempted because the wide range of variable combinations that would have to be explored seemed prohibitive within the time constraints of this project, and because a wider range of simulation results than those performed herein would likely be required to reveal the dimensionless relationships.

Another concern associated with our modeling approach is that an extremely fine near-wall mesh is apparently required to attain a grid-independent solution. Due to time limitations, we did not determine the exact degree of refinement necessary, but, for the tubular expansion case, changing the resolution from 77612 to 123891 nodes, with the majority of the 46279 new points on the finer grid confined to a very small 50 μm wide × 25 mm long region, did not result in mesh independence (Figure 21). The necessity for such a fine grid obviously leads to greatly increased demands on computational resources. This, combined with the relatively poor predictive abilities of continuum models in general and the inherent superiority of a discrete, Lagrangian model for reproducing what are in reality discrete, Lagrangian phenomena, raises the question of how much effort should be put into continuing to improve continuum approximations of platelet and RBC transport. Discrete-cell-based models have already been implemented (106, 152), and although realistic macroscopic simulations of blood flow are not feasible at present, the seemingly daily increases in computing power that continue to occur mean that one day they likely will be.

4.5 Conclusions

In this chapter, the model's ability to predict platelet deposition in two-dimensional disturbed flow was investigated. As in Chapter 3, the adhesive substrate under consideration was type I collagen. First, cases with no agonists or platelet aggregation were simulated to test the ability of our continuum approximation of blood to reproduce the effects of RBCs on platelet transport, as well as its ability to simulate the transport of platelets alone. Next, simulations of non-anticoagulated baboon blood were conducted to see whether the agonist generation terms in our full model could better predict deposition in a stenotic tube than the one-species, one-parameter model of Wootton *et al.* (104), which contained no agonist generation terms.

It was found that the predicted deposition levels are extremely sensitive to the density of the computational mesh, with grid independence not obtained even for an extremely fine near-wall grid in the tubular expansion simulations. Long simulation times hampered our abilities to fully determine the level of refinement required for grid independence for either of the geometries studied.

In general, the model was capable of predicting platelet deposition fairly well in the upstream recirculation regions of the tubular expansion geometry, and in the upstream region and throat of the stenotic geometry. Rather poor predictions were obtained in the downstream fully-developed region of the tubular expansion and the post-stenotic expansion region of the stenosis. These poor predictions are primarily attributed to inadequate platelet transport to the near-wall region, resulting in a predicted platelet-surface flux much lower than that observed experimentally.

In comparison to other, simpler continuum models, our model fairs poorly due to its lack of improved predictive ability in light of its relative complexity, especially due to the extremely high computational cost of solving the stiff, coupled, unsteady equations that it comprises.

However, the key conclusion which was derived from these simulations and which affects not only the present model but also all similar continuum approximations, is that it appears that continuum mass transfer equations incorporating a conventional isotropic diffusion coefficient are not capable of modeling platelet transport in disturbed flow. While we were able to reasonably approximate the effects of RBCs on local platelet concentrations via the use of an artificially skewed inlet boundary condition and an enhanced platelet diffusivity in the Poiseuille flow simulations of Chapter 2, this simple approach failed for the disturbed flows simulated in this chapter.

Thus, our model, as currently constituted, is not adequate for predicting the thrombotic predilections of medical devices, in which much more complex flow fields and unsteady effects prevail. In order to adequately model platelet-mediated thrombogenesis, it may be necessary to consider more complex transport models that more accurately account for the particle-like behavior of RBCs and platelets. In Chapter 5, we take a very preliminary step in this direction by investigating the utility of an “off-the-shelf” multiphase flow model for blood simulations.

5.0 MODEL IMPROVEMENT: TWO-PHASE FLOW SIMULATION

"The road of excess leads to the palace of wisdom"

-William Blake, "Proverbs from Hell"

5.1 Introduction

In Chapter 4, simulations of platelet deposition in disturbed flow revealed that the continuum mass transfer model currently employed is inadequate for simulating platelet transport, both in the presence and absence of RBCs. It was postulated that this deficiency is due to the particulate behavior of these blood elements. In this chapter, we attempt to simulate this behavior using a two-phase fluid model. Because multiphase flow modeling is far from a mature subject and because existing models are extremely complex, no attempt was made to create a model specifically tailored to emulate the properties of blood. Such an endeavor would in itself be enough for one or more additional dissertations. Instead, as a "proof of concept" study, we employ an existing fluid-solid suspension model used for gas-particle flows in an attempt to predict RBC and platelet concentration profiles in fully-developed tube flow. While such a model is not ideally suited for blood simulations, it is hoped that the preliminary results presented herein will stimulate the development of better blood flow models which more accurately take into account the nature of this unique suspension.

5.2 Multiphase Model

5.2.1 Background

Since we are interested in modeling RBCs and platelets as particles, single-phase blood models do not apply and recourse must be made to multiphase flow models which treat the fluid and dispersed phases separately. Such models can be broadly classified into Lagrangian models, which treat the dispersed phase as discrete particles, tracking each individually, and Eulerian models, which treat the dispersed phase as an effective continuum that co-exists with the fluid phase. While the former allow more accurate simulation of fluid-particle interaction forces, the large number of RBCs and platelets in blood makes individual particle tracking a computational impossibility at present. Thus, we chose to work with so-called "two-fluid" or mixture theory models, which treat the fluid and particle phases as interpenetrating continua. We found only one previous model in the literature that employed multiphase flow theory for describing blood flow,

the work presented by Hofer and Perktold (153). These investigators employed the model developed by Phillips *et al.* (154) for shear-induced particle migration in fluid-solid flows. This model treats the suspension as a single continuum with a density and viscosity which depend on the local particle volume fraction. The particle volume fraction is found by solving a transport equation which contains terms to simulate particle migration due to spatially varying particle collision frequencies and suspension viscosity (154). This results in flux terms proportional to the local shear rate and particle volume fraction gradients. In both the original work (154) and the simulations of Hofer and Perktold (153), the particle transport equation is restricted so migration will only be directed down the shear rate gradient.

Hofer and Perktold (153) applied the model of Phillips *et al.* to the problems of fully-developed flow in a cylindrical tube and flow through a stenotic tube using physical parameters (fluid density and viscosity and particle volume fraction) appropriate for blood. No comparison to experiments was made. However, the simulations demonstrated that particles would migrate to the low-shear core of the flow, consistent with the model's intent to drive particles down the shear gradient. Additionally, the suspension velocity profile was shown to be blunter than a Newtonian parabolic profile, consistent with experimental observations for blood (128). However, because of the assumption that no collisions take place in regions of zero shear rate and because the viscosity of the suspension becomes infinite when the particle volume fraction reaches its maximum value of 0.68, the model always predicts that the volume fraction reaches its maximum wherever the shear rate is zero. In tube flow, this results in an artificially sharp concentration profile with a cusp at the centerline, $r = 0$. Such behavior is not consistent with that of blood (153). Furthermore, the model was developed for dense suspensions, and would therefore be inappropriate for simulating an RBC-free dilute suspension of platelets, like those used in the experiments of Karino and Goldsmith (59) which were studied in Chapter 4.

In an attempt to simulate both dilute and dense suspensions corresponding to platelets and RBCs, respectively, in plasma, we chose to use the approach of Masson (155, 156), who employed the gas-solid suspension model of Lun (157) in a finite-volume-based numerical method. Lun's model (157) uses the kinetic theory of gases to derive solid-phase equations governing the elastic or slightly inelastic collisions between spherical particles in a granular flow. The effect of the interstitial fluid on the solid particles is also modeled. Separate fluid- and solid-phase momentum and continuity equations are derived, along with an equation governing

transport of the solid-phase fluctuating kinetic energy, also known as the granular temperature. Due to the employment of the kinetic theory, the resulting equations contain expressions for the solid-phase pressure, stress tensor, and viscosity, which eliminates the need to estimate or fit undetermined coefficients in the constitutive relations.

An important consideration in modeling two-phase flow is the inclusion of the interaction forces governing momentum exchange between the phases. As reviewed by Johnson *et al.* (158), important interactions may include drag, lift, buoyancy, Magnus forces due to particle spin, and Basset history and virtual mass forces due to relative acceleration of the particle with respect to the fluid. Lun's model (157) and Masson's implementation of it (156) consider a granular flow in which the solid-phase density is much greater than the fluid-phase density, as would be the case in gas-solid two-phase flows. This restriction results in the omission of all interphase interaction forces except for the drag and virtual mass forces. Both are considered by Lun, while Masson neglects virtual mass.

There are several attractive features of this model. First, it is valid for a wide range of particle volume fractions, making it useful for both RBC (dense suspension) and platelet-only (dilute suspension) simulations. Second, it contains no "free" parameters to be fit or estimated, reducing the computational effort required. Finally, Masson's finite-volume implementation is very similar to the one used to develop our mass transfer and CFD codes, which considerably eased coding and debugging of this very complex algorithm.

However, this is far from an optimal model for blood. Since the particles are treated as rigid spheres, rotational effects due to the discoid shapes of RBCs and platelets are neglected, as are hydrodynamic effects due to deformation of RBCs, a mechanism which may be important in explaining their migration to the center in fully-developed tube flow (159, 160). Additionally, since the densities of platelets and RBCs are approximately equal to that of plasma, the high-density-ratio assumption that allows most interaction forces to be neglected is not valid. Since no model could be found which incorporated all these desirable properties, Masson's was used in a preliminary attempt to see whether it could reasonably model blood flow.

5.2.2 Model Equations

What follows is a brief overview of the equations used in the multiphase model. For a complete derivation and thorough explanations of all terms, the reader is referred to Masson's dissertation (156). Using Masson's notation, Equation 25 is a general conservation equation in cylindrical coordinates:

$$\frac{\partial}{\partial t}\left(\psi^i \rho\phi\right)+\frac{\partial}{\partial z}\left(\psi^i \rho u_z^i \phi\right)+\frac{\partial}{\partial r}\left(r\psi^i \rho u_r^i \phi\right)=\frac{\partial}{\partial z}\left(\Gamma_e \frac{\partial \phi}{\partial z}\right)+\frac{1}{r}\frac{\partial}{\partial r}\left(r\Gamma_e \frac{\partial \phi}{\partial r}\right)+S_\phi, \qquad [25]$$

where superscript $i = f$ for fluid or s for solid phase: ϕ represents a generic species; ρ is density of the current phase; u_r and u_z are the radial and axial velocity components; respectively; ψ is the volume fraction of the respective phase; Γ_e is the effective diffusion coefficient for the phase under consideration, and S_ϕ is a species-specific source term.

Table 10 lists the specific form of each variable in Equation 25 as used in Masson's model (155). In both Masson's formulation and ours, the fluid-phase continuity equation is used to solve for the fluid-phase pressure, and the solid-phase continuity equation is used to obtain the solid volume fraction.

Table 10. Specific variables for Equation 25

After Masson and Baliga (155).

Conservation equation	ρ	Γ_e	Γ_b	ϕ	S_ϕ
Fluid					
z-momentum	ρ^f	μ^f_e	μ^f_b	u^f_z	$S_{\Gamma z} - S_{Dz} + S^f_z - \psi^f \frac{\partial p^f}{\partial z}$
r-momentum	ρ^f	μ^f_e	μ^f_b	u^f_r	$S_{\Gamma r} - S_{Dr} + S^f_r - \psi^f \frac{\partial p^f}{\partial r} + S_{cyl}$
continuity	ρ^f	0	0	1	0
Solid					
z-momentum	ρ^s	μ^s_e	μ^s_b	u^s_z	$S_{\Gamma z} + S_{Dz} + S^s_z - \psi^s \frac{\partial p^f}{\partial z} - \frac{\partial p^s}{\partial z}$
r-momentum	ρ^s	μ^s_e	μ^s_b	u^s_r	$S_{\Gamma r} + S_{Dr} + S^s_r - \psi^s \frac{\partial p^f}{\partial r} - \frac{\partial p^s}{\partial r} + S_{cyl}$
continuity	ρ^s	0	0	1	0
granular temperature	$1.5 \cdot \rho^s$	κ^s_T	0	T	$W_p + S_\psi + S_T + \Phi^s - \gamma_c - \gamma_D + \gamma_B$

In Table 10, Γ_b is the bulk diffusion coefficient of the current phase; μ^i_e and μ^i_b are effective and bulk viscosities, respectively, of that phase, and p^i is the phase's pressure. S^f_z, S^f_r, S^s_z, and S^s_r would be additional problem-specific body forces, such as gravity, while S_T would be an external granular temperature source. The remaining source terms have the following forms:

$$S_{\Gamma z} = \frac{\partial}{\partial z}\left[\Gamma_e \frac{\partial u^i_z}{\partial z} + \left(\Gamma_b - \frac{2}{3}\Gamma_e\right)\left(\frac{\partial u^i_z}{\partial z} + \frac{1}{r}\frac{\partial}{\partial r}\left(r u^i_r\right)\right)\right] + \frac{1}{r}\frac{\partial}{\partial r}\left(r\Gamma_e \frac{\partial u^i_r}{\partial z}\right) \quad [26]$$

$$S_{\Gamma r} = \frac{1}{r}\frac{\partial}{\partial r}\left\{r\left[\Gamma_e \frac{\partial u^i_r}{\partial r} + \left(\Gamma_b - \frac{2}{3}\Gamma_e\right)\left(\frac{\partial u^i_z}{\partial z} + \frac{1}{r}\frac{\partial}{\partial r}\left(r u^i_r\right)\right)\right]\right\} + \frac{\partial}{\partial z}\left(\Gamma_e \frac{\partial u^i_z}{\partial r}\right) \quad [27]$$

$$S_{cyl} = -\frac{1}{r}\left[\left(\Gamma_b - \frac{2}{3}\Gamma_e\right)\left(\frac{\partial u^i_z}{\partial z} + \frac{1}{r}\frac{\partial}{\partial r}\left(r u^i_r\right)\right) + 2\Gamma_e \frac{u^i_r}{r}\right] \quad [28]$$

$$S_{Dz} = \psi^s \rho^s \zeta_D \left(u^f_z - u^s_z\right) \quad [29]$$

$$S_{Dr} = \psi^s \rho^s \zeta_D \left(u^f_r - u^s_r\right) \quad [30]$$

$$S_\psi = \frac{\partial}{\partial z}\left(\kappa_\psi^s \frac{\partial \psi^s}{\partial z}\right) + \frac{1}{r}\frac{\partial}{\partial r}\left(r\kappa_\psi^s \frac{\partial \psi^s}{\partial r}\right) \quad [31]$$

$$W_p = -p^s\left[\frac{\partial u_z^s}{\partial z} + \frac{1}{r}\frac{\partial}{\partial r}\left(ru_r^s\right)\right] \quad [32]$$

$$\gamma_C = 48\eta(1-\eta)\frac{\left(\psi^s\right)^2 \rho^s g_0}{d_p \pi^{1/2}} T^{3/2} \quad [33]$$

$$\gamma_D = 3\psi^s \rho^s \zeta_D T \quad [34]$$

$$\gamma_B = \left(1 + 0.88\left(\psi^s\right)^{3/2}\right)\gamma_D \quad [35]$$

$$\Phi^s = \left(\mu_b^s - \frac{2}{3}\mu_e^s\right)\left(\frac{\partial u_z^s}{\partial z} + \frac{1}{r}\frac{\partial}{\partial r}\left(ru_r^s\right)\right)^2 + 2\mu_e^s\left[\left(\frac{\partial u_r^s}{\partial r}\right)^2 + \left(\frac{u_r^s}{r}\right)^2 + \left(\frac{\partial u_z^s}{\partial z}\right)^2\right] + \mu_e^s\left(\frac{\partial u_z^s}{\partial r} + \frac{\partial u_r^s}{\partial z}\right)^2. \quad [36]$$

Equations 26-27 represent diffusion source terms which arise from the non-constant viscosity and volume fraction of each phase. The term S_{cyl} in Equation 28 arises due to the use of cylindrical coordinates. Equations 29-30 are the drag forces in the *z*- and *r*-directions, respectively. Equation 31 models the rate of particle kinetic energy diffusion due to gradients in particle volume fraction, while Equation 32 represents the work done by the solid-phase pressure. Finally, Equations 33-36 are kinetic energy production and dissipation terms: γ_C is dissipation due to particle collisions; γ_D is dissipation due to drag; γ_B represents the exchange of energy between the mean and fluctuating parts of the flow, and Φ^s models viscous dissipation.

To close the equations, the following constitutive relations are needed:

$$\mu_e^f = \mu^f \mu_r^f(\psi^s) + \rho^f\left(C_s L_G\right)^2 S_R; \qquad \mu_b^f = 0 \quad [37]$$

$$\mu_r^f(\psi^s) = \left(1 - \psi^s - 0.33\left(\psi^s\right)^2\right)^{-5/2} \quad [38]$$

$$S_R = \left\{2\left[\left(\frac{\partial u_z^f}{\partial z}\right)^2 + \left(\frac{\partial u_r^f}{\partial r}\right)^2 + \left(\frac{u_r^f}{r}\right)^2\right] + \left(\frac{\partial u_z^f}{\partial r} + \frac{\partial u_r^f}{\partial z}\right)^2 - \frac{2}{3}\left(\frac{\partial u_z^f}{\partial z} + \frac{1}{r}\frac{\partial}{\partial r}\left(ru_r^f\right)\right)^2\right\}^{1/2} \quad [39]$$

$$\zeta_D = \frac{3\mu^f}{4\rho^s d_p^2} C_d Re^s; \quad C_d Re^s = \begin{cases} 24 + 3.6\left(Re^s\right)^{0.687}, & Re^s \le 1000 \\ 0.44 Re^s, & Re^s > 1000 \end{cases} \quad [40]$$

$$p^s = \psi^s \rho^s T\left(1 + 4\eta g_0 \psi^s\right) \quad [41]$$

$$\mu_b^s = \frac{8\eta d_p \rho^s g_0 \left(\psi^s\right)^2}{3}\left(\frac{T}{\pi}\right)^{1/2} \quad [42]$$

$$\mu_e^s = \frac{\mu^{s*}}{g_0}\left(1+\frac{8}{5}\eta g_0 \psi^s\right)\left(1+\frac{8}{5}(3\eta-2)\eta g_0 \psi^s\right)+\frac{3}{5}\mu_b^s \quad [43]$$

$$\kappa_T^s = \frac{\kappa^{s*}}{g_0}\left(1+\frac{12}{5}\eta g_0 \psi^s\right)\left(1+\frac{12}{5}(4\eta-3)\eta^2 g_0 \psi^s\right)+\frac{3}{2}\mu_b^s \quad [44]$$

$$\kappa_\psi^s = \frac{\kappa^{s*}}{g_0}\left(1+\frac{12}{5}\eta g_0 \psi^s\right)\frac{12}{5}(2\eta-1)(\eta-1)\frac{\mathrm{d}}{\mathrm{d}\psi^s}\left(\eta g_0 \left(\psi^s\right)^2\right)\frac{T}{\psi^s} \quad [45]$$

$$\mu^{s*} = \frac{\mu^{s'}}{1+\left(\frac{2\zeta_D \mu^{s'}}{\psi^s \rho^s g_0 T}\right)}; \qquad \mu^{s'} = \frac{5\pi\rho^s d_p}{96\eta(2-\eta)}\left(\frac{T}{\pi}\right)^{1/2} \quad [46]$$

$$\kappa^{s*} = \frac{\kappa^{s'}}{1+\left(\frac{6\zeta_D \kappa^{s'}}{5\psi^s \rho^s g_0 T}\right)}; \qquad \kappa^{s'} = \frac{75\pi\rho^s d_p}{486\eta(41-33\eta)}\left(\frac{T}{\pi}\right)^{1/2} \quad [47]$$

$$\eta = \frac{1+e}{2}; \qquad g_0 = \left(1-\frac{\psi^s}{\psi_{MX}^s}\right)^{-2.5\psi_{MX}^s}; \qquad Re^s = \frac{\rho^f d_p \sqrt{\left(u_i^f\right)^2 - 2u_i^f u_i^s + \left(u_i^s\right)^2}}{\mu^f} \quad [48]$$

Equation 37 shows that the fluid-phase effective viscosity μ_e^f depends on the solids volume fraction multiplied by the intrinsic (pure fluid) viscosity μ^f and on a Reynolds-stress-like term which is approximated by Equation 39. The coefficient C_s is a grid-dependent parameter between 0.1 for a coarse grid and 0.2 for a fine grid, and L_G is a measure of grid element length (in cm), taken as the cube root of the average element volume for the grid. Equation 40 is the coefficient for the drag forces (Equations 29-30). The remaining constitutive equations for the solid phase are based on Lun's (157) derivation using kinetic theory. In these equations, ψ^s_{MX} is the maximum volume fraction of solids, g_0 is the equilibrium radial distribution function, d_p is the particle diameter, e is the coefficient of restitution for particle-particle collisions; and Re^s is the particle Reynolds number. The interested reader can consult the original works (156, 157) for more detail.

5.3 Methods

A finite-volume implementation of the model described by Equations 25-48 was coded within the framework of the existing CFD/mass transfer solver using the detailed information available in Masson's dissertation (156). The solution algorithm is identical to that employed previously for solving the equations of fluid motion and species conservation. The seven equations given by Equation 25 and Table 10, along with a pressure correction equation, comprise the system to be solved. It is thus akin to two coupled systems of Navier-Stokes and continuity equations. Pseudo-time-stepping (136) was found to be the optimal method for relaxing this highly nonlinear and strongly coupled system. In contrast to Masson, who used a single time step for all the equations, we usually obtained better convergence using different time steps for different equations.

5.3.1 Code Validation

Because of the complexity of the multiphase model, it was necessary to validate the code before attempting to extend it to blood-flow simulations. For this purpose, a set of benchmark cases simulated by Masson were used. Because the results are germane to the subsequent blood flow simulations, they are presented here, rather than in an appendix.

Masson and Baliga (155) chose fully-developed gas-solid flow in a 3.0 cm diameter vertical pipe as one of the test cases for their code. Although this problem is really one-dimensional, with only radial variations in the dependent variables, they simulated it in a two-dimensional framework. They validated their results against the earlier numerical work of Sinclair and Jackson (161), who solved the one-dimensional problem.

The model of Sinclair and Jackson is similar to that employed by Masson in that both are based on kinetic theory and have the granular temperature as a variable. However, the following parameters are specific to the Sinclair and Jackson model and therefore need to be altered from the forms previously specified in Equations 25-48:

$$\mu_r^f(\psi^s) = \left(1 + 2.5\psi^s + 7.6(\psi^s)^2\right)\left(1 - \frac{\psi^s}{\psi^s_{MX}}\right) \qquad [49]$$

$$\zeta_D = \frac{g}{\mu^f v_t (1-\psi^s)^2} \qquad [50]$$

$$g_0 = \frac{1}{1 - \left(\frac{\psi^s}{\psi^s_{MX}} \right)^{1/3}} \qquad [51]$$

In Equation 50, v_t is the terminal velocity of a particle falling in air under the influence of gravity, and g is the gravitational constant. Additionally, Sinclair and Jackson neglect the Reynolds-like stresses in the effective fluid viscosity (Equation 37). They also ignore the influence of fluid drag when deriving the solid-phase constitutive equations. This means that S_R in Equation 37 and the ζ_D term in Equations 34, 46, and 47 should be set to zero.

Table 11 lists specific parameter and source term values for these cases. The physical properties correspond to those of mineral particles suspended in air at 427 ºC. The non-zero momentum source terms are the gravitational body forces on the fluid and solid phases.

Table 11. Specific parameter values for multiphase validation cases

Parameter or Source Term	Value or Form
μ^f	3.65×10^{-4} g cm^{-1} s^{-1}
ρ^f	4.40×10^{-4} g cm^{-3}
ρ^s	2.50 g cm^{-3}
ψ^s_{MX}	0.65
v_t	1.29×10^{2} cm s^{-1}
g	9.80×10^{2} cm s^{-2}
d_p	1.50×10^{-2} cm
S^f_z	$-\psi^f \cdot \rho^f \cdot g$
S^s_z	$-\psi^s \cdot \rho^s \cdot g$
S^f_r, S^s_r, S_T	0

Because the fully-developed solution should be independent of axial distance z, this problem was solved using periodic boundary conditions at the inlet and outlet. For these boundary conditions, we used the single-phase formulation of Murthy and Mathur (162), adapted for multiphase flow. In the single-phase formulation, either the constant (non-periodic) part of the pressure gradient or the mass flow rate can be specified. In their work, Masson and Baliga

claim to implement periodic BCs for two-phase flow by specifying the fluid-phase pressure drop and the solid-phase mass flow rate (155). However, the numerical results of Sinclair and Jackson (161) clearly demonstrate that, for a given fluid pressure drop and solids mass flow rate, multiple solutions corresponding to different fluid-phase mass flow rates exist. Therefore, in order to obtain a unique solution, we specified both the fluid- and solid-phase mass flow rates in our periodic BC implementation. Additionally, since p^s is constant in fully-developed flow (161), Equation 41 and the specified solids mass flow rate can be used to derive an algebraic equation for ψ^s, eliminating the solid-phase continuity equation.

For the other boundary conditions, zero normal fluxes at $r = 0$ were specified for all dependent variables except normal velocities, which were set to $u^f_r = u^s_r = 0$ at both this location and the wall ($r = 1.5$ cm). Zero normal flux BCs were also specified at the wall for p^f and ψ^s. For u^f_z, u^s_z, and T, specified-flux wall BCs corresponding to those proposed by Sinclair and Jackson (161) were used. For the solid phase, this corresponds to the following specified shear stress:

$$\sigma^s_{rz} = -\frac{\sqrt{3T}\pi\rho^s\psi^s g_0 u^s_z \phi'}{6\psi^s_{MX}}, \qquad [52]$$

where all dependent variables are evaluated at the wall, and ϕ' is a "specularity factor" governing collisional momentum transfer that depends on the smoothness of the wall: $\phi' = 0$ for a smooth wall, $\phi' = 1$ for a rough wall. The value used for these simulations corresponds to that chosen by Masson and Baliga and Sinclair and Jackson, $\phi' = 0.5$. The specified fluid-phase shear stress is:

$$\sigma^f_{rz} = -\frac{2\mu^f_e \psi^s_{MX} T u^f_z}{v_t^2 \psi^s L_{CV}}, \qquad [53]$$

where again everything is evaluated at the wall, and L_{CV} is an estimate of local element length, taken as (element volume)$^{1/3}$. Finally, the expression for the granular temperature wall flux is:

$$q^s_r = \frac{\sqrt{3}\pi\rho^s\psi^s g_0 \left(1 - e_w^2\right) T^{3/2}}{4\psi^s_{MX}} + u^s_z \sigma^s_{rz}, \qquad [54]$$

where the first term represents energy dissipation by particle-wall collisions, with e_w the coefficient of restitution for such events, and the second term is energy generation due to solid-phase slip. Further information on the derivations of these BCs is given in Sinclair and Jackson (161).

For these simulations, a regular grid consisting of three nodes in the *z*-direction and 11 in the *r*-direction was used. This was identical to the mesh used by Masson and Baliga. A very sparse axial grid can be used because there are no entrance length effects with periodic boundary conditions, i.e., the steady-state solution should be independent of *z*. Two different convection schemes were tested. The first was the MAW scheme, which was the one used by Masson and Baliga (155). This scheme was used in preliminary tests to aid in debugging the code. The second was the PSI fluctuation-splitting scheme (135) that we prefer over the MAW scheme due to its lower numerical diffusion. This scheme was used in the blood-flow simulations discussed below.

To validate their code, Masson and Baliga (155) compared their predictions of fluid-phase flow rate and average solids volume fraction to those of Sinclair and Jackson (161). However, as discussed above, they claim to have specified the fluid-phase pressure drop, which does not seem possible given the results of Sinclair and Jackson. Since obtaining a unique solution required the specification of fluid-phase flow rate, we chose instead to compare predicted pressure drops to the specified value used by Masson and Baliga. We report our results in the same dimensionless variables used in both previous works (155, 161). These are the dimensionless volume flow rates, where $i = s$ for solid or f for fluid phase:

$$Q^{i*} = \frac{4}{d_T^2 v_t} \int_0^{d_T/2} \psi^i u_z^i 2\pi r \mathrm{d}r \qquad [55]$$

and the dimensionless fluid-phase pressure drop:

$$\frac{dp^{f*}}{dz^*} = \frac{1}{\rho^s g} \frac{dp^f}{dz} . \qquad [56]$$

We simulated five of the combinations of fluid- and solid-phase flow rates used in Masson and Baliga's work. All cases had the same dimensionless fluid-phase pressure drop, -0.2.

5.3.2 Blood Flow Simulations

After validating the multiphase flow code, we attempted to extend it to blood flow. Due to the limited time available, detailed parameter variation studies were not attempted. Rather, the basic model was applied "as-is" to two of the cases of fully-developed flow studied experimentally by Aarts *et al.* (53): suspensions of platelets with RBC ghosts at 20% hematocrit and platelets in an RBC-free buffer medium, both of which flowed at a wall shear rate of 240 s^{-1} through 3.0 mm diameter tubes. In the first case, flow of the RBC ghosts was simulated by

treating them as rigid spherical particles with an effective diameter of 5.5 μm and an average volume fraction of 0.2. In the second, the platelets were treated as 1.5 μm diameter spheres, with an estimated platelet concentration of 3×10^5 PLT μl^{-1}, corresponding to an average volume fraction of 0.00424. Both platelets and RBCs were treated as neutrally buoyant, with a density of 1.05 g cm^{-3}, equal to that of the suspending fluid, and the fluid-phase viscosity was set to the plasma value of 0.012 g cm^{-1} s^{-1}.

Both the model of Lun (157), which was the original one incorporated into Masson's code (156), and the Sinclair & Jackson model (161) used in the validation cases were applied to this problem. The only parameter alteration made was to the particle-particle coefficient of restitution, *e*, which exerts its influence via the parameter η (Equation 48). For both models, the same periodic formulation used for the validation cases, with fluid- and solid-phase mass flow rates specified, was employed. Flow rates of the two phases were estimated based on the total flow rates of the suspensions and the average solids volume fraction. All boundary conditions were identical to those used for the validation cases, including the specified wall fluxes given by Equations 52-54, with the specularity factor ϕ' and particle-wall restitution coefficient e_w left unaltered at 0.5 and 0.9, respectively. For the Sinclair and Jackson model, the expression for the drag force given by Equation 50, which is based on gravitational sedimentation, was replaced by the following expression selected from the review of Johnson *et al.* (158), which was derived for suspensions of multiple particles:

$$\zeta_D = \frac{9\mu^f}{2\rho^s \psi^s d_p^2} F_d; \qquad F_d = \frac{\psi^s \left\{ 4 + 3\left[\psi^s + \left(8\psi^s - 3\left(\psi^s\right)^2 \right)^{1/2} \right] \right\}}{\left(2 - 3\psi^s\right)^2}. \qquad [57]$$

Additionally, the effect of adding a lift force to the Sinclair and Jackson model was investigated. The expression used for the force of the solid phase on the fluid was the one given by Johnson *et al.* for the Saffman "slip-shear" lift:

$$\mathbf{F_L} = \frac{3(6.46)\rho^f \mu^f \psi^s}{2\pi d_p} \left(\mathrm{tr}\, \mathbf{D_f^2} \right)^{-1/4} \mathbf{D_f} \left(\mathbf{u^s} - \mathbf{u^f} \right), \qquad [58]$$

where "tr" denotes the trace of a matrix and $\mathbf{D_f}$ is the fluid-phase deformation rate tensor:

$$\mathbf{D_f} = \frac{1}{2}\left(\mathrm{grad}\, \mathbf{u^f} + \left(\mathrm{grad}\, \mathbf{u^f} \right)^{\mathrm{T}} \right). \qquad [59]$$

The forces represented by Equation 58 are added to the fluid-phase momentum equations; the negative of this term is added to the solid-phase momentum equations. This force was not incorporated into the Lun model because to do so correctly required incorporating the new interaction terms into the constitutive equations, which would have necessitated extremely complicated mathematical manipulations using the kinetic theory. Such work was deemed beyond the scope of this dissertation. All simulations were conducted on a grid containing three nodes in the *z*-direction (due to the periodic formulation), and 110 nodes in the *r*-direction. No grid dependence studies were conducted.

5.4 Results

5.4.1 Code Validation

Table 12 compares our model's predictions of non-dimensional fluid-phase pressure drop dp^{f*}/dz^{*} and average solid-phase volume fraction to the numerical results of Sinclair and Jackson (161) for the five test cases. The average value of ψ^{s} for case 5 was not reported by Sinclair and Jackson. The percentage errors reported are relative to Sinclair and Jackson's values. Identical results were obtained with either the MAW or PSI convection schemes. Additionally, our results were identical to those of Masson and Baliga to the number of significant figures shown, which is the degree of precision used by those authors. Our predictions also agree very closely with those of Sinclair and Jackson, with no error in the predicted pressure drop and a maximum error of 5.6% in the predicted average solids volume fraction. Since these results also matched those of Masson and Baliga (155), we took them as evidence that the code was functioning properly.

Table 12. Results of multiphase model validation cases

				Current Model		Sinclair & Jackson		% error	
Case	e	Q^{s*}	Q^{f*}	dp^{f*}/dz^{*}	Avg. ψ^{s}	dp^{f*}/dz^{*}	Avg. ψ^{s}	dp^{f*}/dz^{*}	Avg. ψ^{s}
1	1.00	0.34	4.4	-0.2	0.19	-0.2	0.18	0.00	5.56
2	1.00	0.04	1.7	-0.2	0.25	-0.2	0.25	0.00	0.00
3	1.00	-0.34	-0.022	-0.2	0.26	-0.2	0.25	0.00	4.00
4	1.00	-0.62	-0.61	-0.2	0.46	-0.2	0.46	0.00	0.00
5	0.99	-2.10	-2.83	-0.2	0.36	-0.2	--	0.00	--

Since fully-developed pipe flow is very similar to blood flow in a tube, it is of interest to observe the behavior of the model for some of these test cases. Figure 54 shows axial velocity and solids volume fraction profiles for Case 4, which is typical of the four cases for which e = 1.0. The velocity profiles are slightly blunted relative to a Newtonian parabolic profile, and due to the specified-shear-stress boundary conditions (Equations 52 and 53), both phases exhibit slip at the wall. The solids volume fraction is skewed to the wall, equal to approximately 0.4 near the core of the flow and rising to a maximum value of around 0.6 at the wall. Figure 55 shows the same profiles for Case 5, for which e = 0.99, corresponding to inelastic particle-particle collisions. Slightly more blunting of the velocity profile is observed, with both phases again slipping slightly at the wall. However, the solids volume fraction profile is nearly the reverse of Figure 54B, with values reaching very near the maximum packing fraction of 0.65 at the tube centerline, followed by a drop off and then a very slight secondary peak near the wall. The curves shown in these figures are essentially identical (when non-dimensionalized) in trend and magnitude to the plots shown by Masson (156) and Sinclair and Jackson (161) for these cases.

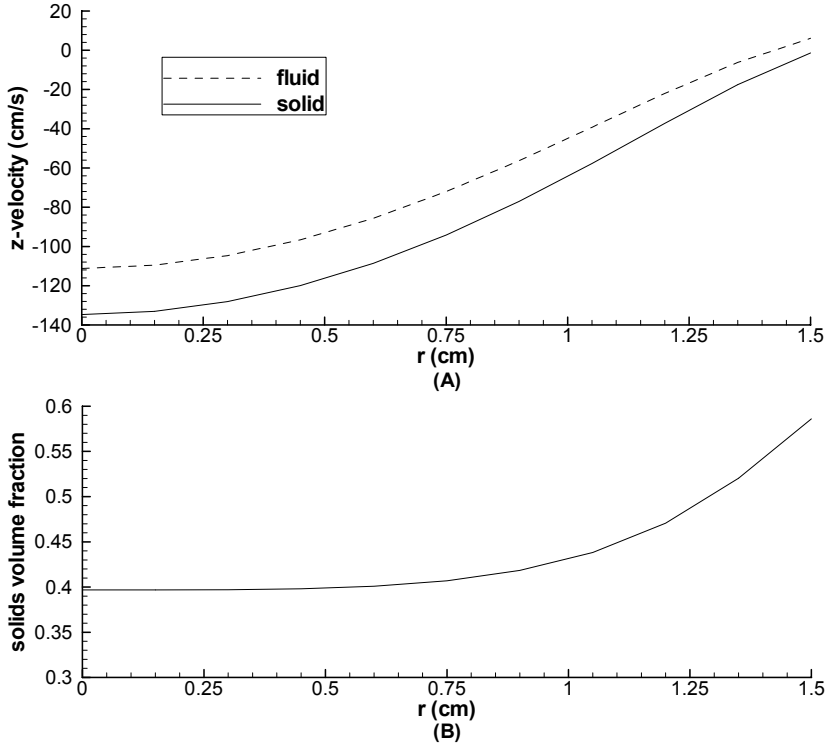

Figure 54. Results: multiphase validation Case 4

(A) Axial velocities. (B) Solids volume fraction.

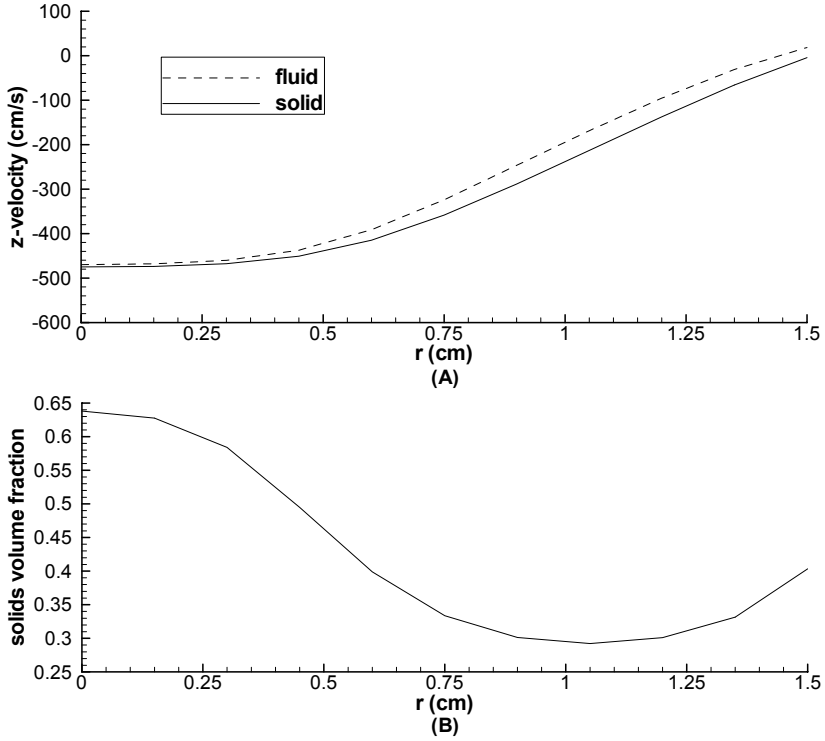

Figure 55. Results: multiphase validation Case 5

(A) Axial velocities. (B) Solids volume fraction.

5.4.2 Blood Flow Simulations

Due to the very long code-debugging process required (approximately one year), relatively little time was available to conduct these studies. Additionally, for most of the attempted simulations, it was very difficult to achieve convergence. Pseudo-time stepping relaxation parameters of the order 10^{-5} to 10^{-6} had to be employed, compared with typical values of order 1 for mass-transfer simulations. Because of this, several hundred thousand to a few million iterations were often required to reduce the residuals by as little as four to five orders of magnitude. Also, sometimes the residuals would stall and not converge further than a three- to four-order-of-magnitude reduction. Thus, no uniform convergence tolerance was employed, and many of the cases may not have achieved iteration independence. For these reasons, the results presented herein should be taken as very preliminary work, and the comparison to experiments as highly qualitative, rather than quantitative.

Based on the results observed for the validation cases, wherein a value of $e = 1.0$ tended to make particles accumulate near the wall (Figure 54) and a value of $e = 0.99$ tended to make them accumulate near the tube axis (Figure 55), a value of $e = 0.99$ was used for the RBC ghost suspension simulations, since the experimental results indicated RBC crowding near the axis. Attempts to use lower values of e were unsuccessful because the cases would not converge to a fully-developed, periodic steady state, i.e., the volume-fraction concentration profiles were not axially invariant. Figure 56 compares the predictions of particle volume fraction (equivalent to hematocrit) to the experimentally measured RBC ghost concentration profiles of Aarts *et al.* (53). In the figure, "S&J MODEL" refers to the Sinclair and Jackson model, while "+lift" indicates this model with the "slip-shear" lift force (Equation 58) added. The base Sinclair and Jackson model best reproduces the shape of the experimental curve, showing depletion of particles from the near-wall region and accumulation near the tube axis. Quantitatively, the degree of both depletion and accumulation are over-predicted. The effect of the lift force is to make the concentration profile essentially flat, except near the wall, where a smaller degree of depletion than observed without the lift force is observed. While the Lun model also predicts near-constant concentration over approximately 80% of the tube radius, it shows an accumulation of particles near the wall, the opposite of the experimentally observed behavior.

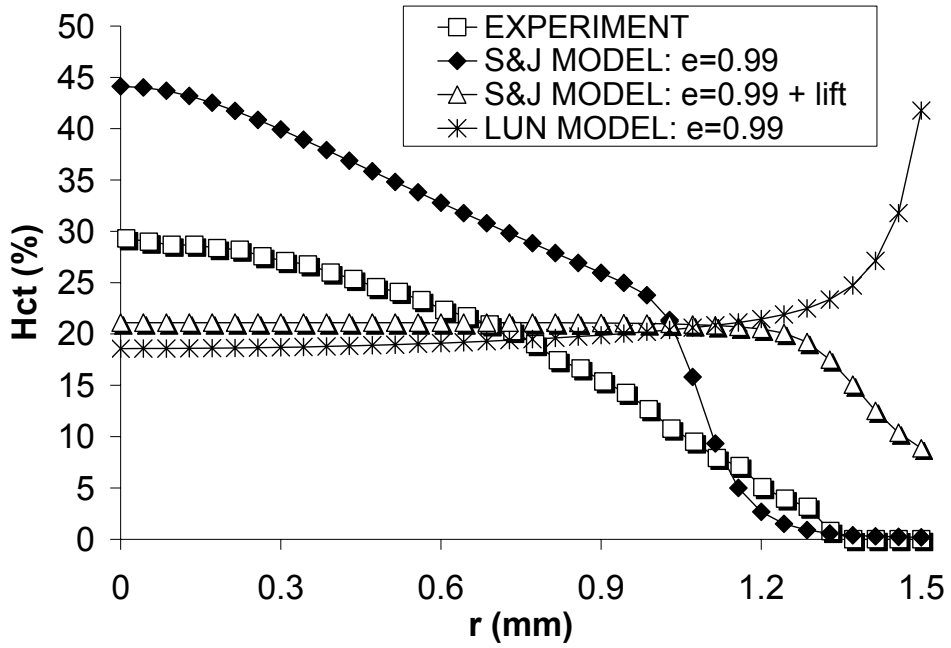

Figure 56. Comparison of experimental and predicted hematocrit: 20% Hct RBC ghost suspension, 240 s^{-1} wall shear rate

"S&J MODEL" refers to equations of Sinclair & Jackson (161). "+lift" refers to addition of lift force.

Figure 57 shows predicted velocity profiles for these cases, along with the single-phase Newtonian profile for this total flow rate. Solid-phase velocity profiles are shown; on the scale of the graph, fluid- and solid-phase profiles are indistinguishable for all three simulations. The Lun model yields a velocity profile very similar to the parabolic Newtonian profile; the specified-shear-stress wall BCs result in very little slip for this case. In contrast, the Sinclair and Jackson model predicts a much more blunted velocity profile, especially when the lift force is included. Also, very large slip velocities, between 4 and 6 cm s^{-1}, are observed at the wall. Attempts to use no-slip wall BCs for comparison were unsuccessful as the code could not be made to converge for these cases.

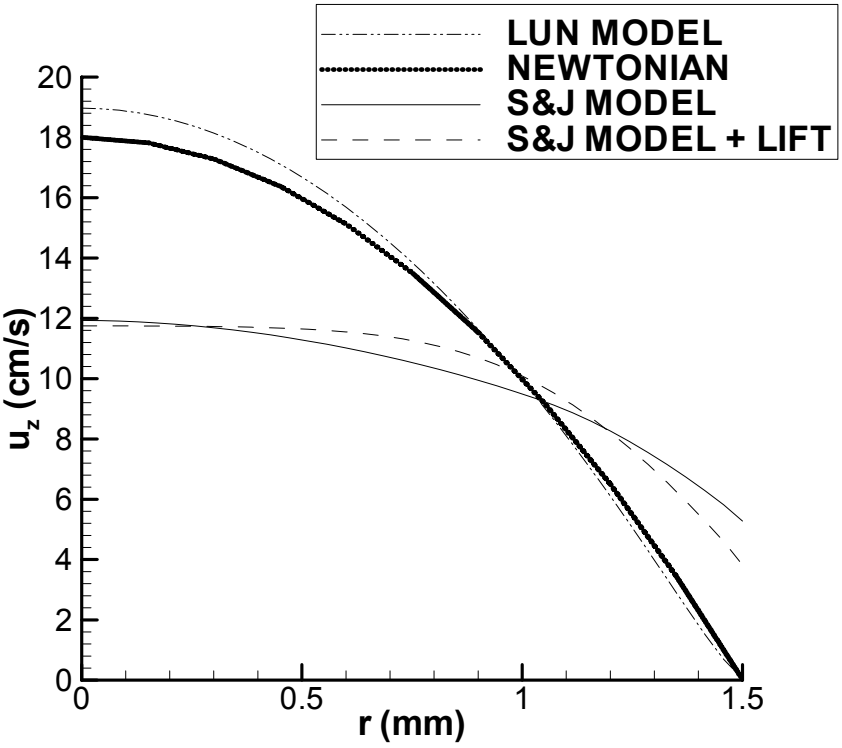

Figure 57. Simulated solid-phase and analytical single-phase Newtonian velocity profiles: 20% Hct RBC ghost suspension, 240 s^{-1} wall shear rate

"S&J MODEL" refers to equations of Sinclair & Jackson (161). "+LIFT" refers to addition of lift force.

Figure 58 shows the results for simulations of RBC-free platelet suspensions, along with the concentration profile measured by Aarts *et al.* (53) for a wall shear rate of 240 s^{-1}. Because the experimentally observed concentration peak occurred roughly midway between the wall and tube axis, simulations at both e = 0.99 and e = 1.0 were conducted. Unfortunately, achieving converged, periodic results was very difficult for these cases. Thus, the results shown are somewhat sporadic: for instance, at e = 1.0 the only case which converged was the Sinclair & Jackson model with lift included – neither the base model nor the Lun model would converge. As Figure 58A shows, neither restitution coefficient yields a concentration profile similar to the experimental one. Both yield a peak at the tube axis, and the model with e = 0.99 predicts a much greater excess than observed experimentally. In Figure 58B the results for the Lun model are shown; a relatively flat concentration profile with a sudden, very high peak at the tube wall is predicted, in very poor agreement with the data of Aarts *et al*.

Figure 59 shows the velocity profiles for these cases, along with the single-phase Newtonian profile for comparison. Again, only solid velocities are shown, since the solid and fluid curves are essentially identical. The velocity profile predicted by the Lun model is indistinguishable from the Newtonian profile, and the results for the two cases using Sinclair and Jackson's equations are identical. Both models yield velocity profiles with a parabolic shape, with the Sinclair and Jackson model displaying a less blunted profile than predicted for the RBC ghost cases. Similar to the results for the RBC ghost simulations, essentially no slip at the wall is observed for Lun's model, while the Sinclair and Jackson cases display very large slip velocities.

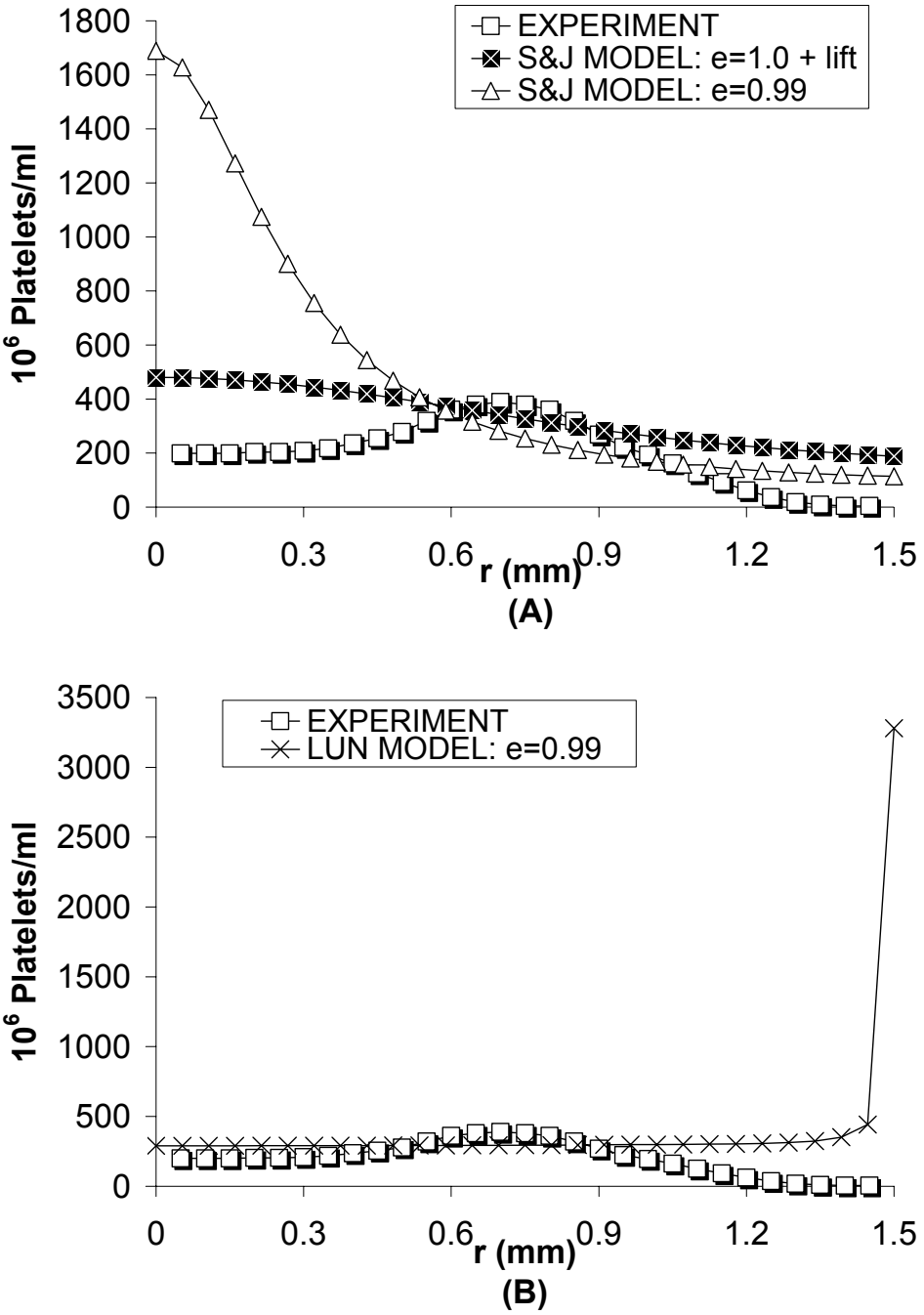

Figure 58. Comparison of experimental and predicted platelet concentration: RBC-free platelet suspension, 240 s^{-1} wall shear rate

(A) Sinclair & Jackson model. "+lift" refers to addition of lift force. (B) Lun model.

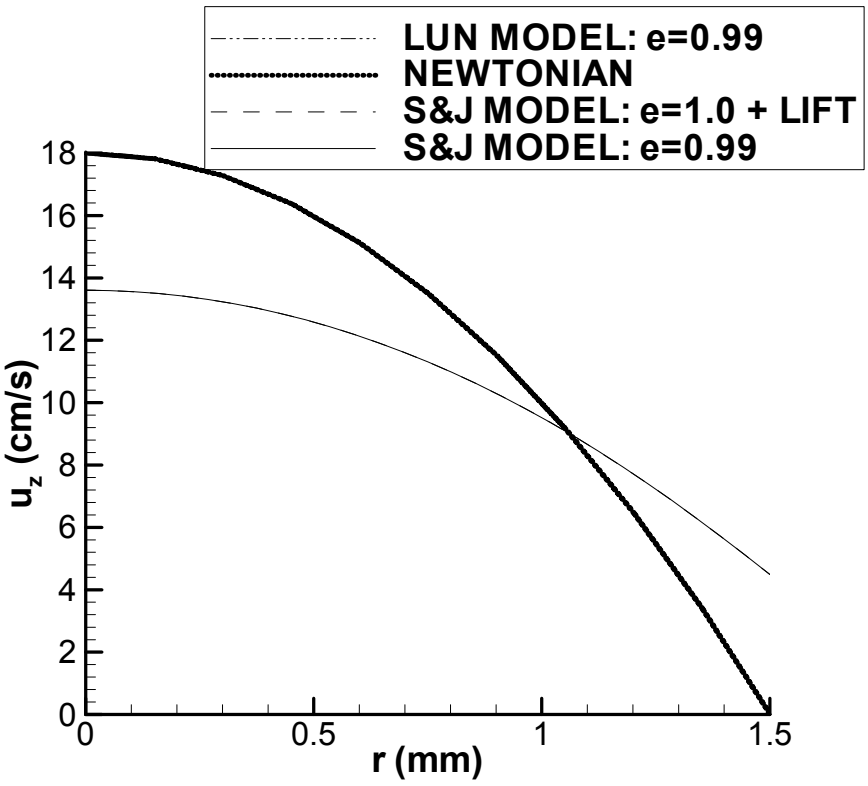

Figure 59. Simulated solid-phase and analytical single-phase Newtonian velocity profiles: RBC-free platelet suspension, 240 s^{-1} wall shear rate

"S&J MODEL" refers to equations of Sinclair & Jackson (161). "+LIFT" refers to addition of lift force.

5.5 Discussion and Conclusions

In general, these studies were severely hampered by convergence difficulties, yielding relatively few simulation results that could be reported. Overall, it appears the model of Sinclair and Jackson (161) is better suited to simulating the fully-developed tube flow cases considered in this chapter than is the model of Lun (157). The model of Sinclair and Jackson neglects the effect of interstitial fluid in deriving the solid-phase constitutive equations, while the Lun model incorporates such effects. For this reason, this result is contrary to what one would expect, as the presence of a liquid in a particle suspension should have a large effect on the particle-phase behavior.

For cases corresponding to flow of 20% Hct RBC ghosts, a particle-particle restitution coefficient of 0.99 and a model neglecting the lift force yields a profile qualitatively similar to the experimental data. This restitution coefficient corresponds to slightly inelastic particle collisions. One would expect collisions between gel-like red cells to be very inelastic, but attempts to use lower values of *e* failed to converge. The velocity profile for this case is also blunter than the parabolic Newtonian profile, in agreement with previously reported results for blood (128). However, the very large slip velocities computed for this model are not consistent with any known behavior of blood. As mentioned previously, cases with no-slip wall BCs failed to converge. Since the fluid-phase wall shear stress BC is based on a somewhat *ad hoc* derivation by Sinclair and Jackson for gas-solid flows in vertical pipes (161), it is likely not adequate for predicting liquid-particle flow. Investigating more accurate boundary conditions is left for future work.

For cases corresponding to RBC-free platelet suspensions, neither model agreed qualitatively or quantitatively with the experimental data. The models tend to predict concentration peaks either at the wall or at the tube axis, while the experimentally observed peak lies roughly halfway along the tube radius. It was somewhat surprising that the model failed for these cases, as the experimentally observed platelet behavior is similar to that of rigid spherical particles, as studied by Segre and Silberberg (148), who also measured concentration peaks at around 60% of the distance from tube axis to the wall. As discussed by Johnson et al. (158), this behavior has been attributed to inertial effects, which the "slip-shear" lift force attempts to mimic. Unfortunately, including this force in the Sinclair and Jackson model did not move the predicted concentration peak away from the tube axis. Again, this model predicts very large, probably unphysical, slip velocities at the tube wall, while the Lun model predicts essentially Newtonian behavior more consistent with a dilute suspension.

Clearly, there are several issues that bear investigation which the limited time for these studies precluded. First is the choice of the model itself. The model selected is designed for flows of rigid, spherical particles suspended in gas; one can therefore question its applicability to flows of highly deformable, discoid particles suspended in a viscous liquid. However, no Eulerian model which included particle deformation effects was available, and Lagrangian models are currently too computationally intensive. Ideally, if an Eulerian model is required, one specific to blood, or at least to deformable particles should be developed and experimentally validated.

Second is the issue of parameter sensitivity. Due to numerical difficulties, we were unable to test the model's sensitivity to variations in e. The maximum particle volume fraction was also left at the value of 0.65 used by Masson; one would expect deformable particles to be capable of tighter packing. Also of interest would be the effects of varying the specularity factor ϕ' and wall-particle coefficient of restitution e_w in the specified-wall-flux BCs (Equations 52-54), as this will influence the magnitude of the slip velocity and the degree of particle accumulation near the wall. Besides these parameter studies, the issue of boundary conditions in general needs to be addressed, as discussed above. It would also be useful to study the effects of additional interaction forces beyond the lift and drag terms included here. Next, there is the issue of numerical convergence and computational effort. Several hundred thousand iterations were often required to achieve a fairly modest three to four order-of-magnitude residual reduction. These case runs typically required two to four days on a relatively lightly loaded processor, for a steady-state simulation using only 330 nodes. Simulations on meshes such as those used in Chapter 4 (of the order of 80000 nodes) would clearly require extremely long computing times. In order to be used for simulations of platelet deposition in the presence of RBCs it would also be necessary to somehow model transport of both particulate species and their interactions. And if the platelets are allowed to deposit, this would require an unsteady solution of the multiphase model, which would very likely be prohibitively time-consuming.

In summary, it would appear these very crude preliminary studies raise more questions than they answer. The most encouraging result is the rough qualitative agreement between the Sinclair and Jackson model and the 20% Hct RBC ghost concentration profiles, which indicates that, with suitable parameter adjustment, this model may be capable of simulating RBC behavior in tube flow. It is hoped that this preliminary effort and these results will stimulate the development of more sophisticated, blood-specific multiphase models, as well as more rigorous testing and development of existing models, and that these can be used to eventually develop a thrombosis model capable of predicting platelet deposition in realistic medical device geometries.

6.0 CONCLUSION

"…I have not failed. I've just found 10,000 ways that won't work."

-Thomas Edison

6.1 Summary

The specific aims of this thesis were to develop and to validate a computational model of thrombosis, with the intent of eventually applying it to blood-contacting medical devices. In Chapter 1, background on the mechanisms of thrombosis, both arterial and venous, and on the state of the art in thrombosis modeling were discussed. Because most cardiovascular devices are placed in the arterial circulation, where platelet-mediated thrombi predominate, a model of platelet thrombosis, including platelet-surface and platelet-platelet adhesion, platelet activation, and agonist generation was developed and its sensitivity to key parameters analyzed in Chapter 2. This model is based on a single-continuum approximation, with resting and activated platelets and their agonists treated as dilute, dissolved species and blood modeled as a Newtonian fluid. The effect of thrombus growth on local flow patterns, as well as the embolizing effects of the flow on wall-bound aggregates, are neglected. Thus, there is no mechanical mechanism for limiting thrombus growth. Chapter 3 presented the results of using this model to simulate platelet deposition onto type I collagen from fully-developed parallel-plate Poiseuille flow. Encouraging results were obtained for both the "training" cases, in which the model parameters were estimated, and the "validation" cases, in which the model was extended to additional shear rates, perfusion times, and anticoagulation conditions. In general, good agreement in both the magnitude and shape of the predicted deposition curves was obtained. Especially encouraging was the model's ability to predict the different deposition curves measured in the presence of partial and complete thrombin inhibition without needing any parameter adjustment. However, for the case with the highest wall shear rate (1500 s^{-1}) and sodium citrate as the anticoagulant, the shape of the deposition curve could not be reproduced.

In Chapter 4, the validation studies were extended to cases of axisymmetric, disturbed flow, again over a collagen substrate. First, a tubular expansion case with no agonist effects was tested to probe the capabilities of the transport-related portions of the model. For these cases, the simulations were unable to accurately predict platelet deposition over the entire length of the tube, either in the presence or absence of RBCs. Typically, good agreement could be obtained in

the upstream recirculation zone, but not in the downstream, fully developed region, where the model predicts diffusion-limited behavior, but the experimental data appear reaction-limited. Surprisingly, the model's predictions in the absence of RBCs were poorer than those in the presence of RBCs at 20% Hct. Additionally, one set of parameters that gave an acceptable fit to both hematocrit levels could not be found; the platelet-surface reaction rate constants had to be treated as lumped parameters governing both RBC-enhanced transport and platelet deposition, which is contrary to our original intent. A further complication was the lack of grid independence observed for these cases, with deposition levels continually decreasing as the near-wall grid was refined. A second set of disturbed-flow test cases, in which non-anticoagulated baboon blood was perfused through a stenotic tube, was used to see if the agonist generation portions of the model would give it better predictive capabilities than the steady-state one-species model of Wootton (104), which had been previously applied to these experimental data. Unfortunately, the additional complexity of our model was not an asset, as our predictions were no better than those of Wootton. Furthermore, the computing time required for these cases approached greater than one month, calling into question the utility of our model's extra equations and unsteady formulation. For both models, platelet deposition was greatly under-predicted downstream of the stenosis, again likely due to deficiencies in the modeling of platelet transport. Thus, the key conclusion of these investigations was that the single-continuum model is inadequate for accurately simulating platelet transport in both the presence and absence of RBCs.

This led to the preliminary work presented in Chapter 5, in which attempts were made to simulate fully-developed tube flow of an RBC-free platelet suspension and of RBC ghost cells at 20% Hct using a multiphase flow model. These studies were hampered by the complexity of the model equations and associated computational costs, as well as the difficulty of obtaining converged solutions. Consequently it was impractical to perform parameter sensitivity studies. Although one model showed reasonable qualitative agreement with the experimentally measured RBC ghost concentration profile, more work in this area is clearly called for before the utility of such a model for blood-related applications can be established.

6.2 Contributions of the Thesis

The primary contribution of this thesis is the development of a thrombosis model which combines platelet transport, activation, and deposition, along with transport and generation of platelet-activating agonists. No previous work predicting agonist concentrations and platelet deposition in disturbed flow with comparisons to experimental results has been performed. Although we did not test our model on a wide range of biomaterials, it has been applied to a broader array of experimental deposition results, for both Poiseuille and disturbed flow, than any previous model. Furthermore, extensive sensitivity studies were carried out, and the model was compared to a simpler one developed by other investigators, providing guidance to those interested in developing improved thrombosis models. Our results for disturbed flow also emphatically illustrate the failure of the single-continuum mass transfer model, the basis for nearly all prior work in this area, to accurately model platelet transport. Finally, we applied multiphase flow modeling to blood flow simulations, going beyond previous efforts in this area, at least in terms of the complexity of the model applied.

6.3 Directions for Future Work

The results of the simulations in Chapters 4 and 5 clearly demonstrate that the main barrier to developing a useful, design-oriented thrombosis model is the lack of an accurate means of simulating platelet transport, both in the presence and absence of RBCs. Ideally, a model should be developed which is tailored specifically to the unique properties of blood, and this model should subsequently be validated against experimental data. Such a model would have to be capable of simulating both the dilute suspension behavior of platelets in RBC-free suspensions and the RBC-induced near-wall excess platelet concentrations caused by RBC migration to the tube axis. Given advances in computing power and the numerical difficulties encountered in the Eulerian model we employed, direct Lagrangian simulations of platelets and RBCs on a single-cell basis may be the best way to accomplish this, as interaction forces can be included easily, and complex derivations of solid-phase constitutive equations are unnecessary.

Given an accurate transport model, there are several additional improvements to the present thrombus deposition model that should be investigated. Chief among these is the lack of interaction between the flow field and the thrombus, i.e. flow disturbances due to thrombus growth and platelet embolization due to fluid forces. Incorporating these elements into the model

is necessary if one desires to predict thrombus stability. This is important from a design perspective because platelet deposition in and of itself may not be a deleterious event, as long as the thrombus which develops eventually stabilizes without occluding critical flow paths and passivates the device surface. Again, such simulations are better suited to a discrete-cell platelet model, since thrombus morphology would not have to be estimated, and embolization of single platelets or aggregates could be simulated much more easily than in an Eulerian framework.

An additional mechanical event that deserves consideration in future models is shear-induced platelet activation, as this event is relevant to cardiovascular devices such as replacement heart valves and rotary blood pumps. Since the level of activation appears to depend on stress level and exposure time, a Lagrangian approach is likely required, again emphasizing the value of a discrete-cell model. However, before such work can begin, the correlation between shear magnitude, exposure time, and level of activation needs to be rigorously experimentally quantified.

Given the sensitivity of the model to agonist generation, investigations of more sophisticated agonist generation and platelet activation source terms should also be performed. Since much more sophisticated coagulation cascade models have already been developed, the accuracy of the thrombin generation functions could be improved by utilizing these, with the downside of a large increase in computational complexity. Experimental validation of the model's prediction of agonist concentrations would also greatly aid in improving the agonist generation and synergism models.

In addition to refining the agonist generation functions, it would be desirable to improve the entire model by performing a rigorous sensitivity and uncertainty study on most, if not all, of its parameters, as discussed in Chapter 4. This might allow the model to be simplified by eliminating some unnecessary parameters. Coupling such a sensitivity analysis with an optimization-based parameter estimation algorithm would automate the parameter fitting process and eliminate the haphazard trial-and-error algorithm used for the cases presented herein. It may also be helpful to investigate dimensionless relationships between the parameters, as this might allow correlations to be developed that would further simplify the process of re-fitting the model when new cases are attempted.

Finally, only a single biomaterial, the highly thrombogenic type I collagen, has been studied in this dissertation. Once the aforementioned modeling issues are addressed, simulations of surfaces more relevant to medical devices should be performed. Since the kinetics of platelet-surface interaction for these surfaces will be different from those for collagen, these studies may reveal additional deficiencies in the model. It would also be desirable to have a way of predicting surface reactivity based on surface composition *a priori*, rather than needing to estimate it based on simulations. This would require further experimental work on platelet-surface interactions.

To summarize, then, there is much work to be done before computational thrombosis models will be mature enough to be used for device design. Hopefully this dissertation has contributed to a better understanding of the issues that need to be addressed, and has provided information that will aid in the development of such a mature model one day.

APPENDIX

APPENDIX

CFD Code Validation

This appendix gives results of two test cases used to validate the CFD solver. These cases were taken from the work of Demirdzic et al. (163), who published benchmark numerical solutions for several problems designed for non-orthogonal grids. The test cases we chose are for lid-driven cavity flow in a cavity with walls inclined 45º to the horizontal. Figure 60 shows the geometry and velocity boundary conditions; each side of the cavity has a length L = 1 cm. The dashed lines are the horizontal and vertical centerlines. Density ρ = 1 g cm^{-3}, and viscosity μ = 0.01 or 0.001 g cm^{-1} s^{-1} to give Reynolds numbers based on side length and lid velocity of 100 or 1000, respectively. Zero normal derivatives of pressure were specified at all walls; additionally, p = 0 dynes cm^{-2} was set in the lower left-hand corner.

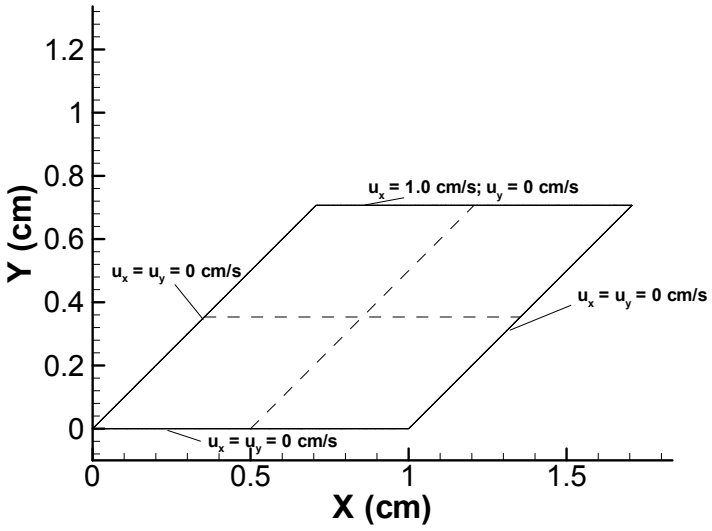

Figure 60. Geometry and velocity BCs for CFD validation cases

Steady-state solutions were obtained at both Reynolds numbers and compared to the benchmark results obtained by Demirdzic *et al.* (163) on their finest grid, which contained 960 × 960 (921600) quadrilateral control volumes. We used five levels of grid refinement: 403, 1631, 6532, 26345, and 50181 nodes. Solutions were considered converged when the normalized RMS residuals for the *x*- and *y*-momentum equations and for mass loss (obtained from the pressure correction equation) were all less than 10^{-10}. For the convection terms in the momentum equations, we used the second-order upwind scheme because of its high accuracy. This scheme was also used to obtain all the single-phase CFD results shown in the dissertation. It was not used for mass transfer or multiphase flow simulations because it can create non-physical negative species concentrations and solid-phase volume fractions. For simulations where strict positivity was required, the first-order-accurate PSI fluctuation-splitting scheme (135) was used.

Figure 61 shows streamlines at Re = 100 and 1000 for the solutions obtained on the 50181 node grid. At Re = 100, a large vortex fills most of the cavity, similar to lid-driven flow with orthogonal walls. However, due to the skewed walls, two smaller, counter-rotating vortices develop in the lower left-hand corner. At Re = 1000, the vortex created by the motion of the lid is squeezed into the upper right-hand corner, and a second large vortex fills the central region of the cavity. Again, two smaller vortices can be seen in the lower left-hand corner.

Figure 62 compares our predictions of u_x along the vertical centerline to the benchmark solution of Demirdzic *et al.* At Re = 100, our predictions are essentially grid-independent and identical to the benchmark solution, even on the very coarse 403 node grid. At Re = 1000, the results on the coarsest grid are quite different from the benchmark case, but agreement is excellent at all other levels of grid refinement.

Figure 63 is a comparison of our CFD solution for u_y along the horizontal centerline and the benchmark numerical results of Demirdzic *et al.* The results are basically identical to those observed for u_x, with good agreement for all grids at Re = 100 and poor agreement only on the 403 node grid at Re = 1000.

For the Re = 1000 case, Demirdzic *et al.* observed grid independence only once an 80 × 80 control-volume grid was used (coarser grids employed in that study contained 10 ×10, 20 × 20 and 40 × 40 control volumes). Thus, our solutions appear to attain grid independence more rapidly than the benchmark solutions, since we observed grid-independent behavior at 1631 nodes, corresponding roughly to Demirdzic's 40 × 40 quadrilateral grid. However, this may be

partially due to the convergence tolerance used, as Demirdzic *et al.* considered their solutions converged once values of the dependent variables stopped changing in the sixth decimal place, which they state typically corresponded to a six to eight order-of-magnitude reduction in the residuals (163). This tolerance is slightly lower than our 10 order-of-magnitude residual reduction tolerance. Nevertheless, given this strong grid independence and the excellent agreement of our CFD predictions with the numerical benchmark cases, we assumed the CFD code could be considered validated.

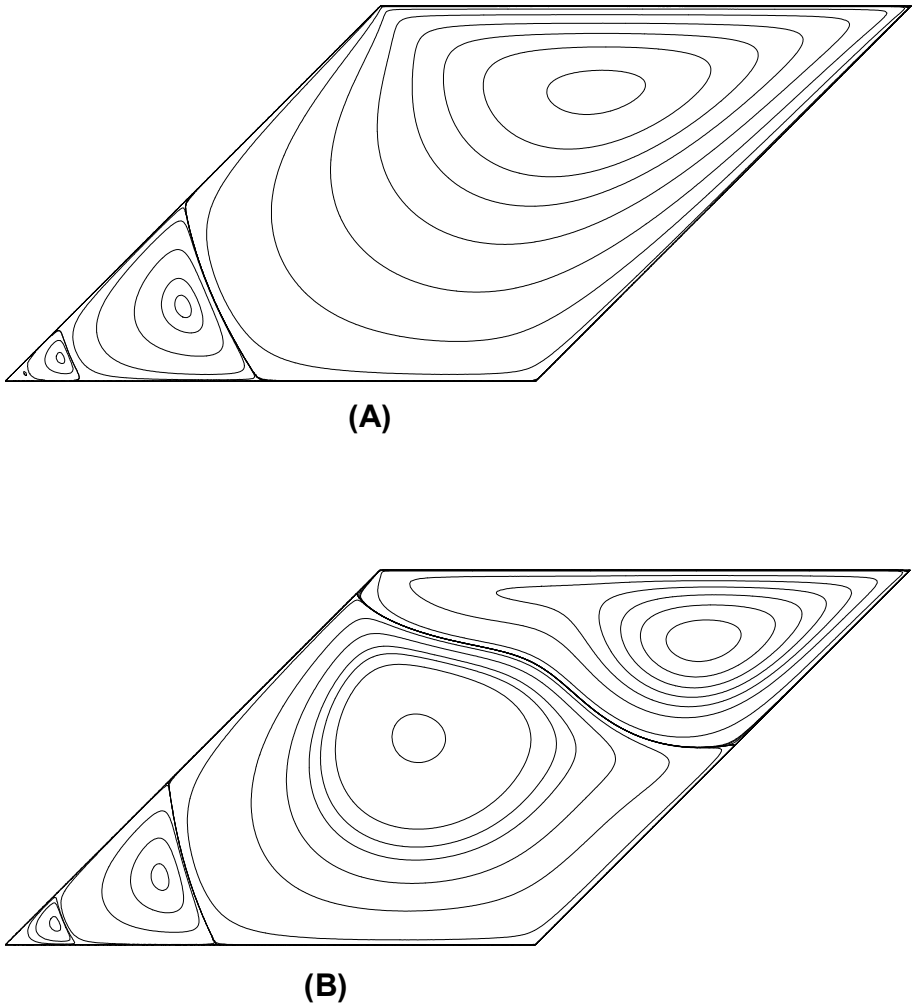

Figure 61. Streamline plots: CFD validation cases

(A) *Re* = 100. (B) *Re* = 1000.

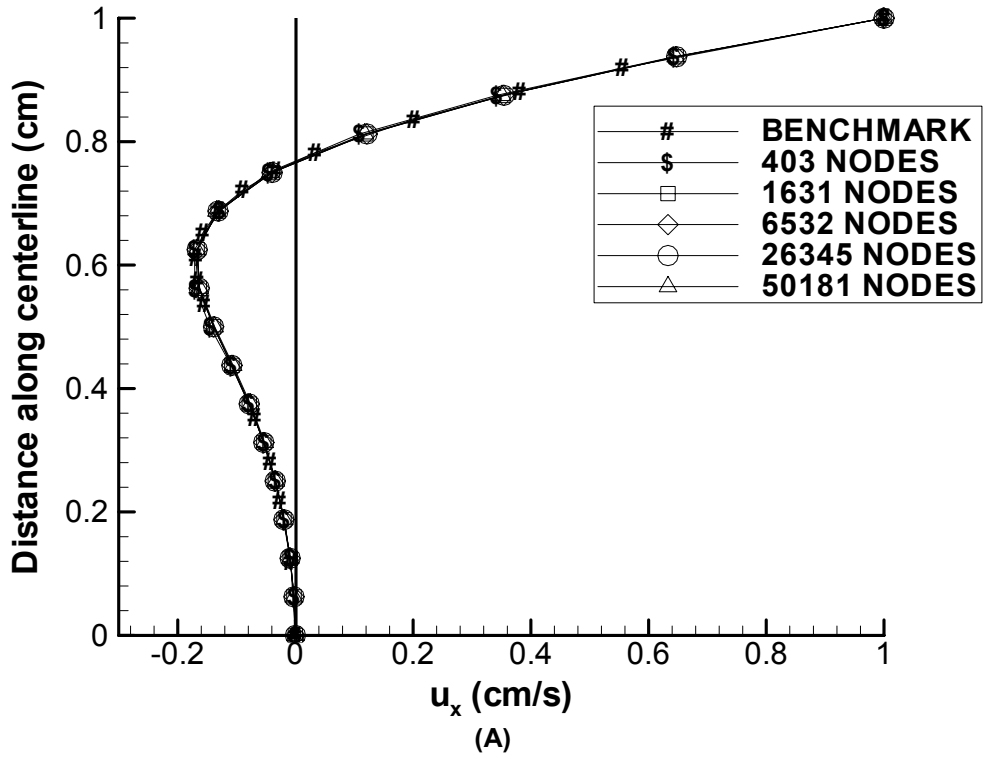

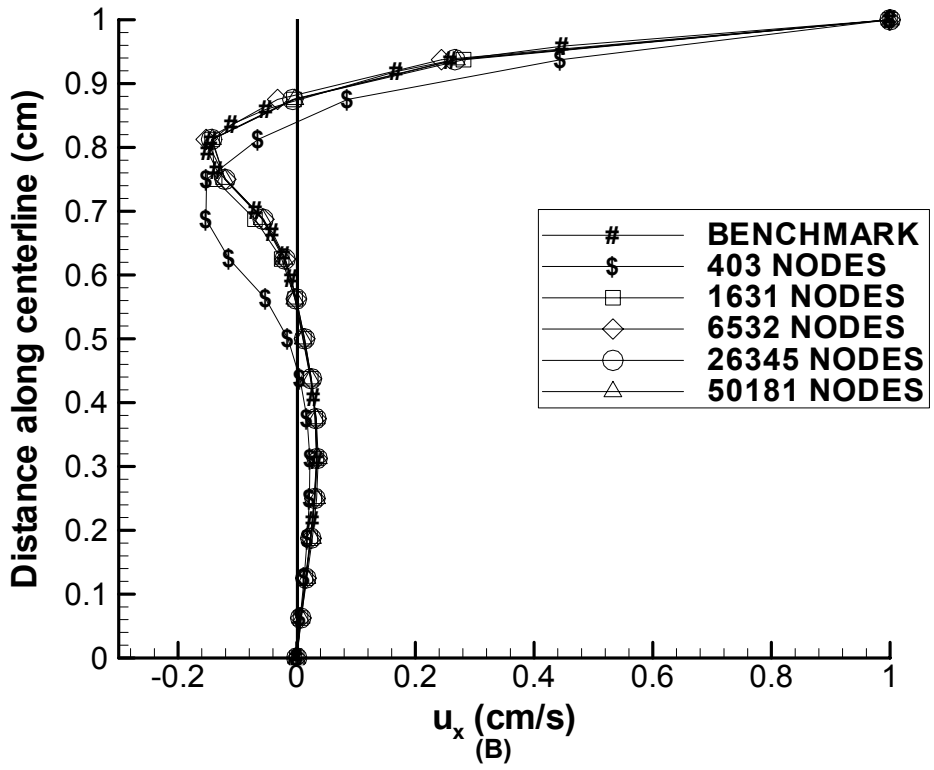

Figure 62. Velocity u_x along vertical centerline: CFD validation cases

(A) Re = 100. (B) Re = 1000.

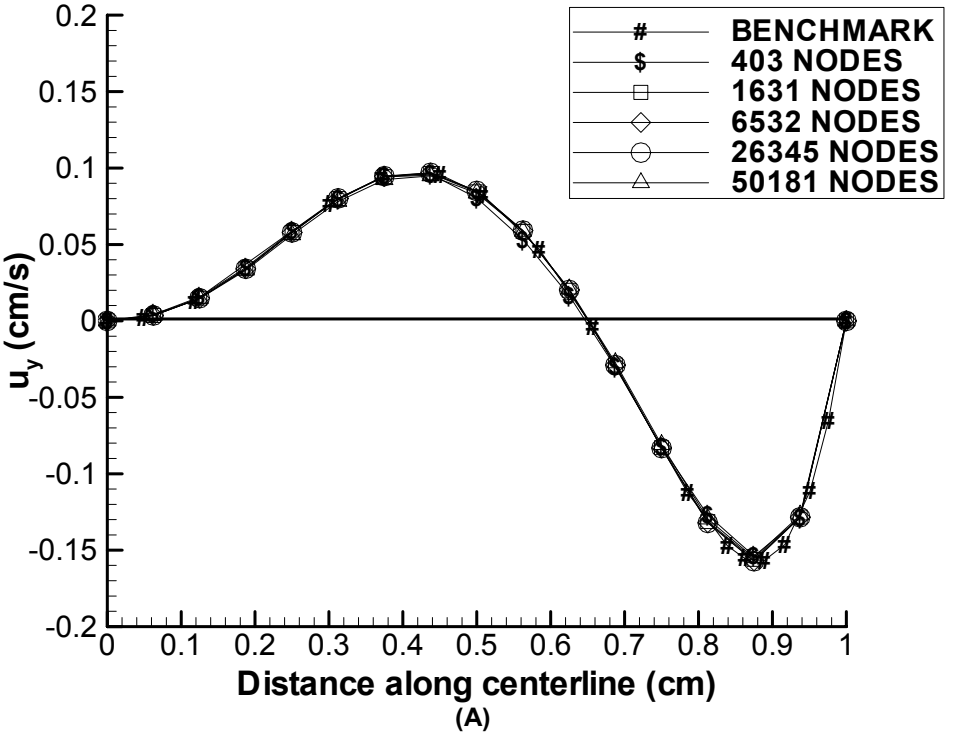

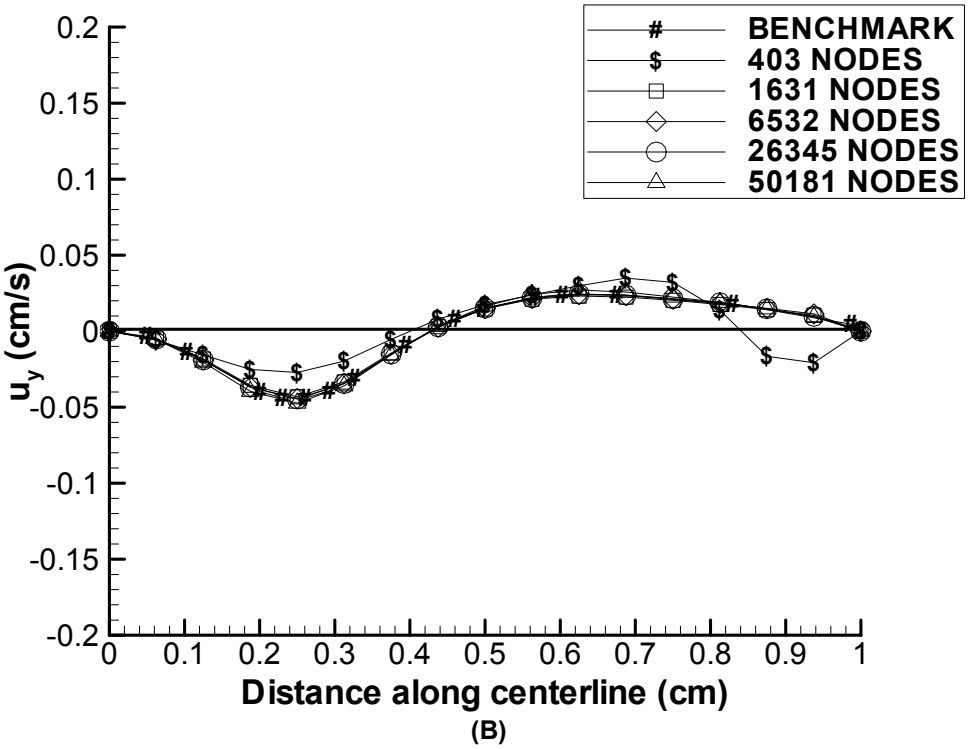

Figure 63. Velocity u_y along horizontal centerline: CFD validation cases

(A) Re = 100. (B) Re = 1000.

BIBLIOGRAPHY

BIBLIOGRAPHY

1. Hanson S.R. Device thrombosis and thromboembolism. *Cardiovasc. Pathol.* 1993;2:157S-165S.

2. Cutlip D.E. Stent thrombosis: historical perspectives and current trends. *J. Thromb. Thrombol.* 2000;10:89-101.

3. Heller L.I., Shemwell K.C., Hug K. Late stent thrombosis in the absence of prior intracoronary brachytherapy. *Cathet. Cardiovasc. Intervent.* 2001;53:23-28.

4. Wang F., Stouffer G.A., Waxman S., Uretsky B.F. Late coronary stent thrombosis: early vs. late stent thrombosis in the stent era. *Cathet. Cardiovasc. Intervent.* 2002;55:142-147.

5. Phillips S.J. Thrombogenic influence of biomaterials in patients with the Omni series heart valve: pyrolytic carbon versus titanium. *ASAIO J.* 2001;47:429-431.

6. Kvidal P., Bergstrom R., Malm T., Stahle E. Long-term follow-up of morbidity and mortality after aortic valve replacement with a mechanical valve prosthesis. *Eur. Heart J.* 2000;21:1099-1111.

7. Sun B.C., Catanese K.A., Spanier T.B., Flannery M.R., Gardocki M.T., Marcus L.S*., et al.* 100 Long-term implantable left ventricular assist devices: the Columbia Presbyterian interim experience. *Ann. Thorac. Surg.* 1999;68:688-694.

8. Schmid C., Wilhelm M., Rothenburger M., Nabavi D.G., Deng M.C., Hammel D*., et al.* Effect of high dose platelet inhibitor treatment on thromboembolism in Novacor patients. *Eur. J. Cardiothorac. Surg.* 2000;17:331-335.

9. Nerem R.M., Seliktar D. Vascular tissue engineering. *Annu. Rev. Biomed. Eng.* 2001;3:225-243.

10. Nishida H., Grooters R.K., Soltanzadeh H., Thiemen K.C., Schneider R.F. Clinical alternative bypass conduits and methods for surgical coronary revascularization. *Surg. Gynecol. Obstet.* 1991;172:161-174.

11. Virchow R. Gesammelte Abhandlungen zur Wissenschaftlichen Medizen. Frankfurt am Main: Meidinger U Comp, 1856.

12. Guyton A.C., Hall J.E. Textbook of Medical Physiology, 9th Edition. Chapter 36: Hemostasis and Blood Coagulation. Philadelphia: W.B. Saunders Co., 1996, 1148 pp.

13. Colman R.W., Cook J.J., Niewiarowski S. Mechanisms of platelet aggregation. In: Hemostasis and Thrombosis: Basic Principles and Clinical Practice, edited by Colman, R.W., Hirsh, J., Marder, V.J.*, et al.* Philadelphia: J.B. Lippincott Co., 1994.

14. Blockmans D., Deckmyn H., Vermylen J. Platelet activation. *Blood Rev.* 1995;9:143-156.

15. Zucker M.B., Nachmias V.T. Platelet activation. *Arteriosclerosis* 1985;5:2-18.

16. Peyrou V., Lormeau J.C., Herault J.P., Gaich C., Pfliegger A.M., Herbert J.M. Contribution of erythrocytes to thrombin generation in whole blood. *Thromb. Haemost.* 1999;81:400-406.

17. Alkhamis T.M., Beissinger R.L., Chediak J.R. Artificial surface effect on red blood cells and platelets in laminar shear flow. *Blood* 1990;75:1568-1575.

18. Hirsh J., Warkentin T.E., Shaughnessy S.G., Anand S.S., Halperin J.L., Raschke R.*, et al.* Heparin and low-molecular-weight heparin: mechanisms of action, pharmacokinetics, dosing, monitoring, efficacy, and safety. *Chest* 2001;119:64S-94S.

19. Hirsh J. Oral anticoagulant drugs. *N. Engl. J. Med.* 1991;324:1865-1873.

20. Stringer K.A., Lindenfeld J. Hirudins: antithrombin anticoagulants. *Ann. Pharmacother.* 1992;26:1535-1540.

21. Kettner C., Shaw E. D-Phe-Pro-ArgCH2C1-A selective affinity label for thrombin. *Thromb. Res.* 1979;14:969-973.

22. Hirsh J., Dalen J.E., Fuster V., Harker L.B., Patrono C., Roth G. Aspirin and other platelet-active drugs. The relationship among dose, effectiveness, and side effects. *Chest* 1995;108:247S-257S.

23. Zawilska K.M., Born G.V., Begent N.A. Effect of ADP-utilizing enzymes on the arterial bleeding time in rats and rabbits. *Br. J. Haematol.* 1982;50:317-325.

24. Del Campo G., Puente J., Valenzuela M.A., Traverso-Cori A., Cori O. Hydrolysis of synthetic pyrophosphoric esters by an isoenzyme of apyrase from Solanum tuberosum. *Biochem. J.* 1977;167:525-529.

25. Cattaneo M., Gachet C. ADP receptors and clinical bleeding disorders. *Arterioscler. Thromb. Vasc. Biol.* 1999;19:2281-2285.

26. Puri R.N., Colman R.W. ADP-induced platelet activation. *Crit. Rev. Biochem. Mol. Biol.* 1997;32:437-502.

27. Gresele P., Arnout J., Deckmyn H., Vermylen J. Mechanism of the antiplatelet action of dipyridamole in whole blood: modulation of adenosine concentration and activity. *Thromb. Haemost.* 1986;55:12-18.

28. Nurden A.T., Poujol C., Durrieu-Jais C., Nurden P. Platelet glycoprotein IIb/IIIa inhibitors: basic and clinical aspects. *Arterioscler. Thromb. Vasc. Biol.* 1999;19:2835-2840.

29. Jaffe E.A. Physiologic functions of normal endothelial cells. In: Vascular Medicine: A Textbook of Vascular Biology and Diseases, edited by Loscalzo, J. Boston: Little, Brown and Co., 1992, pp. 3-46.

30. Weiss H.J. Flow-related platelet deposition on subendothelium. *Thromb. Haemost.* 1995;74:117-122.

31. Brash J.L. The fate of fibrinogen following adsorption at the blood-biomaterial interface. *Ann. NY Acad. Sci.* 1987;516:206-222.

32. Horbett T.A. Principles underlying the role of adsorbed plasma proteins in blood interactions with foreign materials. *Cardiovasc. Pathol.* 1993;2:137S-148S.

33. Andrade J.A., Hlady V., Feng L., Tingey K. Proteins at interfaces: principles, problems, and potential. In: Interfacial Phenomena and Bioproducts, edited by Brash, J.L. and Wojciechowski, P. New York: Marcel Dekker, 1996, pp. 19-55.

34. Marchant R.E., Wang I. Physical and chemical aspects of biomaterials used in humans. In: Implantation Biology, edited by Greco, R.S. Boca Raton: CRC Press, 1994, pp. 13-38.

35. Bertrand O.F., Sipehia R., Mongrain R., Rodes J., Tardif J.C., Bilodeau L.*, et al.* Biocompatibility aspects of new stent technology. *J. Am. Coll. Cardiol.* 1998;32:562-571.

36. Slater J.P., Rose E.A., Levin H.R., Frazier O.H., Roberts J.K., Weinberg A.D.*, et al.* Low thromboembolic risk without anticoagulation using advanced-design left ventricular assist devices. *Ann. Thorac. Surg.* 1996;62:1321-1327; discussion 1328.

37. Rose E.A., Levin H.R., Oz M.C., Frazier O.H., Macmanus Q., Burton N.A.*, et al.* Artificial circulatory support with textured interior surfaces. A counterintuitive approach to minimizing thromboembolism. *Circulation* 1994;90:II87-91.

38. Lee H.B., Khang G., Lee J.H. Polymeric biomaterials. In: Biomedical Engineering Handbook, 2nd. Ed, edited by Bronzino, J.D. Boca Raton: CRC Press, 2000, pp. 39.31-39.23.

39. Merrill E.W. Distinctions and correspondences among surfaces contacting blood. *Ann. NY Acad. Sci.* 1987;516:196-203.

40. Suggs L.J., West J.L., Mikos A.G. Platelet adhesion on a bioresorbable poly(propylene fumarate-co-ethylene glycol) copolymer. *Biomaterials* 1999;20:683-690.

41. Deible C.R., Petrosko P., Johnson P.C., Beckman E.J., Russell A.J., Wagner W.R. Molecular barriers to biomaterial thrombosis by modification of surface proteins with polyethylene glycol. *Biomaterials* 1998;19:1885-1893.

42. Deible C.R., Petrosko P., Johnson P.C., Beckman E.J., Russell A.J., Wagner W.R. Molecular barriers to biomaterial thrombosis by modification of surface proteins with polyethylene glycol. *Biomaterials* 1999;20:101-109.

43. Wendel H.P., Ziemer G. Coating-techniques to improve the hemocompatibility of artificial devices used for extracorporeal circulation. *Eur. J. Cardiothorac. Surg.* 1999;16:342-350.

44. Phaneuf M.D., Berceli S.A., Bide M.J., Quist W.C., LoGerfo F.W. Covalent linkage of recombinant hirudin to poly(ethylene terephthalate) (Dacron): creation of a novel antithrombin surface. *Biomaterials* 1997;18:755-765.

45. Kishida A., Akatsuka Y., Yanagi M., Aikou T., Maruyama I., Akashi M. In vivo and ex vivo evaluation of the antithrombogenicity of human thrombomodulin immobilized biomaterials. *ASAIO J.* 1995;41:M369-374.

46. Phaneuf M.D., Quist W.C., Bide M.J., LoGerfo F.W. Modification of polyethylene terephthalate (Dacron) via denier reduction: effects on material tensile strength, weight, and protein binding capabilities. *J. Appl. Biomatls.* 1995;6:289-299.

47. Weitz J.I., Hirsh J. New anticoagulant drugs. *Chest* 2001;119:95S-107S.

48. Mann B.K., West J.L. Tissue engineering in the cardiovascular system: progress toward a tissue engineered heart. *Anat. Rec.* 2001;263:367-371.

49. Ratner B.D. The blood compatibility catastrophe [editorial]. *J. Biomed. Matls. Res.* 1993;27:283-287.

50. Haycox C.L., Ratner B.D. In vitro platelet interactions in whole human blood exposed to biomaterial surfaces: insights on blood compatibility. *J. Biomed. Matls. Res.* 1993;27:1181-1193.

51. Goldsmith H.L., Skalak R. Hemodynamics. *Annu. Rev. Fluid Mech.* 1975;7:213-247.

52. Barbee J.H., Cokelet G.R. The Fahraeus effect. *Microvasc. Res.* 1971;3:6-16.

53. Aarts P.A., van den Broek S.A., Prins G.W., Kuiken G.D., Sixma J.J., Heethaar R.M. Blood platelets are concentrated near the wall and red blood cells, in the center in flowing blood. *Arteriosclerosis* 1988;8:819-824.

54. Schultz J.S., Ciarkowski A., Goddard J.D., Lindenauer S.M., Penner J.A. Kinetics of thrombus formation. *ASAIO Trans.* 1976;21:269-277.

55. Antonini G., Guiffant G., Quemada D., Dosne A.M. Estimation of platelet diffusivity in flowing blood. *Biorheology* 1978;15:111-117.

56. Harker L.A., Slichter S.J. Arterial and venous thromboembolism: kinetic characterization and evaluation of therapy. *Thromb. Diath. Haemorrh.* 1974;31:188-203.

57. Slack S.M., Turitto V.T. Fluid dynamic and hemorheologic considerations. *Cardiovasc. Pathol.* 1993;2:11S-21S.

58. Reininger A.J., Heinzmann U., Reininger C.B., Friedrich P., Wurzinger L.J. Flow mediated fibrin thrombus formation in an endothelium-lined model of arterial branching. *Thromb. Res.* 1994;74:629-641.

59. Karino T., Goldsmith H.L. Adhesion of human platelets to collagen on the walls distal to a tubular expansion. *Microvasc. Res.* 1979;17:238-262.

60. Kroll M.H., Hellums J.D., McIntire L.V., Schafer A.I., Moake J.L. Platelets and shear stress [see comments]. *Blood* 1996;88:1525-1541.

61. Wurzinger L.J., Opitz R., Wolf M., Schmid-Schonbein H. "Shear induced platelet activation"--a critical reappraisal. *Biorheology* 1985;22:399-413.

62. Weiss H.J., Lages B., Hoffmann T., Turitto V.T. Correction of the platelet adhesion defect in delta-storage pool deficiency at elevated hematocrit--possible role of adenosine diphosphate. *Blood* 1996;87:4214-4222.

63. Hellums J.D. 1993 Whitaker Lecture: biorheology in thrombosis research. *Ann. Biomed. Eng.* 1994;22:445-455.

64. Savage B., Saldivar E., Ruggeri Z.M. Initiation of platelet adhesion by arrest onto fibrinogen or translocation on von Willebrand factor. *Cell* 1996;84:289-297.

65. Savage B., Almus-Jacobs F., Ruggeri Z.M. Specific synergy of multiple substrate-receptor interactions in platelet thrombus formation under flow. *Cell* 1998;94:657-666.

66. Basmadjian D. The hemodynamic and embolizing forces acting on thrombi--II. The effect of pulsatile blood flow. *J. Biomech.* 1986;19:837-845.

67. Basmadjian D. The hemodynamic forces acting on thrombi, from incipient attachment of single cells to maturity and embolization. *J. Biomech.* 1984;17:287-298.

68. Basmadjian D. Embolization: critical thrombus height, shear rates, and pulsatility. Patency of blood vessels. *J. Biomed. Matls. Res.* 1989;23:1315-1326.

69. Wilson R.S., Marmur A., Cooper S.L. A model of deposition and embolization of proteins and platelets on biomaterial surfaces. *Ann. Biomed. Eng.* 1986;14:383-400.

70. Goodman P.D., Hall M.W., Sukavaneshvar S., Solen K.A. In vitro model for studying the effects of hemodynamics on device induced thromboembolism in human blood. *ASAIO J* 2000;46:576-578.

71. Sorensen E.N., Burgreen G.W., Wagner W.R., Antaki J.F. Computational simulation of platelet deposition and activation: I. Model development and properties. *Ann. Biomed. Eng.* 1999;27:436-448.

72. Basmadjian D. The effect of flow and mass transport in thrombogenesis. *Ann. Biomed. Eng.* 1990;18:685-709.

73. Grabowski E.F., Friedman L.I., Leonard E.F. Effects of shear rate on the diffusion and adhesion of blood platelets to a foreign surface. *Ind. Eng. Chem. Fundam.* 1972;11:224-232.

74. Leonard E.F., Grabowski E.F., Turitto V.T. The role of convection and diffusion in platelet adhesion and aggregation. *Ann. NY Acad. Sci.* 1972;201:329-342.

75. Stubley G.D., Strong A.B., Hale W.E., Absolom D.R. A review of mathematical models for the prediction of blood cell adhesion. *PhysicoChem. Hydrodyn.* 1987;8:221-235.

76. Turitto V.T., Baumgartner H.R. Platelet deposition on subendothelium exposed to flowing blood: mathematical analysis of physical parameters. *ASAIO Trans.* 1975;21:593-601.

77. Zydney A.L., Colton C.K. Augmented solute transport in the shear flow of a concentrated suspension. *PhysicoChem. Hydrodyn.* 1988;10:79-96.

78. Keller K.H. Effect of fluid shear on mass transport in flowing blood. *Fed. Proc.* 1971;30:1591-1599.

79. Eckstein E.C., Belgacem F. Model of platelet transport in flowing blood with drift and diffusion terms. *Biophys. J.* 1991;60:53-69.

80. Yeh C., Calvez A.C., Eckstein E.C. An estimated shape function for drift in a platelet-transport model. *Biophys. J.* 1994;67:1252-1259.

81. Buchanan J.R., Jr., Kleinstreuer C. Simulation of patricle-hemodynamics in a partially occluded artery segment with implications to the initiation of microemboli and secondary stenoses. *J. Biomech. Eng.* 1998;120:446-454.

82. Zarnitsina V.I., Pokhilko A.V., Ataullakhanov F.I. A mathematical model for the spatio-temporal dynamics of intrinsic pathway of blood coagulation. I. The model description. *Thromb. Res.* 1996;84:225-236.

83. Khanin M.A., Leytin V.L., Popov A.P. A mathematical model of the kinetics of platelets and plasma hemostasis system interaction. *Thromb. Res.* 1991;64:659-666.

84. Gregory K., Basmadjian D. An analysis of the contact phase of blood coagulation: effects of shear rate and surface are intertwined. *Ann. Biomed. Eng.* 1994;22:184-193.

85. Pokhilko A.V., Ataullakhanov F.I. Contact activation of blood coagulation: trigger properties and hysteresis. Kinetic recognition of foreign surfaces upon contact activation of blood coagulation: a hypothesis. *J. Theor. Biol.* 1998;191:213-219.

86. Baumann P., Heuck C.C. Simulation of the extrinsic pathway of the plasmatic clotting system. *Haemostasis* 1991;21:329-337.

87. Khanin M.A., Rakov D.V., Kogan A.E. Mathematical model for the blood coagulation prothrombin time test. *Thromb. Res.* 1998;89:227-232.

88. Kuharsky A.L., Fogelson A.L. Surface-mediated control of blood coagulation: the role of binding site densities and platelet deposition. *Biophys. J.* 2001;80:1050-1074.

89. Pohl B., Beringer C., Bomhard M., Keller F. The quick machine--a mathematical model for the extrinsic activation of coagulation. *Haemostasis* 1994;24:325-337.

90. Gir S., Slack S.M., Turitto V.T. A numerical analysis of factor X activation in the presence of tissue factor-factor VIIa complex in a flow reactor. *Ann. Biomed. Eng.* 1996;24:394-399.

91. Willems G.M., Lindhout T., Hermens W.T., Hemker H.C. Simulation model for thrombin generation in plasma. *Haemostasis* 1991;21:197-207.

92. Basmadjian D., Sefton M.V. A model of thrombin inactivation in heparinized and nonheparinized tubes with consequences for thrombus formation. *J. Biomed. Matls. Res.* 1986;20:633-651.

93. Chung T.W., O'Rear E.A. A model for analyzing the formation of thrombin in vessels. *Computers Biol. Med.* 1994;24:31-41.

94. Adams G.A., Feuerstein I.A. Platelet adhesion and release: interfacial concentration of released materials. *Am. J. Physiol.* 1981;240:H99-108.

95. Adams G.A., Feuerstein I.A. Maximum fluid concentrations of materials released from platelets at a surface. *Am. J. Physiol.* 1983;244:H109-114.

96. Fogelson A.L., Wang N.T. Platelet dense-granule centralization and the persistence of ADP secretion. *Am. J. Physiol.* 1996;270:H1131-1140.

97. Folie B.J., McIntire L.V. Mathematical analysis of mural thrombogenesis. Concentration profiles of platelet-activating agents and effects of viscous shear flow. *Biophys. J.* 1989;56:1121-1141.

98. Hubbell J.A., McIntire L.V. Platelet active concentration profiles near growing thrombi. A mathematical consideration. *Biophys. J.* 1986;50:937-945.

99. Strong A.B., Stubley G.D., Chang G., Absolom D.R. Theoretical and experimental analysis of cellular adhesion to polymer surfaces. *J. Biomed. Matls. Res.* 1987;21:1039-1055.

100. Badimon L., Badimon J.J. Mechanisms of arterial thrombosis in nonparallel streamlines: platelet thrombi grow on the apex of stenotic severely injured vessel wall. Experimental study in the pig model. *J. Clin. Invest.* 1989;84:1134-1144.

101. Schoephoerster R.T., Oynes F., Nunez G., Kapadvanjwala M., Dewanjee M.K. Effects of local geometry and fluid dynamics on regional platelet deposition on artificial surfaces. *Arterioscler. Thromb.* 1993;13:1806-1813.

102. Wagner W.R., Hubbell J.A. Local thrombin synthesis and fibrin formation in an in vitro thrombosis model result in platelet recruitment and thrombus stabilization on collagen in heparinized blood. *J. Lab. Clin. Med.* 1990;116:636-650.

103. David T., Thomas S., Walker P.G. Platelet deposition in stagnation point flow: an analytical and computational simulation. *Med. Eng. Phys.* 2001;23:299-312.

104. Wootton D.M., Markou C.P., Hanson S.R., Ku D.N. A mechanistic model of acute platelet accumulation in thrombogenic stenoses. *Ann. Biomed. Eng.* 2001;29:321-329.

105. Fogelson A.L. Continuum models of platelet aggregation: formulation and mechanical properties. *SIAM J. Appl. Math.* 1992;52:1089-1110.

106. Fogelson A.L. A mathematical model and numerical method for studying platelet adhesion and aggregation during blood clotting. *J. Comp. Phys.* 1984;56:111-134.

107. Parmentier E.M., Morton W.A., Petschek H.E. Platelet aggregate formation in a region of separated blood flow. *Phys. Fluids* 1977;20:2012-2021.

108. Gartner M.J., Wilhelm C.R., Gage K.L., Fabrizio M.C., Wagner W.R. Modeling flow effects on thrombotic deposition in a membrane oxygenator. *Artif. Org.* 2000;24:29-36.

109. Bluestein D., Gutierrez C., Londono M., Schoephoerster R.T. Vortex shedding in steady flow through a model of an arterial stenosis and its relevance to mural platelet deposition. *Ann. Biomed. Eng.* 1999;27:763-773.

110. Bluestein D., Rambod E., Gharib M. Vortex shedding as a mechanism for free emboli formation in mechanical heart valves. *J. Biomech. Eng.* 2000;122:125-134.

111. Stein P.D., Sabbah H.N. Measured turbulence and its effect on thrombus formation. *Circ. Res.* 1974;35:608-614.

112. Bluestein D., Niu L., Schoephoerster R.T., Dewanjee M.K. Fluid mechanics of arterial stenosis: relationship to the development of mural thrombus. *Ann. Biomed. Eng.* 1997;25:344-356.

113. Griffith M.J. The heparin-enhanced antithrombin III/thrombin reaction is saturable with respect to both thrombin and antithrombin III. *J. Biol. Chem.* 1982;257:13899-13902.

114. Griffith M.J. Kinetics of the heparin-enhanced antithrombin III/thrombin reaction. Evidence for a template model for the mechanism of action of heparin. *J. Biol. Chem.* 1982;257:7360-7365.

115. Ware J.A., Smith M., Salzman E.W. Synergism of platelet-aggregating agents. Role of elevation of cytoplasmic calcium. *J. Clin. Invest.* 1987;80:267-271.

116. Huang E.M., Detwiler T.C. Characteristics of the synergistic actions of platelet agonists. *Blood* 1981;57:685-691.

117. Frojmovic M., Wong T., van de Ven T. Dynamic measurements of the platelet membrane glycoprotein IIb-IIIa receptor for fibrinogen by flow cytometry. I. Methodology, theory and results for two distinct activators. *Biophys. J.* 1991;59:815-827.

118. Frojmovic M.M., Mooney R.F., Wong T. Dynamics of platelet glycoprotein IIb-IIIa receptor expression and fibrinogen binding. II. Quantal activation parallels platelet capture in stir-associated microaggregation. *Biophys. J.* 1994;67:2069-2075.

119. Rosing J., van Rijn J.L., Bevers E.M., van Dieijen G., Comfurius P., Zwaal R.F. The role of activated human platelets in prothrombin and factor X activation. *Blood* 1985;65:319-332.

120. Rosenberg R.D. Heparin-antithrombin system. In: Hemostasis and Thrombosis: Basic Principles and Clinical Practice, edited by Colman, R.W., Hirsh, J., Marder, V.J., *et al.* Philadelphia: J.B. Lippincott Co., 1982, pp. 962-985.

121. Munter W.A., Stein P.D. Newtonian behavior of blood at high rates of shear. *Biorheology* 1973;10:501-508.

122. Batchelor G.K. An Introduction to Fluid Dynamics. Cambridge: Cambridge University Press, 1967, 615 pp.

123. Matzdorff A.C., Kemkes-Matthes B., Voss R., Pralle H. Comparison of beta-thromboglobulin, flow cytometry, and platelet aggregometry to study platelet activation. *Haemostasis* 1996;26:98-106.

124. Langford E.J., Wainwright R.J., Martin J.F. Platelet activation in acute myocardial infarction and unstable angina is inhibited by nitric oxide donors. *Arterioscler. Thromb. Vasc. Biol.* 1996;16:51-55.

125. Kennedy S.D., Igarashi Y., Kickler T.S. Measurement of in-vitro P-selectin expression by flow cytometry. *Am. J. Clin. Pathol.* 1997;107:99-104.

126. Zydney A.L., Colton C.K. Continuous flow membrane plasmapheresis: theoretical models for flux and hemolysis predictions. *ASAIO Trans.* 1982;28:408-412.

127. Wagner W.R. Biochemical and biophysical mechanisms of mural thrombosis on natural surfaces. Ph.D. Thesis, Chemical Engineering. Austin: University of Texas, 1991.

128. Goldsmith H.L., Turitto V.T. Rheological aspects of thrombosis and haemostasis: basic principles and applications. ICTH-Report--Subcommittee on Rheology of the International Committee on Thrombosis and Haemostasis. *Thromb. Haemost.* 1986;55:415-435.

129. Weiss H.J. Platelets: Pathophysiology and Antiplatelet Drug Therapy. New York: Alan R. Liss, Inc., 1982, 165 pp.

130. Jones R.L., Wilson N.H., Marr C.G. Thromboxane-like activity of prostanoids with aromatic substituents at C16 and C17. In: Chemistry, Biochemistry, and Pharmacological Activity of Prostanoids, edited by Roberts, S.M. and Scheinmann, F. Oxford: Pergamon Press, 1979, pp. 210-220.

131. Frojmovic M.M., Mooney R.F., Wong T. Dynamics of platelet glycoprotein IIb-IIIa receptor expression and fibrinogen binding. I. Quantal activation of platelet subpopulations varies with adenosine diphosphate concentration. *Biophys. J.* 1994;67:2060-2068.

132. Skarja G.A., Kinlough-Rathbone R.L., Perry D.W., Rubens F.D., Brash J.L. A cone-and-plate device for the investigation of platelet biomaterial interactions. *J. Biomed. Matls. Res.* 1997;34:427-438.

133. Grunkemeier J.M., Tsai W.B., Horbett T.A. Hemocompatibility of treated polystyrene substrates: contact activation, platelet adhesion, and procoagulant activity of adherent platelets. *J. Biomed. Matls. Res.* 1998;41:657-670.

134. Anderson W.K., Bonhaus D.L. An implicit upwind algorithm for computing turbulent flows on unstructured grids. *Computers Fluids* 1994;23:1-21.

135. Struijs R., Deconinck H., Roe P.L. Fluctuation splitting for multidimensional convection problems: an alternative to finite volume and finite element methods. In: Comput. Fluid Dyn., Von Karman Institute for Fluid Dynamics, Lecture Series 1990-03, 1990.

136. Weiss J.M., Smith W.A. Preconditioning applied to variable and constant density time-accurate flows on unstructured meshes. *AIAA Paper 94-2209* 1994.

137. Sorensen E.N., Burgreen G.W., Wagner W.R., Antaki J.F. Computational simulation of platelet deposition and activation: II. Results for Poiseuille flow over collagen. *Ann. Biomed. Eng.* 1999;27:449-458.

138. Hubbell J.A., McIntire L.V. Visualization and analysis of mural thrombogenesis on collagen, polyurethane and nylon. *Biomaterials* 1986;7:354-363.

139. Alevriadou B.R., Moake J.L., Turner N.A., Ruggeri Z.M., Folie B.J., Phillips M.D*., et al.* Real-time analysis of shear-dependent thrombus formation and its blockade by inhibitors of von Willebrand factor binding to platelets. *Blood* 1993;81:1263-1276.

140. Sakariassen K.S., Baumgartner H.R. Axial dependence of platelet-collagen interactions in flowing blood. Upstream thrombus growth impairs downstream platelet adhesion. *Arteriosclerosis* 1989;9:33-42.

141. Turner N.A., Moake J.L., Kamat S.G., Schafer A.I., Kleiman N.S., Jordan R.*, et al.* Comparative real-time effects on platelet adhesion and aggregation under flowing conditions of in vivo aspirin, heparin, and monoclonal antibody fragment against glycoprotein IIb-IIIa. *Circulation* 1995;91:1354-1362.

142. Wagner W.R., Hubbell J.A. Evidence for a role in thrombus stabilization for thromboxane A2 in human platelet deposition on collagen. *J. Lab. Clin. Med.* 1992;119:690-697.

143. Prakash C., Patankar S.V. A control volume-based finite-element method for solving the Navier-Stokes equations using equal-order velocity-pressure interpolation. *Numer. Heat Transfer* 1985;8:259-280.

144. Ruge J.W., Stuben K. Algebraic multigrid. In: Multigrid Methods, edited by McCormick, S.F. Philadelphia: SIAM, 1987, pp. 73-130.

145. Masson C., Saabas H.J., Baliga B.R. Co-located equal-order control-volume finite element method for two-dimensional axisymmetric incompressible fluid flow. *Int. J. Num. Meth. Fluids* 1994;18:1-26.

146. Grabowski E.F., Didisheim P., Lewis J.C., Franta J.T., Stropp J.Q. Platelet adhesion to foreign surfaces under controlled conditions of whole blood flow: human vs rabbit, dog, calf, sheep, pig, macaque, and baboon. *ASAIO Trans.* 1977;23:141-151.

147. Schneider P.A., Kotze H.F., Heyns A.D., Hanson S.R. Thromboembolic potential of synthetic vascular grafts in baboons. *J. Vasc. Surg.* 1989;10:75-82.

148. Segre G., Silberberg A. Behaviour of macroscopic rigid spheres in Poiseuille flow: Part 2. Experimental results and interpretation. *J. Fluid. Mech.* 1962;14:136-157.

149. Leighton D., Acrivos A. The shear-induced migration of particles in concentrated suspensions. *J. Fluid. Mech.* 1987;181:415-439.

150. Brown C.H.d., Leverett L.B., Lewis C.W., Alfrey C.P., Jr., Hellums J.D. Morphological, biochemical, and functional changes in human platelets subjected to shear stress. *J. Lab. Clin. Med.* 1975;86:462-471.

151. Boggs P.T., Byrd R.H., Rogers J.E., Schnabel R.B. User's reference guide for ODRPACK version 2.01 -- software for weighted orthogonal distance regression. *NIST IR 4834, U.S. Government Printing Office,* 1992.

152. Malcevic I. A parallel dynamic-mesh Lagrangian method for Navier-Stokes flows with deformable boundaries. Ph.D. Thesis, Civil and Environmental Engineering. Pittsburgh: Carnegie Mellon University, 2001.

153. Hofer M., Perktold K. Computer simulation of concentrated fluid-particle suspension flows in axisymmetric geometries. *Biorheology* 1997;34:261-279.

154. Phillips R.J., Armstrong R.C., Brown R.A. A constitutive equation for concentrated suspensions that accounts for shear-induced particle migration. *Phys. Fluids A* 1992;4:30-40.

155. Masson C., Baliga B.R. Simulation of gas-solid particle flows over a wide range of concentration. *Int. J. Num. Meth. Fluids* 1998;28:1441-1479.

156. Masson C. Numerical prediction of gas-solid particle flows over a wide range of concentration in irregular geometries. Ph.D. Thesis, Mechanical Engineering. Montreal: McGill University, 1993.

157. Lun C.K.K. Kinetic theories of granular flows. Ph.D. Thesis, Civil Engineering. Montreal: McGill University, 1985.

158. Johnson G.A., Massoudi M., Rajagopal K.R. A review of interaction mechanisms in fluid-solid flows. *U.S. Dept. of Energy Technical Report DOE/PETC/TR-90/9,* 1990.

159. Goldsmith H.L., Marlow J. Flow behaviour of erythrocytes. I. Rotation and deformation in dilute suspensions. *Proc. Royal Soc. London - Series B* 1972;182:351-384.

160. Goldsmith H.L. Red cell motions and wall interactions in tube flow. *Fed. Proc.* 1971;30:1578-1590.

161. Sinclair J.L., Jackson R. Gas-particle flow in a vertical pipe with particle-particle interactions. *AIChE J.* 1989;35:1473-1486.

162. Murthy J.Y., Mathur S. Periodic flow and heat transfer using unstructured meshes. *Int. J. Num. Meth. Fluids* 1997;25:659-677.

163. Demirdzic I., Lilek Z., Peric M. Fluid flow and heat transfer test problems for non-orthogonal grids: bench-mark solutions. *Int. J. Num. Meth. Fluids* 1992;15:329-354.